Mound and Vent Structures Associated With Gas Hydrates Offshore Vancouver Island: Analysis of Single-channel and Deep-towed Multichannel Seismic Data

by

Tao He

B.Sc, Peking University, 1999
M.Sc, Peking University, 2002

A Dissertation Submitted in Partial Fulfillment
of the Requirements for the Degree of

DOCTOR OF PHILOSOPHY

in the

SCHOOL OF EARTH AND OCEAN SCIENCES

Supervisory Committee

Mound and Vent Structures Associated With Gas Hydrates Offshore Vancouver Island: Analysis of Single-channel and Deep-towed Multichannel Seismic Data

by

Tao He

B.Sc, Peking University, 1999
M.Sc, Peking University, 2002

Supervisory Committee

Dr. George D. Spence (School of Earth and Ocean Sciences)
Supervisor

Dr. Roy D. Hyndman (School of Earth and Ocean Sciences)
Departmental Member

Dr. N. Ross Chapman (School of Earth and Ocean Sciences)
Departmental Member

Dr. Harry W. Dosso (Department of Physics and Astronomy)
Outside Member

Dr. Michael Riedel (Department of Earth and Planetary Sciences, McGill University)
Additional Member

Abstract

Supervisory Committee

Dr. George D. Spence (School of Earth and Ocean Sciences)
Supervisor

Dr. Roy D. Hyndman (School of Earth and Ocean Sciences)
Departmental Member

Dr. N. Ross Chapman (School of Earth and Ocean Sciences)
Departmental Member

Dr. Harry W. Dosso (Department of Physics and Astronomy)
Outside Member

Dr. Michael Riedel (Department of Earth and Planetary Sciences, McGill University)
Additional Member

The study focuses mainly on two gas hydrate-related targets, located on the Northern Cascadia Margin, offshore Vancouver Island: (1) a recently identified 70-80-m high carbonate mound, Cucumber Ridge, located ~3.5-km west of Ocean Drilling Program (ODP) Site 889 and Integrated Ocean Drilling Program (IODP) Site U1327, and (2) a large cold vent, Bullseye vent, which is up to ~500 m in diameter and was drilled by IODP at Site U1328. The objective of this thesis is to analyze seismic data that provide indicators of locally focused fluid flow and characteristics of the gas hydrate occurrence associated with these two features. A grid of closely-spaced single channel seismic (SCS) data was collected at Cucumber Ridge in July/August 2001, and deep-towed multichannel seismic (MCS) lines were collected using Deep-towed Acoustics and Geophysics System (DTAGS) at the Bullseye vent area and at Cucumber Ridge in October 2002.

The high-resolution SCS data, with a frequency bandpass of 40-150 Hz, recorded coherent reflectivity down to about 400 m beneath the seafloor, and provide excellent images of the subseafloor structure of Cucumber Ridge and of the gas hydrate bottom-simulating reflector (BSR) beneath it. Cucumber Ridge is interpreted to have developed as a structural topographic high in the hanging wall of a large reverse fault formed at the base of the current seaward slope. The fault zone provides pathways for fluids including gas to migrate to the seafloor where diagenetic carbonate forms and cements the near-

surface sediments. Over the seismic grid, heat flow was derived from the depth of the BSR. A simple 2-D analytical correction for theoretical heat flow variations due to topography is applied to the data. Across the mound, most of the variability in heat flow is explained by topographic effects, including a local 6 mW/m^2 negative anomaly over the central mound and a large 20 mW/m^2 positive anomaly over the mound steep side slope. However, just south of the mound, there is a 6-7 mW/m^2 positive anomaly in a 2-km-long band that has predominantly flat seafloor. Most of this anomaly is probably unrelated to topographic effects, but rather likely due to warm upward fluid flow along faults or fracture zones.

Towed ~300 m above seafloor, the high frequency (220-1k Hz) DTAGS signal can provide high vertical resolution images with increased lateral resolution. The major problems of DTAGS are significant nonlinear variations of the source depths and receivers locations. New routines were developed for optimal DTAGS data processing, mainly including (1) cable geometry estimation by node depths, direct arrivals and seasurface reflections using a Genetic Algorithm inversion method, (2) acoustic image stitching based on accurate relative-source positioning by crosscorrelation of redundant data between two adjacent shots, and (3) velocity inversion of wide-angle traveltimes using a nonlinear global grid search method.

The final processed DTAGS images resolve multiple seismic blanking zones and fine details of subseafloor features in the slope sediments. At Bullseye vent, where a 35-m-thick near-surface massive hydrate layer was drilled at U1328, the DTAGS data resolved the upper part of layer as a dipping diffraction zone, likely corresponding to a fracture zone. The inverted velocity structure in upper 100 m sediments successfully revealed a 17-m-thick layer of high velocity (~1650 m/s) just below seafloor, probably related to carbonate presence. A local high velocity zone, with a positive velocity anomaly of ~40-80 m/s in the upper 50 m beneath seafloor, was observed over the ~100-m wide region between U1328 and the deepest part of a seafloor depression; the high velocity zone is consistent with the dipping diffraction zone in the DTAGS image and with the massive hydrate drilled at U1328.

Table of Contents

Supervisory Committee ..... **ii**

Abstract ..... **iii**

Table of Contents ..... **v**

List of Tables ..... **x**

List of Figures ..... **xi**

Acknowledgments ..... **xvii**

Dedication ..... **xviii**

Chapter 1 Introduction **1**

1.1 General Overview 1

1.2 Organization of Thesis 1

1.3 Marine Gas Hydrates 2

1.4 Tectonic Setting 5

1.5 Mound and Vent Structures: Background 8

1.5.1 Mud/Carbonate Mound Structures 8

1.5.2 Cold Vents 11

1.6 Previous Gas Hydrate Studies Offshore Vancouver Island 13

1.6.1 Seismic Study Review 15

1.6.2 Non-seismic Methods 16

1.7 Study Area and Data Integration 17

1.8 Study Objectives 20

Chapter 2 Seismic Data Collection **21**

2.1 Teledyne's 2001 Survey at Cucumber Ridge 21

2.1.1 Survey Design 21

2.1.2 Seismic Equipment and Data Acquisition 21

2.1.3 Navigation and Bulk Shifting of Survey Lines 23

2.2 DTAGS2's 2002 Experiment 24
2.2.1 Survey Design 24
2.2.2 Seismic Equipment and Data Acquisition 27
2.2.3 Navigation Only Using Ship's DGPS Signal 29
2.2.4 Navigation within Acoustic Transponder Net 32

Chapter 3 Teledyne Single Channel Seismic Data Processing 38
3.1 Geometric Spreading Compensation 38
3.2 Butterworth Bandpass Filtering 38
3.3 Source Signature Deconvolution 41
3.3.1 Why Source Signature Deconvolution Is Needed 41
3.3.2 Methods of Source Signature Deconvolution 42
3.4 Predictive Deconvolution 49
3.5 Time Migration 50
3.6 Amplitude Balancing 53
3.7 Final Image Result 55

Chapter 4 DTAGS Multichannel Seismic Data Processing 57
4.1 Source Cross-correlation 57
4.2 Bandpass Filtering, Vibroseis Deconvolution and Spectral Balancing 59
4.2.1 Bandpass Filtering 59
4.2.2 Vibroseis Deconvolution 61
4.2.3 Spectral Balancing 65
4.3 Source and Receiver Depth Corrections 66
4.3.1 Onboard Processing for Imaging 68
4.3.2 Source Depth Variations and Nonlinear Array Tilting 72
4.3.3 DTAGS Cable Geometry Inversion 76
4.3.3.1 Picking SSR Times and Direct Arrivals 76
4.3.3.2 Invert the Whole Cable Geometry Using GA Method 78
4.3.3.3 Time Corrections for Cable Geometry and Source Depth Variations 84

4.4 DTAGS Data Imaging 89
4.4.1 Receiver Statics 89
4.4.2 Shot Statics and Image Stitching 92
4.4.3 DTAGS Imaging Process Summary 100
4.4.4 Post DTAGS Images on Map 102
4.4.5 Fine Tuning with Previous Seismic Grid 103
4.4.6 Image Comparisons 106

Chapter 5 Analysis and Interpretation: Cucumber Ridge 110
5.1 BSR Derived Local Variations of Heat Flow 110
5.1.1 Local Heat Flow Calculated From BSR Depths 111
5.1.1.1 Velocity-Depth Relationship and BSR Depth Calculation 111
5.1.1.2 Temperatures at Seafloor and the BSR 112
5.1.1.3 Thermal Conductivity and Heat Flow Calculation 114
5.1.1.4 Error and Uncertainty Estimates for the BSR Method 115
5.1.1.5 Comparison with ODP/IODP Sites 889 and U1327 Heat Flow 117
5.1.1.6 Comparison with Heat Flow from Sediment Heat Probe Measurements 119
5.1.2 BSR Heat flow observations 119
5.1.2.1 Regional Variations 119
5.1.2.2 Topographic Effect on Superficial Heat Flow over Mound 120
5.2 Seafloor Observations at Cucumber Ridge 124
5.3 Seismic Observations of Mound Structures 125

Chapter 6 Analysis and Interpretation: Bullseye Vent 135
6.1 Seismic Observations at Bullseye Vent 135
6.2 Blank Zones on the 2002 DTAGS2 Transit Line DT16 143
6.3 Velocity Analysis across Bullseye Vent 146
6.3.1 Standard Stacking Velocity Analysis 148
6.3.1.1 CMP Binning, CDP Sorting and Super-CDP Gathering 148
6.3.1.2 Time Corrections for Cable Geometry 149
6.3.1.3 Velocity Analysis 150

6.3.1.4 Uncertainty Estimation 155
6.3.2 Velocity Analysis Using Inverse Method 158
6.3.2.1 Inverse Assumptions 158
6.3.2.2 Inverse Algorithm 159
6.3.2.3 Model Test 167
6.3.2.4 Invert Field Data – Example of DT09 Segment across Bullseye Vent 171
1. Pick Target Reflectors 171
2. Inversion Results and Error Estimation 173
3. Interpretation 184
4. Comparison 187

Chapter 7 Discussions 192
7.1 Do Heat Flow Variations Indicate Fluid Flow? 192
7.2 Genesis of Cucumber Ridge Carbonate Mound 193
7.3 Focused Fluid Flow Venting – Mounds vs. Pockmarks 196

Chapter 8 Summary 199
8.1 A Methodology for Optimal DTAGS Data Processing 199
8.2 Evolution Model for Cucumber Ridge 200
8.3 Local High Fluid Flow over a Regional Heat Flow Map 201
8.4 Seismic Observations around Bullseye Vent 201
8.5 Suggestions for Future Work 203
8.5.1 DTAGS Cable Geometry Control and Data Recording 203
8.5.2 Optimal Inversions for Cable Geometry and Sediment Velocity 204
8.5.3 Interesting Targets for Later Cruise Project 204

References 205

Appendix A Excluded Process from the 2001 Teledyne SCS Data 215
A.1 Psudo-3D Binning and Trace Interpolation 215
A.2 Images after 2.5D Migration 220

Appendix B Frequency-Matching Method Used to the 2004 Teledyne Data... 222

Appendix C Equations for DTAGS Cable Geometry..... 226

C.1 Equation 4.3 and Equation 4.4 226

C.2 Equation 4.9 and Equation 4.10 227

List of Tables

Table 1.1 Overview of previous hydrate-related seismic surveys offshore Vancouver Island 14

Table 2.1 DTAGS Configuration during the 2002 DTAGS2 cruise 29

Table 4.1 Example of stitching result for survey line DT10 96

Table A.1 Summary of 3D Binning Result For 2001 Teledyne Data 217

List of Figures

Figure 1.1 Gas hydrate structure I. 3
Figure 1.2 Total organic carbon in the earth. 3
Figure 1.3 Temperature-depth conditions for the stability of gas hydrate 3
Figure 1.4 Origin of BSR 4
Figure 1.5 General tectonic setting of Northern Cascadia margin 6
Figure 1.6 Illustration of fluid expulsion model for gas hydrate formation 7
Figure 1.7 The exposed and the sediment-covered mounds on Orphan Knoll. 9
Figure 1.8 Seismic profile (GeoB02-430) across Mound Culebra 10
Figure 1.9 Images on Hydrate Ridge by a deep-towed video survey in 1996 12
Figure 1.10 Map showing seismic data sets used in the study area 18
Figure 2.1 Track lines of 2001 Teledyne grid 22
Figure 2.2 Seismic equipment deployment on the survey ship 23
Figure 2.3 Calculated shift times for the 2001 Teledyne SCS lines. 25
Figure 2.4 The advantage of deep-tow geometry in deeper water 26
Figure 2.5 Location of DTAGS2 survey lines in the region 27
Figure 2.6 The DTAGS tow body. 28
Figure 2.7 Sound pressure level as a function of frequency. 28
Figure 2.8 The ship's navigation (blue) and interpolated shot positions (red). 30
Figure 2.9 (a) Relative offsets before and after corrections for the abnormal values. (b) The distance of current shot by accumulating all previous offsets. 31
Figure 2.10 Positions of rover before and after manual correction 33
Figure 2.11 Decomposed coordinates of rover navigation for line DT09. 35
Figure 2.12 The offsets between current shot and the previous one 36
Figure 3.1 Seismogram panels showing direct arrivals recorded by Teledyne streamer and their autocorrelation functions 39
Figure 3.2 Mean amplitude spectrum of direct arrivals 40
Figure 3.3 Seismogram panels showing upper sediment reflections 40
Figure 3.4 Mean amplitude spectrum of upper sediment reflections 41

Figure 3.5 Extracted wavelet from the recorded seismogram in Figure 3.3 44
Figure 3.6 The computed amplitude spectra. 44
Figure 3.7 (a) Source signature recorded at shot hydrophone in the 1999 COAMS survey and (b) frequency spectrum for three sleeve gun records. 45
Figure 3.8 Minimum phase shaping filter using Claritas wavelet application. 46
Figure 3.9 Signature deconvolution test for uppermost sediment reflections 47
Figure 3.10 Spiking and signature deconvolution tests 49
Figure 3.11 (top) Image panels for different deconvolution strategies on direct arrival. (bottom) The corresponding autocorrelation functions. 51
Figure 3.12 (top) Uppermost sediment image panels for different deconvolution design windows. (bottom) The corresponding autocorrelation functions. 52
Figure 3.13 Seismic images time migration test 54
Figure 3.14 Final seismic imaging results 56
Figure 4.1 Pilot sweep and its amplitude spectrum. 58
Figure 4.2 Shot 111 acoustic panels of DTAGS2 survey line DT09 60
Figure 4.3 Envelope version of image panels in Figure 4.2. 61
Figure 4.4 The amplitude spectra corresponding to Figure 4.2. 62
Figure 4.5 Test panels for zero-phase Butterworth bandpass filtering. 63
Figure 4.6 Panels showing the Klauder wavelet 65
Figure 4.7 Test panels for spectral balancing on Shot 111 67
Figure 4.8 Survey lines and locations of piston coring around Bullseye vent 68
Figure 4.9 (a) Onboard footprint of DTAGS line DT09 (southwest half) 69
Figure 4.9 (b) Onboard footprint of DTAGS line DT09 (northeast half) 70
Figure 4.10 The depth variations of the four nodes along line DT09 71
Figure 4.11 Envelope of data waveforms from Shot 111 of survey line DT09. 73
Figure 4.12 Source and array geometry correction (Walia and Hannay, 1999) 74
Figure 4.13 Enlarged part showing envelope of sea surface reflections 75
Figure 4.14 Enlarged last 9 traces showing direct arrivals 77
Figure 4.15 Raypaths of sea-surface reflection and direct arrival 78
Figure 4.16 Average water velocities along DTAGS survey line DT10. 79

Figure 4.17 Illustration of variables and parameters for GA inversion. 80
Figure 4.18 GA optimizing process for Shot 2230 of survey line DT10..... 81
Figure 4.19 Inverted cable geometry and new SSR time for Shot 2230 82
Figure 4.20 The plotting of fitness values T_t for all shots of line DT10..... 83
Figure 4.21 Illustration of time correction for source/last receiver pair. 84
Figure 4.22 Illustration of computing average velocity along raypath. 86
Figure 4.23 Shot gathers before (top) and after (bottom) time corrections 88
Figure 4.24 (a) The cross-correlation lags of the receiver gather. (b) The lags are close to random variations after removing the geology patterns. 90
Figure 4.25 (a) Shot-gather-sorted cross-correlation lags of Shot 2301 (blue) and filtered low frequency geology structures (red). (b) Residual lags after geology information removed and final statics after rejecting "wild" points..... 92
Figure 4.26 RMP locations when Shot 111 marching away from Shot 110 94
Figure 4.27 Cross-correlation seismogram of overlapping trace pairs 94
Figure 4.28 The comparison of navigation intervals to optimal shot spacings. 95
Figure 4.29 Images of Shots 2202-2204, showing stitching areas 96
Figure 4.30 Comparison of lags for different uses. 98
Figure 4.31 Shot statics of survey line DT10 99
Figure 4.32 Stitched image for Shots 2202-2204 of survey line DT10. 100
Figure 4.33 Flow chart of DTAGS data processing for imaging..... 101
Figure 4.34 Acoustic image (100% coverage) of the survey line DT09 102
Figure 4.35 Bathymetry map showing the 2002 DTAGS2 survey line DT09 (rover corrected) crossing obliquely with Teledyne 2000 pseudo-3D grid. 103
Figure 4.36 The final shift result for DTAGS2 line DT09 104
Figure 4.37 Depths comparison between the bathymetry and seafloor reflections 105
Figure 4.38 Map view of a hydrate-related pockmark and associated seismic wipeout zone around Bullseye venting field (From Gettrust et al., 2004)..... 108
Figure 4.39 Map view and associated DTAGS seismic section with similar display as Figure 4.38. 108
Figure 4.40 DT09 of DTAGS and BT14 of Teledyne 2000 crossed each other 109

Figure 5.1 (a) A P-wave constant gradient velocity model. (b) Temperature-depth vertical profile in the seawater column. (c) The pressure–temperature phase diagram for the methane hydrate stability field. (d) Variation of thermal conductivity with depth below seafloor 113
Figure 5.2 BSR-derived heat flow map 118
Figure 5.3 The effect of seafloor topography on surficial heat flow. 120
Figure 5.4 Local heat flow variations and 2D model topographic corrections along 2001 Teledyne survey line SCS-42 across peak of the central mound..... 122
Figure 5.5 Local heat flow variations and 2D model topographic corrections along 2001 Teledyne survey line SCS-1 just south of the mound..... 123
Figure 5.6 Seabed-video images over the carbonate mound by (ROPOS)..... 124
Figure 5.7 Map view of selected seismic lines across Cucumber Ridge..... 126
Figure 5.8 Migrated seismic images of SCS33 and XL01 127
Figure 5.9 Migrated seismic image shows the NW part of IN11 129
Figure 5.10 Seismic images of SCS70 (migrated) and DT22..... 130
Figure 5.11 Seismic images of SCS16 (migrated) and DT21..... 132
Figure 5.12 NW seismic sections of IN26 (migrated) and DT16..... 134
Figure 6.1 Location of 2002 DTAGS2 lines, Teledyne 2000 single channel 3-D grid and COAMS 1999 multichannel grid around Bullseye vent..... 136
Figure 6.2 SE-NW seismic section showing hydrate cap details from Teledyne 2000 crossline XL75 137
Figure 6.3 Depth map of hydrate cap picked from Teledyne 2000 3-D grid 137
Figure 6.4 3D display of the same hydrate cap..... 138
Figure 6.5 SE-NW seismic sections showing hydrate cap details from DT16..... 139
Figure 6.6 SE-NW seismic sections showing hydrate cap details from DT17..... 140
Figure 6.7 SW-NE seismic section from DTAGS2 line DT09..... 141
Figure 6.8 Summary of the logging data at Site U1328 in the upper 150 m 142
Figure 6.9 (a) Conventional multichannel seismic image of IN26. (b) Acoustic image (100% coverage) of transit line DT16..... 144
Figure 6.10 CSEM resistivities..... 145

Figure 6.11 (a) Part of DT16 showing blanking zones 1 and 2 in amplitude envelope. (b) Part of 3.5 kHz subbottom profiler, displayed in amplitude envelope..... 147
Figure 6.12 Flow chart showing DTAGS data flow for CDP. 150
Figure 6.13 Constant velocity gathers (CVG) at super-CDP S317 151
Figure 6.14 Constant velocity gathers (CVG) at super-CDP S377 152
Figure 6.15 RMS velocity and interval velocity on super-CDP S317..... 153
Figure 6.16 RMS velocity and interval velocity on super-CDP S377..... 154
Figure 6.17 One-layer model simulating cable geometry corrections..... 156
Figure 6.18 Sensitivity test for interval velocity of sediment layer 1..... 157
Figure 6.19 Model illustration of the ray path through 2 sediment layers..... 161
Figure 6.20 Example of ray paths to the farthest trace.. 162
Figure 6.21 Ray paths showing sampling rate..... 164
Figure 6.22 A hypothetical one-layer model consisting of 4 sub-layers 168
Figure 6.23 The result for inverting the hypothetical model 169
Figure 6.24 Inverted model results after adding a 10 times level noise 170
Figure 6.25 The comparisons of true model, inverted noise-free model and inverted model with 10 times level noise added..... 171
Figure 6.26 Picked reflectors for model inversion on DT09 172
Figure 6.27 Target layers 1-4 within a shot gather..... 174
Figure 6.28 Inverted depths and corresponding average velocity distribution..... 175
Figure 6.29 Details of inversion results for layer1. 176
Figure 6.30 Details of inversion results for layer2. 177
Figure 6.31 Details of inversion results for layer3. 178
Figure 6.32 Details of inversion results for layer4. 179
Figure 6.33 Histograms of the reflection point distribution 180
Figure 6.34 Results for sensitivity of average sediment velocity. 182
Figure 6.35 Shot-to-shot comparison of maximum horizontal source-receiver offsets between linear cable geometry and inverted cable geometry 183
Figure 6.36 Inversion result by using linear cable geometry..... 184
Figure 6.37 Shear strength measurements at Holes U1328B and U1328C 186

Figure 6.38 Comparison of inverted average velocities and interval velocities 187
Figure 6.39 Comparisons of the inversion results with the U1328 drillhole logs .. 189
Figure 6.40 Hole U1328C vertical seismic profile. 191
Figure 7.1 Local heat flow variations and 2D model topographic corrections along the 1999 COAMS grid IN-18 across flat area east of the central mound 194
Figure 7.2 Three deepwater types of seafloor responses 197
Figure A.1 The psudo-3D binning area for the 2001 Teledyne SCS data 216
Figure A.2 (a) Original pseudo-3D inline IL-1103 showing typical inline seismic section with empty bins. (b) Interpolated seismic section of IL-1103. 218
Figure A.3 (a) Original pseudo-3D crossline CL-1175 showing typical cross-line empty bins. (b) Interpolated seismic section of CL-1175 219
Figure A.4 Seismic structures below the carbonate mound. 221
Figure B.1 Typical direct arrivals of the 2004 Teledyne SCS data and the corresponding autocorrelation function 222
Figure B.2 Ringy power spectrum of direct arrivals 223
Figure B.3 (left) uppermost sediments reflections with bubble ghost and clear BSR. (right) Corresponding autocorrelation function 224
Figure B.4 Extracted wavelet from the recorded seismogram in Figure B.3 using the Frequency-Matching method 225
Figure B.5 The computed amplitude spectra of the 2004 Teledyne data for the Frequency-Matching method.. 225
Figure C.1 Illustration of ray path related with Equation 4.3 and Equation 4.4. .. 226

Acknowledgments

First, I would like to thank my supervisor Dr. George D. Spence for his great support during the thesis and many brilliant discussions. I also would like to thank my committee members Dr. Roy D. Hyndman, Dr. N. Ross Chapman, Dr. Michael Riedel and Dr. Harry W. Dosso for their support and suggestions during the thesis. I especially enjoyed the happy time with my officemates Martin Scherwath and Ranjan Dash. This is also the point to remember my friends in the E-Hut and PGC for interesting scientific and social discussions: here first of all Yan, Songhua, Hangfang, Caroll, Iulia, Ivana, and especially Mae, who gives me many helpful suggestions for this thesis.

I learned much at sea during exciting cruises onboard CCGS John P. Tully. At this point I would also like to thank the captain and crews of the CCGS John P. Tully and their enthusiastic support during the different cruises. Special thanks go to Bob MacDonald and Ivan Frydecky for their marine technical support during seismic data and core acquisition, and to the ROPOS team for their excellent operations of the submersible. The shiptime and most of the marine equipment were provided by the Pacific Geoscience Centre, Geological Survey of Canada.

I want to thank the research grant and co-op position for financial support by hydrate research group at the University of Victoria, which has been supported for many years through grants from the Natural Sciences Engineering Research Council to Spence, Chapman, and Hyndman.

I further want to express many thanks to Seismic Micro Technology for donating the integrated geoscience interpretation software package “The Kingdom Suite” to the University of Victoria. The seismic work carried out would be impossible without state of the art seismic processing software.

Dedication

I want to thank my dear wife and my parents for their support and patience with me being so far away from home. Without them this work would have never been possible. Also this thesis is especially dedicated to my lovely baby: you are the biggest power to push daddy to finish this thesis as soon as possible.

我由衷地将这部博士论文献给我亲爱的妻子、父母和弟弟，谢谢你们一直以来对我的关心和照顾。这部论文也是献给我即将诞生的小宝宝，你的到来为爸爸增添了莫大的动力。

Chapter 1

Introduction

1.1 General Overview

This dissertation presents data processing results and associated studies from (1) high resolution single channel seismic surveys around a carbonate mound and (2) deep-towed multichannel seismic surveys across vent sites. Deep sea gas hydrate occurs in both regions. The study area, located on the accretionary prism of the northern Cascadia subduction zone offshore Vancouver Island, Canada, has been the focus of marine gas hydrate studies with many detailed scientific experiments, especially 2-D seismic (single channel and multichannel) surveys, regional wide angle ocean bottom seismic surveys, heat flow probe measurements and deep ocean drilling (Ocean Drilling Program Leg 146, Site 889/890; Integrated Ocean Drilling Program Expedition 311, Site U1327/1328).

1.2 Organization of Thesis

The first chapter of this thesis describes the tectonic setting of the Northern Cascadia Margin, general characteristics of mud/carbonate mounds and cold vents associated with gas hydrates, experiments carried out so far in the study area, and major objectives of this study. Details of the 2001 Teledyne single channel seismic (SCS) data collection at Cucumber Ridge and the deep-towed multichannel seismic (MCS) data collection during the 2002 DTAGS2 survey, including necessary navigation corrections, are given in Chapter 2. Data processing for these two surveys are described in Chapter 3 and 4, respectively. Data analysis and interpretation at Cucumber Ridge are given in Chapter 5, including mapped heat flow variations from BSR depths. The analysis and interpretation for DTAGS data, mainly around Bullseye vent, are presented in Chapter 6, including acoustic features of subseafloor sediments and velocity analysis using a newly-developed inversion method. Chapter 7 discusses some results from above seismic analyses, including (a) heat flow estimates from BSR-depth variations and inferred fluid flow, (b) origin of the carbonate mound, and (c) two indicators of locally focused fluid

flow – seafloor mounds and pockmarks. The summary of this dissertation and suggestions for future work are given in the last chapter, Chapter 8.

1.3 Marine Gas Hydrates

The ice-like deep sea gas hydrates have clathrate structure (Figure 1.1) and are found stable up to temperatures of 10-30 ^{o}C at depths several hundred metres beneath the seafloor on most continental slopes around the world, mainly beneath continental margins having thick sedimentary sections.

Gas hydrate has been a very active research topic in the last 20 years, because:

1. Methane is a very significant greenhouse gas and its global warming potential is about 20 times greater than an equivalent volume of CO_2 (Shine, 1990). Thus, natural gas hydrate may also play a role in climate change.

2. Gas hydrate is estimated to contain a very large amount of methane, and therefore could be an important hydrocarbon fuel resource in future. Hunt (1979) indicated that gas hydrate can fill up to 90% of the sediment pores and the volume ratio of free methane gas to solid hydrate is about 150:1. Gas hydrate may represent a vast fuel reservoir, but the various estimates of total carbon content in marine and permafrost gas hydrate are speculative. The estimates made in the late 1980s–early 1990s indicates that global hydrate-bound gas is 21×10^{15} m^3 of methane at STP (or 10,000 Gt of methane carbon (e.g., Kvenvolden, 1993; Figure 1.2). However, recent studies only support a much smaller value in the range $(1–5)\times10^{15}$ m^3 of methane (~500–2500 Gt of methane carbon) (Milkov, 2004).

3. Gas hydrate has also been associated with some geological hazards, such as slumping or instability during drilling. The stability of gas hydrate is primarily controlled by pressure and temperature (Figure 1.3). The second-order controls include the gas compositions and pore fluid salinity (e.g. Clennell et al., 1999). Thus, a disturbance in local temperature and pressure regime can easily cause hydrate dissociation and methane release into the ocean. McIver (1982) also suggested that potential geohazards may be produced because of pore overpressure and a zone of low shear strength where the methane gas is released. Such hazards include failure from

gravitational loading, or massive submarine slumps and slides initiated by seismogenic disturbance.

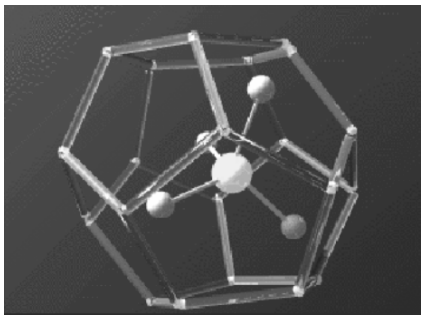

Figure 1.1 Gas hydrate structure I showing carbon (centre) and hydrogen (attached to centre) trapped in ice lattice. (Source: United States Geology Survey).

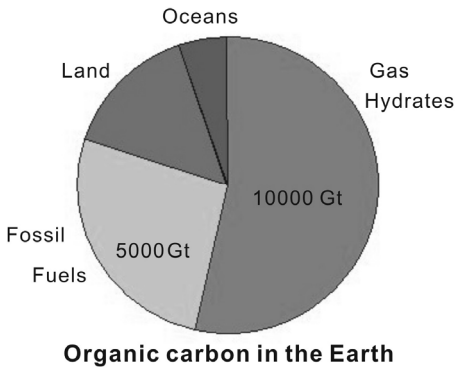

Figure 1.2 Total organic carbon in the earth.

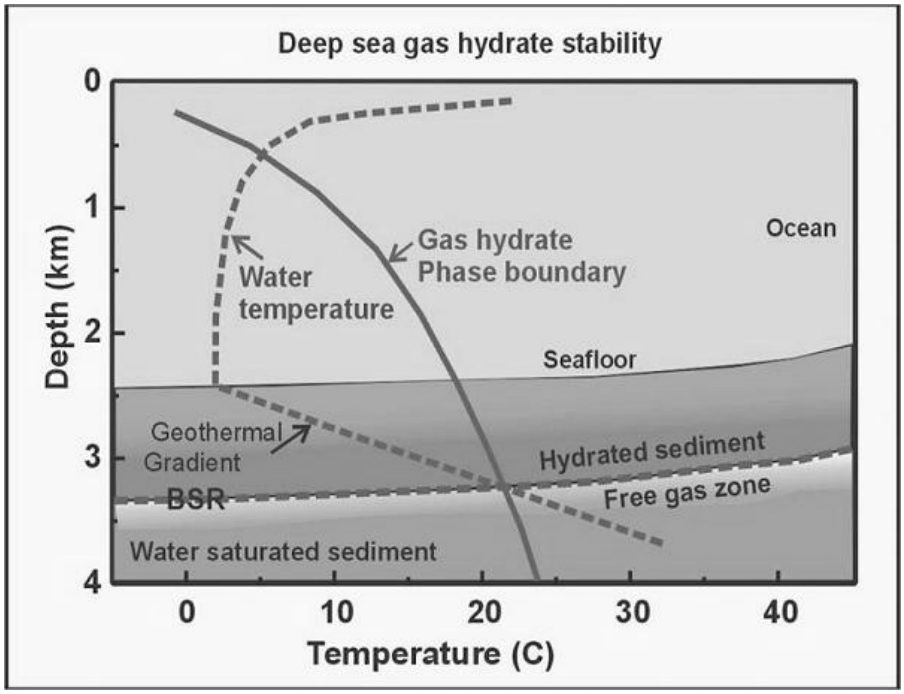

Figure 1.3 Temperature-depth conditions for the stability of marine gas hydrate (from Hyndman and Dallimore, 2001). The heavy line represents the gas hydrate phase boundary, while the dashed line presents a simplified temperature profile. The field of hydrate stability is defined by the intersection of the phase boundary with the temperature profile.

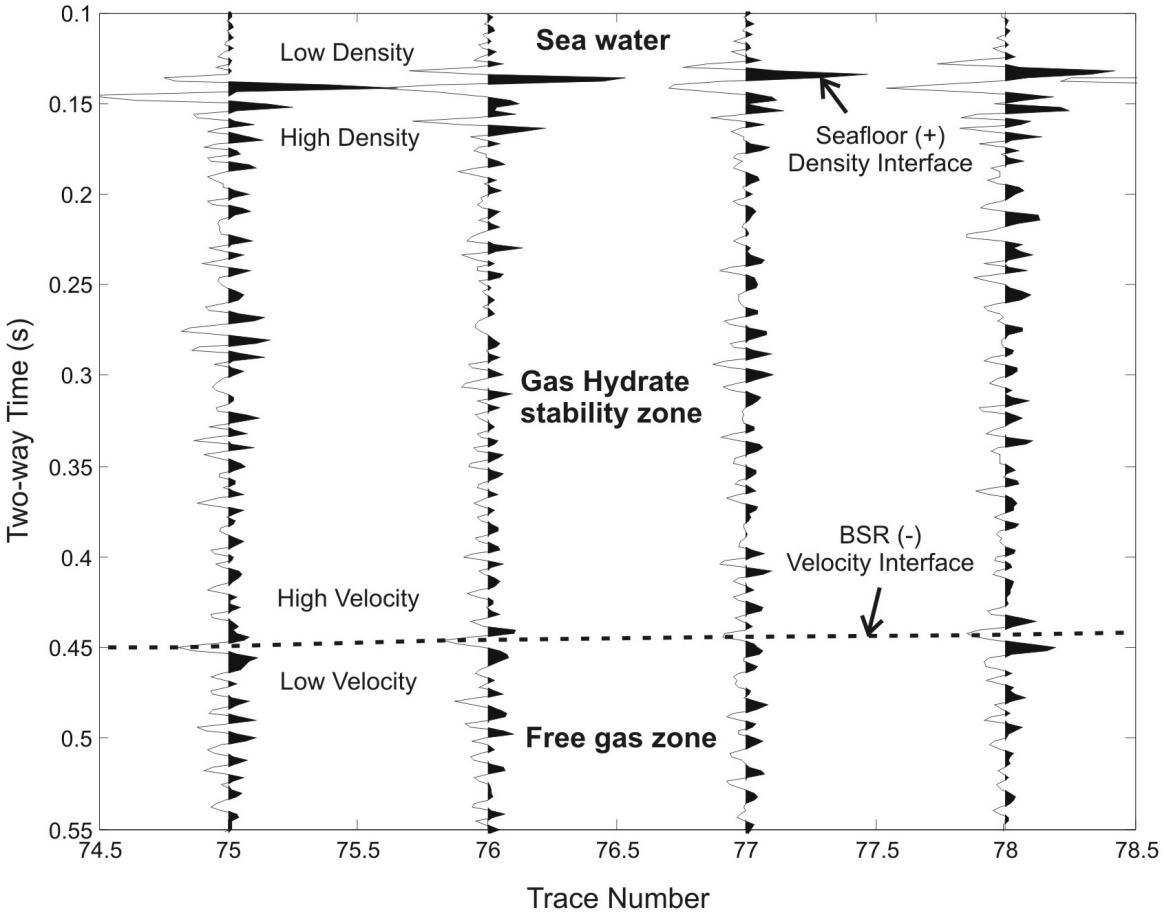

Figure 1.4 Origin of BSR. If seafloor is defined to have positive polarity, produced mainly by density contrast at the interface of seawater and sediments, then BSR has a negative polarity, produced by a negative velocity contrast.

The primary seismic indicator of marine gas hydrate is the presence of a Bottom Simulating Reflector (BSR) that parallels the seafloor on seismic reflection profiles. The BSR is characterized by a high amplitude negative reflection (assuming positive reflection polarity of the seafloor) (Figure 1.4). This change in polarity indicates a negative impedance contrast. Because seismic impedance is the product of density and seismic velocity and density is not expected to change much in hydrate-bearing sediments, the negative contrast is mainly related to a decrease in seismic velocity. Normally seismic velocity is increased by the presence of hydrate due to the replacement of pore water of a velocity of about 1500 m/s with the solid, ice-like hydrate of a velocity of about 3300 m/s (Lewin and Associates Inc., 1983). The decrease in velocity below the BSR is likely due

to the presence of free gas below the stability zone. As mentioned earlier, hydrate stability is a function of pressure and temperature. For example, during an ice age with low sea level, decreased pressure will cause the base of the hydrate stability field to move up through the sediments and result in hydrate dissociation. However, this free gas may not be released because of the barrier of overlying hydrated sediments.

1.4 Tectonic Setting

The study area is located on the Vancouver Island continental slope (Northern Cascadia accretionary margin) (Figure 1.5). Seaward of the deformation front, the entire sediment section of the Cascadia basin is 2–3 km thick and consists of pre-Pleistocene hemipelagic sediments overlain by a rapidly deposited Pleistocene turbidites (Davis and Hyndman, 1989). The incoming subducting sedimentary cover is scraped off the oceanic plate at the deformation front along mega-thrusts that extend down to near the top of the ocean crust. The sedimentary prism is formed as a result of almost complete accretion. The base of the slope is outlined by elongate anticlinal ridges with elevations as much as 700 m above the adjacent basin. Landward of the deformation front, the seafloor rises rapidly through a series of well-defined thrust faults. The study area is located at a bathymetric bench with a depth of 1200–1400 m. ODP Site 889 and nearby IODP Site U1327 were located near a topographic high on this bench (Figure 1.5). At this site Westbrook et al. (1994) described that sediments below 128 mbsf (meters below seafloor) are deformed, compacted and cemented Cascadia Basin sediments; above the accreted basin sediments, in-situ deposited and little deformed slope basin sediments consist of a sequence of silty clays and clayey silts interbedded with fine sand turbidities.

The northern Cascadia margin has been the focus of many subduction zone investigations, including those of the LITHOPROBE multidisciplinary program (Hyndman, 1995). The offshore data collection includes detailed gravity, magnetics, bathymetry, SeaMARC II, acoustic imagery, geological sampling, heat probe, seismic refraction, and single and multichannel seismic reflection data (Clowes et al., 1987; Davis et al., 1987; Yorath et al., 1987; Davis and Hyndman, 1989; Davis et al., 1990; Hyndman et al., 1990; Hyndman et al., 1994). These studies show that (1) the oceanic

crust is produced at the nearby Juan de Fuca ridge system; (2) the Juan de Fuca plate converges orthogonally to the North American plate at a rate of 45 m/m.y.; and (3) as indicated by magnetic anomalies, the age of crust is around 6 Ma old at the deformation front (Figure 1.5).

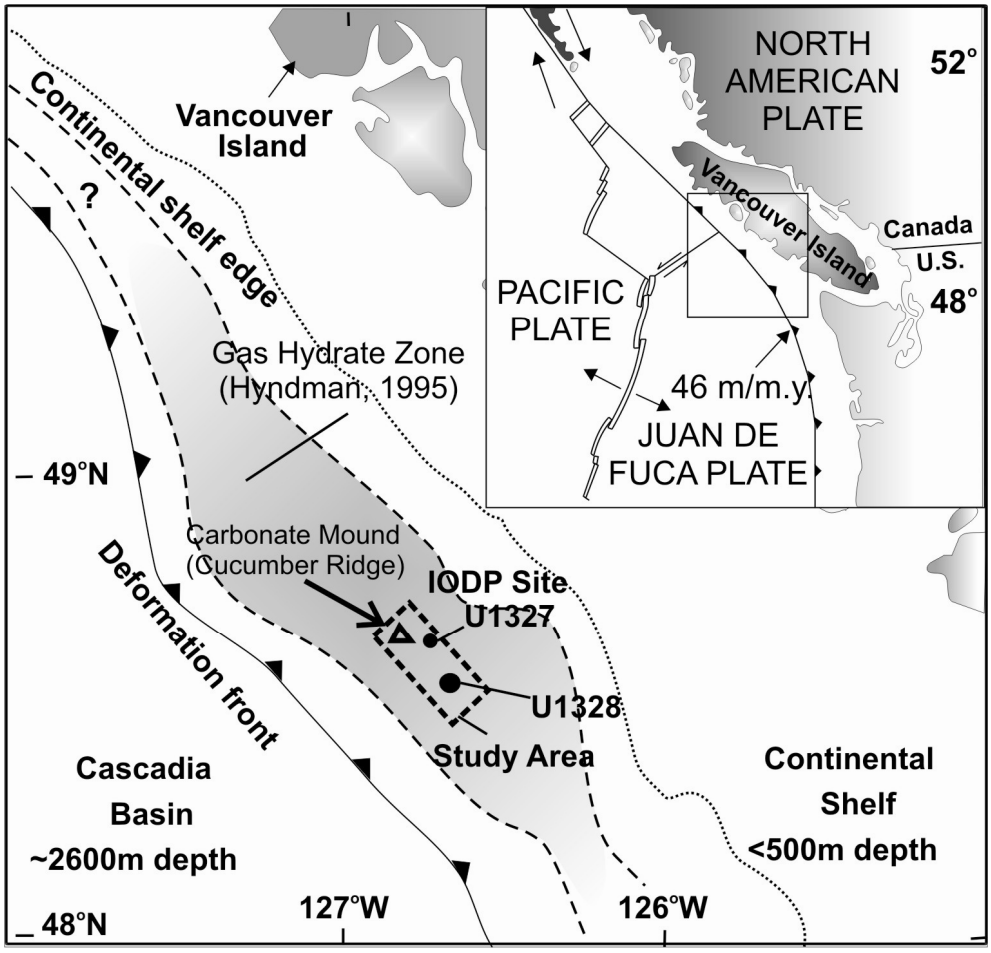

Figure 1.5 General tectonic setting of Northern Cascadia margin. The dashed box indicates the study area of the detailed survey location on mid-slope region off Vancouver Island.

The Cascadia margin also contains one of the best-studied occurrences of gas hydrate. Off Vancouver Island, a hydrate BSR occurs in a 30 km wide band parallel to the coast beneath much of the continental slope (Figure 1.5). In the model of Hyndman and Davis (1992), gas hydrate forms within the Cascadia accretionary margin by removal of methane from regional diffusive upward fluid flow driven by tectonic compression (Figure 1.6). In this model the concentration of gas hydrate is expected to be highest near

the base of the gas hydrate stability zone (GHSZ) above the BSR, and gradually decreases upward. However, this model does not account for the recent results from Expedition 311, which shows that by far the largest concentrations of gas hydrate (in sections several tens of meters thick and exceed 80% of the pore volume) occur at a shallow depth of ~100 meters below seafloor (e.g., at Sites U1326 and U1327), where the amount of methane exceeded the local methane solubility threshold in the pore fluid (Expedition 311 Scientists, 2006a). Also the concentration of near-surface gas hydrate formation is likely higher for focused fluid/gas flow within active cold vent fields associated with fault-related conduits (e.g., Site U1328). Focused flow represents an alternate mechanism to the widespread fluid flow model although it is unknown how important these cold vents are in the total budget of fluid flow in an accretionary prism at this time (Expedition 311 Scientists, 2006a).

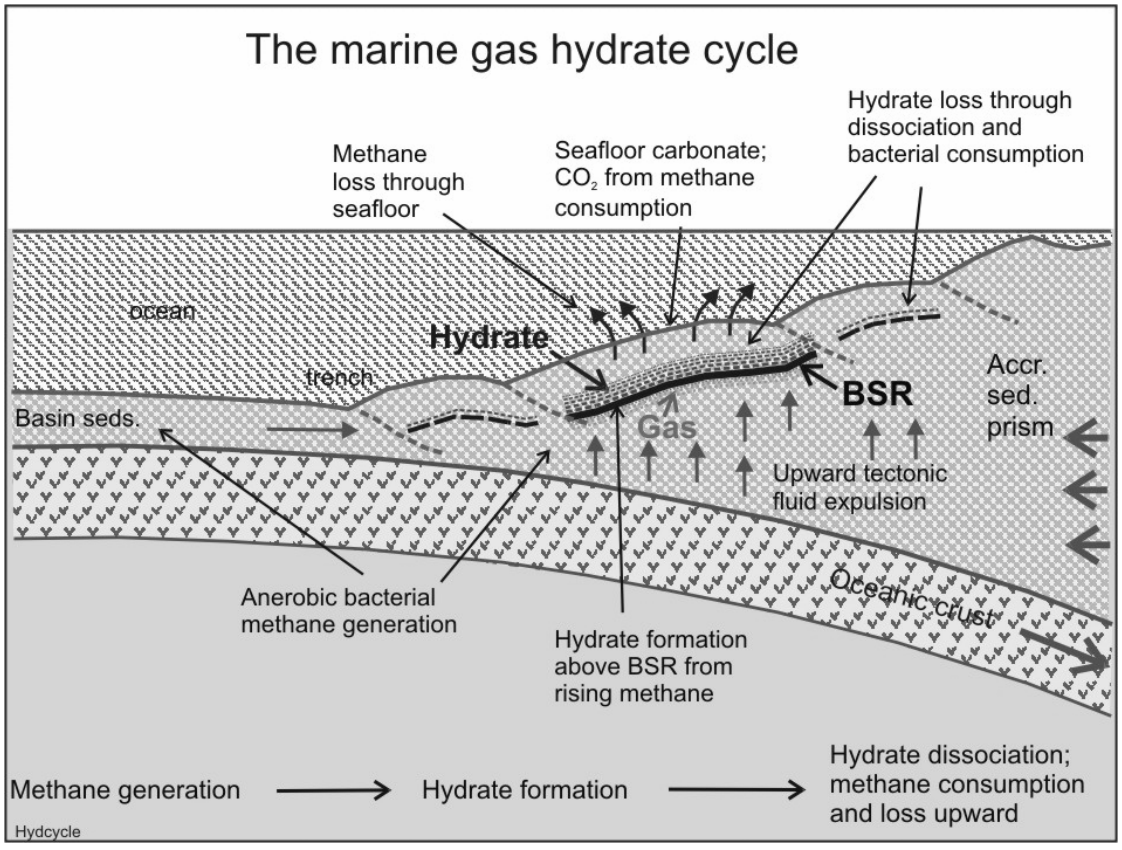

Figure 1.6 Illustration of fluid expulsion model for gas hydrate formation through removal of the methane carried by upward migrating pore fluids. (After Hyndman and Davis, 1992)

1.5 Mound and Vent Structures: Background

Worldwide, two types of locally focused fluid flow occur. These are cold vents, and somewhat larger carbonate mound structures. In the study area, both features occur: the Bullseye vent field is an example of the former, up to ~500 m across (Riedel et al., 2002; 2006a), while Cucumber Ridge is an example of the latter structure. To compare these two locations with other locations worldwide, the typical characteristics of mud/carbonate mounds and vents are described below.

1.5.1 Mud/Carbonate Mound Structures

As one of the manifestations of focused fluid flow, formations of mud and carbonate mounds are observed on detailed side-scan sonar, swath bathymetry maps and seismic sections, particularly those associated with 3D surveys. On passive margins, recent reports are of bioherms in the Porcupine Basin offshore Ireland (Baileya et al, 2003) and in the north-eastern Orphan Basin offshore Newfoundland on the east coast of Canada (Enachescu, 2004), and mud volcanoes on the southwest African continental margin off South Africa (Ben-Avraham et al., 2002). On active margins, examples are mud diapirism on the Mediterranean Ridge (Cita et al., 1989), mud volcanoes near Barbados (Westbrook and Smith, 1983) and active mud domes offshore Nicoya Peninsula, Costa Rica (Grevemeyer et al., 2004).

Although the processes are not totally understood, most carbonate mounds along the continental margins of the world have been interpreted to originate (a) directly by development of bioherms, such as coral reefs, often associated with hydrocarbon upwelling (Enachescu, 2004), or (b) initially by forming a fluid expulsion mud volcano followed by authigenic carbonate formation (Kopf, 2002).

Typical examples of the bioherm origin are the deep-sea carbonate mounds recently found in the north-eastern Orphan Basin and on the Orphan Knoll offshore Newfoundland (Figure 1.7) (Enachescu, 2004). Based on evidence from seismic profiles, sidescan sonar data, bottom photography and sampling, Enachescu (2004) suggested that these giant carbonate mounds seem a melange of reef carbonate produced by the rapid

growth and breakdown of cold-water corals, and/or siliceous organisms and precipitates. The bioherm origin may result from a mixed organic-inorganic environment very favorable for coldwater marine organisms. The organisms are fed from either hydrocarbon rich vents or hydrothermal fluids rising through deep-seated faults at the water bottom.

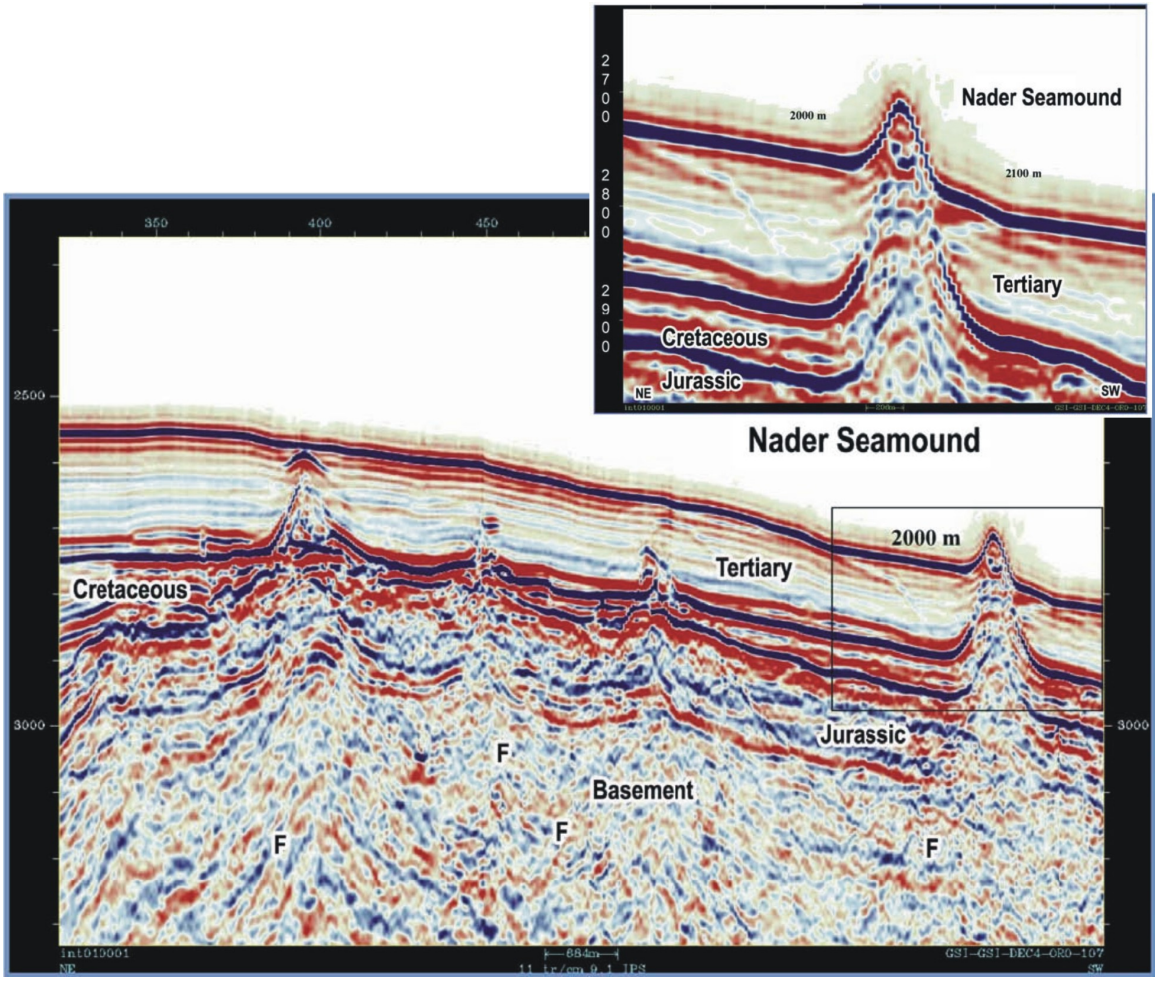

Figure 1.7 Detail of seismic line showing the exposed and the sediment-covered mounds on Orphan Knoll. The mound roots connect to deep-seated faults (F). Box identifies zoom contained in the inset figure of expanded view showing the emerged and probably exposed Nader Seamound on the Orphan Knoll. Mound reveals evident recent growth through late Tertiary to Recent time. The Nader Seamound is 800-400 m wide and at least 300 m tall, if considering its root in Jurassic sediments. (After Enachescu, 2004)

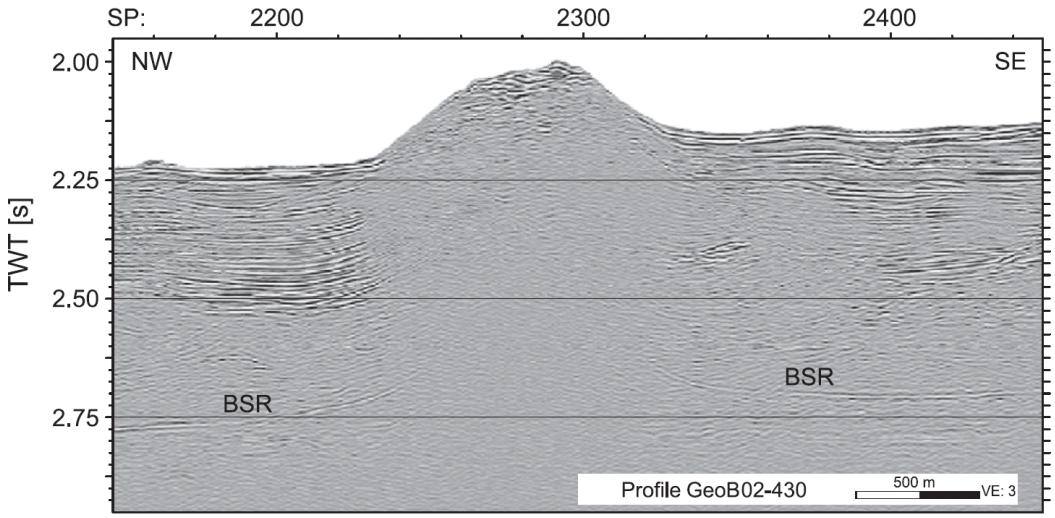

Figure 1.8 Time-migrated high-resolution multichannel seismic profile (GeoB02-430) across Mound Culebra. The most prominent feature is a bottom simulation reflector (BSR). Note the lack of seismic reflections beneath the mound. The diminished reflector amplitudes beneath the mound is likely due to lack of signal penetration, perhaps caused by upward fluid flow. (From Grevemeyer et al., 2004)

Milkov (2000) summarized two mechanisms for mud volcano formation: (1) sediment-carrying fluid migrates through the body of a seafloor-piercing diapir and a mud volcano forms directly on top of it as a consequence; (2) more commonly, a mud volcano forms as a result of the rise of fluidized mud along faults and fractures. These two mechanisms may also occur simultaneously. In any case, the upward flowing fluids bring hydrocarbon to the water bottom, which either feeds seafloor carbonate organisms or is oxidized directly into carbonate. The diagenetic carbonate cements the mud and turns the feature into a carbonate mound.

A recent report on an active mud dome (Mound Culebra) in a compressional tectonic setting offshore Nicoya Peninsula, Costa Rica (Grevemeyer et al., 2004) presents an example of the first mechanism in the classification of Milkov (2000) for modern carbonate build-up. As described by Grevemeyer et al. (2004), Mound Culebra is characterized by vent biota nurtured by methane emission, broadly authigenic carbonate formation at its crest, and a high heat flow anomaly landward of the mound probably due to fluids rising from depth below the dome. However, no faults that might carry fluids upward are apparent on the seismic image across this dome (Figure 1.8). The growth of

Mound Culebra may be driven mainly by buoyancy and related to the extrusion of fluid-rich, fine-grained sediments according to Kopf (2002). The warm fluids, originating at greater depth, migrated upward along permeable fractures and triggered the ascent of the liquefied mud with a density inversion (Hensen et al., 2003). Also the methane included in the fluids may have further lowered the density of the mud (e.g., Hedberg, 1974).

1.5.2 Cold Vents

As described by Riedel et al. (2006a), cold vents are locations of locally focused fault-related fluid flow usually associated with methane venting and often with gas hydrate formation. Cold vents may represent a much more important factor in the fluid-carbon-gas budget in accretionary prisms and play a more important role in climate change than previously thought. Thus, cold vents have increasingly become a major part of research activities.

Only a limited number of cold vents are active and emanating gas bubbles, which can be directly observed visually with a remotely operated submersible. Sometimes a vigorous gas plume will cause an acoustic anomaly in the water column, which can be detected by narrow beam echosounders (e.g., Figure 1.9, Suess et al., 2001). For those dead or intermittent cold vents, however, there are many other indicators. The main manifestations of cold vents, as observed on the seafloor, are (1) chemo-synthetic communities nurtured by methane emission (Lewis and Cochrane, 1990; Riedel et al., 2006a), (2) massive carbonate crusts (Ritger et al., 1987), (3) near-seafloor/floating gas hydrate (MacDonald et al., 1994; Suess et al., 2001), and (4) seabed pockmarks (Hovland et al., 1993). Seismically, other indicators are (1) blank zones (Riedel et al., 2002), (2) shallow/elevated BSRs (Wood et al., 2004; Tréhu et al., 2003), and (3) local velocity pull-up/pull-down features (Scholl et al., 1978). Examples of these indicators are found globally, including on the Cascadia margin (Ritger et al., 1987; Riedel et al., 2006a), Gulf of Mexico (MacDonald et al., 1994), Chile margin (Bangs et al., 1993), Nankai Trough (Ashi et al., 2002; Nouzé et al., 2004), Aleutian Trench (Suess et al., 1998), Black Sea (Egorov et al., 1998), East Sea of Korea (Lee et al., 2005), and Storegga margin (Vogt et al., 1999).

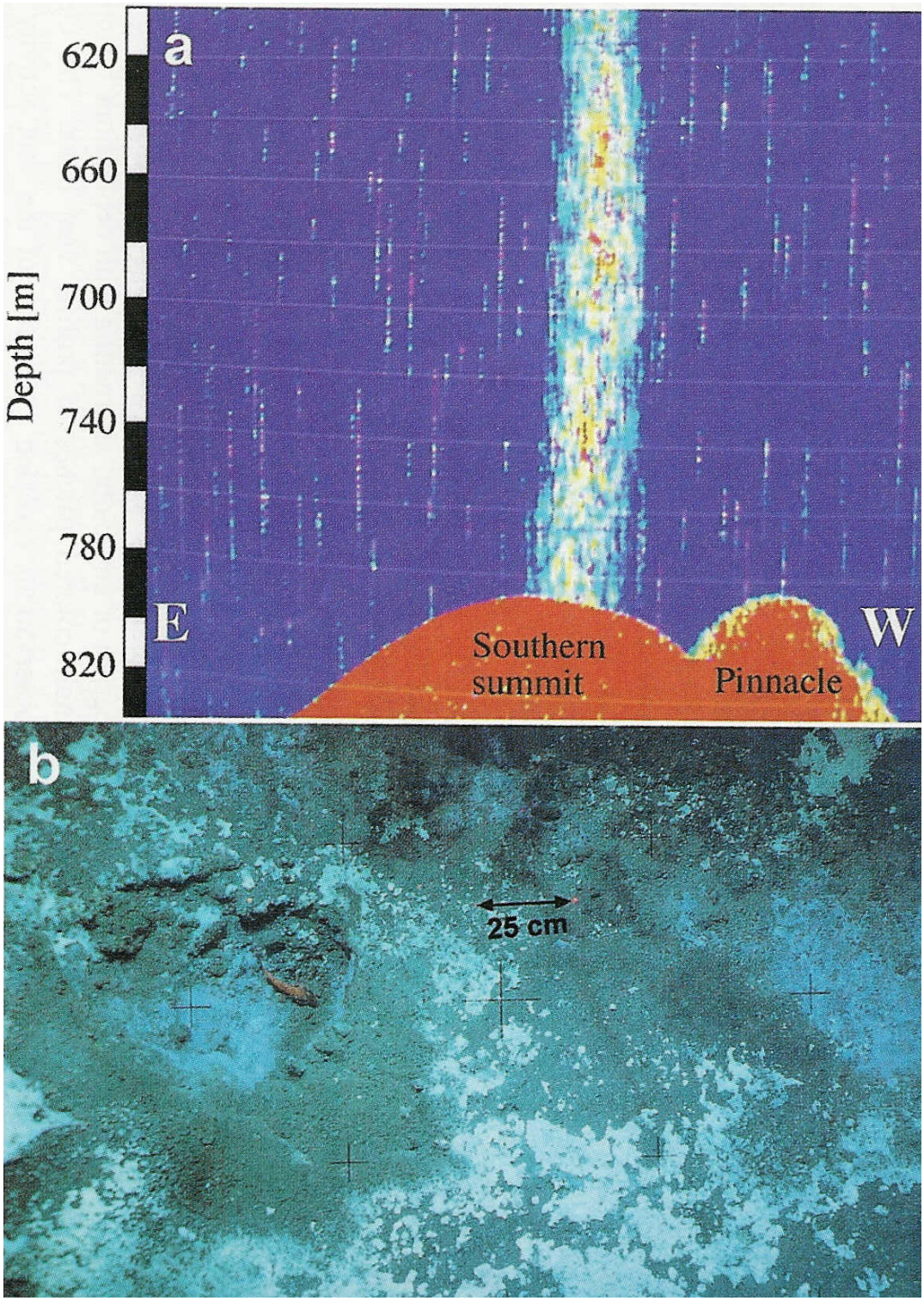

Figure 1.9 Images on Hydrate Ridge by a deep-towed video survey in 1996: (a) Plume image above southern summit and pinnacle; (b) Seafloor image of microbial mat and orifice of vent (circular depression). (After Suess et al., 2001)

There are several different mechanisms proposed for the origin of the seismic blanking and for the associated implications concerning the nature of the fluid venting. Wood et al. (2002) proposed that the entire blank zone is a gas chimney of rising warm fluids, which significantly perturb the base of gas hydrate stability zone. Riedel et al. (2002) suggested that much of the blanking is due to near-surface carbonate or to the massive hydrate layer at the surface; additional blanking may be due to scattered accumulations of hydrate in the subsurface. Zühlsdorff and Spiess (2004) argued that the oblong shape of pockmarks and surface small mounds associated with the cold vents are created by natural hydraulic fracturing, induced by a local elevation in the seafloor and BSR; the blanking zones below them are produced by free gas bubbles within those hydraulic fractures, particularly in the period following a fluid expulsion event.

Hydrate Ridge, located in an accretionary prism on the southern Cascadia margin, offshore Oregon, is currently the best-studied location of focused fluid flow associated with thrust faults (e.g., Suess et al., 2001). The active venting of fluids and gases and exposures of methane hydrates at the seafloor on Hydrate Ridge are related to the well known fault pattern due to the evolution and growth of the accretionary complex of the Cascadia convergent margin. Suess et al. (2001) showed submersible and deep-towed images of seafloor manifestations associated with methane hydrate, such as pockmarks, sediment drifts, carbonate pinnacles, hydrate exposures, bacterial mats and clam colonies. Reported by Tréhu et al. (2004), recent ODP drilling (Leg 204) revealed that the sediments of the summit of southern Hydrate Ridge contain hydrate with concentrations as high as 30%–40% of total sediment volume.

1.6 Previous Gas Hydrate Studies Offshore Vancouver Island

Since late 1980's, intensive studies for gas hydrate occurrence have been carried out on the Northern Cascadia accretionary margin offshore Vancouver Island. Table 1.1 summarizes the data collection surveys as well as the publications related to the data processing and interpretation.

Table 1.1 Overview of previous hydrate-related seismic surveys offshore Vancouver Island

YEAR OF SURVEY	SEISMIC SOURCE AND FREQUENCY RANGE	RECEIVER	PUBLICATIONS
1989	Airgun array; up to 100 Hz	144-ch MCS	Hyndman & Spence (1992); Yuan et al. (1994,1996,1999); Chen et al. (2007)
1993	Airgun (0.651, 1.971), 30-175 Hz	SCS, OBS	Spence et al. (1995); Hobro et al. (1998); Fink & Spence (1999); Zühlsdorff et al. (1999,2000)
1996	Airgun, up to 100 Hz	24-ch short-offset MCS	MSc thesis by Y. Mi (1998); Ganguly et al. (2000)
1997	Helmholtz resonator (sweep), 250-650 Hz	48-ch DTAGS (complicated array shape)	Walia & Hannay (1999); Gettrust et al. (1999); Chapman et al. (2002)
1998	Airgun, 40 cu.in., up to 200 Hz	102-ch MCS COAMS (Generally Poor data quality)	Currie et al. (1999)
1999	Airgun, 40 cu.in., up to 200 Hz; 3.5 kHz subbottom profiles	102-ch MCS COAMS, SCS, OBS	Riedel et al. (2002); Zykov & Chapman (2004)
2000	GI gun (0.7l/0.7l), up to 200 Hz; 3.5 kHz subbottom profiles	SCS (Sonne cruises)	Zühlsdorff et al. (2000); Zühlsdorff & Spiess (2004)
2001	Airgun, 40 cu.in., up to 200 Hz	SCS (clear image of BSR)	He et al. (2007)
2002	Helmholtz resonator (sweep), 220-1000 Hz	48-ch DTAGS2 (nonlinear tilting)	Gettrust et al. (2004); this study
2003	Airgun, 40 cu.in., up to 200 Hz	SCS (need re-digitize)	
2004	Airgun, 40 cu.in., up to 200 Hz	SCS (clear image of BSR)	
2005	Airgun, 210 cu.in., up to 180 Hz	SCS, OBS	

* COAMS: Canadian Ocean Acoustics Measurement System

1.6.1 Seismic Study Review

There are mainly three kinds of seismic data sets collected on the northern Cascadia Margin in recent decades:

1) Conventional surface-towed airgun seismic surveys, including 2D/3D single channel seismic (SCS) and multichannel seismic (MCS) data.

2) Deep-towed Acoustics and Geophysics System (DTAGS), whose source is a Helmholtz resonator emitting a chirp-like sweep signal in the frequency range of 250-650 for the original version and 220-1000 Hz for the most recent model. This system achieves much higher vertical resolution in imaging the subsurface than surface-towed systems.

3) Ocean Bottom Seismometers (OBS), which can provide additional constraints on the velocity-depth function in the area of interest through travel time or waveform inversion.

Processed data indicate that the BSR on seismic images is not always obvious. The BSR is absent in the basins of younger turbidite sediments, but is clearly visible in sedimented areas that lack any kind of lateral coherent reflectivity. One explanation from Hyndman and Davis (1992) is that only accreted sediments allow vertical fluid flow and methane gas migration, which would result in a continuous BSR. On the other hand, the basins with the layered structure inhibit any sort of vertical fluid flow, so that the amount of methane gas available may not be enough to produce gas hydrate.

Comparison of results from various size airgun data and the DTAGS'97 survey as well as modeling studies showed that the seismic reflectivity response of the BSR is frequency dependent. The BSR can be better described as resulting from a layer of some finite thickness, in which the seismic velocity decreases gradually (Fink and Spence, 1999; Chapman et al., 2002), rather than having a simple sharp interface.

In addition to conventional seismic processing and interpretation, related studies such as Amplitude Versus Offset (AVO) analysis with an elastic approximation to the Zoeppritz equations (Chen et al., 2007) and elastic full waveform inversion (FWI) (Yuan et al., 1999) were also carried out. The analyses of these data also included correlations of the BSR reflection coefficient with topography and geological structure (Spence et al., 1995; Fink and Spence, 1999; Zühlsdorff et al., 1999 and 2000) and local heat flow

variations based on the BSR depth (Ganguly et al., 2000; He et al., 2007). Additional constraints on seismic velocities are based on sonic and VSP data from the ODP Leg 146 and IODP Expedition 311 (Westbrook et al., 1994; McKay, 1994; Riedel et al., 2006b).

1.6.2 Non-seismic Methods

Other techniques also provide direct and indirect constraints on the character, distribution, and concentration of the gas hydrate:

- 1992, 2005: deep sea drilling (ODP Leg 146 and IODP Expedition 311) with well logs, core measurement, geochemistry analysis, etc (Westbrook et al., 1994; Riedel et al., 2006b).
- 1987, 1992, 2000: Heat flow probe measurements in very shallow sediments near seafloor (Davis et al., 1990; Hyndman et al., 1994; Riedel et al., 2006a).
- 1996, 2000, 2001, 2002: Piston coring sediment sampling for characteristics of gas hydrate with density, porosity, geochemistry analysis, etc. (MSc thesis by Y. Mi (1998); Novosel et al., 2005; Riedel et al., 2006a).
- 2001: Undersea imaging/video using remotely operated submersible (ROPOS) (Riedel et al, 2006a; He et al., 2007).
- 2002: Magnetic susceptibility measurements (Novosel et al., 2005).
- 2002, 2004: Swath bathymetry and acoustic imaging of topography of seafloor (Zühlsdorff and Spiess, 2004).
- 2003, 2004: Marine controlled-source electromagnetic (CSEM) profiling (Yuan and Edwards, 2000; Schwalenberg et al., 2005).
- 2004, 2005: Seafloor compliance measurements (Willoughby and Edwards, 1997; Willoughby et al., 2005).

1.7 Study Area and Data Integration

The study area is located on the mid-slope of the subduction accretionary sedimentary prism offshore Vancouver Island. The area encompasses a region between a gas/fluid vent field and a carbonate mound (Figure 1.10).

In the southern portion of the study area, the vent field has dimensions of about 2 km × 4 km (blue dashed rectangle, Figure 1.10). The field consists of at least four vents associated with near-surface faults. The vent field, first recognized during the 1997 DTAGS cruise (Chapman et al., 2002), is characterized by near-vertical seismic blank (or wipeout) zones that are between 80 m and several 100 m wide. Each vent shows a clear east-west orientation as identified from 3-D seismic imaging (Expedition 311 Scientists, 2005). The most prominent vent in the field, referred to as Bullseye vent (red polygon, Figure 1.10), was the drilling location of IODP Site U1328 (48^{o}40' N, 126^{o}51' W).

The carbonate mound, informally called Cucumber Ridge (red circle, Figure 1.10), is about 1.5 km long, 1 km wide and 70-80 m high. Cucumber Ridge is at north end of the study area, ~3.5 km west of Ocean Drilling Program (ODP) Site 889 and Integrated Ocean Drilling Program (IODP) Site U1327.

Many seismic experiments were carried out at this region (refer to Table 1.1), but only the following data sets are used in this study:

1999 COAMS MCS Grid and 3.5 kHz Subbottom Profiles

In 1999, a COAMS multichannel seismic survey was carried out in support of a new proposal to ODP for a second Vancouver Island drilling leg (now IODP Expedition 311). It includes a main 3D grid and 8 perpendicular crossing reference lines (Figure 1.10, green rectangle and perpendicular lines). Based on the results of the previous seismic surveys, the location of the 1999 COAMS 3-D seismic experiment was chosen between the two nearby prominent topographic highs and covered most of our study area, from Cucumber Ridge in the north end to Bullseye vent in the south end, including ODP Site 889/890 (Leg 146) and IODP Site U1327/1328 (Expedition 311). The location also covered the area where blank zones (yellow dashed rectangle, Figure 1.10) were observed during the 1997 DTAGS cruise and repeated during the 2002 DTAGS2 survey. The 1999

COAMS multi-channel seismic data set was fully processed and time migrated by Riedel (2001).

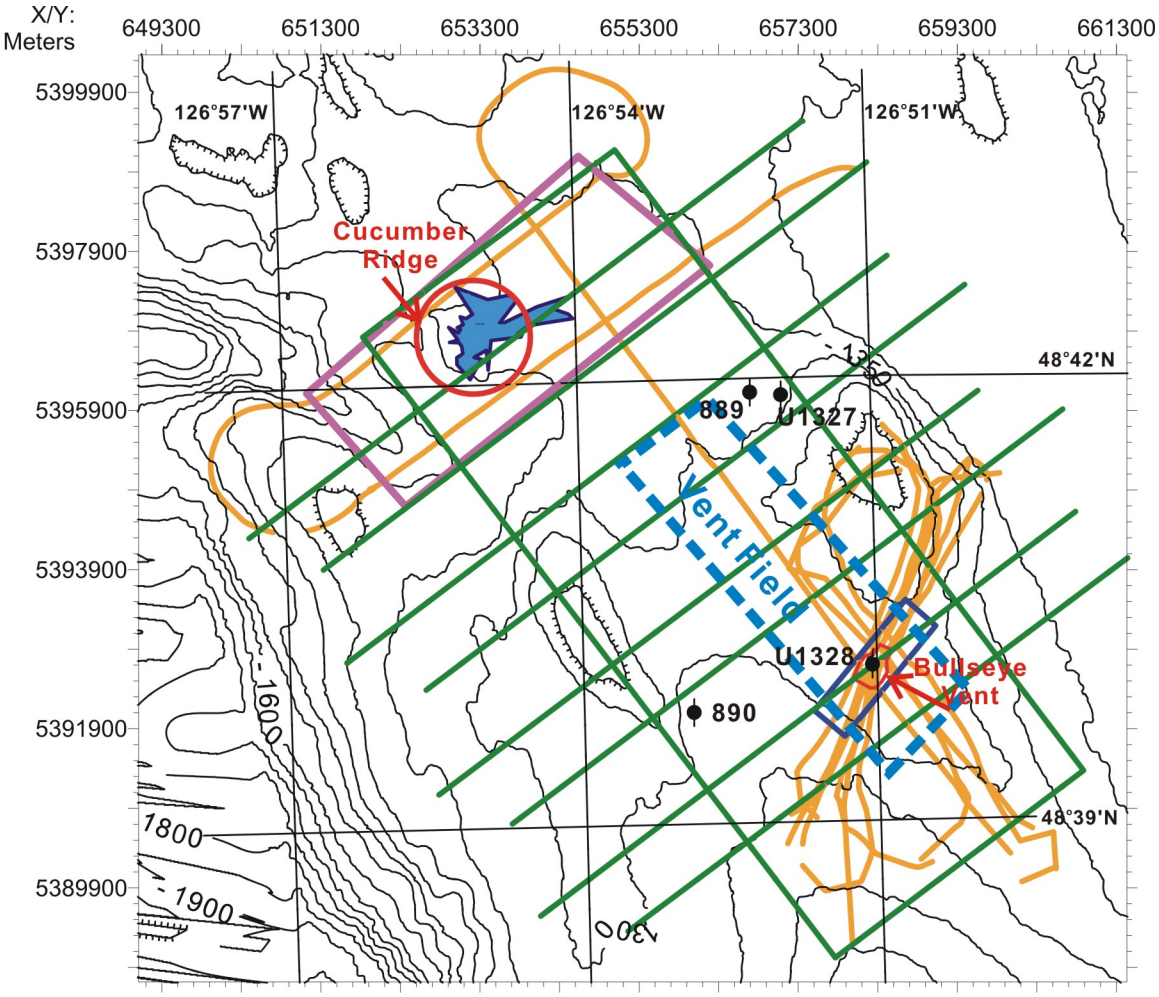

Figure 1.10 Map showing seismic data sets used in the study area on mid-slope region offshore Vancouver Island. The 2001 Teledyne grid around the Cucumber Ridge carbonate mound (red circle at north) is outlined by purple color box. The 2000 Teledyne grid around Bullseye vent mound (red polygon at south) is outlined by a blue color box. The 2002 DTAGS2 survey lines are indicated in orange. The deep green rectangle almost covering the whole region and lines perpendicular to it is the 1999 COAMS multi-channel seismic main 3-D grid and the crossing reference lines, respectively. Note that the 3.5 kHz subbottom profiles were coincident with the 1999 COAMS main grid and reference lines. Additionally the blue filled polygon outlines the ROPOS survey area. The dashed blue rectangle approximately outlines the whole area of venting field. The locations of ODP Sites 889/890 and IDOP Sites U1327/1328 are also labeled. The bathymetric contour interval is 50 m.

On each line of the 1999 COAMS survey, the high resolution 3.5 kHz subbottom profiler data were also recorded using an ORE Model 140 transceiver, which is mounted inside the hull of the ship CCGS J. P. Tully. Normally the data were plotted using the amplitude envelope without other processing (see details in Riedel, 2001). The 3.5 kHz subbottom profiler can give a high-resolution image, comparable to the also high-resolution DTAGS image in this study.

2000 Teledyne SCS Grid

In July 2000, a single channel seismic survey was performed to investigate detailed 3D (parallel 2D) structures of the main vent, Bullseye Vent, in the vent field (blue rectangle, Figure 1.10). This data set was also fully processed and compiled into a pseudo-3D grid by Riedel (2001). In this study, the 2000 Teledyne grid is used to align and shift DTAGS lines as well as for image comparison.

2001 Teledyne SCS Grid

In July-August 2001, a survey was carried out to investigate the potential seafloor vents in the study area that may be sites of significant fluid and methane flux. At Cucumber Ridge, high resolution (sample rate of 0.5 ms) single channel seismic lines were collected (purple rectangle, Figure 1.10), using the same source and streamer as in 2000 (Spence et al, 2002). The 2001 Teledyne single channel data set was fully processed in this study with details in Chapter 2 and 3.

2002 Deep-towed MCS Profiles

In October 2002, a collaborative experiment, the DTAGS2 experiment, between the University of Victoria, the Geological Survey of Canada, and Naval Research Laboratory (Washington, DC and Stennis Space Center, Mississippi) was carried out mainly around Bullseye vent and extended to Cucumber Ridge (orange lines, Figure 1.10): 11 profiles crossed the vent field and 3 profiles crossed the Cucumber Ridge area. With its characteristics of high frequency range (220-1000 Hz) and small Fresnel zone radius, DTAGS provides very high resolution images of the sediment layers. The data

collection and processing for DTAGS require specific methods developed in this study (details in Chapter 2 and 4).

The above wide range of seismic data sets were integrated into a single seismic interpretation package (Kingdom Suite software by Seismic Micro-Technology), with the proper survey line geometry and seafloor bathymetry (Figure 1.10). The system was used for seismic data display and interpretation. Event identification and picking can thus be compared from line to line and localized with respect to seafloor features.

In addition to the main seismic data sets, other experiments in the study area provide complementary information. These data sets include piston cores for physical properties and chemical state of the shallow sediments, Conductivity-Temperature-Depth measurements with water column sampling, heat probe measurements, and bottom-video observation and push cores from unmanned remotely operated submersible (ROPOS). These data sets provide ground truth for the seismic data and give detailed insight into the mechanism of fluid/gas venting. The locations of these experiments, together with ODP/IODP sites, were also imported into Kingdom Suite and labeled on the bathymetry map, providing crossing reference for the seismic information.

1.8 Study Objectives

The major objectives of this study were:

1. to image seismic features below the carbonate mound at Cucumber Ridge and gas/fluid vent field around Bullseye Vent,

2. to map heat flow derived from the depth of the bottom-simulating reflector (BSR) at the mound and in the surrounding region,

3. to examine indicators of upward fluid flow, characteristic of the gas hydrate occurrence,

4. to infer the origin of Cucumber Ridge carbonate mound,

5. to resolve velocity structures around the hydrate cap feature at Bullseye vent field.

Chapter 2

Seismic Data Collection

Within this chapter the data collection details of the 2001 Teledyne survey at Cucumber Ridge and 2002 DTAGS2 survey are described. These include survey design, different seismic equipment, data acquisition parameters and navigation equipment.

2.1 Teledyne's 2001 Survey at Cucumber Ridge

2.1.1 Survey Design

Cucumber Ridge is a 70-80 m high carbonate mound ~3.5 km west of ODP Site 889 and IODP Site U1327, with dimensions at its base ~1 km wide perpendicular to the continental margin and ~1.5 km long parallel to the continental margin (Figure 1.10). This mound was found during the 1999 COAMS seismic survey on the northern Cascadia margin (Riedel, 2001), and then a bottom-video observation was carried out through the remotely-operated submersible ROPOS during a cruise in May 2001 (Figure 2.1) (Beaudet et al., 2001; Riedel, 2001).

To determine the seismic structure of this mound and to infer its origin, a Teledyne SCS survey was carried out over the mound in July/August 2001 (Spence et al., 2002). The 2001 Teledyne SCS data set is a closely spaced single channel grid, consisting of 79 seismic lines, each about 3 km in length separated by about 25 m (Figure 2.1). The single channel data sets provide high resolution images of the seismic structures below the carbonate mound.

2.1.2 Seismic Equipment and Data Acquisition

Figure 2.2 shows the summary of deployment geometry for seismic equipment on the survey ship C.S.S. John P. Tully during the 2001 cruise. The position of the airgun, streamer and Differential GPS (DGPS, which has typical errors of metres) are indicated, and the relative distances to the stern of the ship are marked.

The seismic source was a single 40 in^3 (0.65 litre) sleeve airgun, towed at a depth of ~2 m at a distance of ~25 m behind the centre of the ship stern. The sleeve gun has a wave shape kit, which uses 50% of the volume to reduce the bubble collapse energy by injecting 20 in^3 of air a few milliseconds after the first release.

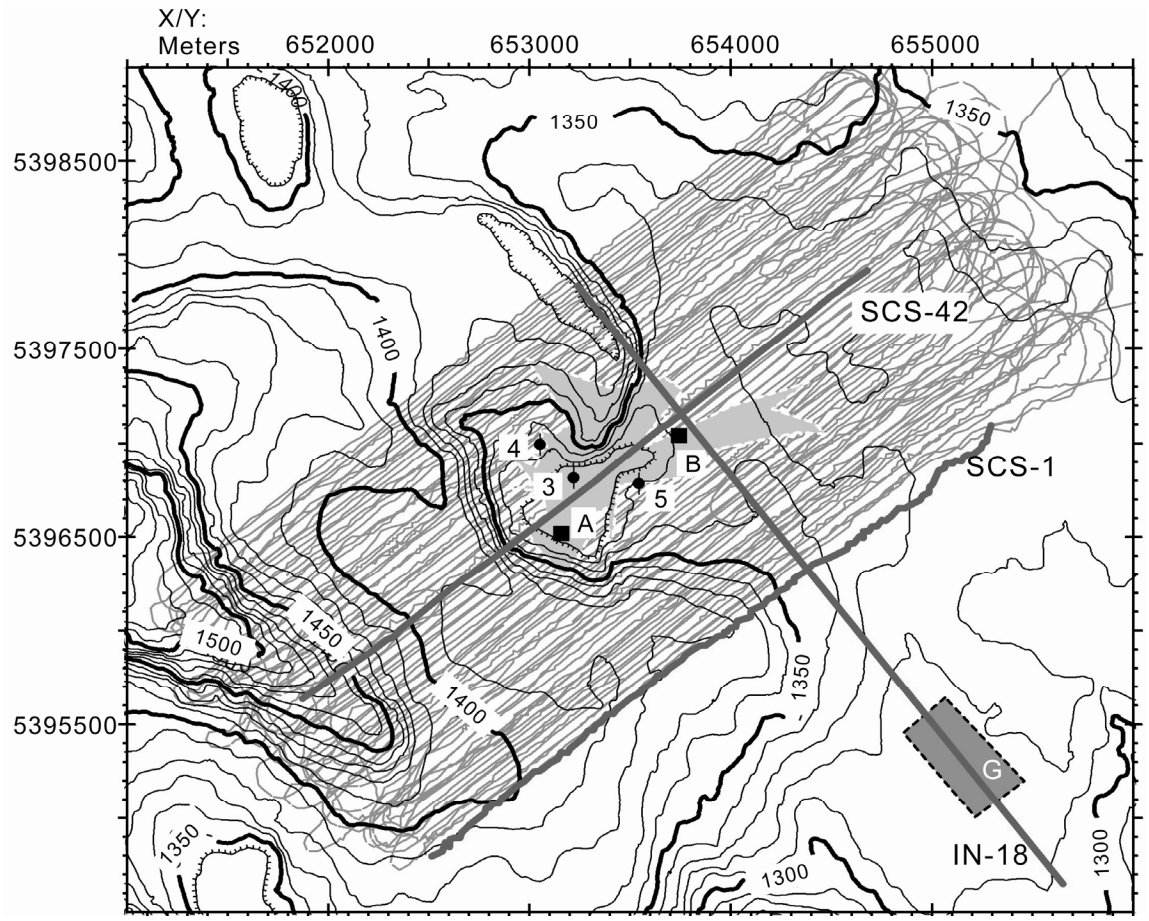

Figure 2.1 Track lines of 2001 Teledyne grid, superimposed on 10 m interval bathymetry. The thick lines SCS-42, SCS-1, and IN-18 are selected seismic sections shown in Figure 5.4, Figure 5.5 and Figure 7.1, respectively. The 1999 COAMS inline grid IN-18 crosses the flat area southeast of Cucumber Ridge (dark gray rectangle), where the average heat flow value G of 74 mW/m2 was selected to represent the regional background heat flow. The light grey area around Cucumber Ridge outlines the ROPOS survey area and the solid squares are locations of images in Figure 5.6 where ROPOS found fractured carbonate (A) and biological communities (B). The piston coring locations 3-5 are also labeled.

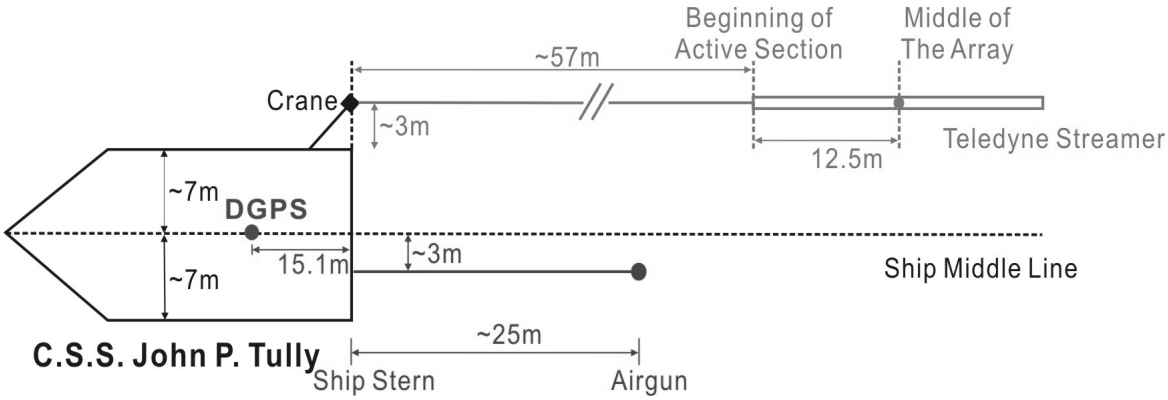

Figure 2.2 Deployment geometry for seismic equipment on the survey ship C.S.S. John P. Tully during the 2001 cruise.

The reflections were detected using the Teledyne Ltd. streamer, towed from a block on the crane which extended ~3 m from the starboard side of the ship. The array had a depth of ~4 m with the head of the array ~57 m behind the stern of the ship. The Teledyne single channel streamer itself is 50 m long and oil filled, composed of a 15 m spring section – vibration isolation module (VIM), a 25 m long active section with 50 hydrophones spaced every 0.5 m and a 10 m long spring section (VIM) at the tails. The array sums 50 hydrophones over a total length of 25 m to increase signal-noise ratio.

The preamplifier in the Teledyne streamer had a lowcut filter set to 40 Hz. The signal coming from the preamplifier was then filtered with a Krohn-Hite filter at 60-2000 Hz. The seismic data were recorded with a sample rate of 0.5 ms and record length of 5 s.

2.1.3 Navigation and Bulk Shifting of Survey Lines

The navigation used DGPS with the ship's antenna ~15.1 m from the centre of the stern (Figure 2.2). Every 3 seconds, it recorded latitude/longitude along with the water depth picked from the ship's 12 kHz transceiver; a constant water velocity of 1492.6 m/s was assumed for calculation of water depth.

Although the airgun was intended to fire by distance at an interval of about 12.5 m (at a nominal ship speed of 4 kts, this corresponded to a shot time interval of about 6 s), the shot interval actually varied between about 10 m and 15 m due to variations of ship direction and wind speed during entire survey. Also, up to 20% of the shots were missed

due to misfire problems associated with variable ship speed; if the ship speed was too fast, recording the data to disk was not complete before the next shot position was reached.

The latitude/longitude values of the field data geometry at reflection points were converted to Universal Transverse Mercator (UTM) coordinates using WGS84 datum. The Teledyne 2001 SCS data set was then imported into the seismic packages of GLOBE Claritas and The Kingdom Suite for data processing, display and interpretation.

Because the 2001 Teledyne single channel seismic data were acquired over a period of several days during the survey, the data most likely included static shifts from tides and from variable ship bearing and speed to adjust for wind conditions. Therefore a bulk time shift to each survey line is required. This is especially important for pseudo-3D processes to improve horizontal consistency both in inline and cross-line directions.

To determine the time shifts for each line, inlines 18-23 from the 1999 COAMS main 3D grid were carefully chosen as independent reference lines; these 6 lines crossed the 2001 Teledyne survey lines east of the central mound where the seafloor is relatively flat (Figure 1.10). For the seafloor reflection on a given Teledyne SCS line, the traveltime differences between the SCS line and the 6 independent reference lines were calculated, and then the average value of the differences was used as the bulk static shift for this SCS survey line. Figure 2.3 shows the calculated time shifts for each line of the 2001 Teledyne data set. The variations, with a maximum shift of 6 ms, indicated the necessity of bulk shifting.

2.2 DTAGS2's 2002 Experiment

2.2.1 Survey Design

In October 2002, a deep-towed high-resolution multichannel seismic survey took place on the north Cascadia Margin, offshore Vancouver Island; the experiment was part of a collaborative study of deep sea gas hydrate among the US Naval Research Laboratory, the University of Victoria and the Geological Survey of Canada.

The primary goals of this experiment were to obtain high resolution structural details at the Bullseye vent area and at the carbonate mound of Cucumber Ridge,

including the extent of associated gas hydrate and underlying gas, and to determine the associated seismic velocities. As described by Gettrust et al. (1999, 2004) the DTAGS was well suited to this work because of 1) the higher vertical resolution provided by high frequency characteristic of DTAGS, which operates with shorter wavelengths (less than 3 m) compared to wavelengths in the range of 25-50 m for normal multichannel seismic data with 30-60 Hz frequency bandwidth, 2) greater sampling in wave number space using shorter, more manageable hydrophone arrays, and 3) a smaller Fresnel zone radius due to the deep-tow geometry providing a much shorter distance from the source to the reflectors. Furthermore, the deep-towed system allows recording of wider-angle reflection data, and thereby it may provide useful information for moveout velocity analysis and Amplitude-Versus-Offset (AVO) analysis (Figure 2.4).

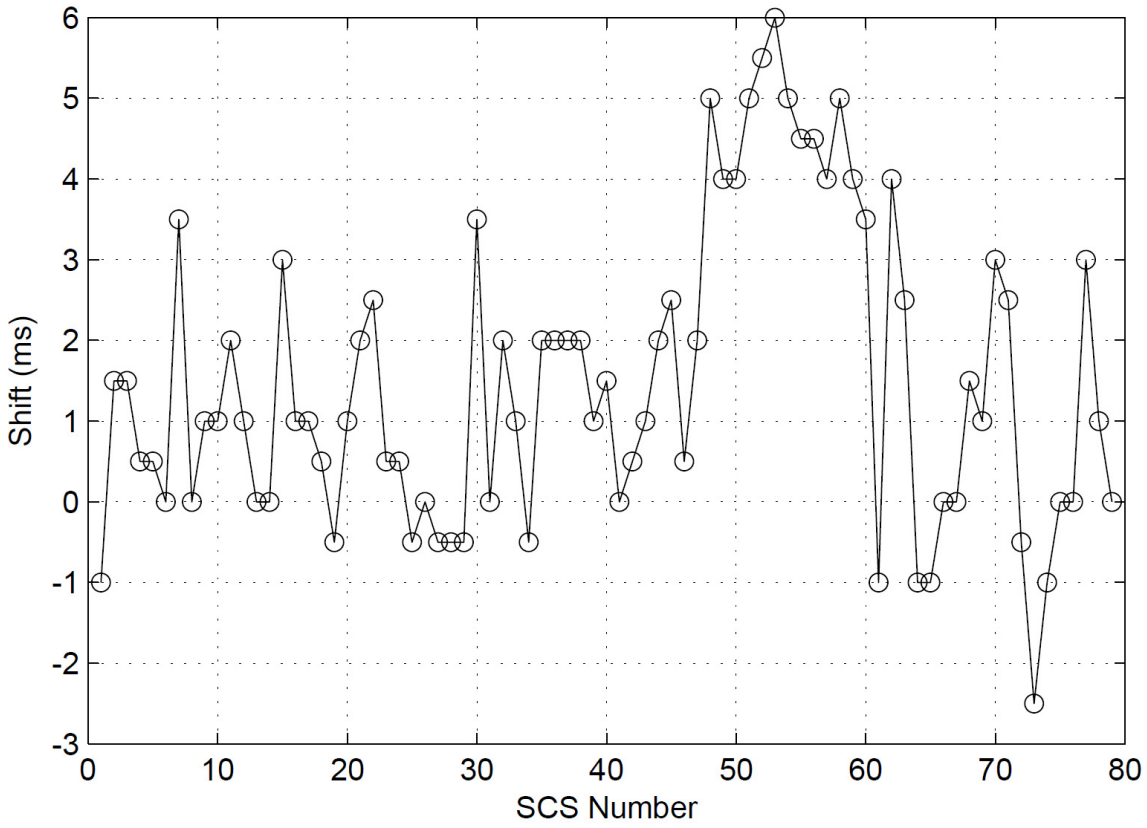

Figure 2.3 Calculated shift times for the 2001 Teledyne SCS lines. The negative value means to shift survey line up.

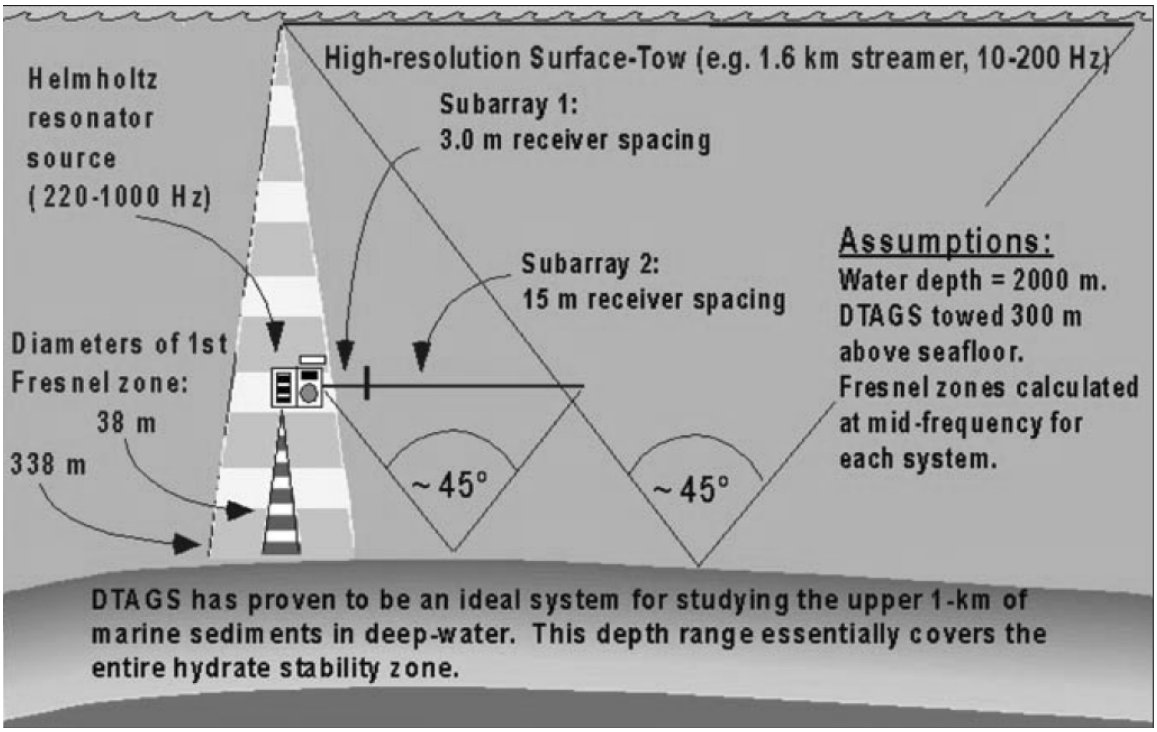

Figure 2.4 Diagram presenting the advantage of deep-tow geometry in deeper water. Note that this geometry coupled with a higher frequency source significantly reduces the size of the first Fresnel zone, thus improving the resolution of lateral change in structure. (From Gettrust et al., 2004)

A total of 11 lines were deployed to cross Bullseye vent field (Figure 1.10 and Figure 2.5): 7 lines in the SW-NE direction, plus 4 other lines in the SE-NW direction. As well, a transition line DT16 from Bullseye vent to Cucumber Ridge repeated the 1999 DTAGS experiment line, crossing all blanking zones and the plateau area east of Cucumber Ridge. Another 2 lines across the steep western edge of Cucumber Ridge added new information on the subseafloor structures around this mound. Around Bullseye vent field, an acoustic transponder net system was also deployed to navigate the deep-towed system precisely.

Since the depths of source and receivers of DTAGS varied significantly and nonlinearly during the entire survey, special methods were developed to do time corrections for individual trace and image stitching for neighboring shot gathers. The processing details are described in Chapter 4.

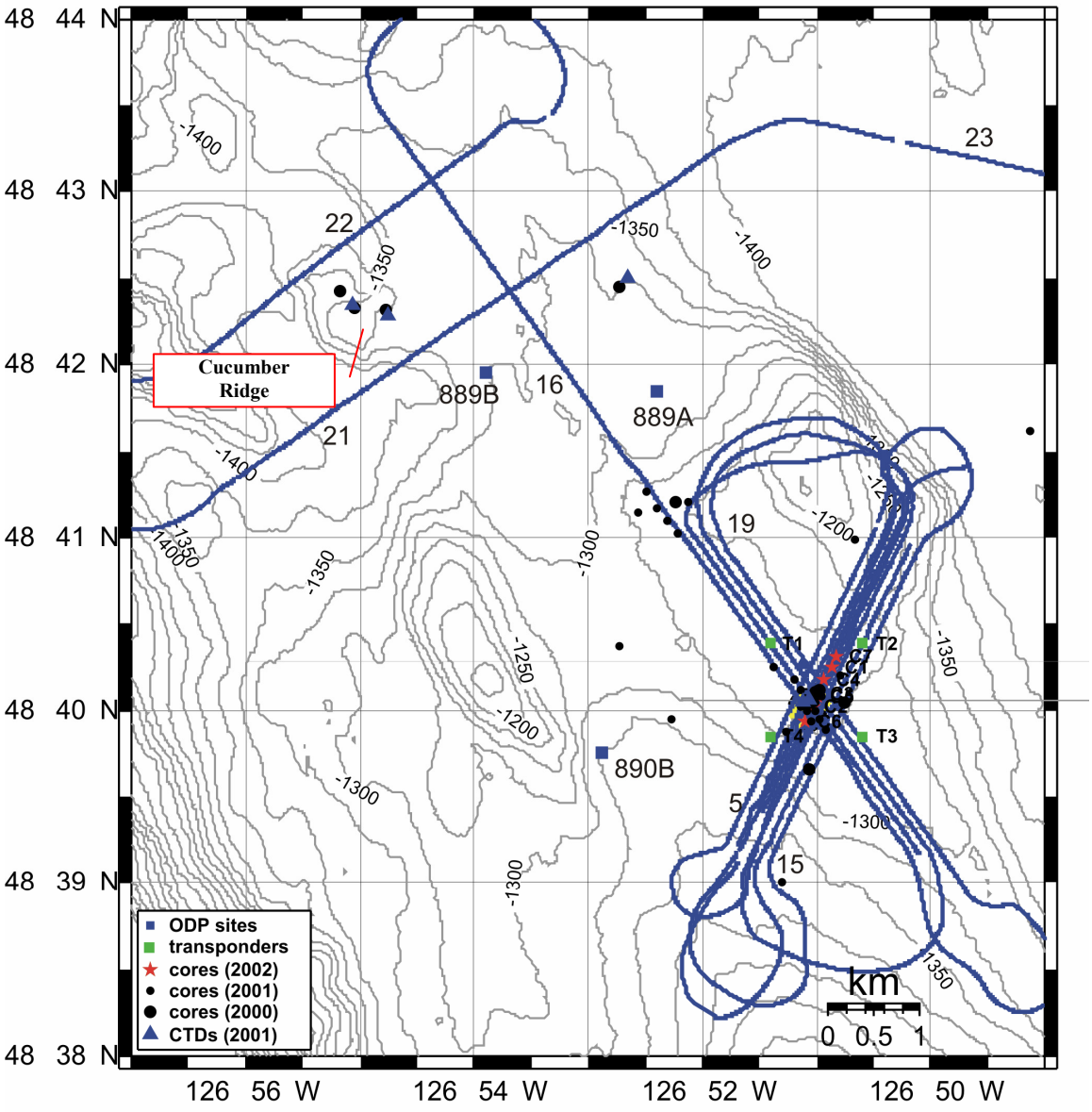

Figure 2.5 Location of DTAGS2 survey lines in the region of Bullseye vent field and Cucumber Ridge. Transponder deployment during this expemriment and other information (ODP sites, piston corings, Conductivity-Temperature-Depth measurements) are also labelled. Bathymetry is from a Sonne cruise in 1999. (From Spence et al., 2002)

2.2.2 Seismic Equipment and Data Acquisition

According to Gettrust et al. (2004), the source of DTAGS system was an upgraded Helmholtz resonator, emitting a chirp-like sweep signal in the frequency range of 220-1000 Hz (Figure 2.6). The sound pressure level of the new source was ~200

dB//1Pascal @ 1 m), sufficient to sample the upper marine sediments (Figure 2.7). One other advantage of the Helmholtz resonator source is that source signal variability does not adversely impact seismic data processing compared to air/water guns, because there is no cavitation and the source signal is highly repeatable.

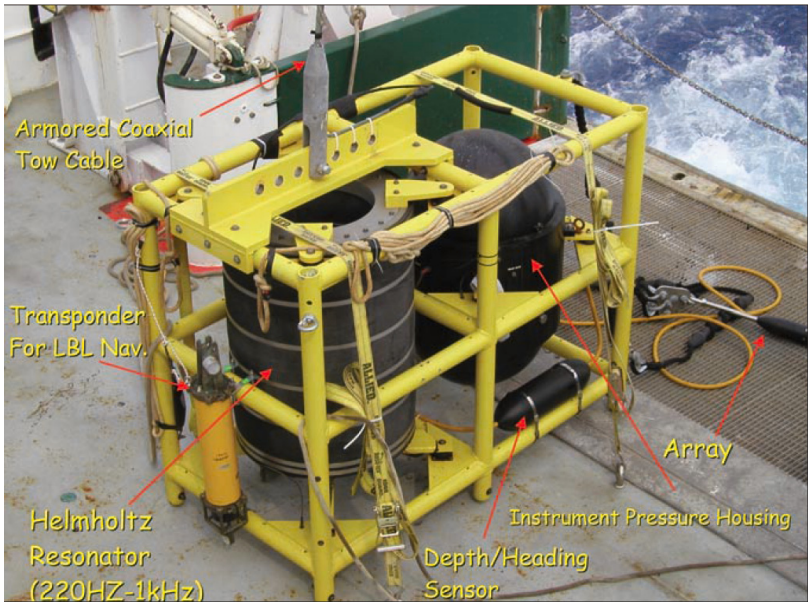

Figure 2.6 The DTAGS tow body. Note the Helmholtz resonator is open at the top. By free flooding the resonator, the source signal becomes depth independent. (From Gettrust et al, 2004)

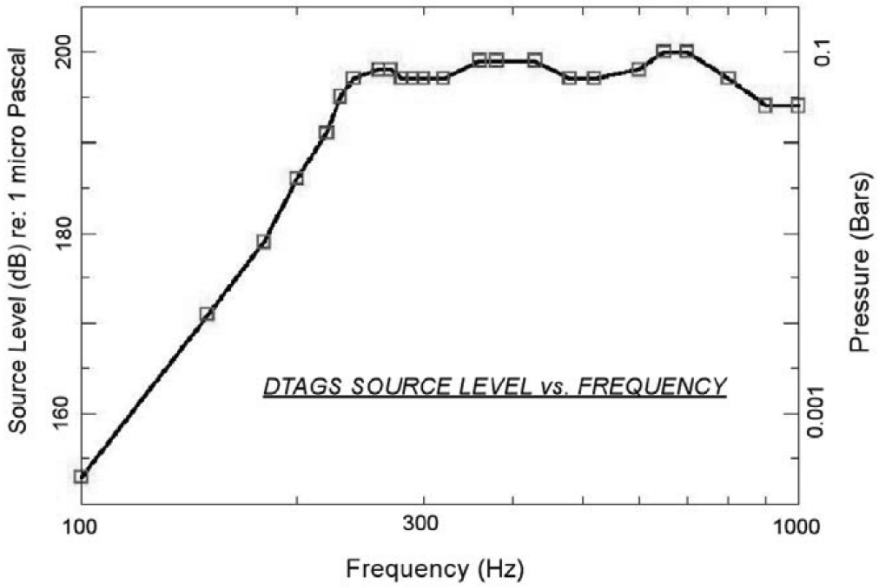

Figure 2.7 Sound pressure level as a function of frequency. The normal frequency band used operationally is 220 Hz – 1 kHz. (From Gettrust et al., 2004)

Table 2.1 DTAGS Configuration during the 2002 DTAGS2 cruise

Acoustic array	24 channels with group spacing of 3 m (minimum offset: 9 m, maximum offset: 78 m; however, the first two channels were dead)
Geophysical array	24 channels with group spacing of 15 m. (minimum offset: 93 m, maximum offset: 438 m)
Source	Helmholtz resonator generating 250 ms long sweep (220-1k Hz).
Source strength	~200 dB, sufficient to penetrate the upper 400 m of the sediments.

As described by Spence et al. (2002) the solid core hydrophone streamer (Figure 2.6) has two subarrays of total 48 independent nodes: the first 24 nodes are the acoustic group, spaced at 3-m intervals; the following 24 nodes are the geophysical group, spaced at 15-m intervals (Table 2.1). Since the DTAGS channels are single hydrophones, the receiver response is omnidirectional. Using a 24-bit Sigma-Delta converter at each hydrophone, data were digitized at 2000 samples/s (sampling interval of 0.5 ms) with a recording length of 1.9 s including a 250 ms delay.

2.2.3 Navigation Only Using Ship's DGPS Signal

During the 2002 DTAGS2 survey, the seismic source was fired every 30 s. Thus, an average ship speed of ~2.0 knots provided a shot spacing of ~30 m. However, the ship speed was as low as ~1 knot when changing direction against the strong wind and as high as ~4 knots in transit turns from one line to the next. The navigation system WINFROG recorded ship's DGPS location and local time every 5 seconds. The WINFROG also recorded shot times and stored them in trace headers. All navigation locations in longitude and latitude were converted to UTM coordinates in meters (WGS84 datum and zone 9) (e.g., survey line DT10, Figure 2.8).

After rejecting apparent wild navigation points due to the jumping of DGPS readings, the ship's locations where the source fired were obtained by interpolating the corresponding shot times from the ship's times (Figure 2.8). Then the offset of the current shot relative to the previous one was calculated (blue line, Figure 2.9a). At this step, some additional hidden DGPS errors were discovered, such as the sudden jumps

indicated by the blue line at Shot 2311 and Shot 2312. These bad points were corrected by averaging the ***X*** (East) and ***Y*** (North) coordinates on either side of these abnormal values, thus obtaining the offsets as shown by the red line (Figure 2.9a). The corrected offsets were used as the reference for the optimal shot spacing during the later shot image stitching process, as detailed in Chapter 4.

For each shot, a distance ***D*** accumulated from the first shot (Figure 2.9b) increases along the direction of the ship heading, with 0 at the location of ship's DGPS antenna of the first shot. For a stitched survey image, the axis is defined as a straight line with 0 at the source of the first shot and increasing also along the direction of the ship heading. Therefore, each trace has a unique distance ***d*** measured from its reflection mid-point to the 0 position on the axis. By comparing ***d*** and ***D***, the ***x*** and ***y*** coordinates of each trace can be interpolated from ***X*** and ***Y***, respectively. In this way, the DTAGS streamer is assumed to follow the ship's track.

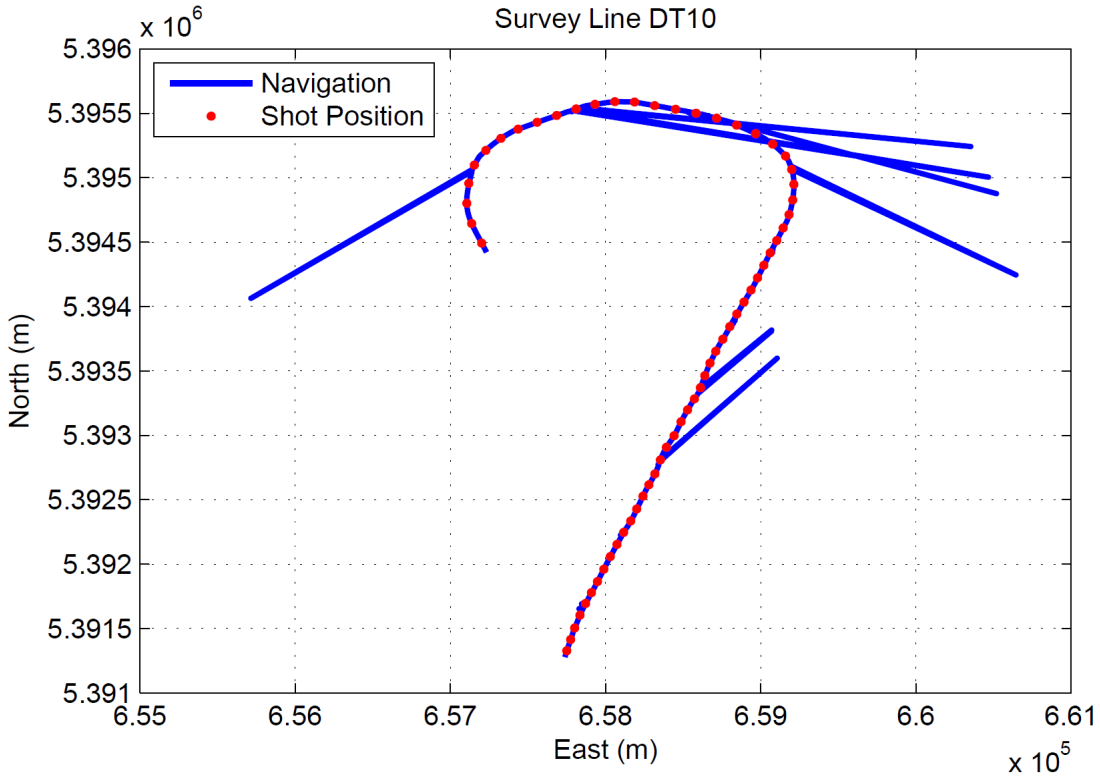

Figure 2.8 The ship's navigation (blue) and interpolated shot positions (red). Note the jumps of DGPS readings (wild navigation points). To make the figure clear, only 1 of 4 shot positions was plotted.

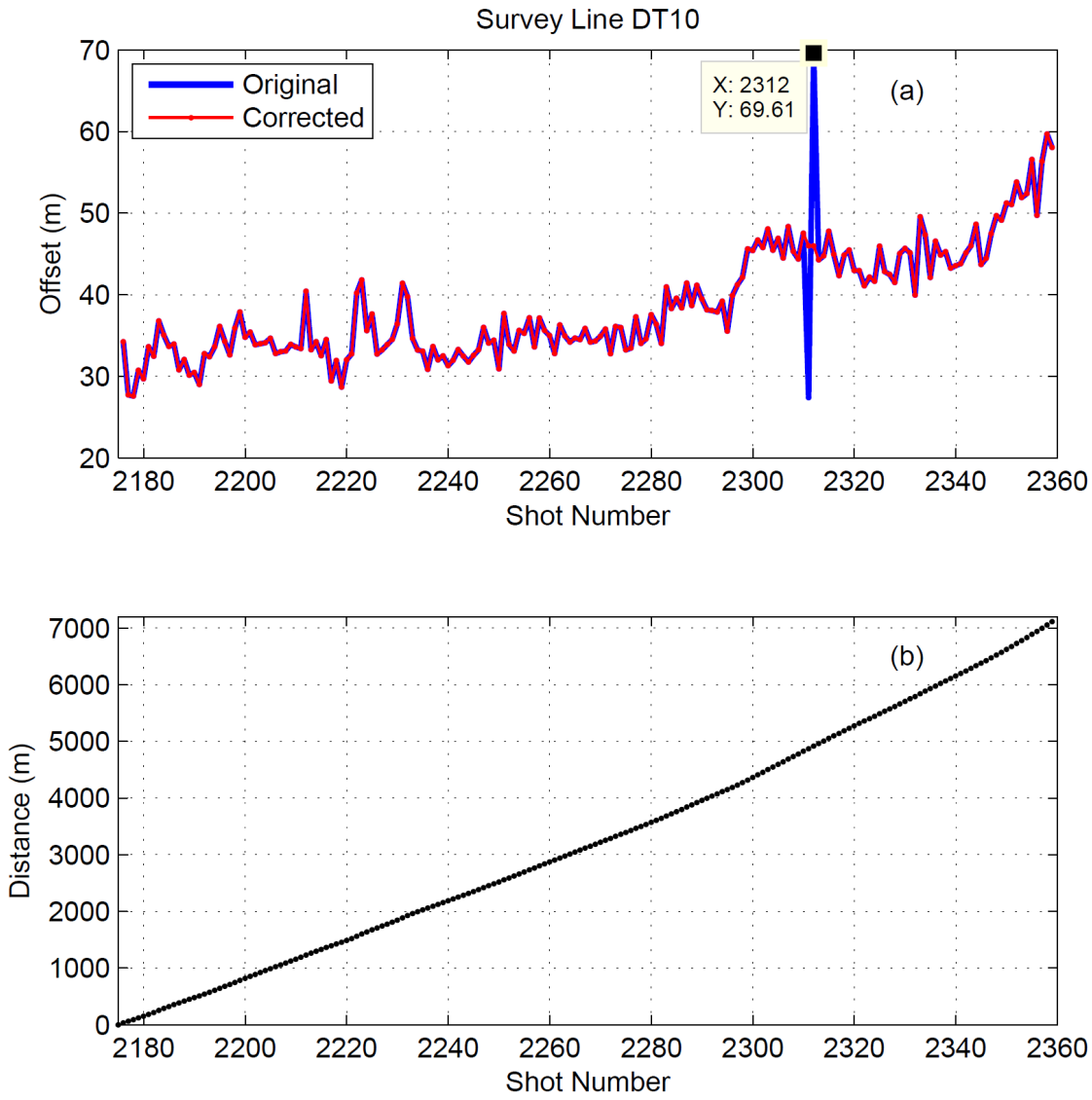

Figure 2.9 (a) Relative offsets between the current shot and the previous one, before (blue) and after (red) corrections for the abnormal values at Shots 2311-2312. (b) The distance of current shot relative to the first one by accumulating all previous offsets.

For example, the survey line DT10 has shot numbers ranging from 2175 to 2360. Firstly a constant distance $\boldsymbol{l}$ was assumed for the DTAGS source behind the ship DGPS antenna, then the head ($\boldsymbol{d_{2175}}$) and end ($\boldsymbol{d_{2360}}$) of the stitched DT10 image were aligned to corresponding shot distances ($\boldsymbol{D_{2175}}$-$\boldsymbol{l}$ and $\boldsymbol{D_{2360}}$-$\boldsymbol{l}$). For a given trace with distance $\boldsymbol{d_i}$, the corresponding shot distance $\boldsymbol{D_i}$ thus can be obtained by interpolation, which is between two adjacent shot distances $\boldsymbol{D_m}$ and $\boldsymbol{D_n}$ ($\boldsymbol{i}$ is the trace number, while $\boldsymbol{m}$ and $\boldsymbol{n}$ are shot

numbers). Therefore the ***x*** and ***y*** coordinates of each trace ***i*** can be calculated using following equations:

$$x_i = X_m + \frac{X_n - X_m}{D_n - D_m} \cdot (D_i - D_m) \qquad \text{(Equation 2.1)},$$

$$y_i = Y_m + \frac{Y_n - Y_m}{D_n - D_m} \cdot (D_i - D_m) \qquad \text{(Equation 2.2)}.$$

This trace coordinate acquisition method is simple and only uses ship's DGPS navigation, which is normally reliable and contains few errors; however, in practice distance ***l*** of the DTAGS source behind the ship DGPS antenna varied shot by shot. Therefore this method can not ensure that every image trace is accurately located on the map for the whole survey line. Thus in actual use ***l*** is determined subjectively to post the relevant image segment to the appropriate map location by trial-and-error.

2.2.4 Navigation within Acoustic Transponder Net

During the 2002 DTAGS2 survey, navigation was also performed acoustically with a transponder net deployed in 2001 with the intent of obtaining precise navigation for the DTAGS system. As described by Spence et al. (2002), a 4-element long baseline (LBL) acoustic seafloor array was arranged on four corners of a square of 1 km sides at the Bullseye site in approximately 1275 m of water (see Figure 2.5 for seafloor transponder locations). The 5th relay transponder, called rover, was attached to the DTAGS source, which was horizontally offset by up to 1 km behind the ship. The LBL net was driven by a Sonatech, Inc Model NS-011 transceiver. With this configuration, the DGPS from the ship and known locations of transponders on the seafloor are used via acoustic travel times to determine the position (x, y, and z) of the rover. However, most of z positions of the rover do not fall within reasonable values and are unusable. During operation, navigation using all four transponders was possible within the array and up to about 100 to 200 m outside, and sometimes up to 1 km outside. The navigation software WINFROG calculated real-time positions of the ship and rover. This allowed a real time visual assessment of the positions of the ship and rover.

Spence et al. (2002) estimated that communication with the array resulted in accurate locations for the DTAGS rover about 30% to 75% of the time; within the 1 km square area, precision and accuracy of the navigation were estimated at 1 and 4 m respectively. These estimates were based on expected positions and consistency of positions of the towed instruments as viewed on the WINFROG graphic interface.

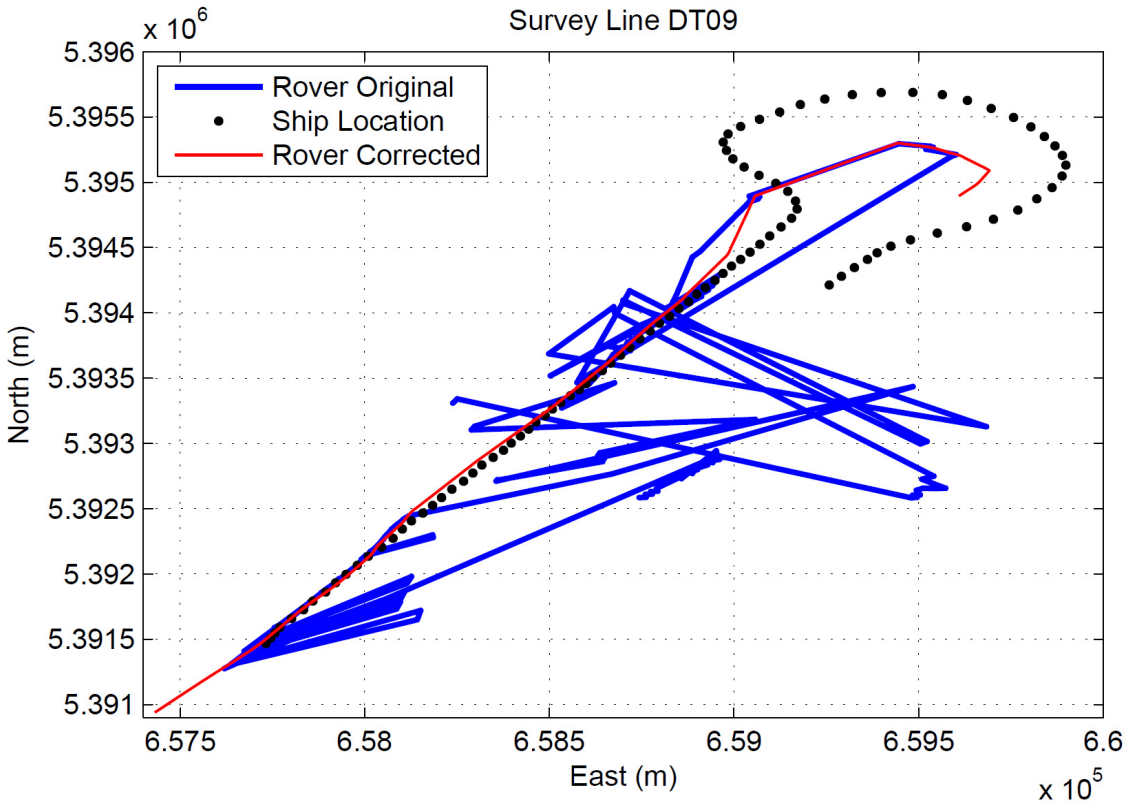

Figure 2.10 Positions of rover (a relay transponder) before (blue) and after manual correction (red). The ship's navigation (black) is used as the guide for this correction. Note that the rover was attached to the DTAGS source and towed behind the ship with a powered cable. The cable was 1351-m-long during survey line DT09, but its length changed during other DTAGS2 survey lines depending on the seafloor depth.

Figure 2.10 shows in UTM coordinates the rover navigation (blue line) provided by the acoustic transponder net and ship's DGPS antenna locations (black dots) where the source fired during survey line DT09. It is surprising to see that the rover navigation was wild with many irregular position jumps occurring not only during DT09 but also along

all DTAGS survey lines. When the rover navigation coordinates of DT09 were decomposed into East and North components (blue lines in Figure 2.11), it is easy to see that the serious jumping problem of the rover was mainly due to two reasons:

1. When the navigation system tried to produce a record but the rover could not be located by the acoustic transponder net for unknown reasons, the recording just repeated the previous good position. Therefore, the navigation segments having repeated readings on Figure 2.11 were reduced to a single point on Figure 2.10. However, the number of repeated readings was so large that the discontinuities produced large blank areas over the rover track on Figure 2.10.
2. Some strong acoustic noise from unknown sources interfered with the real rover signals, and thus the acoustic transponder net did not resolve real positions of the rover. This led to unpredictable outliers obviously deviated from the ship track, especially near the start and end parts of the track when the ship made a turn and was out of transponder net.

These irregular jumps of rover navigation made it very difficult to position the DTAGS accurately and impaired the value of using the acoustic transponder net. An effort was made to fix this problem manually and thus to retrieve useable information.

Based on the visual observations of Figure 2.11, a first test is run by picking East-North pairs most possibly belonging to the rover track. For example, if the east value at record number 200 seems correct, the linked north value at record number 200 should also be correct; these two values form a valid East-North pair. Thus the East or North values for the remaining records can be interpolated between picked valid East-North pairs. Then the test rover track is plotted and compared to the ship locations (Figure 2.10). Since the rover track should not deviate from the trend of ship too much, some inappropriately picked East-North pairs were replaced with new picks, which made the test rover track approach the ship's track. With iterative application of these steps the optimal rover track (red line, Figure 2.10) and its corresponding East-North coordinates can be determined (red lines in Figure 2.11).

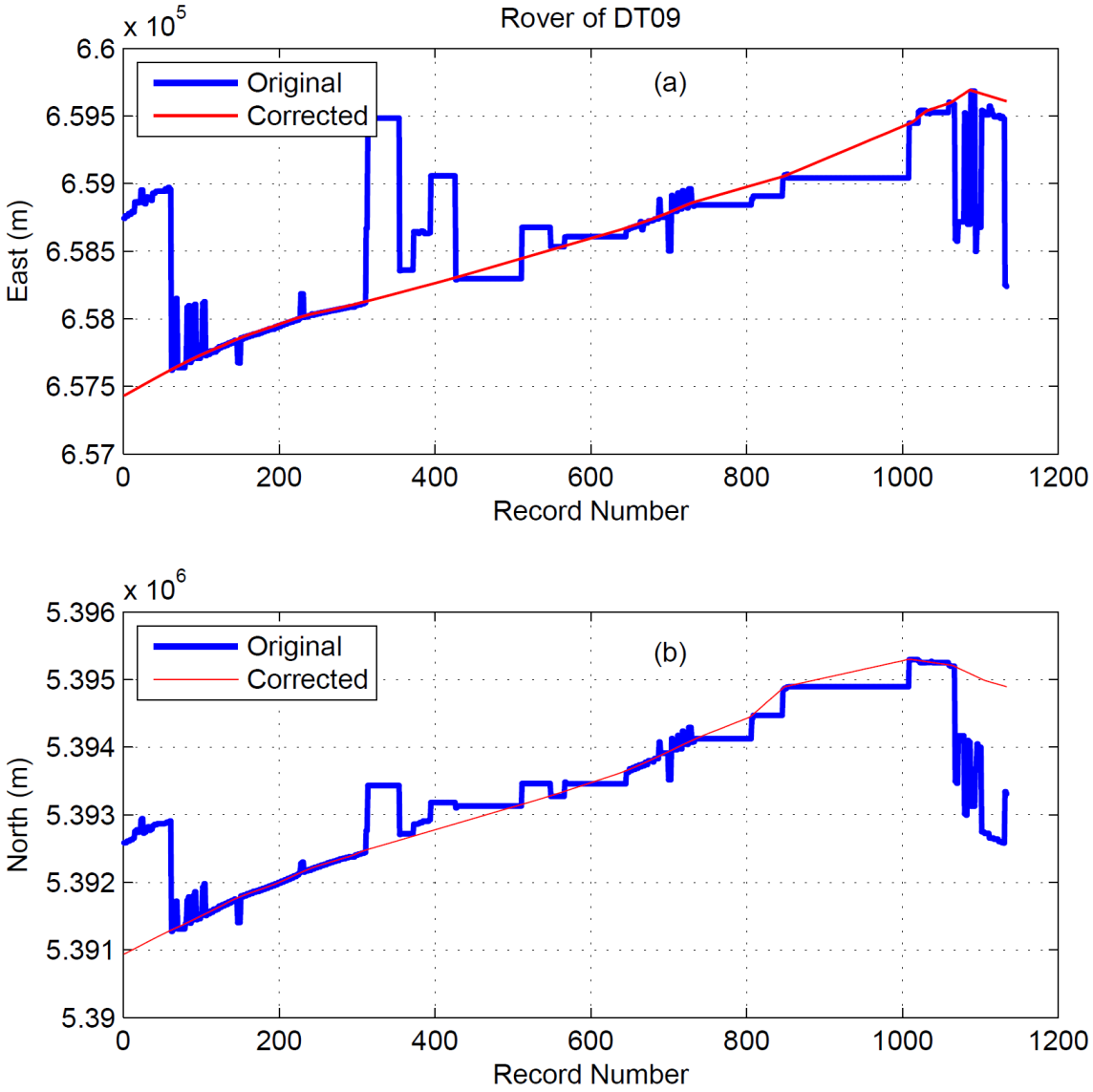

Figure 2.11 Decomposed UTM coordinates of rover navigation for survey line DT09. (a) The original (blue) and corrected (red) East coordinates against navigation record number. (b) The original (blue) and corrected (red) North coordinates against navigation record number.

After the rover navigation was corrected, the DTAGS shot locations were determined by interpolating the corresponding shot times into the recording times. Then the offset of current shot relative to the previous one was calculated (Figure 2.12). During the main part of the survey line DT09, where the track was close to a straight line and within the transponder net, the offsets of the rover had a variation trend similar to but

gentler than ship's offsets due to the cushion effect of the very long cable (~1351 m for survey line DT09) between the rover and the ship. This cable also reduced the dragging force transferred from the ship during the turns, leading to the largest discrepancy between offsets of ship and rover at start and end of survey. Since the assumption of a straight rigid cable was incorrect during real survey, the rover navigation predicted the DTAGS shot locations more accurately than the ship navigation did. However, there were still uncorrectable problems of rover positioning, such as the unreasonable large offsets at Shots 251-258 of survey line DT09 (Figure 2.12). Therefore the corrected rover navigation was not accurate enough for DTAGS image stitching and CMP (Common Midpoint) binning as originally designed, but as a whole provided more reliable absolute rover positioning than the ship's navigation.

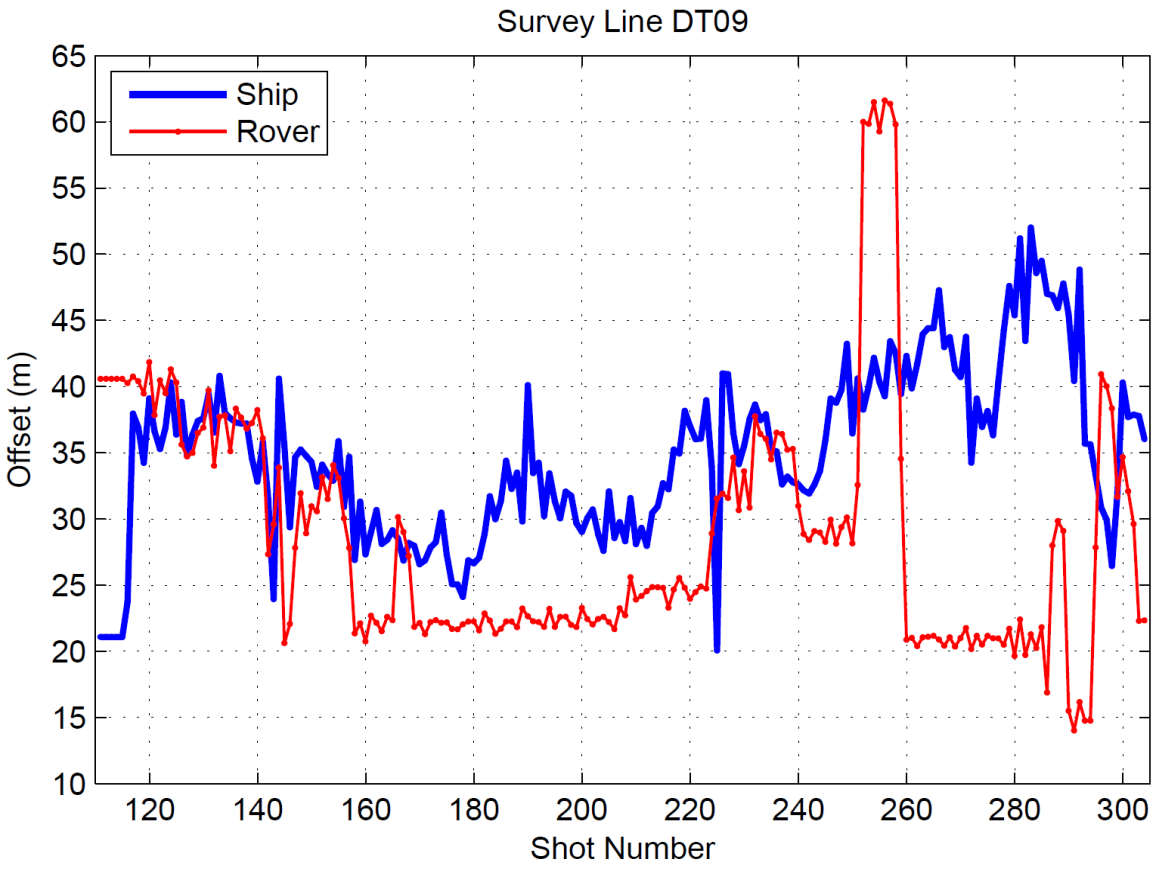

Figure 2.12 The offsets between current shot and the previous one for the ship's antenna (blue) and DTAGS rover (red).

To post a stitched DTAGS image on the map based on rover navigation, the ***x*** and ***y*** coordinates of each trace were determined using same posting method described in above section 2.2.3 for the ship's navigation:

1. Calculate the distance of each shot relative to the first one by accumulating successive offsets.
2. Since the source location is exactly same as the rover, the stitched image simply is aligned by putting its 0 position to the 0 distance of the rover and putting its end at the largest rover distance.
3. Interpolate trace coordinates to the rover distance to get corresponding ***x*** and ***y*** values.

Chapter 3

Teledyne Single Channel Seismic Data Processing

Within this chapter, the processing details of the 2001 Teledyne SCS data are given, including geometric spreading compensation, source signature deconvolution, spiking and predictive deconvolution, Butterworth band-pass filtering, and amplitude balancing. Finite-difference time migration was applied to the originally recorded lines. Additional processes (e.g., 3D binning and 2.5D time migration) were also tried, but results were unsatisfactory; these processes are described in Appendix A.

3.1 Geometric Spreading Compensation

The first step of seismic data processing normally is to compensate for the attenuation in seismic wave amplitude due to geometrical spreading of the wavefront through the various velocity layers, and for attenuation due to energy dissipation. The attenuation is removed by multiplying the samples of the trace by a vector of scalars, deduced semi-empirically.

Since most of seismic features are located at relatively shallow depths (about 1 second of two-way time from seafloor), a simple geometric spreading compensation was used for trace amplitudes only by multiplying each sample with its appropriate traveltime, assuming constant velocity and ignoring the energy absorption by sediments. The geometric spreading compensation was completed using SPHDIV module in Claritas. Since the amplitudes of shallow and deeper reflectors were well balanced after the geometric spreading compensation, no corrections were made for sediments attenuation.

3.2 Butterworth Bandpass Filtering

Survey line SCS-1, located south of Cucumber Ridge mound where the seafloor is relatively flat, was selected as an example profile for bandpass filter tests and for other processing tests of the 2001 Teledyne data.

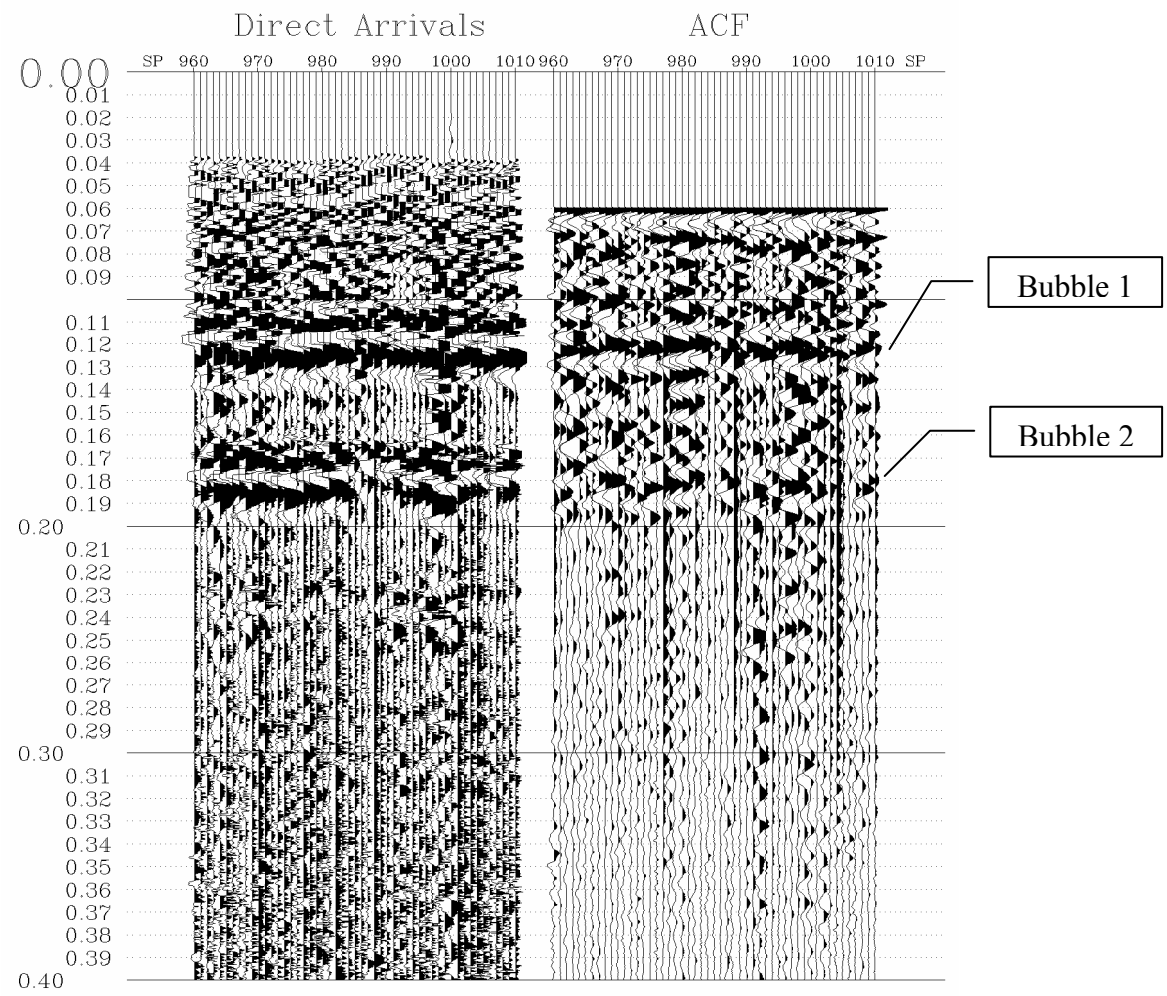

Figure 3.1 Seismogram panels showing direct arrivals recorded by Teledyne streamer and their autocorrelation functions (time-shifted to make the large amplitude of the autocorrelation function approximately match the bubble events). Note that a spherical divergence correction (multiplication by travel time *t*) was applied to both panels.

The direct arrival and its autocorrelation are shown in Figure 3.1. Since Teledyne streamer array sums 50 hydrophones over a total length of 25 m to increase the signal-noise ratio, the direct-arrival waveform is corrupted due to interference effect of time-varying arrivals. The seasurface ghost may produce additional interference effects. The amplitude spectrum of the direct arrivals extends from about 40 Hz to a high frequency limit of only about 100 Hz (Figure 3.2). Although the bubble events can still be distinguished as simple events, particularly the first two after the primary pulse, the

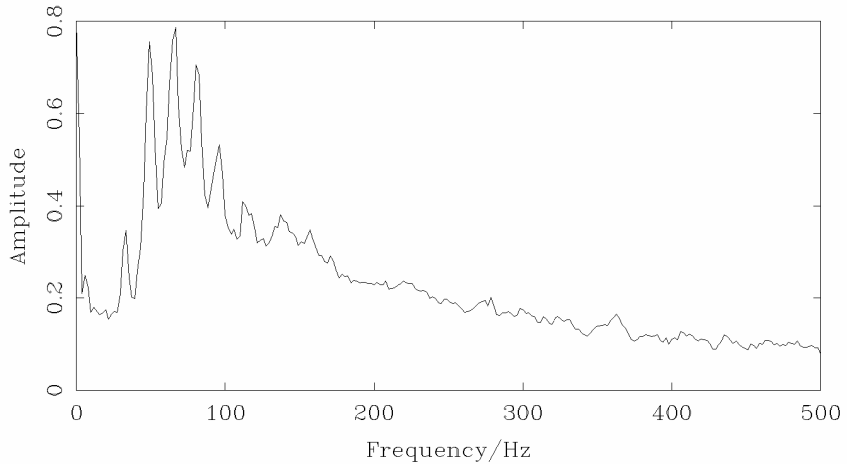

Figure 3.2 Mean amplitude spectrum of direct arrivals (Figure 3.1) over a time window from 0 to 400 ms.

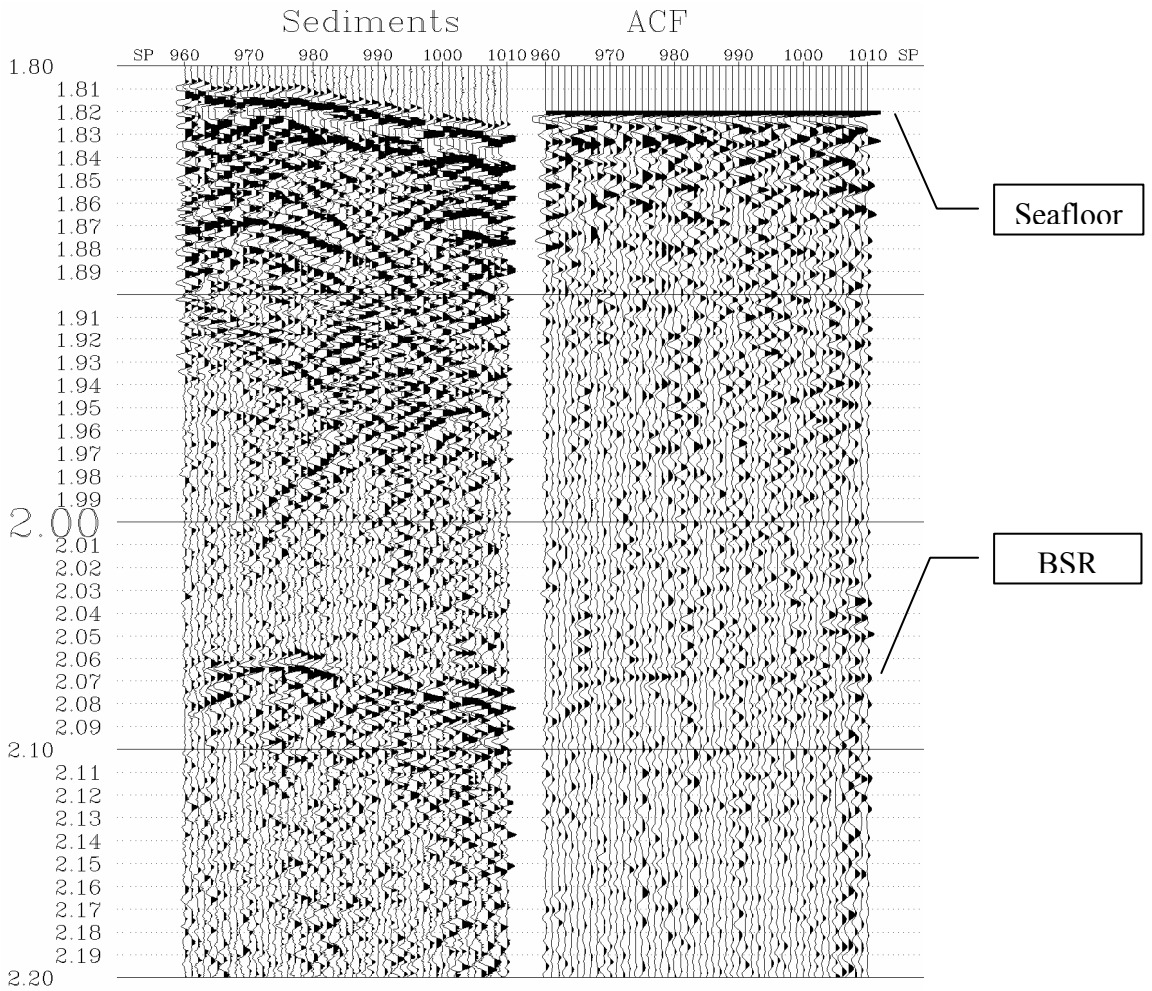

Figure 3.3 Seismogram panels showing upper sediment reflections recorded by Teledyne streamer and their autocorrelation function (time-shifted to make the large amplitude of the autocorrelation function approximately matching the seismic events). Note that in both panels, a spherical divergence correction (multiplication by travel time *t*) was applied.

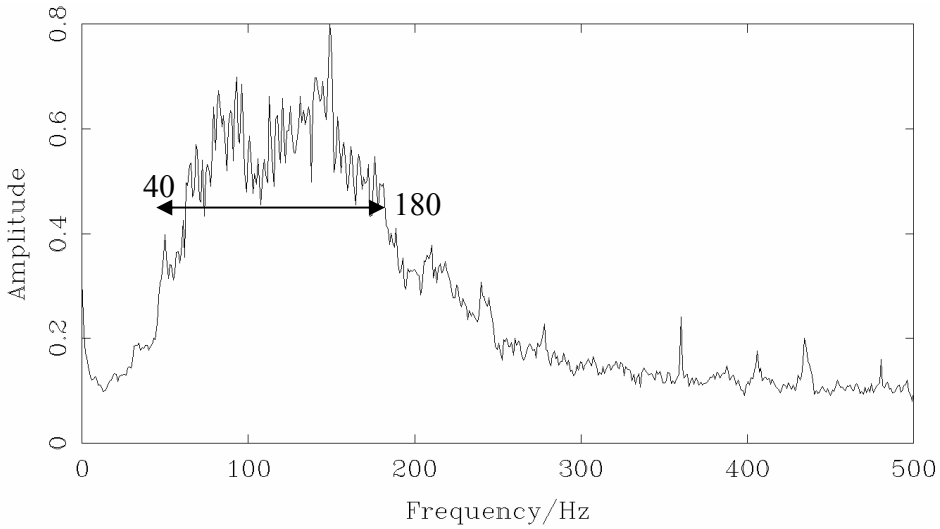

Figure 3.4 Mean amplitude spectrum of upper sediment reflections (Figure 3.3) over a time window from 1800 to 2200 ms.

energy of later-arriving bubbles decays quickly (Figure 3.1). Despite these difficulties with the direct arrivals, good quality sub-seafloor reflections were obtained. For the purpose of suppressing bubble ghosts, the wave shape kit appeared to be successful, since no obvious bubble events are associated with sediment reflections (Figure 3.3). As well, the frequency spectrum for the sediment reflections (Figure 3.4) extended out to frequencies of nearly 180 Hz.

To emphasize the dominant frequency of the signal, a Butterworth bandpass zero-phase filter was applied. The low cut frequency was set to 40 Hz, with a slope to zero amplitude at 15 Hz; the high cut frequency was set to 150 Hz (a little bit lower for whole sediment section rather than the high limit of 180 Hz during test for only upper sediments of 400 ms, refer to Figure 3.6), with a slope to zero amplitude at 220 Hz.

3.3 Source Signature Deconvolution

3.3.1 Why Source Signature Deconvolution Is Needed

To suppress the bubble reflections, a predictive Wiener deconvolution was included in the final data processing, which is based on following 3 assumptions:

1. the seismic trace is modeled as the convolution of the source wavelet with the earth impulse response, i.e., the time series of reflections with amplitudes equal to the reflection coefficients,
2. the reflection coefficient series is a white noise sequence, and
3. both the seismic wavelet and earth impulse response are assumed to be minimum phase.

The raw data (i.e. no digital filters, only analog signals) received by each hydrophone must be minimum phase because physically it must be causal, which is built into the minimum phase assumption. However, the Teledyne streamer is a stack of all hydrophones and a digital bandpass filter is applied to the data before display. Therefore, the final recorded wavelet must be treated as mixed-phase. Ideally, source signature deconvolution processing should first convert the recorded seismic data to their minimum phase equivalent before applying spiking or predictive deconvolution.

3.3.2 Methods of Source Signature Deconvolution

The process of source signature deconvolution involves the following steps:

(a) Acquire source signature wavelet.
(b) Design a shaping filter that can convert the source signature wavelet to its minimum-phase equivalent.
(c) Apply the shaping filter to the shot record by convolving it with each trace.
(d) Apply spiking deconvolution to output data from step (c).
(e) Apply zero-phase Butterworth bandpass filter to reduce high-frequency artificial noise introduced by spiking deconvolution.

Since zero-phase Butterworth bandpass filtering at step (e) should be determined before spiking/predictive deconvolution, the same filter as in section 3.2 is used.

1. Acquire Source Signature Wavelet

If the far-field signature of the source can be recorded in marine seismic exploration, optionally this wavelet can be used to design the shaping filter to convert recorded seismic signals to their minimum phase equivalent. However, a special

hydrophone to record the source signature wavelet was not available. Thus, additional methods were tried to represent the source signature wavelet.

(a) Frequency-Matching method

First a Frequency-Matching method was tried to estimate statistically the source signature wavelet. The average frequency spectrum over a specified time range for the selected traces is calculated and a zero-phase wavelet that has the same spectrum is extracted. Since the extracted wavelet is zero-phase, the method should be used only when the seismic data have been processed to zero phase. The advantage of this method over a computed theoretical wavelet is that the frequency of the wavelet will match that of the seismic data. However, an extracted wavelet may be inferior to a theoretical wavelet if there is a heavy geological imprint or correlated noise in the seismic data, and therefore at least half a second of data should be used when extracting a wavelet.

To apply the Frequency-Matching method, a time window from 1.5 to 2.5 s was chosen from the seafloor to depths well below the BSR, in order to minimize geologic effects and correlated noise effects. The seismic data in the window were converted to zero phase using Claritas and then exported to Kingdom Suite. Figure 3.5 and Figure 3.6 show the extracted wavelet and corresponding computed amplitude spectrum for the test data of Figure 3.3. However, the test result was very disappointing: the very poor signal-noise ratio (Figure 3.6) implied that Frequency-Matching method was not appropriate for special Teledyne data using a sleeve airgun, especially when compared with a successful case of the 2004 Teledyne data using a single airgun as a seismic source (See Appendix B for results of applying Frequency-Matching method to the 2004 Teledyne data collected at Nootka area).

It is believed that problems in applying the Frequency-Matching method were caused by the array effect on the wavelet, especially for the relatively high frequency source, which produced an unusual high noise spectrum for the 2001 data set. As discussed in section 3.2, the primary pulse appears to be corrupted by interference from the time-varying arrivals (Figure 3.1). Although the sediment reflections appear to be well recorded, the problems that corrupted the direct arrivals also have subtle effects on the waveforms of the reflected arrivals.

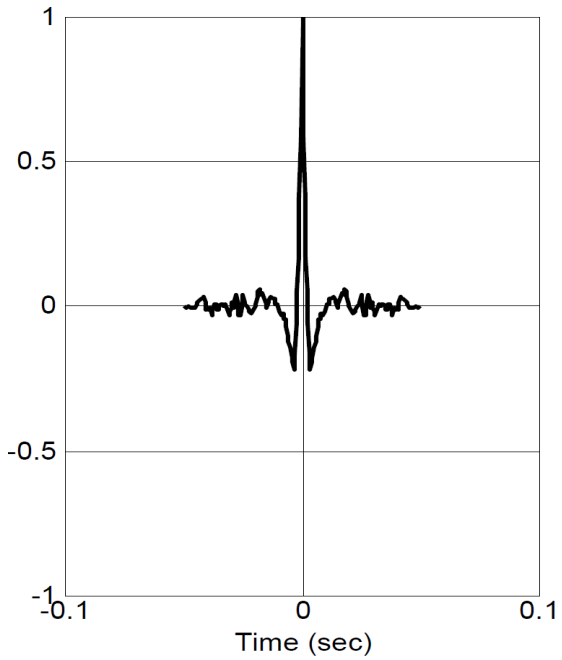

Figure 3.5 Extracted wavelet from the recorded seismogram in Figure 3.3 (2001 Teledyne survey line SCS-1) using the Frequency-Matching method from the Kingdom Suite. The wavelet is zero phase and 100 ms in length with sample interval of 0.5 ms.

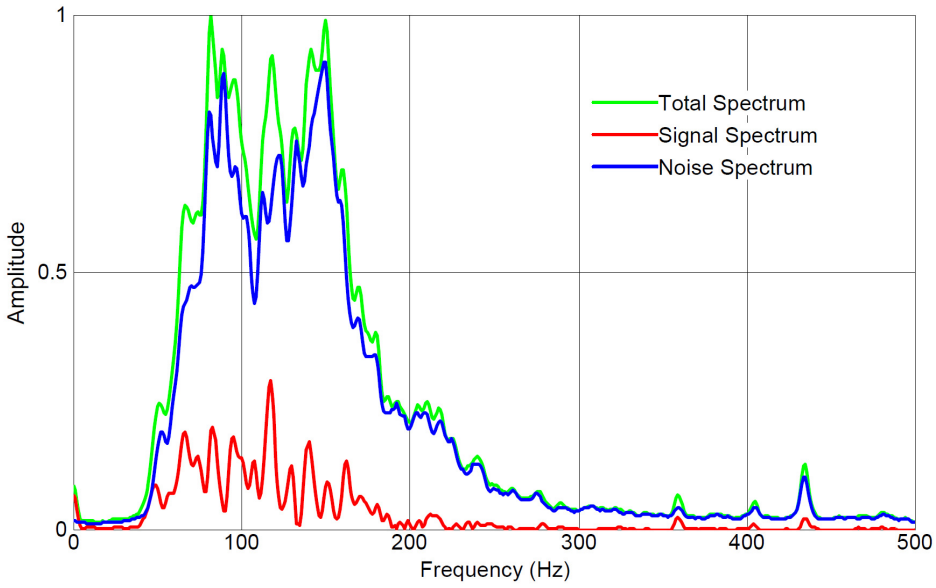

Figure 3.6 The computed amplitude spectra of the 2001 Teledyne data for the Frequency-Matching method. The green line is the total amplitude of the input data, the red line is the amplitude of extracted wavelet "signal", and the blue line is the amplitude of "noise" (remnant of the green subtracting the red). The very poor signal-noise ratio indicated that the Frequency-Matching method cannot produce acceptable source signature wavelet for the 2001 Teledyne data.

(b) Wavelet recorded at shot hydrophone during 1999 survey

In the 1999 COAMS survey, a shot point hydrophone was towed ~3 m below and ~3 m in front of the air gun to record the signature of the gun source (Figure 3.7). In fact, the recorded waveforms in 1999 are not the real signature wavelet, because it is the near-field recording; however, they can be good representations of the far-field wavelet if the seas are not rough and little noise is added. Fortunately, the 2001 Teledyne survey used the same sleeve airgun as the 1999 COAMS survey, and therefore the source signature wavelet recorded in 1999 in theory can be used for the 2001 Teledyne data. As shown in later section 3.7, the seismic image quality is greatly improved after source signature deconvolution using this wavelet.

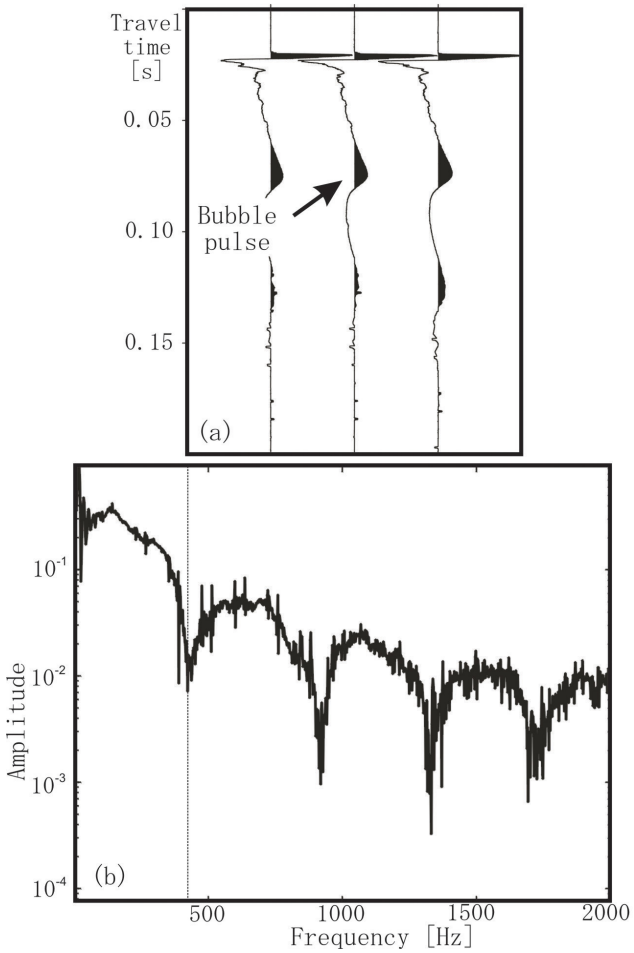

Figure 3.7 (a) Source signature recorded at shot hydrophone in the 1999 COAMS survey and (b) frequency spectrum for three sleeve gun records. The first notch at about 450 Hz corresponds to a gun depth of about 2 m. (From Riedel, 2001)

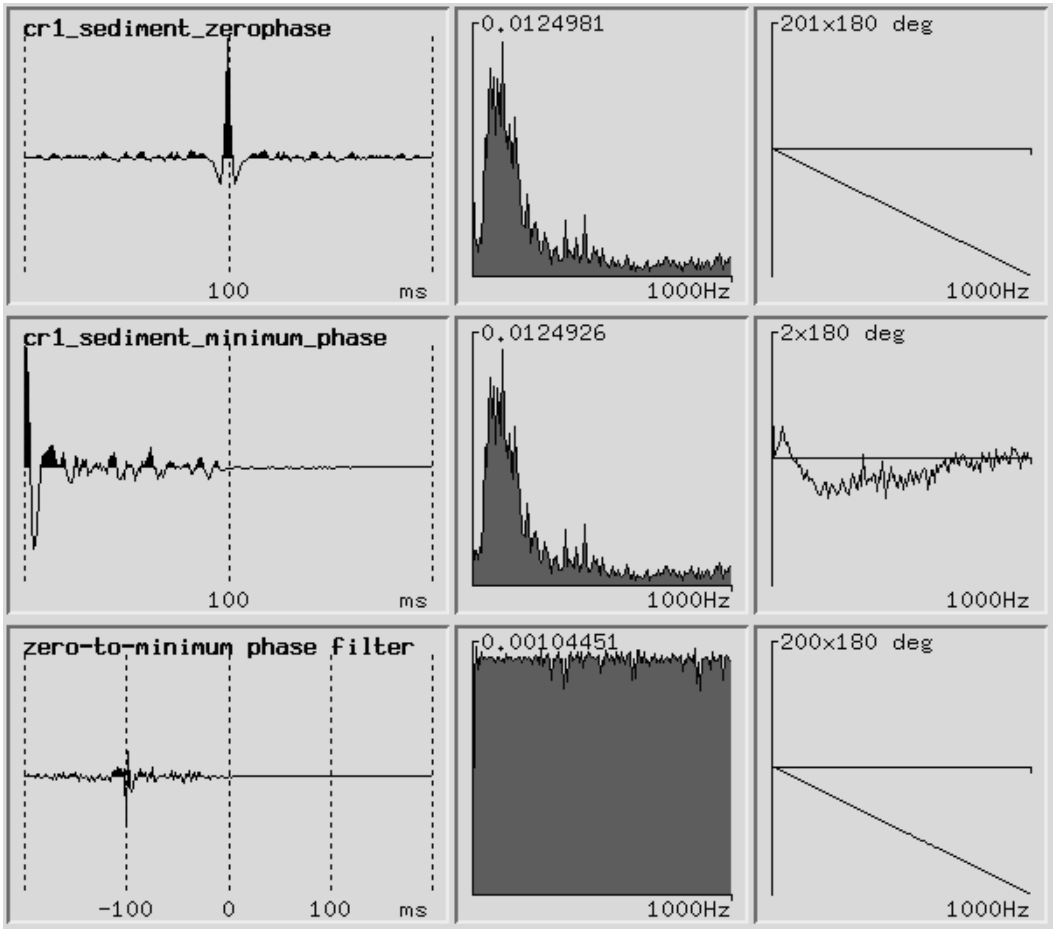

Figure 3.8 Screen capture of minimum phase shaping filter using Claritas wavelet application.

2. Design Shaping Filter

To design the shaping filter that converts the source signature wavelet to its minimum phase equivalent, the source signature wavelet was passed to the wavelet application of Claritas. Figure 3.8 shows an example of the main design steps and results. The figure has 3 rows for 3 steps; each row has 3 windows, from left to right showing waveform, amplitude spectrum and unwrapped phase spectrum. The first row is the same wavelet as in Figure 3.5 extracted by Frequency-Matching method. The second row is the minimum phase equivalent of the wavelet, which has the same amplitude spectrum but smallest shift in phase to achieve that frequency response. The third row is the designed shaping filter, which can produce the minimum phase wavelet of row 2 if convolved with the original wavelet of row 1. This shaping filter is then exported as a SEGY or txt file, which will be used to implement the source signature deconvolution on field data.

3. Apply Shaping Filter to Field Data

The acquired shaping filter is applied to the field data by convolution. In Figure 3.9 the test data from line SCS-1 (left) are convolved with the shaping filter for the Frequency-Matching method (middle) and for the shot hydrophone recording (right). Note that a time shift may be present on different convolved seismic sections, due to arbitrary initial times of the SEGY wavelet file (e.g., ~20 ms on Figure 3.7, and 100 ms on Figure 3.8), and simple static shift is applied to realign the seismic reflections.

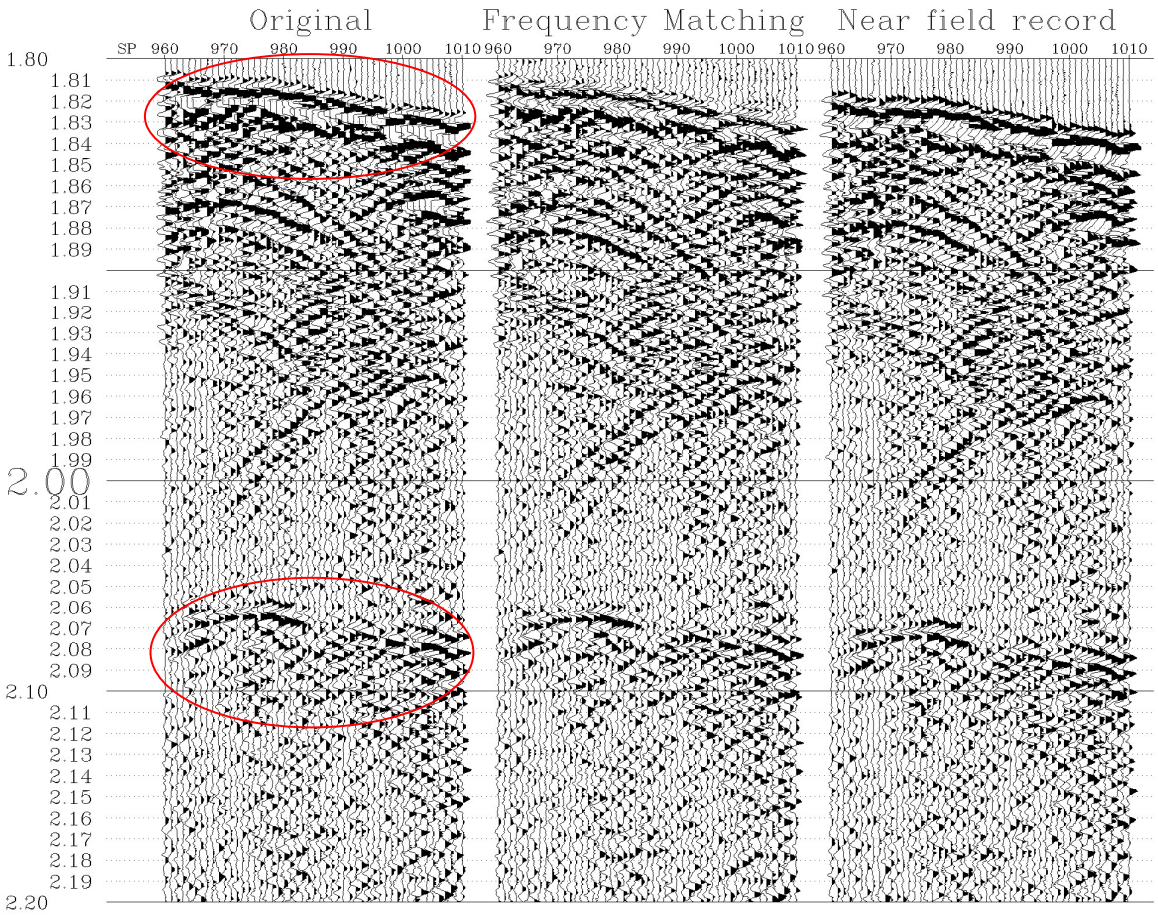

Figure 3.9 Uppermost sediment reflections of Cucumber Ridge survey SCS-1 (left; same as Figure 3.3) and results after convolving with shaping filter for Frequency-Matching method (middle) and for shot hydrophone recording (right), respectively.

Compared with the original seismic image at left, the middle image shows degraded quality of the seafloor and BSR reflections. For the image on the right, using the shot hydrophone recorded wavelet, phase continuity is improved with more prominent seafloor and BSR reflections.

Source signature processing aims at converting the seismic record to its minimum-phase equivalent, so it has not made any impact on the degree of vertical resolution. By changing phase, however, the reflections may be restored to their true time positions. Thus the image is improved, and picking of the seafloor and BSR reflections is less ambiguous and more accurate.

4. Apply Spiking Deconvolution

In theory, after the deterministic step of source signature processing above, statistical spiking deconvolution should be applied to flatten the spectrum. As described by Yilmaz (2001, pp. 178-179) the spiking deconvolution is the process by which the seismic wavelet is compressed to a zero-lag spike. When applied to the seismogram, the spiking deconvolution yields the earth's impulse response. Because the spiking deconvolution operator is strictly the inverse of the wavelet, its performance depends not only on filter length, but also on whether the input wavelet is minimum phase. If the wavelet is minimum phase, then the process produces a stable inverse (the filter coefficients forms a convergent series), which also is minimum phase. On the other hand, if the wavelet were maximum or mixed-phase, it does not have a stable inverse.

Spiking Wiener deconvolution (Claritas module PSDECON) was applied to the data. Autocorrelation functions of each trace are smoothed in a running mix of 25 traces before being used to derive the deconvolution filter. PSDECON therefore acts as a constrained trace-by-trace filter. The output shows less spatial variation, and should allow deconvolution to be applied to data with a lower signal/noise ratio without damaging weaker signals.

Figure 3.10 compares the effect of a combination of source signature deconvolution and spiking deconvolution. Since spiking deconvolution flattens the spectrum and introduces high frequency artificial noise, a bandpass filter of 15-45 to 150-

220 Hz was applied to all panels. It shows that the spiking deconvolution compressed the wavelet vertically (middle and right); with source signature deconvolution (right), the wavelet was compressed more intensely, especially seen at reflections near seafloor. The effects on BSRs cannot be judged easily, with continuity improved for some segments but poorer for other segments.

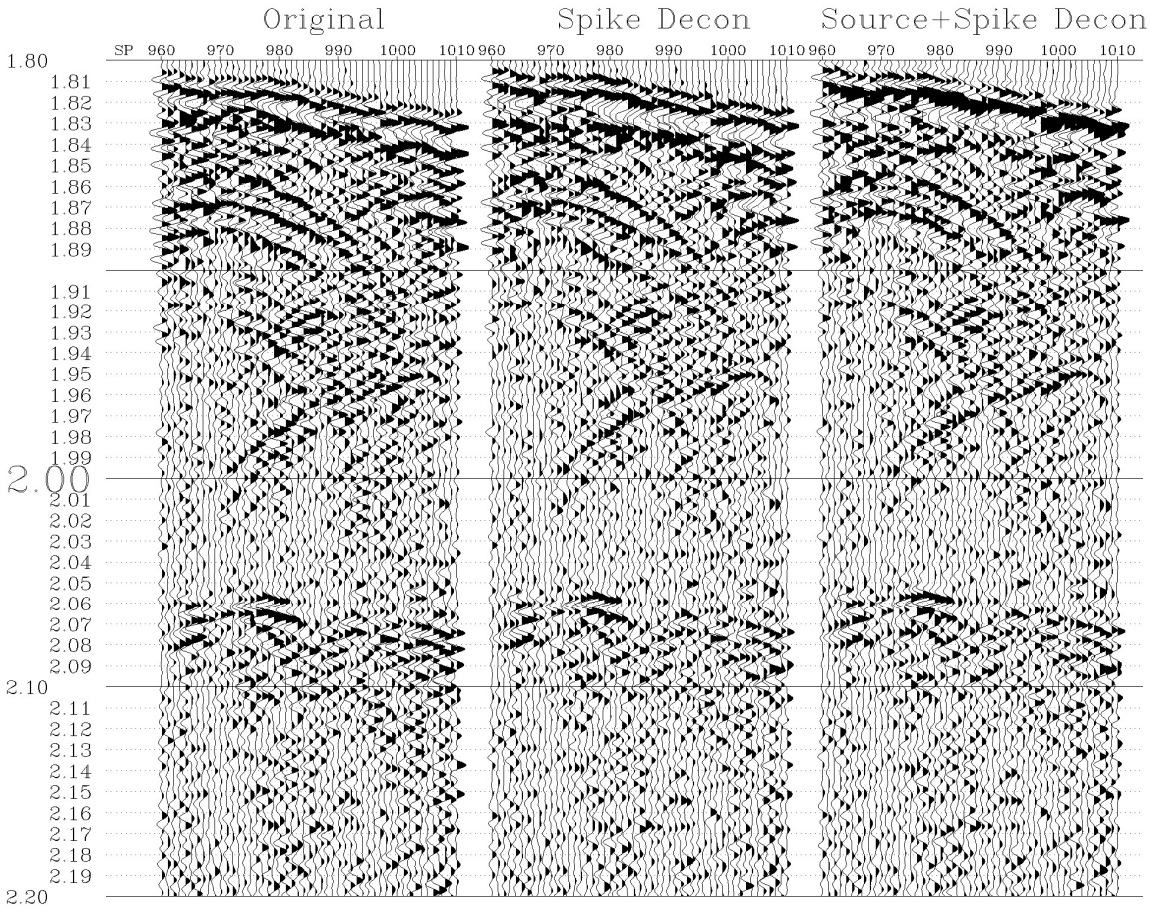

Figure 3.10 Original reflection from line SCS-1 (left), result after spiking deconvolution only (middle) and result after source signature deconvolution followed by spiking deconvolution. A bandpass Butterworth filter of 15-40 to 150-220 Hz was applied to all panels.

3.4 Predictive Deconvolution

Bubble pulses lagging the primary reflections may lead to false sediment reflections and may reduce vertical resolution by interference with primary reflections. Although the wave shape tool of the sleeve gun reduced the bubble energy efficiently,

there were still noticeable bubble events recorded (Figure 3.1). A predictive deconvolution method was thus used to reduce bubble amplitudes further. This was done with the DECONW module of Claritas, which can affect time-varying and spatially-varying spike or predictive (with optional gap) deconvolution of a seismic trace over a set of application time gates. Note that the most obvious bubbles occurred at 60 ms and 120 ms on the autocorrelation function (Figure 3.2); a predictive deconvolution with gap length of 30 ms and a filter length of 500 ms (better results with larger filter length but running slower) should be enough to implement bubble reduction.

Figure 3.11 shows results for different deconvolution strategies on the direct arrival part of the SCS-1 example used previously. The same bandpass filter of 15-40 to 150-220 Hz was applied to all panels to remove high frequency artificial noise introduced by deconvolution process. The corresponding autocorrelation functions are shown below the images. Balancing wavelet compression and bubble removal, it is apparent that the best result is achieved when source signature, spiking and predictive deconvolutions are all applied in sequence.

When applied to sediment reflections, there are two options to design the deconvolution filter: 1) use strong reflections from the uppermost sediments, or 2) use the direct arrival as in Figure 3.11. Figure 3.12 shows the image panels and their autocorrelation functions for comparing these two options. Since the wave shaping tool of the sleeve gun already reduced bubble energy to the level of background noise, it is hard to use attenuation of the bubble ghost event as a judging criteria. However, option 1 (middle panel) has the best image quality and clean autocorrelation functions after the 30 ms gap.

3.5 Time Migration

To further improve the image quality, finite difference time migration was applied to remove the diffractions and correct dipping events. FDMIG module of Claritas is a routine based on an X-T domain implicit 45 degree migration. Despite the 45-degree algorithm, FDMIG gives reasonable results up to about a 60 degree dip.

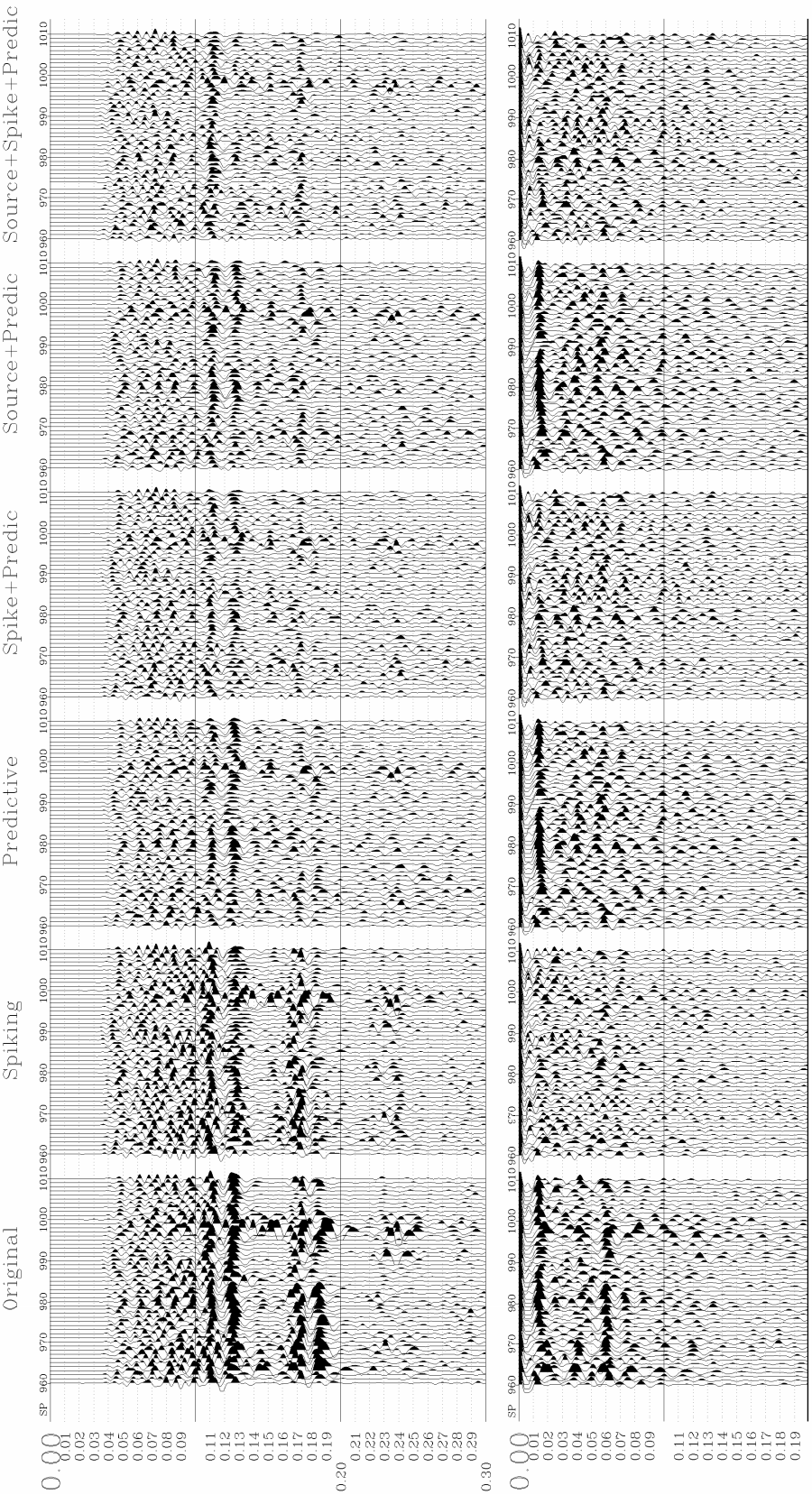

Figure 3.11 (top) Image panels of process results for different deconvolution strategies on direct arrival of example Teledyne 2001 SCS-1 (Figure 3.1). The bandpass filter of 15-40 to 150-220 Hz was applied to remove high artificial noise introduced by deconvolution process. (bottom) The corresponding autocorrelation functions.

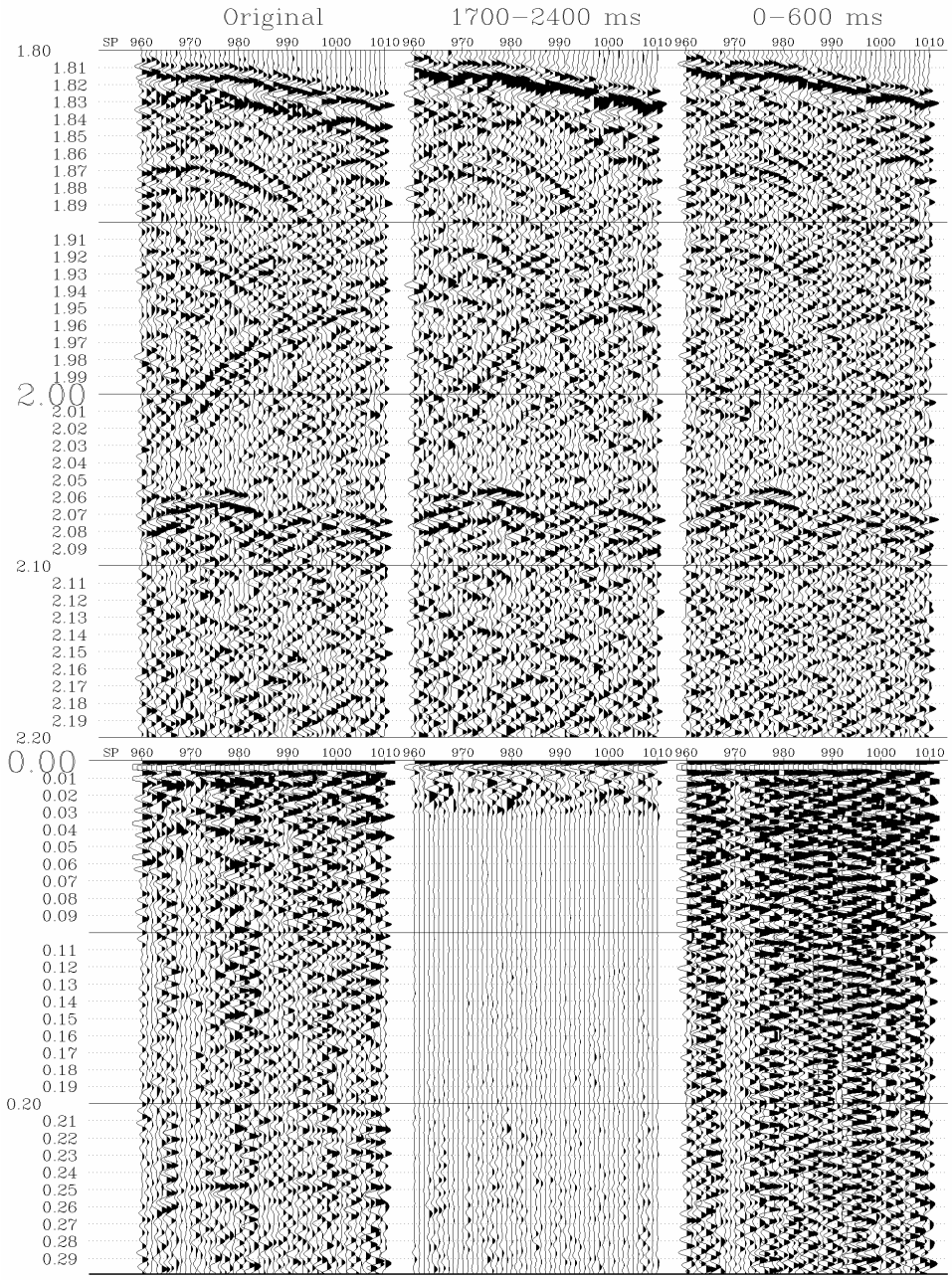

Figure 3.12 (top) Uppermost sediment (Figure 3.3) image panels of deconvolution results for different design windows. The deconvolution processes include source signature deconvolution, spike deconvolution and predictive deconvolution with gap length of 30 ms and filter length of 500 ms. The bandpass filter of 15-40 to 150-220 Hz was also applied. The middle panel used the uppermost sediment reflections from 1700 to 2400 ms as the design window for the deconvolution filter, while the right one used the direct arrival part from 0 to 600 ms. (bottom) The corresponding autocorrelation functions.

There are two key parameters for time migration: trace distance and velocity field. Since FDMIG requires a constant trace distance to compute migration time, a pseudo-3D binning should theoretically provide the best trace distance control; however, in practice the results were not satisfactory due to the empty bin issue (details in Appendix A). Therefore time migration was applied to the originally recorded lines by assuming a constant shot interval of 12.5 m.

The velocity field for FDMIG can vary in time and space, and is defined in a text file which should contain interval velocities. Based on P-wave structure from semblance velocities and full waveform inversion of multichannel seismic data in a region of hydrate concentration ~ 2 km seaward of the ODP Site 889 (Yuan et al., 1996) and ~2 km southeast of Cucumber Ridge of this study, the initial velocity field was estimated by a simple velocity-depth relationship:

$$v = 1516 + 0.5556 \times z \qquad \text{(Equation 3.1)},$$

where v is the P-wave velocity in m/s and z is the subseafloor depth in m. The two-way time t corresponding to depth z was found simply by calculating the average velocity between the seafloor and depth z; a table of v vs. t was then constructed for filling the velocity field of FDMIG. Since the result of time migration is very subjective, FDMIG also provides a SCALE parameter: by multiplying with the scale value, the velocity values change correspondingly without modifying the text file of velocity field.

Figure 3.13 compares the seismic images before and after time migration, with different velocity fields changed by SCALE parameter. From diffractions in the red box, it is apparent that the best result achieved when SCALE is set to 0.7: below this value, the seismic events were under-migrated; above this value, however, over-migration occurred. After migration, BSRs are more prominent and less ambiguous to pick, which was important for later stages of the study where heat flow was calculated from the BSR (details in section 5.1).

3.6 Amplitude Balancing

Before output to display or stack, amplitude balancing is normally used to balance the constituent traces of a gather. The BALANCE module of Claritas scales individual

traces by a slowly varying or constant scalar, so that the average power (or average amplitude) of the output trace is constant for all traces output from this process. BALANCE affects a horizontal (i.e. spatial) balance, as opposed to the vertical (i.e. time) balancing effect of geometric spreading compensation (SPHDIV in section 2.3.1).

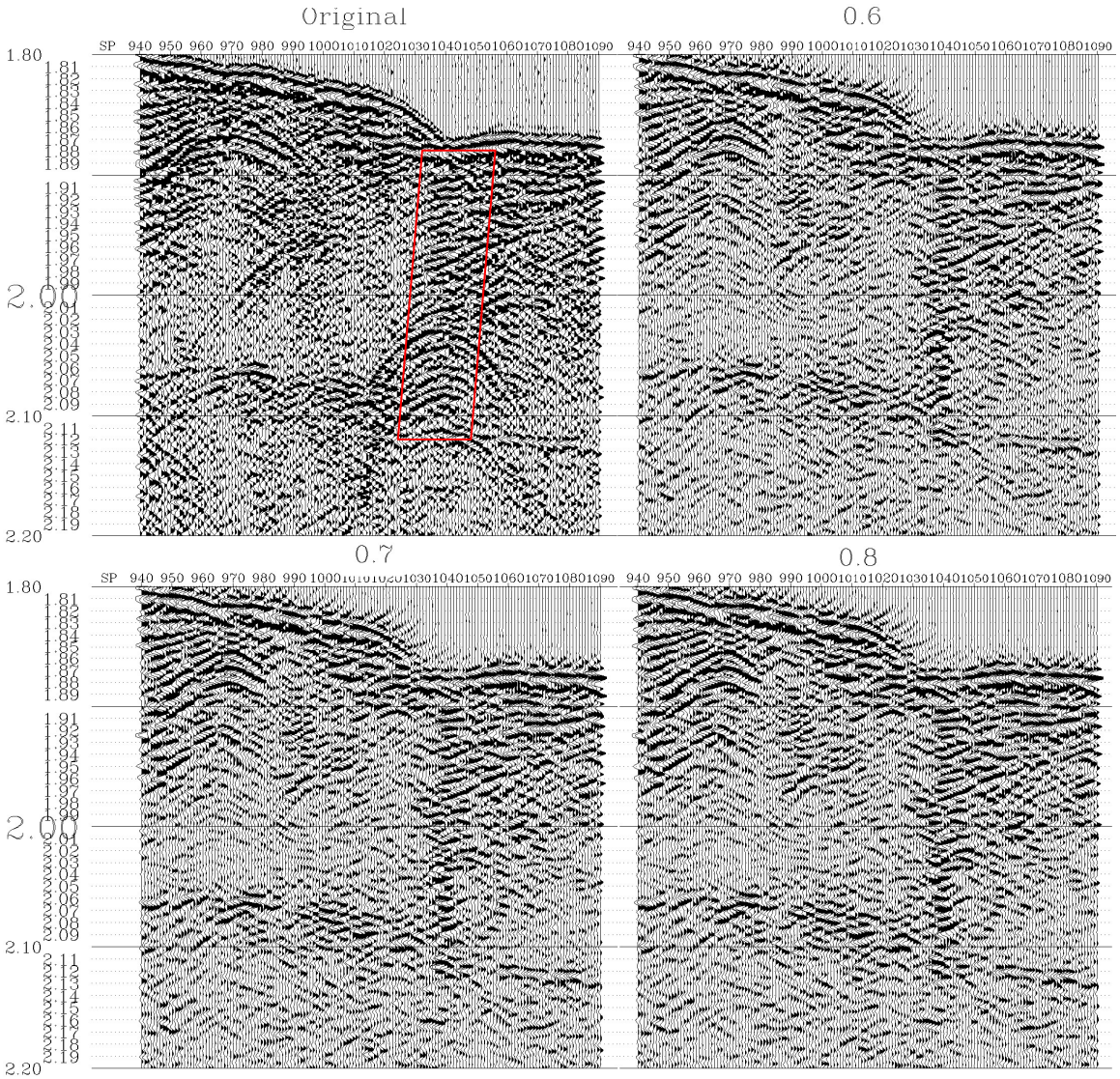

Figure 3.13 Seismic images before time migration (original) and after time migration using linear velocity field from 1516 m/s at seafloor to 1738 m/s at depth of ~492 ms below seafloor in two way time, with different SCALE values 0.6, 0.7 and 0.8. Data processing includes spherical divergence compensation, bandpass filtering and amplitude balancing. The red box outlines a diffraction zone used to compare image quality.

Compared to another commonly used display enhancement method AGC (Automatic Gain Control), BALANCE is preferred since it is a linear process. It will not alter the frequency content of the trace, and will not destroy relative amplitude information.

The trace may be scaled according to absolute amplitude or power (i.e., amplitude squared). For the case of the 2001 Teledyne data, a scalar was derived from the average amplitude of the trace within a single window over the 5 s trace length, and all trace values are then divided by this scalar, so that the average amplitude of the trace data values becomes 1.0.

3.7 Final Image Result

Figure 3.14 shows the final seismic imaging result of all data processing steps discussed above. With source signature deconvolution, image (b) achieved better wavelet compression vertically and thus enhanced signals of strong seismic events like the seafloor and the BSR.

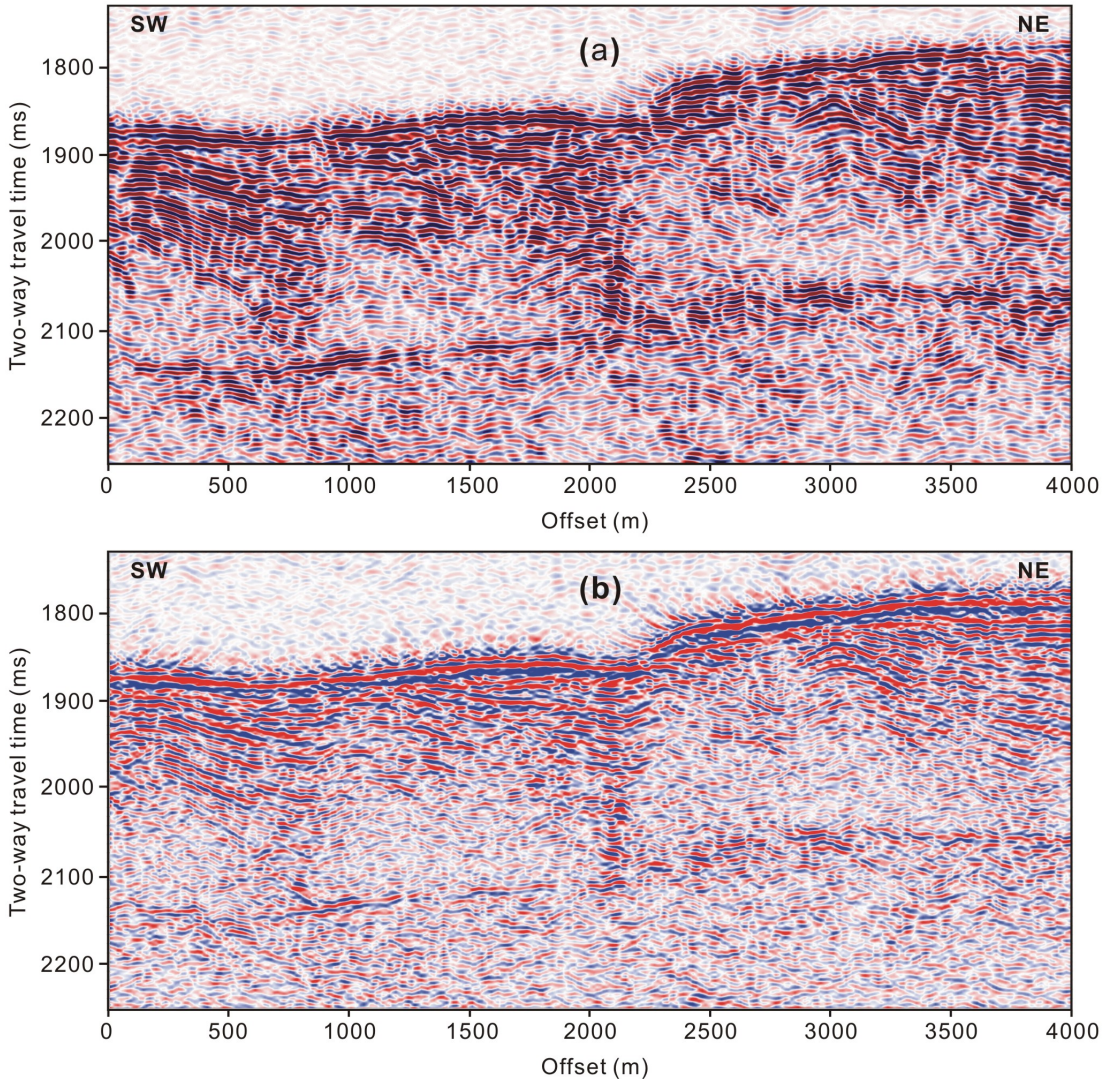

Figure 3.14 Final seismic imaging results of all data processing discussed above (a) without and (b) with source signature deconvolution.

Chapter 4

DTAGS Multichannel Seismic Data Processing

Within this chapter the details of DTAGS data processing are given. A specific technique was developed in this study to overcome the problems caused by the nonlinearly tilting DTAGS streamer during the entire survey. Depths of the sources and receivers were determined by a Genetic Algorithm inversion method, using the known depths at cable nodes, direct arrivals and the reflections from the sea surface. To achieve high quality seismic images and velocity analyses, careful attention was paid to statics of source and receivers and image stitching for neighbouring shot gathers. The final processed images resolve fine structures of sediment layering down to ~300 ms below the seafloor. After posting the DTAGS lines and the Teledyne 2000 grid on the bathymetry map in Kingdom Suite, trace shifts were made to horizontally and vertically align all images at their intersection points.

4.1 Source Cross-correlation

The Vibroseis-like source of DTAGS is a 250 ms long sweep signal in the form of a frequency-modulated sinusoid that is tapered on both ends (Figure 4.1). The initial step of processing the DTAGS data was to cross-correlate the field recording with the source signal. Although deconvolution (frequency domain division) in theory gives a better spectrum than correlation, correlation (frequency domain multiplication) is in practice more stable because division by values near zero will produce unreasonably large amplitudes at the corresponding frequencies.

As described by Chapman et al. (2002), there are 4 options to get an approximation of the pilot sweep: 1) the normal incidence data from the monitor hydrophone located near the source, but the signal proved to be too noisy because of electrical interference; 2) the direct wave recorded at the very near hydrophone, about 15 m from the source; 3) the early portion (250 ms) of the subseafloor reflection at the nearest hydrophone, but fine-scale velocity and density variations near the sea floor cause

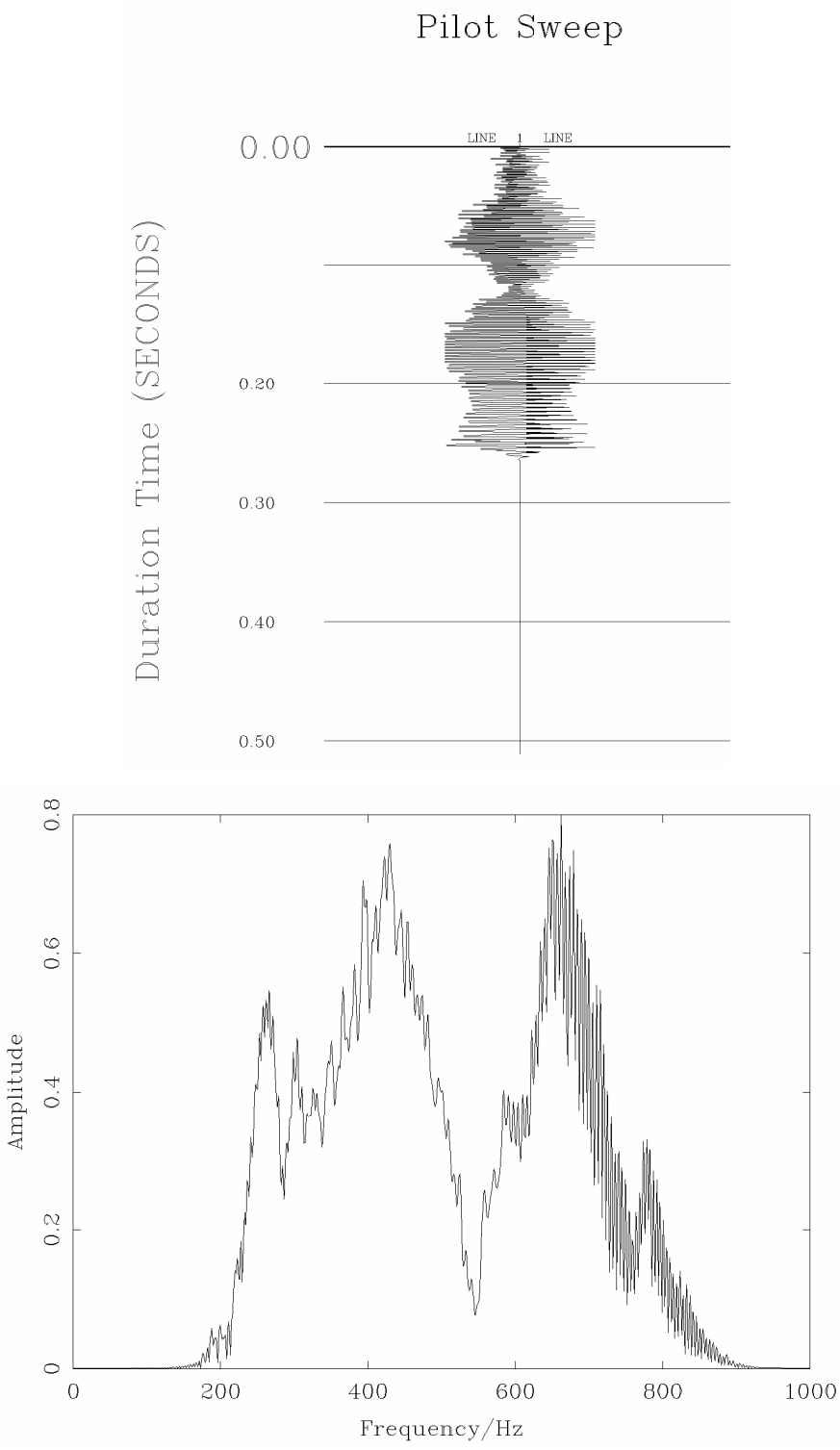

Figure 4.1 Pilot sweep (provided by W. Wood, NRL), extracted from direct-wave signal at the very near hydrophone, and its amplitude spectrum.

interference in this signal that varies from trace to trace because of the high DTAGS frequencies; 4) the sea-surface reflection, but this signal was also extremely variable, perhaps from small variations in the water velocity with depth or because the scale of the sea-surface roughness was comparable to the DTAGS wavelengths. Therefore, the second option – the direct-wave signal at the very near hydrophone was used as the pilot sweep; as in previous studies, this appeared to give the most distinct sea-floor and deeper reflectors.

In this study, the pilot sweep was provided by W. Wood (NRL) (Figure 4.1). The amplitude spectrum has the approximate form of a boxcar, cosine tapered up from 220 Hz up to 330 Hz, full on from 330 Hz to 650 Hz, and cosine tapered down from 650 Hz to 700 Hz. Note the hole in the spectrum at about 542 Hz, over which a notch filter of 500-540-545-585 was used.

4.2 Bandpass Filtering, Vibroseis Deconvolution and Spectral Balancing

Acoustic channels of Shot 111 (22 live traces) from DTAGS2 survey line DT09 were chosen as the test data for processes of frequency analysis, Vibroseis deconvolution and spectral balancing. Panel 1 of Figure 4.2 is the cross-correlation between the raw field record and the pilot sweep of Figure 4.1. The shallow sediment layering is well resolved and noise levels are reasonable. Since the Vibroseis-like seismogram is sometimes not stable in amplitude and phase, seismic events are shown greater coherence and more easily identified on an envelope image (Figure 4.3). Figure 4.4(a) shows the mean amplitude spectrum of the 22 live acoustic traces of Shot 111 (Panel 1, Figure 4.2).

4.2.1 Bandpass Filtering

Based on characteristics of the raw data amplitude spectrum (Figure 4.4a), a series of bandpass filter test were run (Figure 4.5), all with same low cut frequency of 250 Hz but with different high cut frequencies of 515 Hz, 650 Hz and 790 Hz. It is apparent that Panel 2 on Figure 4.5 shows the cleanest image and highest amplitudes on most seismic events. Although some high frequency signal may be lost in the first 20 ms after the

seafloor reflection, the overall improvement at greater depths justified the rejection of frequency above 545 Hz. Therefore, the frequency limits of 220-250 to 510-545 Hz were chosen for later processes.

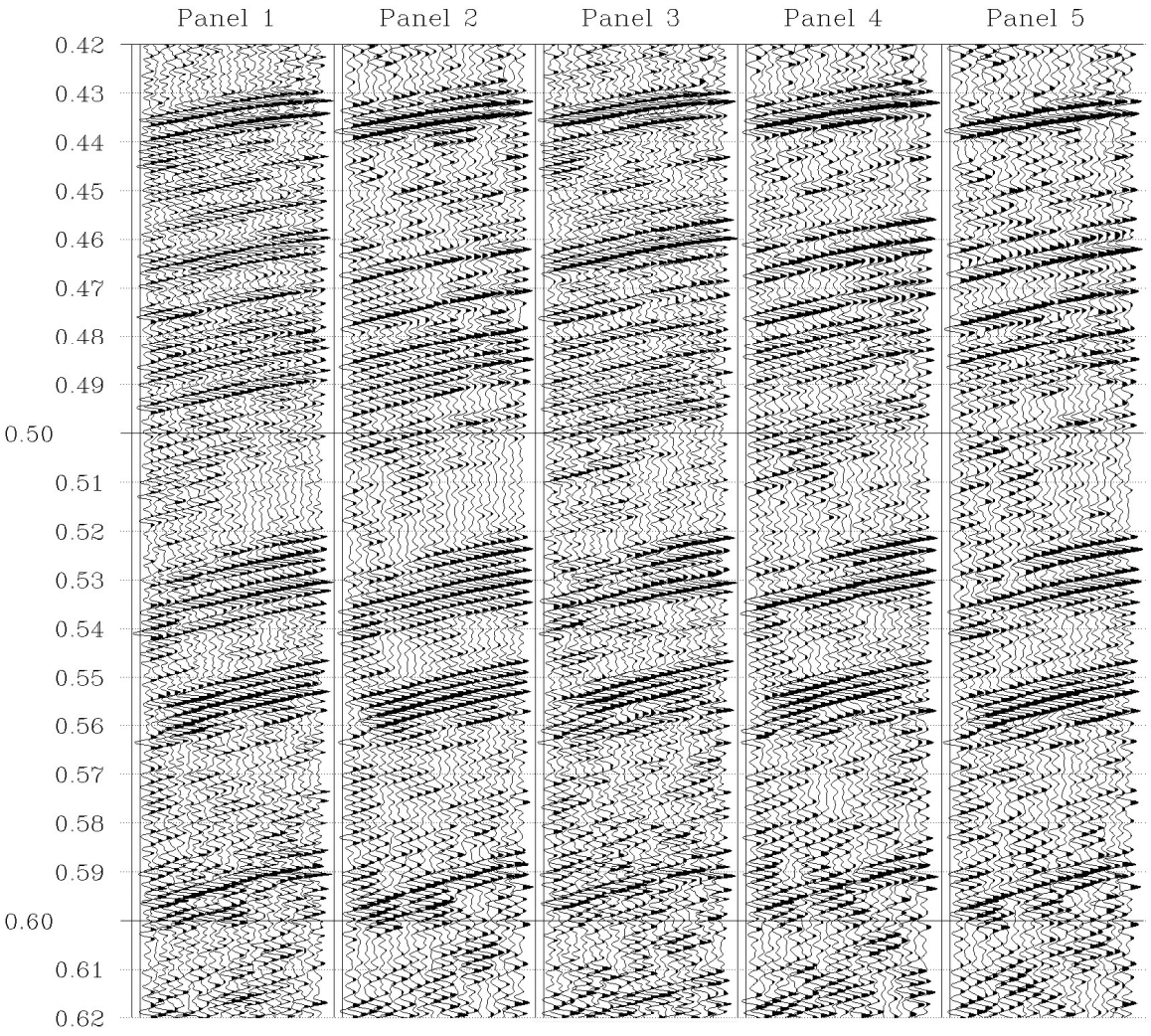

Figure 4.2 Shot 111 panels of DTAGS2 survey line DT09, only showing the acoustic channels (22 live channels). (Panel 1) The cross-correlation of the field record with pilot sweep in Figure 4.1. (Panel 2) The zero-phase Butterworth bandpass filtered version of Panel 1. Frequency limits were 220-250 to 510-545 Hz. (Panel 3) The spiking deconvolved version of Panel 1. (Panel 4) The spiking deconvolved version of Panel 1, followed by a zero-phase Butterworth bandpass with frequency limits of 220-250 to 510-545 Hz. (Panel 5) Spectral balanced version of Panel 1. Frequency limits were 220-250 to 510-545 Hz, same as Panel 2.

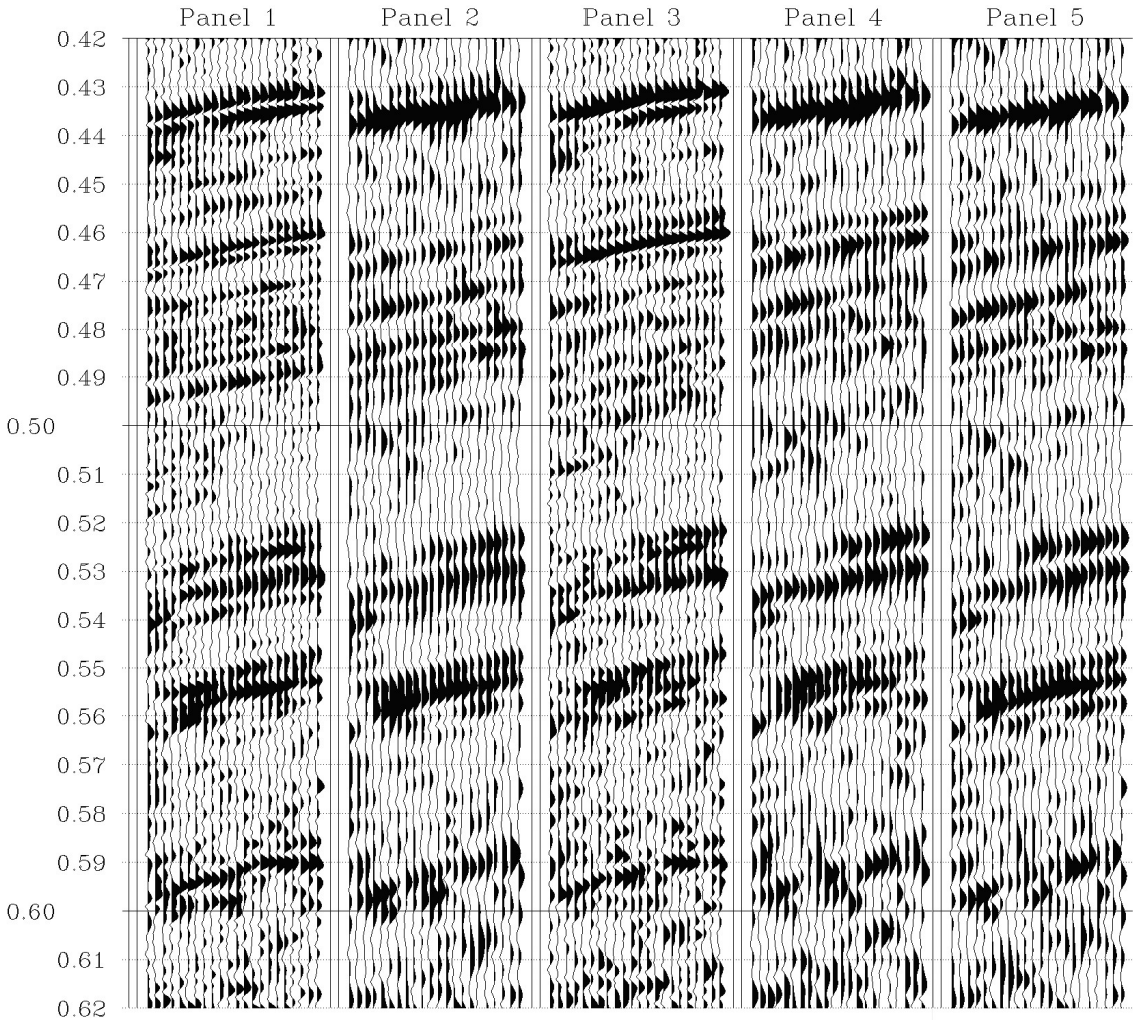

Figure 4.3 Envelope version of image panels in Figure 4.2.

4.2.2 Vibroseis Deconvolution

For an explosive source, the basic convolution model is given by

$$x(t) = s(t) * w(t) * e(t) \qquad \text{(Equation 4.1)},$$

where $x(t)$ is the recorded seismogram, $s(t)$ is the source signature signal, $w(t)$ is the unknown wavelet including the propagation effects in the earth and the response of the recording system, and $e(t)$ is the earth impulse response. The deconvolution process aims at resolving the correct $e(t)$ (Yilmaz, 2001).

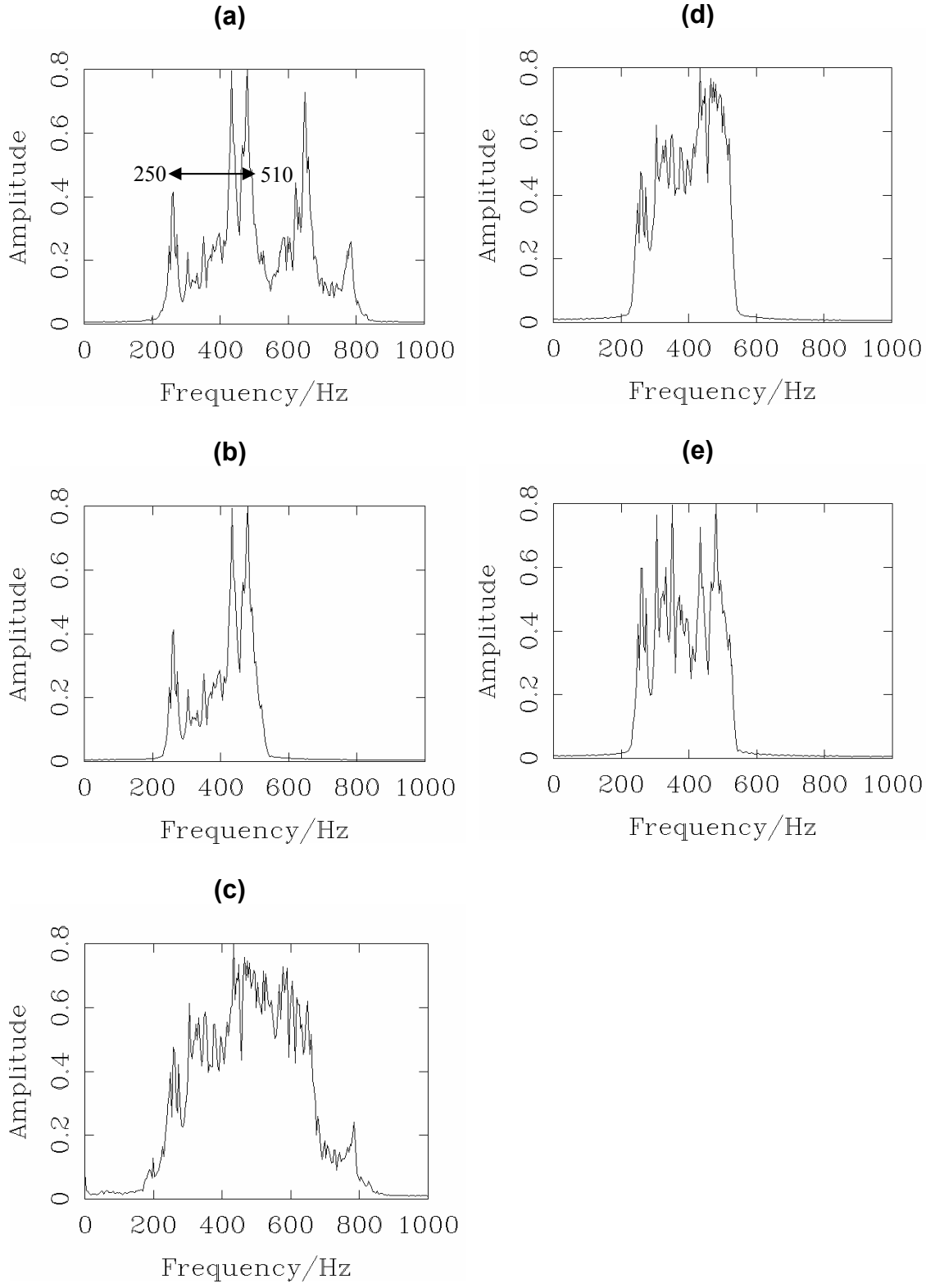

Figure 4.4 The amplitude spectra corresponding to the seismogram panels in Figure 4.2.

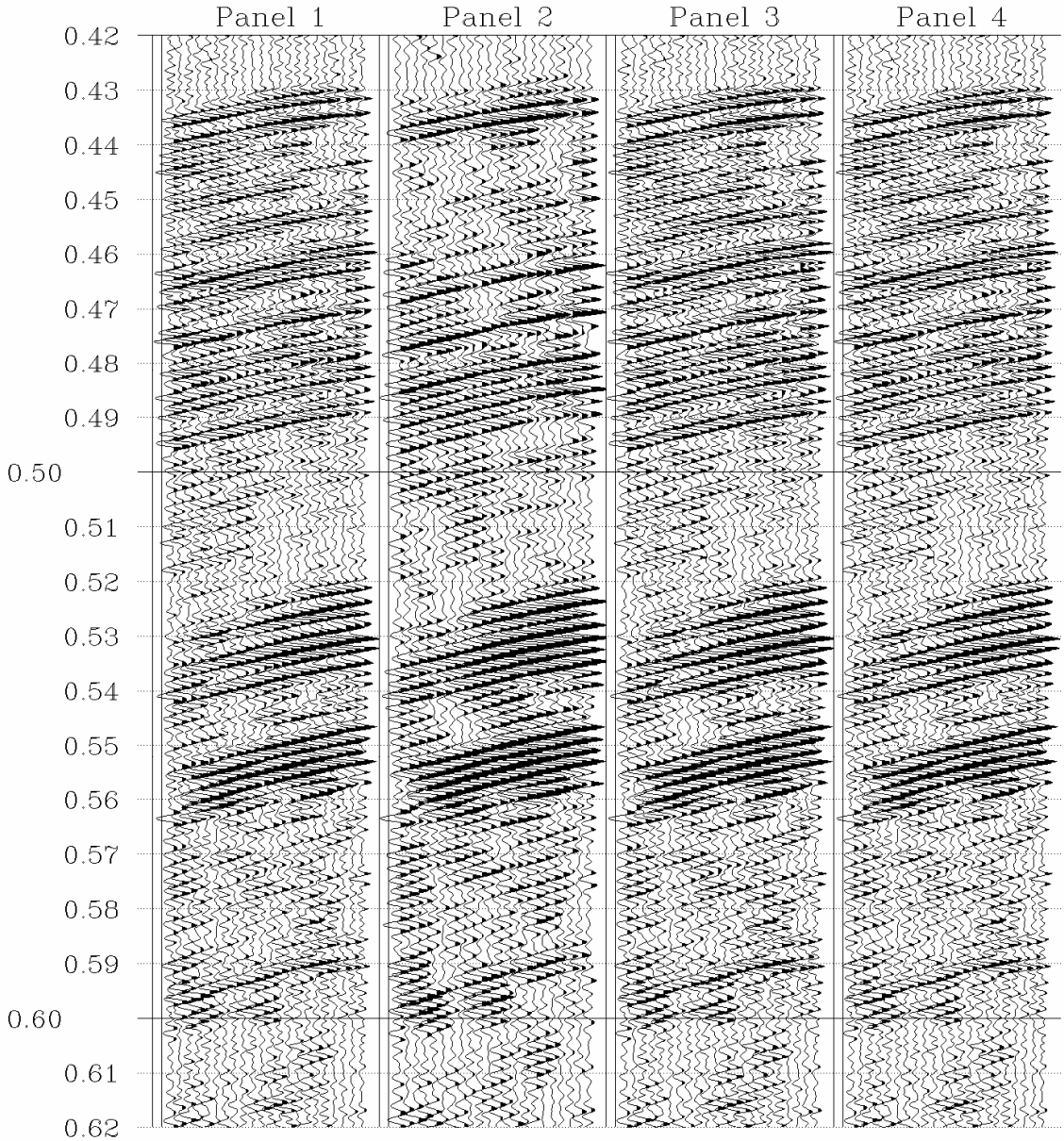

Figure 4.5 Test panels for zero-phase Butterworth bandpass filtering. (Panel 1) original data of Shot 111. (Panel 2) after bandpass filter with frequency limits of 220-250 to 510-545 Hz. (Panel 3) after bandpass filter with frequency limits of 220-250 to 650-790 Hz. (Panel 4) after bandpass filter with frequency limits of 220-250 to 790-900 Hz.

For the DTAGS system, which has a Vibroseis-like source, a similar convolution model can also be given by

$$x'(t) = k(t) * w(t) * e(t) \qquad \text{(Equation 4.2)},$$

where $x'(t)$ is the cross-correlation of recorded seismogram with the pilot sweep signal, $k(t)$ is the autocorrelation of the sweep signal, which is called the Klauder wavelet. The Klauder wavelet itself must be zero-phase because it is an autocorrelation. Assuming $w(t)$ is minimum-phase, convolution of $k(t)$ with $w(t)$ will produce a mixed-phase wavelet, which cannot satisfy the minimum-phase assumption for spiking deconvolution (Yilmaz, 2001).

To recover $e(t)$ properly from Vibroseis data, a filter was designed to convert the Klauder wavelet to its minimum-phase equivalent, then followed by a spiking deconvolution. Figure 4.6 shows the design process for this match-filter using the WAVELET application of Claritas. Note that the phase spectrum of the Klauder wavelet and its minimum-phase equivalent are almost the same, and consequently the match-filter is close to a δ function. Therefore, in practice the process skipped the step of converting the Klauder wavelet to its minimum-phase equivalent and directly applied spiking deconvolution, treating the Vibroseis data as explosive data.

The spiking deconvolution test is shown in Panel 3 of Figure 4.2. Despite the fact that the basic minimum-phase assumption is violated, spiking deconvolution without conversion of the Klauder wavelet to its minimum-phase equivalent seems to work well for DTAGS data. The wavelets of seismic events were successfully compressed, and the amplitude spectrum was broadened between the frequency limits of 250 to 650 Hz (Figure 4.4c).

After spiking devolution (Panel 3, Figure 4.2), some events were reduced in amplitude and were less coherent. This effect was more noticeable on the corresponding envelope image (Panel 3, Figure 4.3). Since the spiking deconvolution introduces high frequency artificial noise into the data, a zero-phase Butterworth bandpass filter was applied and the resulting image was shown in Panel 4 of Figure 4.2. Although the bandpass filter can only remove a small part of the noise (probably due to the high frequency nature of DTAGS data), the image of Panel 4 was a little bit better than the image of Panel 3, but not as good as the image of Panel 2, which used only bandpass filter.

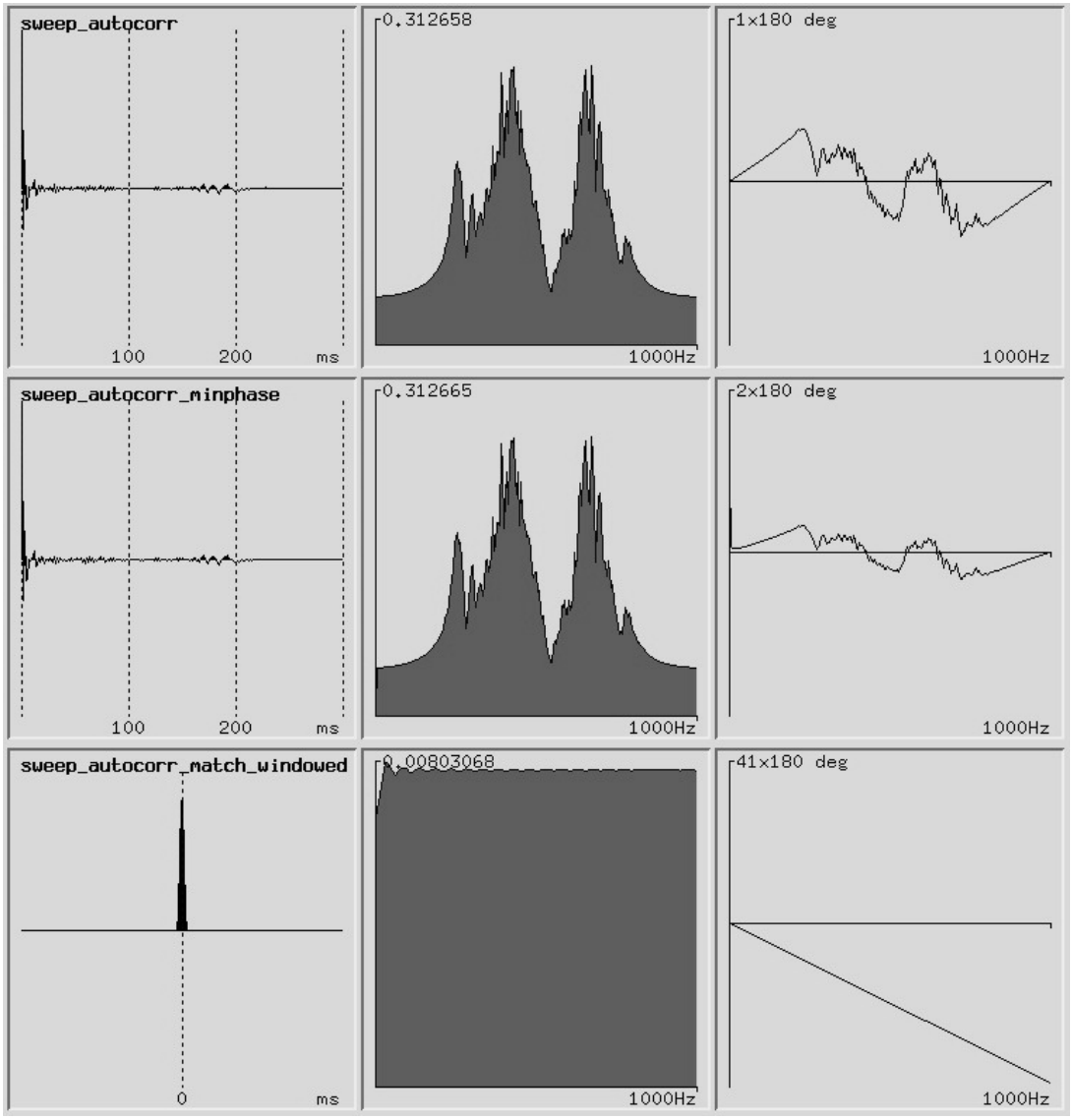

Figure 4.6 Panels showing the Klauder wavelet (the autocorrelation of pilot sweep) (top), its minimum phase equivalent (middle) and the match-filter that converts the Klauder wavelet to its minimum phase equivalent (bottom), including their amplitude spectra and phase spectra.

4.2.3 Spectral Balancing

For a broad band signal such as the DTAGS data, spectral balancing is often used as a replacement for a bandpass filter. Spectral balancing is a zero-phase deconvolution, effected by spectral equalization in the frequency domain whilst leaving the phase spectrum unchanged. This operation mainly involves the following steps (Coppens and Mari, 1984):

1. Performing a Fast Fourier Transform (FFT) to get the amplitude spectrum.
2. Performing a running mean over the amplitude spectrum (i.e. a low-pass filter).
3. Changing the ends of the running mean (essentially a fudge).
4. Adding a small amount to the running mean to avoid divide-by-zero.
5. Dividing the original amplitude spectrum by the running mean so that average amplitudes are now constant along the spectrum (and about 1.0).
6. Effecting the band-pass filter by zeroing parts of the amplitude spectrum and using a cosine taper in between the on and off regions.
7. Performing an inverse FFT to reproduce a time trace.

Figure 4.7 shows test panels of spectral balancing for the same frequency limits as Figure 4.5. Similar to the bandpass filter test, the best image quality was achieved at Panel 2 when frequency limits were set to 220-250 to 510-545 Hz. The corresponding amplitude spectrum (Figure 4.4e) shows a more balanced spectrum compared to the spectrum of the bandpass-filtered data (Figure 4.4b).

The panels of Figure 4.2 compare image quality for different processing strategies. Of all panels the spectral balanced data with frequency limits of 220-250 to 510-545 Hz (Panel 5) show improved image quality: some seismic events are enhanced by compressing the wavelet slightly, and a relatively clean image was achieved by rejecting some of the higher frequencies in the spectrum. When comparing the envelope images in Figure 4.3, Panel 5 of spectral balancing presented the seafloor as a single reflector, which is helpful to align the images of shot/receiver gathers in later stages of DTAGS shot image stitching.

Based on above discussion, the best image quality was achieved by only applying spectral balancing with selected bandpass frequency limits of 220-250 to 510-545 Hz.

4.3 Source and Receiver Depth Corrections

Although the near bottom configuration and wide high-frequency bandwidth of DTAGS allow much better resolution of the subseafloor structures in the upper ~400 m, the short 2-6 m wavelengths of seismic data dictated accurate positioning of the source

and receivers and accurate travel time corrections before standard processing of the multichannel seismic data, such as to properly determine moveout velocities and to stack the data. The process discussion in the following sections mainly used the DTAGS2 survey line DT09 (see Figure 4.8 for line location) as an example, for which a decent seismic image was available after onboard processing (Figure 4.9).

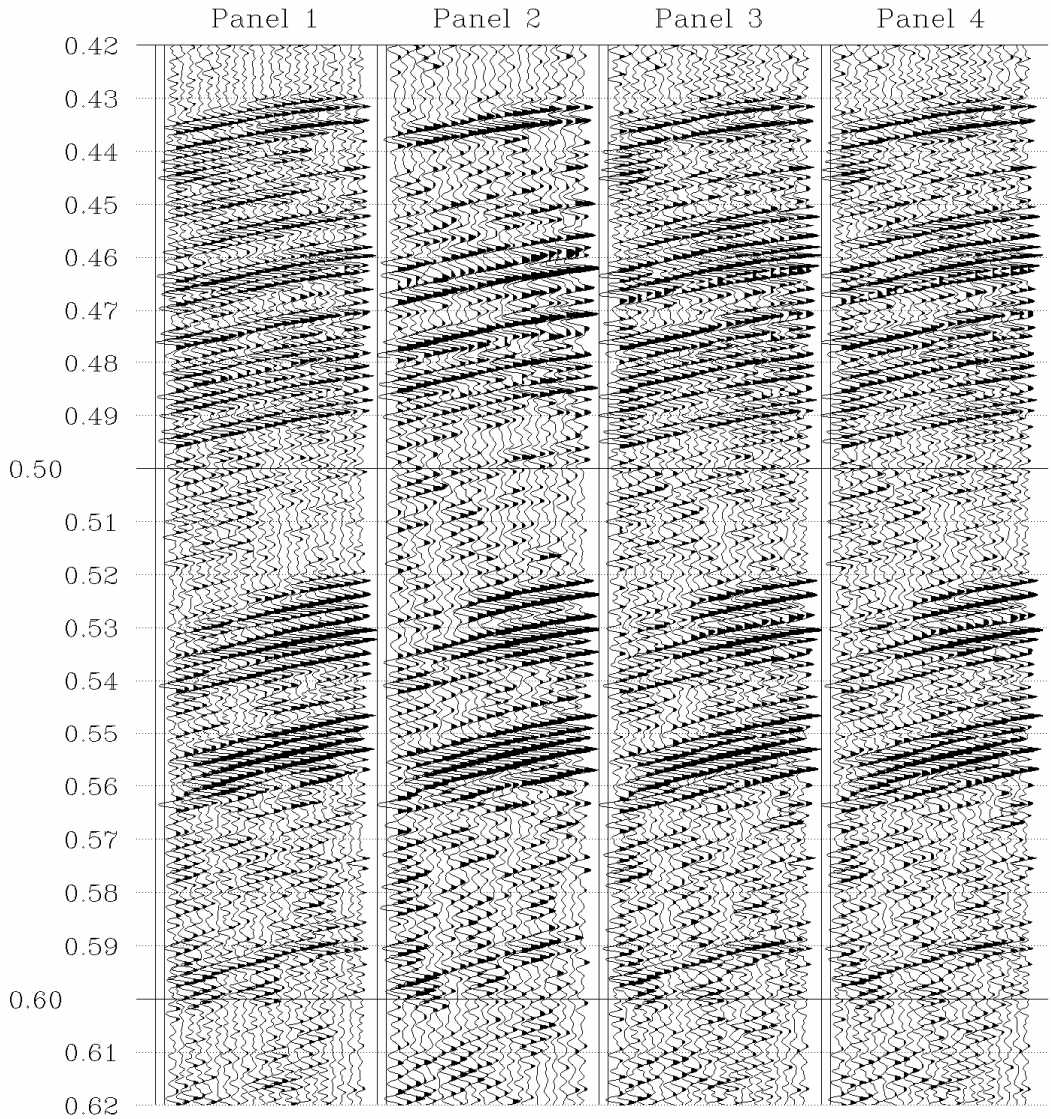

Figure 4.7 Test panels for spectral balancing on Shot 111 of DTAGS survey line DT09. (Panel 1) original data of Shot 111. (Panel 2) after spectral balancing with frequency limits of 220-250 to 510-545 Hz. (Panel 3) after spectral balancing with frequency limits of 220-250 to 650-790 Hz. (Panel 4) after spectral balancing with frequency limits of 220-250 to 790-900 Hz.

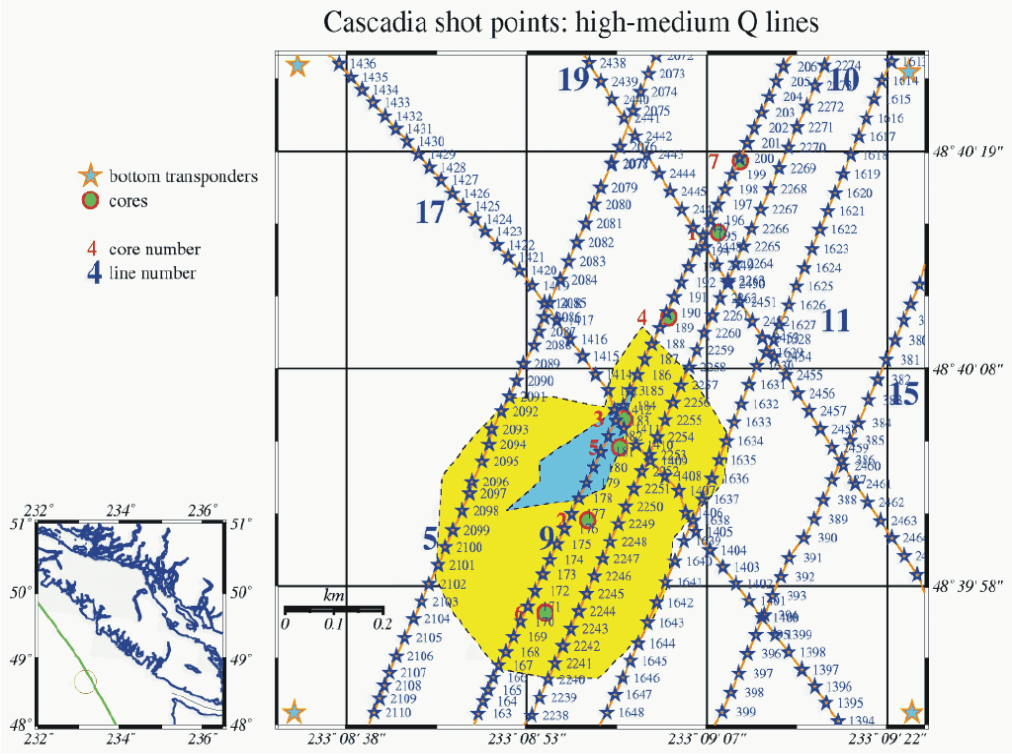

Figure 4.8 Survey lines and locations of piston coring in 2002 around Bullseye vent. The area in yellow indicates the region of seismic blanking during previous high resolution seismic cruises. The blue area outlines the region where hydrate has been recovered in piston coring during cruises in 2000 and 2001, with a maximum depth of recovery of 8 m. Locations of the 4 seafloor transponders are also labelled.

4.3.1 Onboard Processing for Imaging

There were four "engineering" nodes on the streamer for the DTAGS2 experiment: Node 1 was on the source at 0 m and the other three were on hydrophone Channel 28 at 138 m, Channel 38 at 288 m and Channel 48 (the last channel) at 438 m. These nodes recorded pressure and temperature, as well as the seismic signal. The pressure gauges at the 4 nodes yielded several pressure readings during the 30 seconds between shots. These pressures were averaged, converted to depth (including a local density correction based on a temperature measurement in the node) and placed in the SEGY trace header. Note that the simple average may be inadequate if conditions are changing rapidly and one should weight the sensor readings close to the shot time more heavily than those acquired near the adjacent shots (W. Wood, personal communication, 2004). Figure 4.10 shows the depth variations of the 4 nodes during survey line DT09.

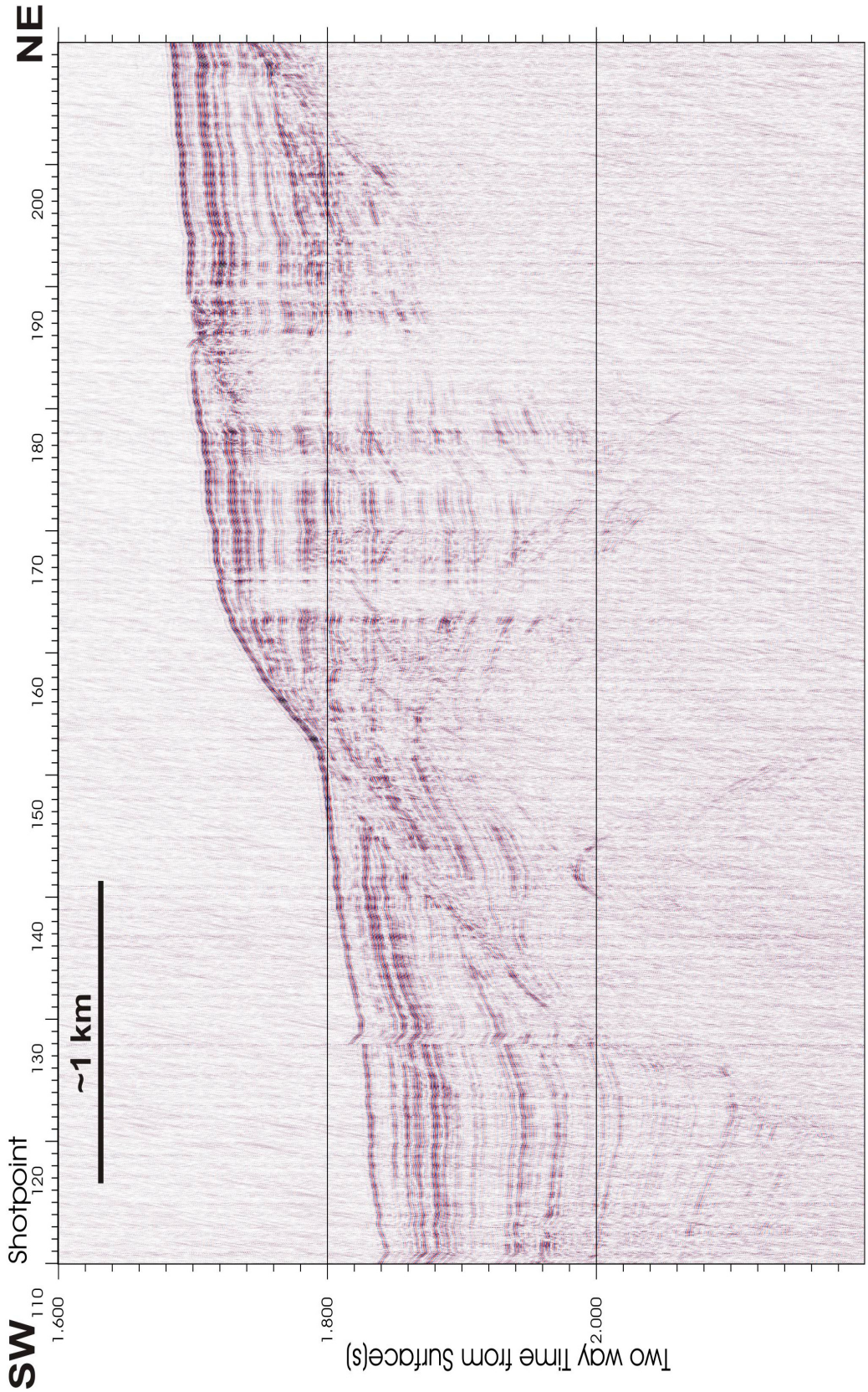

Figure 4.9(a) DTAGS DT09 (southwest half) through the transect of piston coring sites. Onboard analysis included approximate correction for source depth and foot-print processing (Spence, 2002).

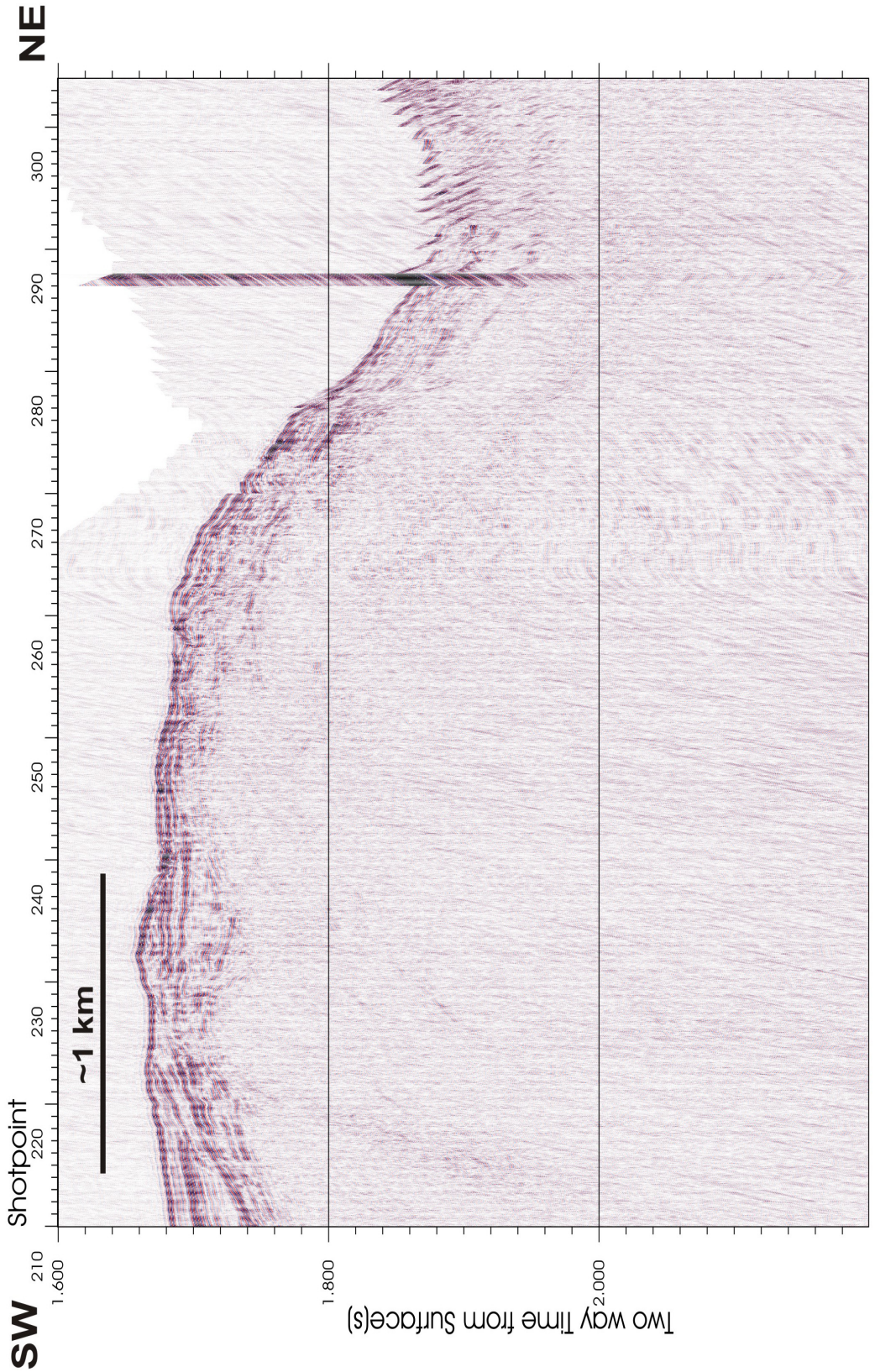

Figure 4.9(b) DTAGS DT09 (northeast half) through the transect of piston coring sites. Onboard analysis included approximate correction for source depth and foot-print processing (Spence, 2002).

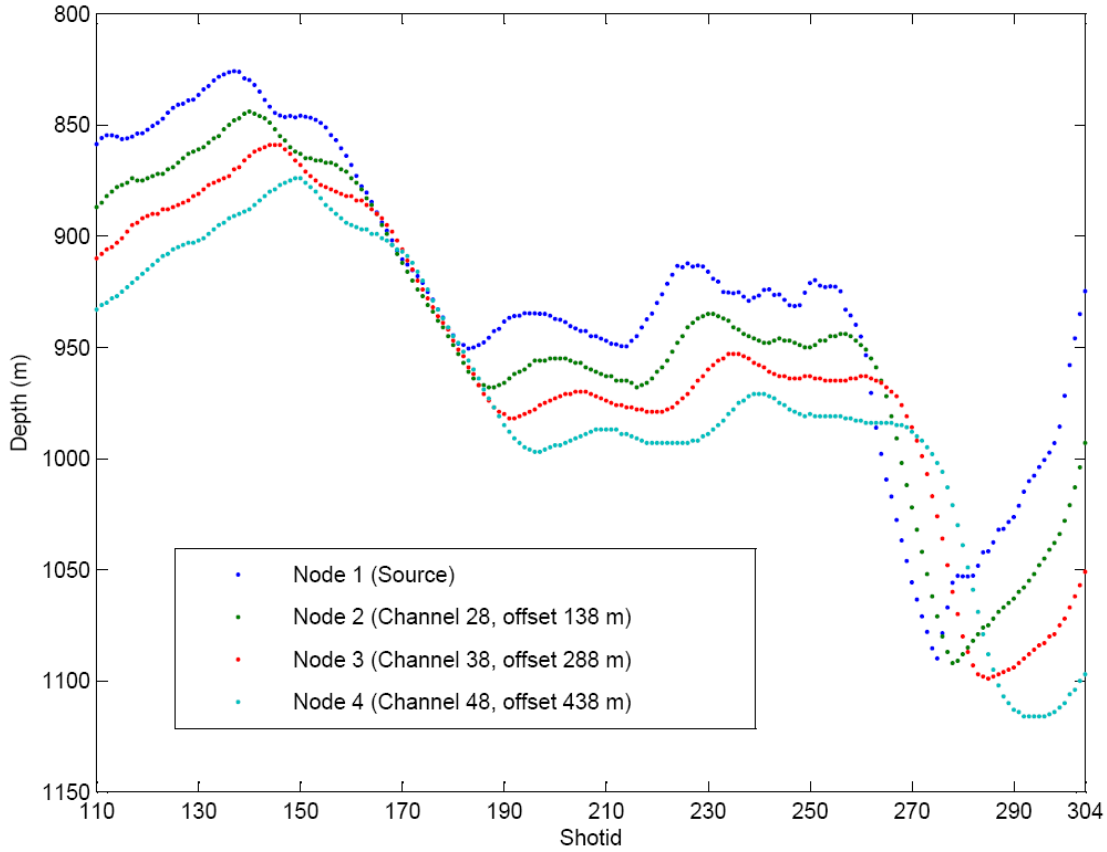

Figure 4.10 The depth variations of the four nodes on DTAGS streamer along survey line DT09, showing an example of non-linear cable geometry.

For the onboard "foot-print" image, the depths at the 4 nodes were linearly interpolated to get the streamer shape, and then each trace was shifted according to the depth. The near acoustic sections of shot gathers were placed side by side, such that the bounce point of the near offset of one gather matches up to the bounce point of the far offset on the next shot gather. After a normal moveout correction with water velocity of 1492 m/s, a single channel record section is formed. Errors in the streamer position created discontinuities between shot gathers in this section, and so a discontinuous time shift was applied to remove this effect (W. Wood, personal communication, 2004). Although most of subseafloor structures are resolved, the "foot-print" image of DT09 (Figure 4.9) indicates that the simple linear assumption of the cable geometry is not accurate enough even for imaging. Moreover the velocity analysis needs a much better method to align the reflection events.

4.3.2 Source Depth Variations and Nonlinear Array Tilting

The ideal system geometry for collecting high-quality reflection data requires a constant-depth source with a horizontal array. However, in practice, this optimal geometry is difficult to achieve and maintain for a deep-towed system. Significant variation in source depth occurred along a seismic line, and nonlinear array tilting, particularly in the longer Geophysical Array, was noted throughout most of the DTAGS experiment (Figure 4.10). These variations caused considerable reflection time errors relative to an optimal horizontal system. The variations required correction before conventional seismic processing could be applied.

Rowe and Gettrust (1993) used readings from a few depth sensors located along the hydrophone array to estimate the approximate tilting of the streamer, and this approach was also used for the onboard "foot-print" during the 2002 survey. However, these readings were neither accurate enough to calculate time corrections nor sufficient to achieve the whole geometry of the non-linear array geometry.

Since DTAGS normally recorded sufficiently long times, the seismic trace included strong sea-surface reflections (SSR) (Figure 4.11). The SSR provided more accurate two-way-time and consequently depth for each hydrophone group assuming constant water velocity during a shot interval. Walia and Hannay (1999) developed a fully automated method to determine the precise nature of the array geometry and the source depth at every shot instant using SSR times. In their method for each shot gather an automatic SSR two-way-time picking was done on the source monitor auxiliary channel and on six other low noise receiver channels. A cubic spline interpolation was then applied to obtain the SSR times for rest of the channels. The routine picked SSR times based on the maximum amplitude of the envelope instead of the real wavelet, since the cross-correlated wavelet was not consistent from trace to trace for the DTAGS high frequency bandwidth data, due to the roughness of the sea surface caused by the water waves and/or due to an inadequate pilot sweep. Once source and receiver depths were calculated using straight-line raypaths, the reflection time arrival of every depth point was corrected to a constant datum at a mean source depth of the whole survey line (Figure 4.12). To account for the angular dependency of the reflected raypath, travel time

corrections were applied to the data by marching a time window ~20 ms along the seismic trace. The results of this method illustrated that after correction, the reflection hyperbolas were restored and the source depth variations from shot to shot were also corrected (Walia and Hannay, 1999).

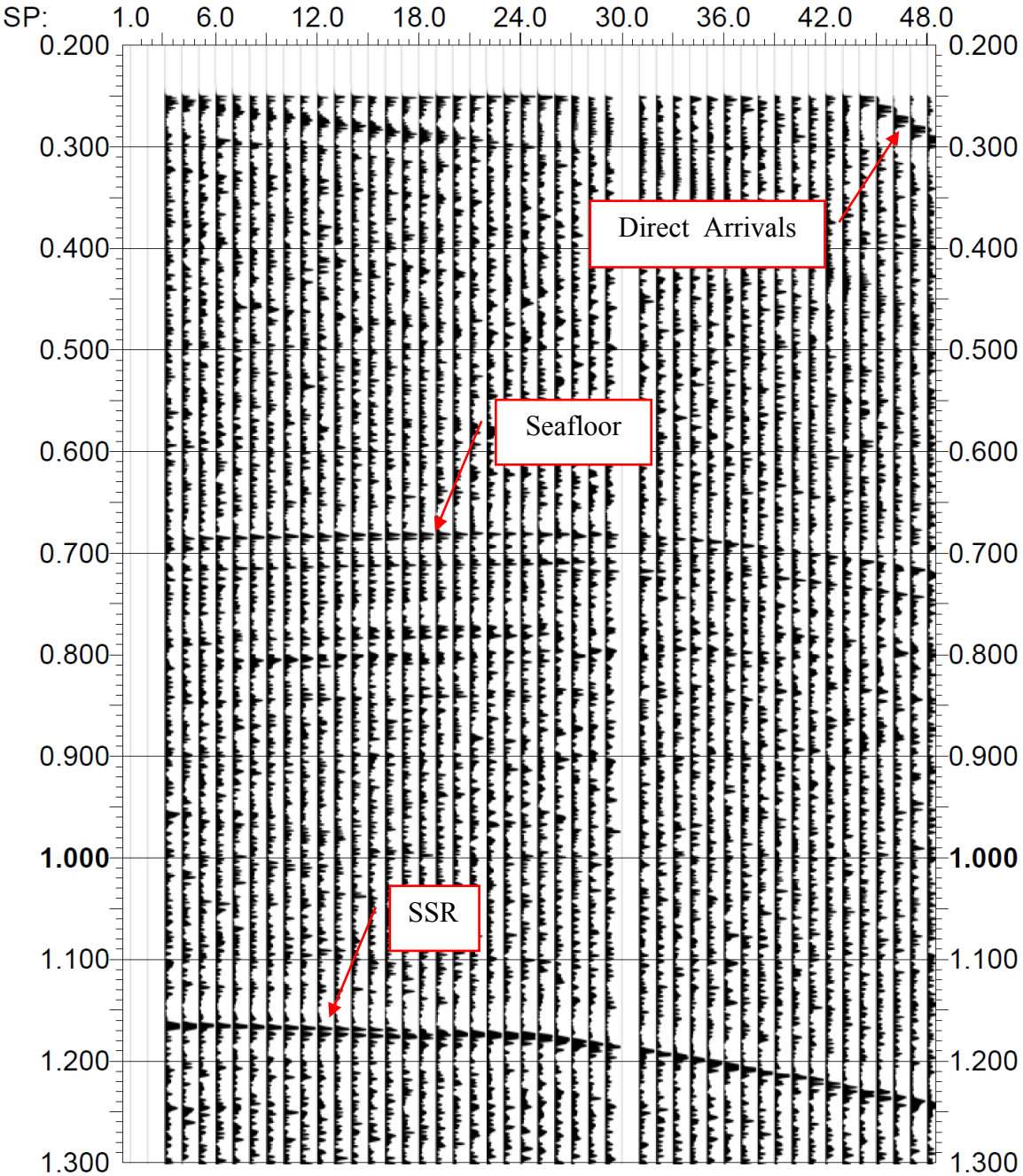

Figure 4.11 Envelope of data waveforms from Shot 111 of survey line DT09. Start of data recording is 0.25 s after the shot time.

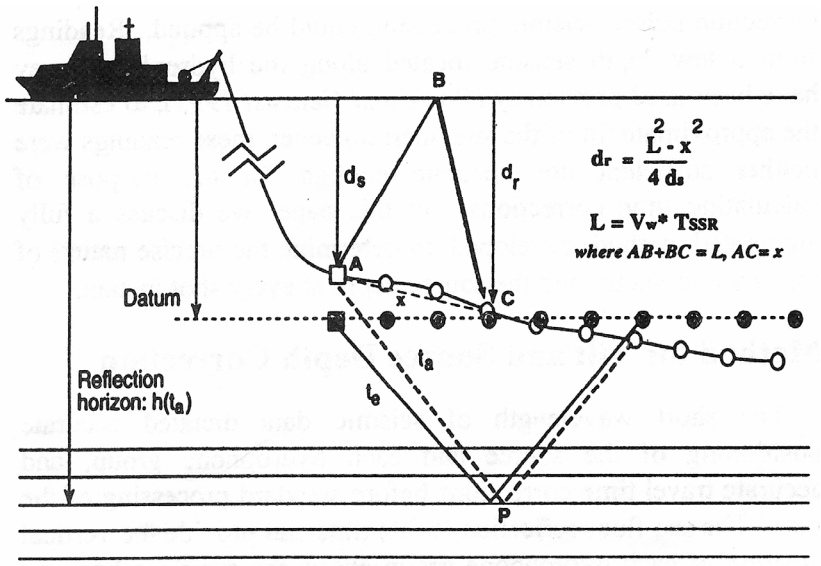

Figure 4.12 Source and array geometry correction computed from the sea-surface reflection time for every trace of a shot gather. The reference datum was selected at a mean source depth for the entire seismic line and the reflection time arrival of every depth point was corrected to the datum. $\mathbf{V_W}$ is water velocity, $\mathbf{T_{SSR}}$ is the two-way-time of the sea-surface reflection, $\mathbf{t_a}$ is actual two-way time of a depth point for the tilted array, $\mathbf{t_e}$ is estimated two-way-time for the datum, $\mathbf{d_s}$ and $\mathbf{d_r}$ are the depth of the source and the receiver respectively calculated from the sea-surface reflection. (From Walia and Hannay, 1999)

However, there are several restrictions for Walia and Hannay's method:

1. They did not fully use the direct measurements from the depth sensors on the cable. The engineering nodes use a pressure sensor with a local thermometer to calculate depth. If the local temperature (within the node capsule) is slightly different than the water along the ray travel path then there will be a discrepancy between the measured depths and the true values. Compared to the constant water velocity assumption for the whole survey line, however, the depth readings should be more accurate using corrected seawater density calculated from real-time temperature measurements.
2. An automatic picking SSR time on maximum amplitude of trace envelope is convenient; however, the phase changes with offset and shot depth, and this may cause errors in picking. This phase changing effect can be seen in the whole shot

gather of 48 channels (Figure 4.13). Normally the interval between two neighboring peaks is ~10 ms in two-way-travel time, or ~7.5 m. Because the maximum variation in shot or receiver depths along the line was 50-100 m, this picking error will cause 7.5%-15% relative variation in depths that may be significant in aligning reflections for velocity analysis or stacking. Greater consistency of SSR times can be achieved by picking at first zero-crossing (e.g., see Figure 4.13, traces 12-24).

3. The channels chosen for automatic picking of the SSR time may not always have low noise over the whole survey line. A poor signal will lead to large picking error, and thus affect the whole cable depth corrections when interpolated to the rest of the channels. A better procedure is to pick these events manually, time consuming but much more reliable.

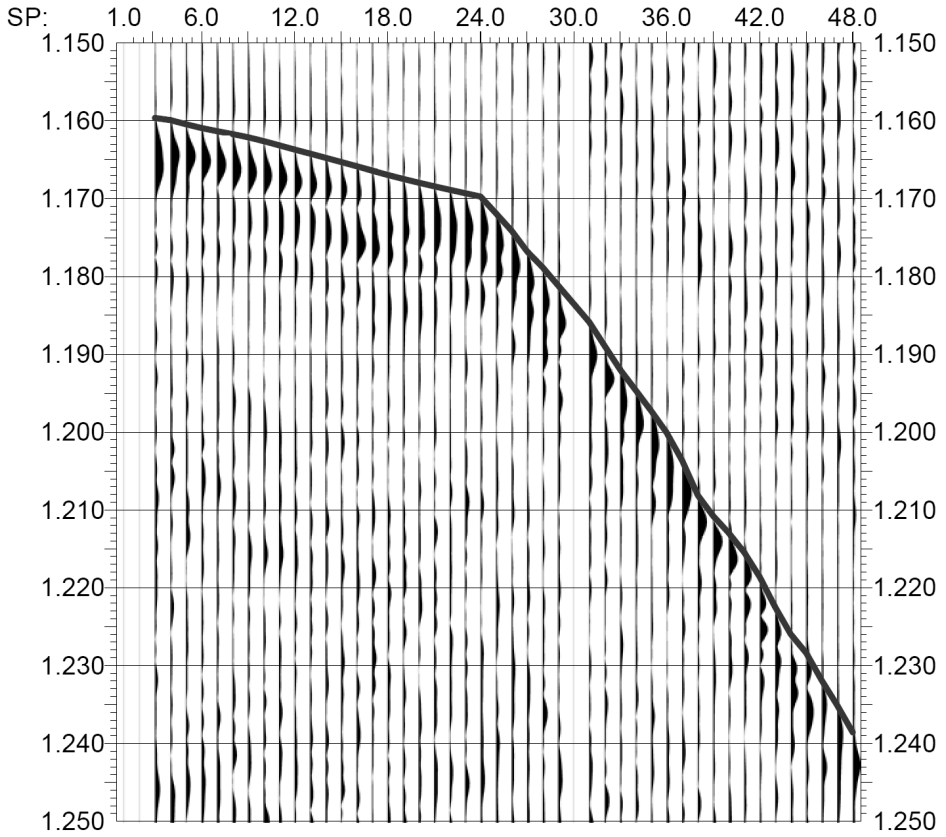

Figure 4.13 Enlarged part of Figure 4.11 from 1.15 s to 1.25 s, showing envelope of sea surface reflections in detail and picked SSR times as solid line.

4. Although correcting source and receiver depths to a constant datum for the entire line simplified the time correction process, the reflector alignment or velocity analysis may be difficult for shots that have large deviation to the mean value of depths. After correction the cable is horizontal with constant offsets for each source-receiver pair, which implies small depth deviations since the source-receiver offset must change to keep the raypath unchanged when the source or receiver is moved vertically to the datum level. If the depth correction is too large, the assumption of a small deviation is violated and the offset needs readjustment correspondingly. A better procedure is to use a floating datum, which is the average depth of the source-receiver pair and thus minimizes the vertical shifts for both source and receiver.
5. A constant sediment velocity was assumed to calculate the time corrections for cable geometry; consequently errors occurred due to inaccurate velocity profiles, although the errors are differential. In this study a linear velocity profile is used, and for the upper sediments the difference relative to using a constant sediment velocity was a fraction of a millisecond, i.e. almost unnoticeable.

4.3.3 DTAGS Cable Geometry Inversion

Assuming that the depth readings are accurate and the cable geometry is smooth to first order at locations of engineering nodes, an improved method was developed using the SSR times to invert DTAGS cable geometry to a polynomial spline shape.

4.3.3.1 Picking SSR Times and Direct Arrivals

All picks were made manually on the trace envelope. For SSR time picking, the picking points were chosen at the first zero-crossing of the SSR wavelet (Figure 4.13), not at the maximum amplitude of the wavelet as in the method of Walia and Hannay (1999). Picking at the first zero-crossing of the SSR wavelet ensures the consistency of SSR times within one shot gather. This consistency is important because errors in picking will in practice lead to large errors in the inverted cable shape. The picked times are then wholly shifted about 7 ms downward to the approximate locations of envelope peaks. The

last 2-4 receivers at farthest end of the cable normally recorded the direct arrival wavelet (Figure 4.14). The picking of direct arrivals is also done at the times of first zero-crossing followed by a 7 ms downward shift.

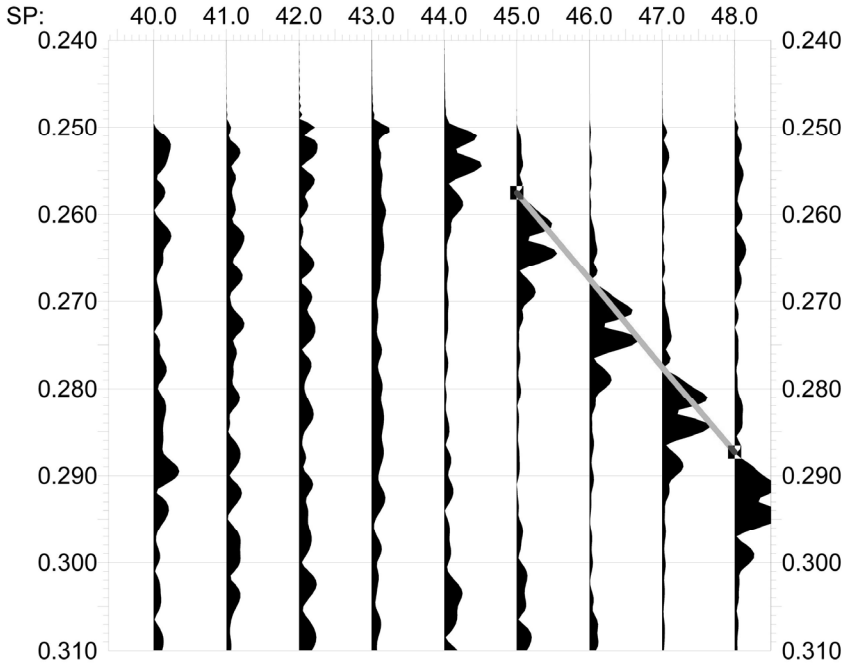

Figure 4.14 Enlarged last 9 traces of Figure 4.11 from 0.24 s to 0.31 s, showing direct arrivals, which were only seen on traces 45-48 due to delay in start of recording time. The picked times were shown as solid line.

Because one of the engineering nodes was attached to the last receiver, this is a unique point on the cable at which the depth, SSR time and direct arrival time can all be obtained. Combined with the source depth reading, the horizontal far-end offset of the cable at the last receiver (***x'***) can be determined, as well as the best water velocity (V_w) individually for each shot gather (Figure 4.15), using following equations:

$$V_w = \sqrt{\frac{4 d_r d_s}{T_{SSR}^2 - T_{direct}^2}} \qquad \text{(Equation 4.3)}$$

$$x' = \sqrt{(T_{direct} V_w)^2 - (d_r - d_s)^2} \qquad \text{(Equation 4.4)}$$

where T_{SSR} is the two-way-time of the sea-surface reflection, T_{direct} is one-way time of direct arrival, d_s and d_r are the depth of the source and the receiver, respectively,

calculated from measured pressure and temperature. See Appendix C for details in deriving Equation 4.3 and Equation 4.4. Figure 4.16 shows an example of average water velocities calculated for each shot gather of DTAGS survey line DT10. The anomalous velocity near 1488 m/s corresponds to the bad shot 2256, which only has noise traces and was muted in the final image.

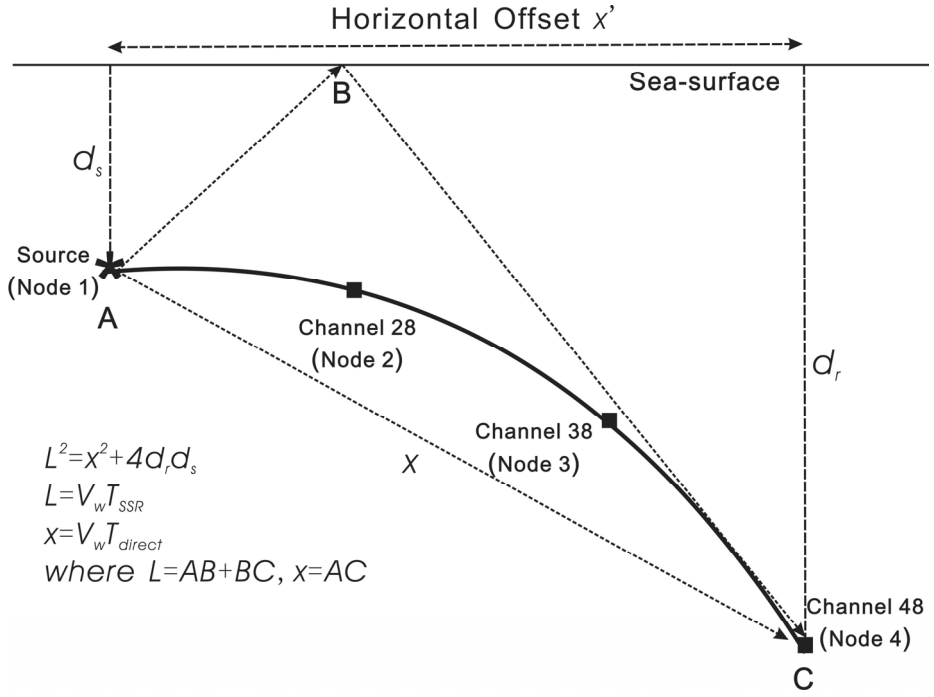

Figure 4.15 Raypaths of sea-surface reflection and direct arrival from source to the last receiver. V_w is water velocity, T_{SSR} is the two-way-time of the sea-surface reflection, T_{direct} is one-way time of direct arrival, d_s and d_r are the depth of the source and the receiver, respectively, calculated from measured pressure and temperature.

4.3.3.2 Invert the Whole Cable Geometry Using GA Method

For any shot gather, once the water velocity (V_w) and farthest horizontal offset (x_{48}) at Channel 48 of Node 4 are determined by Equation 4.3 and Equation 4.4, a GA (Genetic Algorithm) method provided by Matlab is used to determine the horizontal offsets for the other two middle nodes (x_{28} of Channel 28 and x_{38} of Channel 38). The optimization function of the GA method is to minimize a "fitness value" defined as the sum (T_t) of residual SSR times between the calculated (T_{SSR}) and the picked (T_{pick}) times for all channels (Channel 1-48) within a shot gather:

$$T_t = \sum_{i=1}^{48} \left| T_{SSR\ \ i} - T_{pick\ \ i} \right| \qquad \text{(Equation 4.5)},$$

and

$$T_{SSR\ \ i} = \sqrt{x_i^2 + (d_i + d_0)^2} \,/\, V_w \qquad \text{(Equation 4.6)},$$

where $\boldsymbol{x_i}$ is the horizontal offset of channel $\boldsymbol{i}$ from the source, $\boldsymbol{d_i}$ is the vertical depth of channel $\boldsymbol{i}$ from sea surface, and $\boldsymbol{d_0}$ is the vertical depth of the source from sea surface.

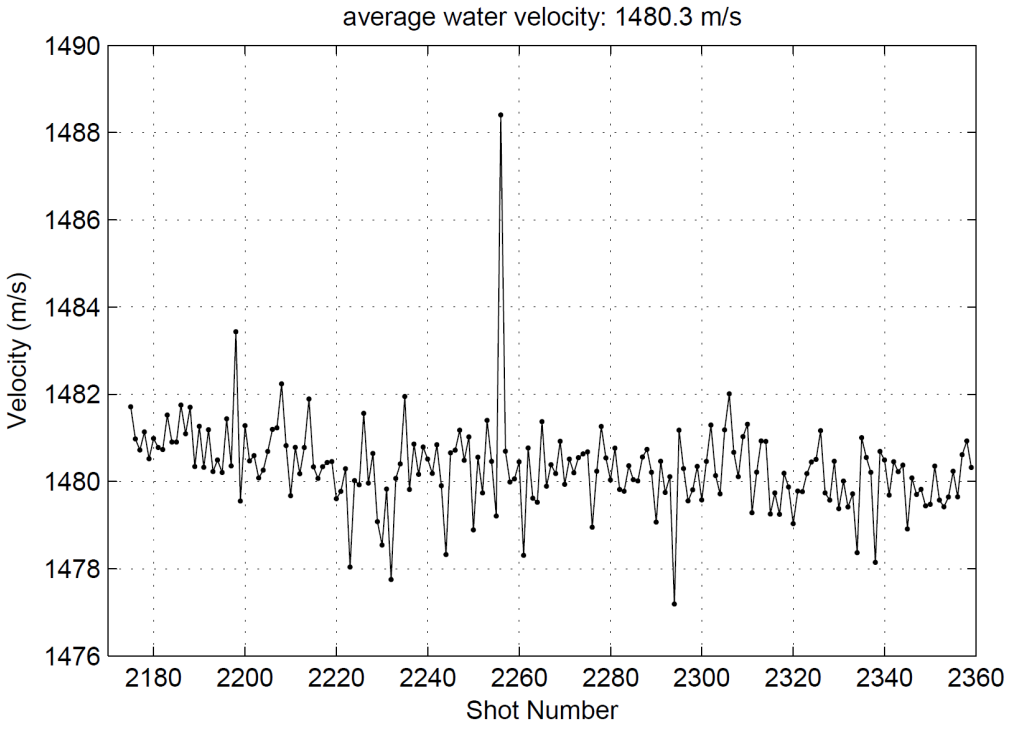

Figure 4.16 Average water velocities along DTAGS survey line DT10.

There were 5 designated variables to be optimized the during inversion process (Figure 4.17): 2 horizontal offsets of $\boldsymbol{x_{28}}$ and $\boldsymbol{x_{38}}$ for the two middle nodes, and 3 depths ($\boldsymbol{d_{24}}$, $\boldsymbol{d_{33}}$, $\boldsymbol{d_{43}}$), which were added at Channel 24, 33 and 43 to achieve better control of cable geometry. The GA inversion process can be summarized as below:

1. The stopping criteria are checked. If none of the stopping criteria is met, go to step 2.
2. For each iteration, the GA method randomly chooses $\boldsymbol{x_{28}}$, $\boldsymbol{x_{38}}$, $\boldsymbol{d_{24}}$, $\boldsymbol{d_{33}}$, and $\boldsymbol{d_{43}}$ from their value ranges.

3. The horizontal offsets of remaining receivers then are linearly interpolated between the 4 nodes (the source and channels 28, 38, 48).
4. Using the "known" horizontal offsets and depths of 4 nodes plus other 3 depths generated by GA method, the depths of remaining receivers are calculated using a polynomial fitting curve.
5. Since the cable geometry is fixed with depth and horizontal offset for each receiver, the new SSR times are calculated using Equation 4.6.
6. A fitness value $\boldsymbol{T_t}$ is calculated by summing the residual SSR times between the calculated and previously picked times (Equation 4.5).
7. The physical constraint of total cable length is checked. For example, the sum of the direct distances of AB and BC must not be greater than the length between the source and Channel 28 (Node 1) when the cable is straight. Therefore, if the cable is broken due to an inappropriate inversion result, the current fitness value is rejected by setting it to positive infinity.
8. The fitness value $\boldsymbol{T_t}$ (Equation 4.5) is compared to the one from the previous iteration. If current value is smaller, it is accepted, and the process begins at step 1; otherwise it is rejected, new parameter values are selected in step 2.

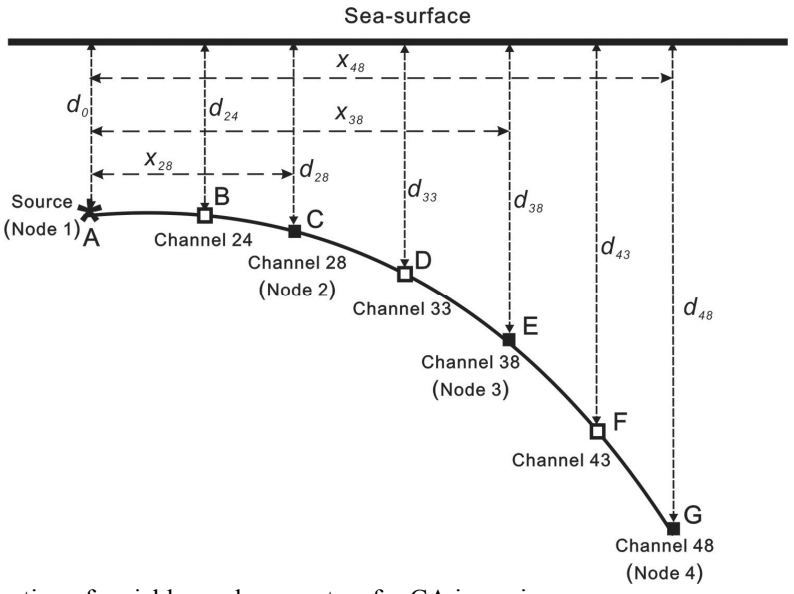

Figure 4.17 Illustration of variables and parameters for GA inversion.

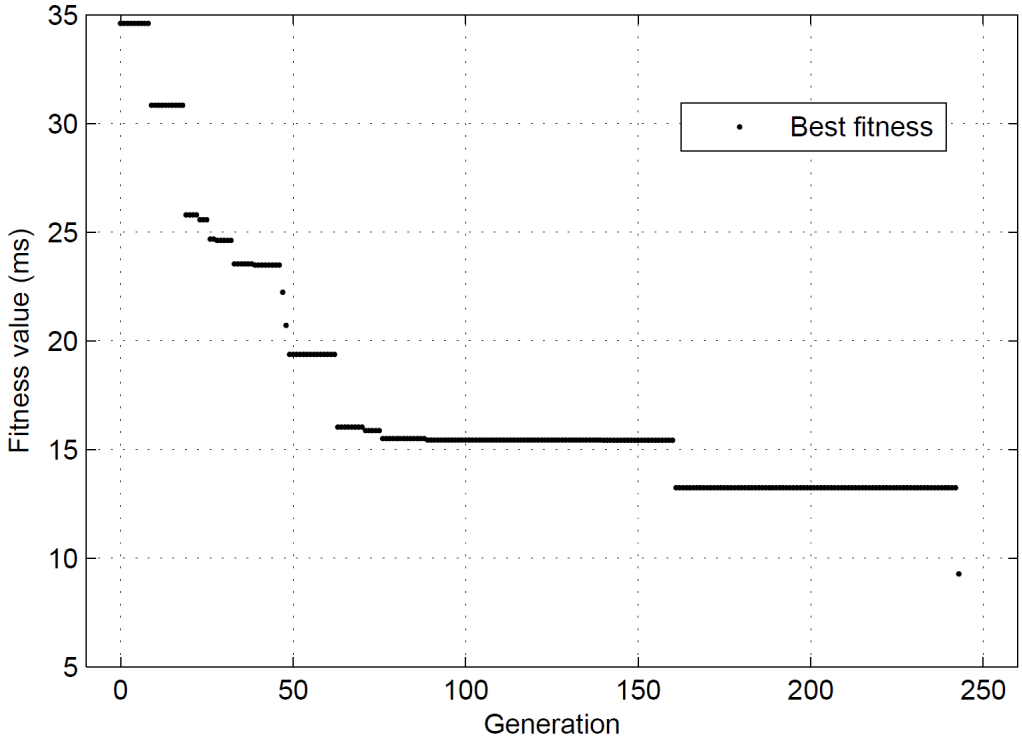

Figure 4.18 Optimizing process of GA method for Shot 2230 of survey line DT10. The polynomial fitting order was 5. The fitness value $\boldsymbol{T_t}$ is given by Equation 4.5.

Since the order of polynomial fitting affects the inverted cable geometry, the GA routine in practice runs two times for each shot: one uses an order 3 polynomial, and the other uses order 5. The inversion result with smaller final fitness value is accepted.

The GA used for DTAGS cable inversion has population size of 50 and will produce infinite generations except when one of following stopping conditions is satisfied: 1) the fitness value $\boldsymbol{T_t}$ (total residual SSR times, Equation 4.5) < 10 ms; 2) no smaller fitness value for 300 generations; 3) no smaller fitness value for 30 minutes; 4) tolerance on fitness value is less than the termination value of 1e-32. Normally the routine stops for condition 1 or 4, and very rarely for condition 2; no instance has happened for condition 3 at present. That is, the GA can generate optimal results within 10-30 seconds for one shot gather, using a desktop with a 1.4 GHz CPU.

Shot 2230 of DTAGS2 survey line DT10 was randomly chosen as an example of the GA inversion. Figure 4.18 shows that the GA optimizing process with polynomial

fitting order of 5 stopped when condition 1 of the inversion process (fitness value less than 10 ms) was met with a final fitness of 9.3 ms after ~250 iterations. For shot 2230 the fitness value was 40.2 ms when the polynomial fitting order was set as 3, much larger than for order 5.

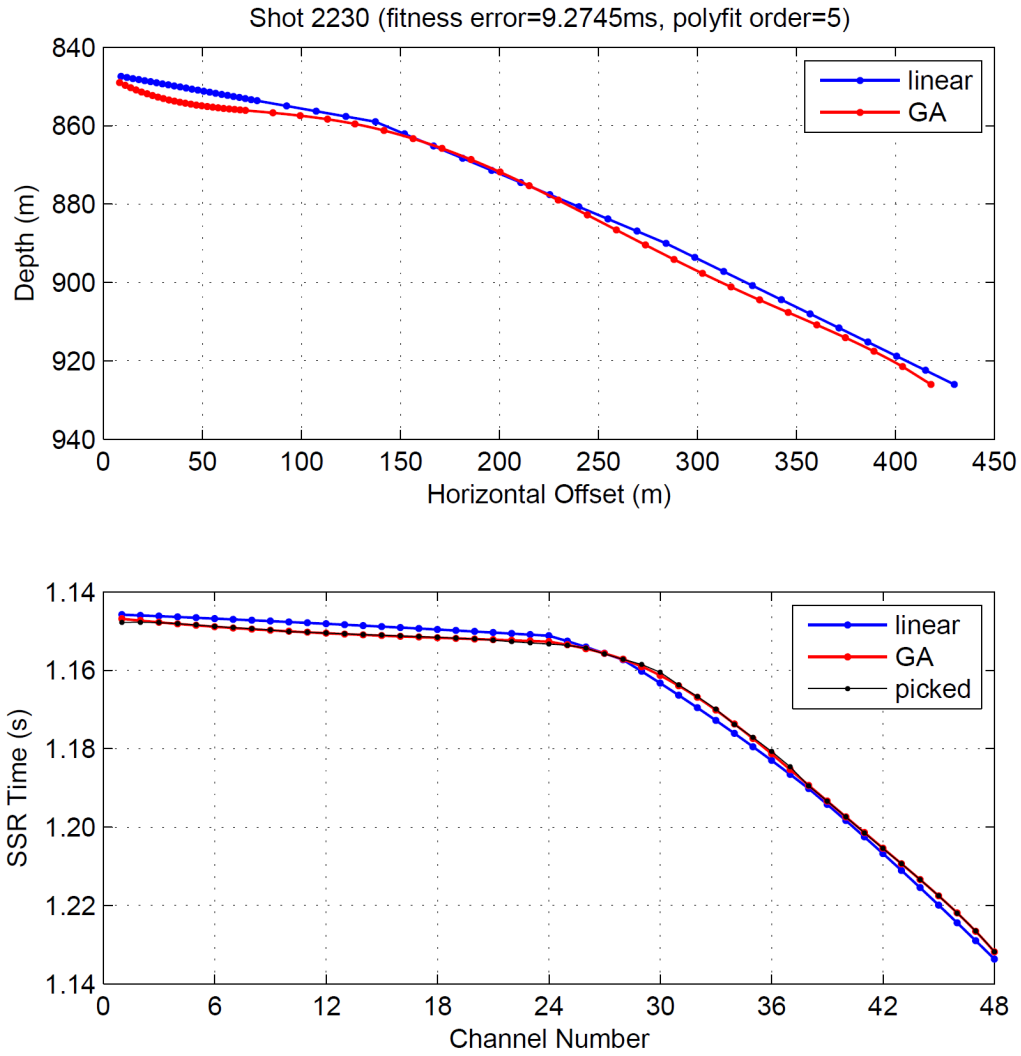

Figure 4.19 Inverted cable geometry (upper) and new SSR time (bottom) for Shot 2230 of survey line DT10.

Figure 4.19 shows the inversion results for Shot 2230. Compared to the linear cable geometry assumption (blue lines, Figure 4.19) used for the onboard "foot-print", a more naturally curving cable was achieved using the inverse method (red lines, Figure

4.19). Note that the cable depths varied from ~850 m at first receiver to ~930 m at last receiver over a horizontal distance of ~420 m, and that the 3-5 m mismatch between the GA inverted geometry and the linear cable assumption produces 3-4 ms difference in corresponding SSR times. Since the DTAGS cable was closer to the seafloor than to the sea surface, the time difference between the GA method and linear assumption will be even larger for sediment reflections. Considering that a 1 ms time difference will produce a noticeable mismatch for DTAGS imaging, the GA inverted cable geometry is more reliable than the one using a linear assumption.

After ~2 hours running, the GA routine yielded the optimal cable geometry for the whole survey line DT10. Figure 4.20 shows the final fitness value of minimum residual SSR times for each shot gather. Even for the largest fitness value $\boldsymbol{T_t}$ of 44 ms, the average SSR residual ($\boldsymbol{T_t}$/48) between the GA inverted time and the picked seismogram time is less than 1 ms, which is sufficient quality control for inversion errors.

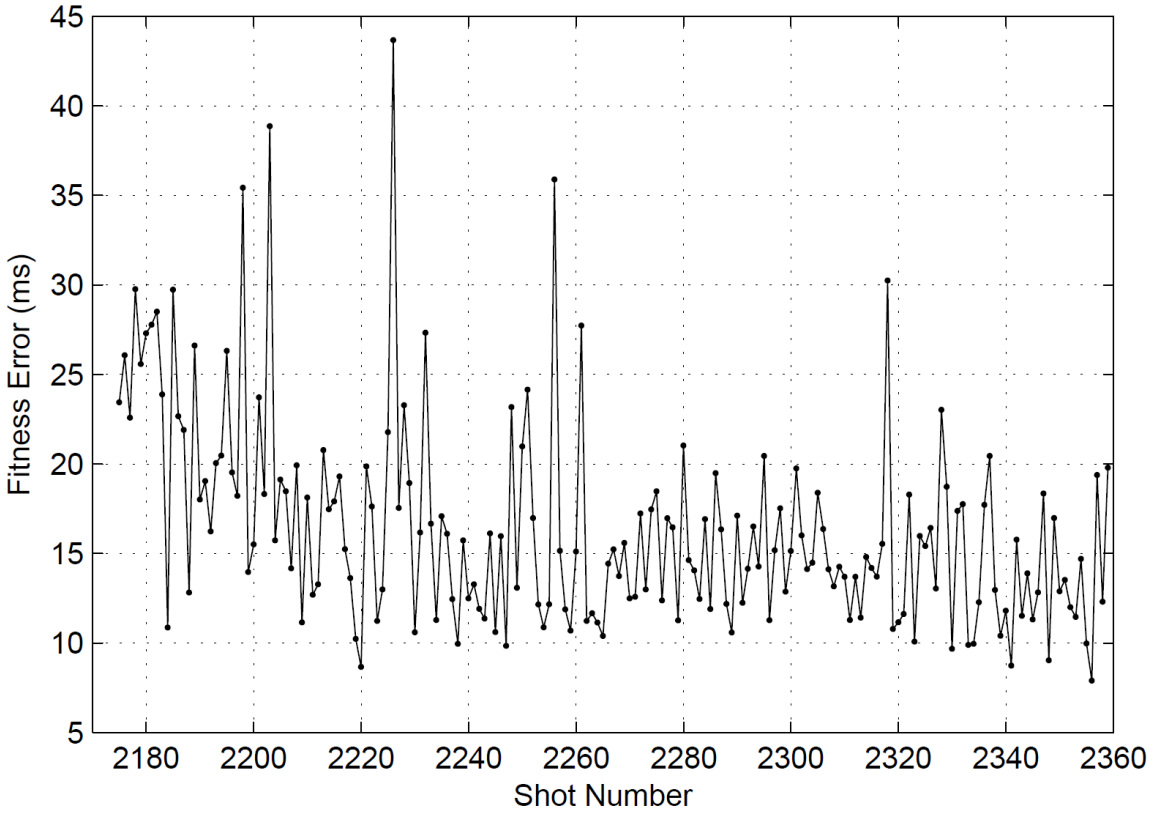

Figure 4.20 The plotting of fitness values $\boldsymbol{T_t}$ (Equation 4.5) for all shots of survey line DT10.

4.3.3.3 Time Corrections for Cable Geometry and Source Depth Variations

Unlike a constant depth used as datum for the whole survey line by Walia and Hannay (1999), an individual datum was chosen at the mean depth of each source and receiver pair (Figure 4.21). That is, a floating datum system was used in this method not only for different shot instants, but also for different source-receiver pairs within the same shot gather. Therefore, the time corrections for cable geometry and source depth variations are separated into two steps in my method.

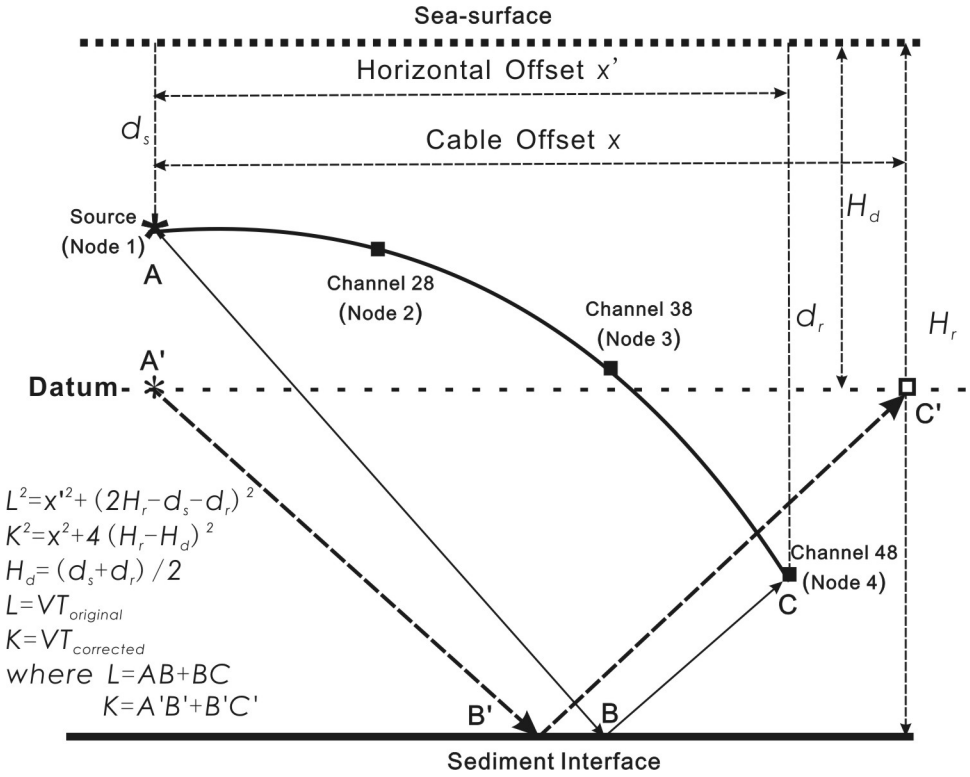

Figure 4.21 Illustration of time correction for source/last receiver pair. The original raypath AB+BC from source to the last receiver reflected at point B of sediment interface, after time correcting, is replaced by new raypath of A'B'+B'C', on which source and receiver are at the same datum at their mean depth and their distance is corrected to their original offset ***x*** on the cable. ***V*** is the average velocity estimated by water velocity calculated previously and sediment velocity structure assumption, $\boldsymbol{T_{original}}$ is the original two-way-time of AB+BC, $\boldsymbol{T_{corrected}}$ is the two-way-time of A'B'+B'C' after time correction, $\boldsymbol{H_d}$ and $\boldsymbol{H_r}$ are the depth of the datum and sediment reflector respectively measured from sea-surface, $\boldsymbol{d_s}$ and $\boldsymbol{d_r}$ are the depth of the source and the receiver respectively.

Step 1: Time Correction for an Individual Source/Receiver Pair

Figure 4.21 uses the sediment reflection raypath from the source to the last receiver to illustrate the basic idea of computing time corrections to move reflection arrivals measured on the curved DTAGS array to the proper times for a horizontal system at a datum depth. Since the cable geometry has been determined using GA method, the depths of source (d_s) and receiver (d_r) as well as horizontal offset (x') are known values. On the seismogram, a sediment interface is found at two-way time $T_{original}$, corresponding to a depth of H_r measured from the sea surface. Assuming an average velocity V over the raypath of AB+BC, the reflector depth H_r is given by Equation 4.7:

$$H_r = \left(\sqrt{\left(VT_{original}\right)^2 - x'^2} + d_r + d_s \right) / 2 \qquad \text{(Equation 4.7).}$$

For time correction, the source and receiver should be placed at the same datum H_d, which is chosen at the mean depth of the individual source-receiver pair. Also the distance of source and receiver is corrected to their original offset (x) on the horizontal cable, which is a known value for the fixed cable configuration during a survey. Therefore, a new raypath A'B'+B'C' is established, which has a new two-way travel time $T_{corrected}$ given by Equation 4.8:

$$T_{corrected} = \sqrt{x^2 + 4(H_r - H_d)^2} / V \qquad \text{(Equation 4.8),}$$

where $H_d=(d_s+d_r)/2$, V is the same average travel velocity used in Equation 4.7. The steps represented by Equations 4.7 and 4.8 are similar to those for Equation 4.3 and Equation 4.4, and are derived using mirror reflection rule.

A two-layer model (Figure 4.22) was used to estimate the average velocity V. The upper layer of the model is the seawater with constant velocity Vw. In the lower layer, the sediments have a linear velocity profile: seawater velocity Vw at the seafloor and a velocity Ve of 1700m/s at 400 mbsf based on previous conventional multichannel seismic data in 1989 (Equation 3.1, Yuan et al., 1996). The raypath AE+EC has a two-way travel time t. Since the incident angle is small for acoustic channels of the DTAGS cable, AD+FC can be approximately replaced by seafloor reflection AB+BC (t_0), and the length (s) of DE or EF can be approximately estimated using the known linear velocity profile:

$$\frac{s}{\left(Vw+\left(Vw+\frac{Ve-Vw}{D}\cdot s\right)\right)/2}=(t-t_0)/2 \qquad \text{(Equation 4.9)},$$

$$\Rightarrow \quad s=\frac{Vw}{\frac{2}{t-t_0}-\frac{Ve-Vw}{2\cdot D}} \qquad \text{(Equation 4.10)}.$$

Therefore the average velocity V has following equations:

$$\begin{aligned} t\cdot V &= AE+EC \\ &\approx (AB+BC)+(DE+EF) \\ &\approx t_0\cdot Vw+2\cdot s \end{aligned} \qquad \text{(Equation 4.11)},$$

$$\Rightarrow \quad V=\frac{Vw}{t}\cdot\left(t_0+\frac{1}{\frac{1}{t-t_0}-\frac{Ve-Vw}{4\cdot D}}\right) \qquad \text{(Equation 4.12)}.$$

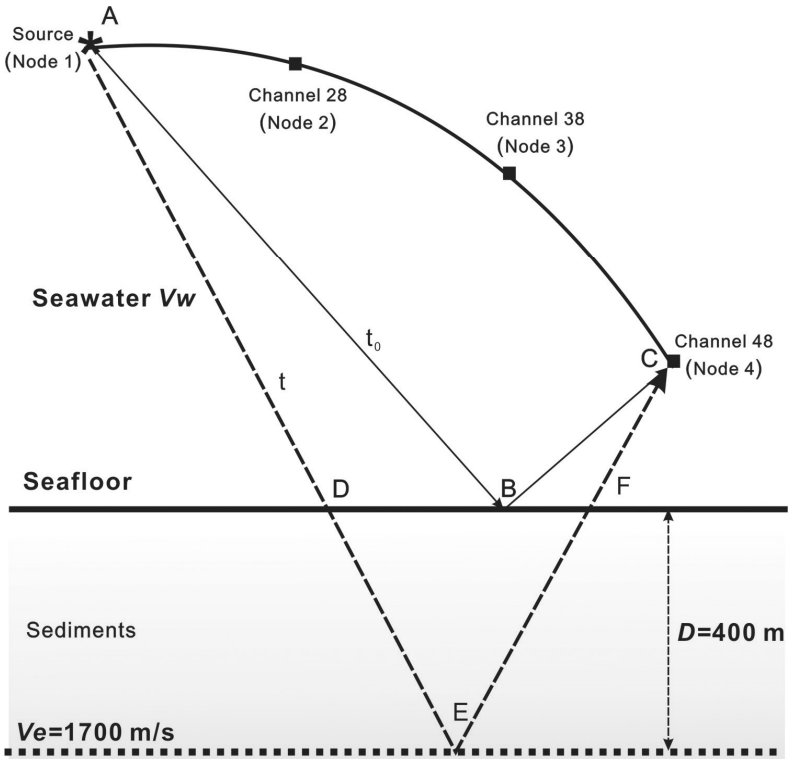

Figure 4.22 Illustration of computing average velocity along raypath.

Since the raypath changes for varying incident/reflection angles at different reflection depths (Figure 4.22), the time correction in practice is calculated by iteratively marching a small time window through the seismic trace data. Previous study by Walia and Hannay (1999) had shown that a window length of 20 ms is adequate considering the optimal overlap or gap between the adjacent windows after they have been time-shifted. At each iteration the depth H_r of the reflector, corresponding to the start time $T_{original}$ for the marching window, is calculated using an average velocity discussed above. This depth H_r is then used to predict the expected time $T_{corrected}$ for the horizontal source-receiver system at the datum depth H_d. Time corrections ($T_{corrected}$) for the top and bottom of the marching window were calculated separately, and the data in the original window were stretched/contracted and time-shifted to fit the new window accordingly.

Step 2: Time Shift from Floating Datum to Sea Surface for Imaging

Once the time corrections for source-receiver pairs have been applied, a NMO (normal moveout) process is used to shift traces to vertical incidence using constant seawater velocity. The DTAGS data is finally corrected for imaging by shifting the trace data downward by a two-way-time at seawater velocity for the vertical raypath from the sea-surface to the datum depth. A few shot gathers are shown in Figure 4.23 before and after time corrections for both the nonlinear tilting array geometry and source depth variations; the true reflection hyperbolas have been restored and the source depth variation from shot to shot has also been corrected.

There is obvious benefit of this precise shot and receiver time correction using a floating datum system and separated correction processes. Shifting the nonlinearly tilted array to the horizontal floating datum at the mean depth of the source and receiver pair minimizes the difference of incident/reflection angle from the original raypath to the corrected raypath for different reflection depths when the horizontal source-receiver offset changes from x' to x (Figure 4.21), and therefore minimizes related errors in the stacking velocities.

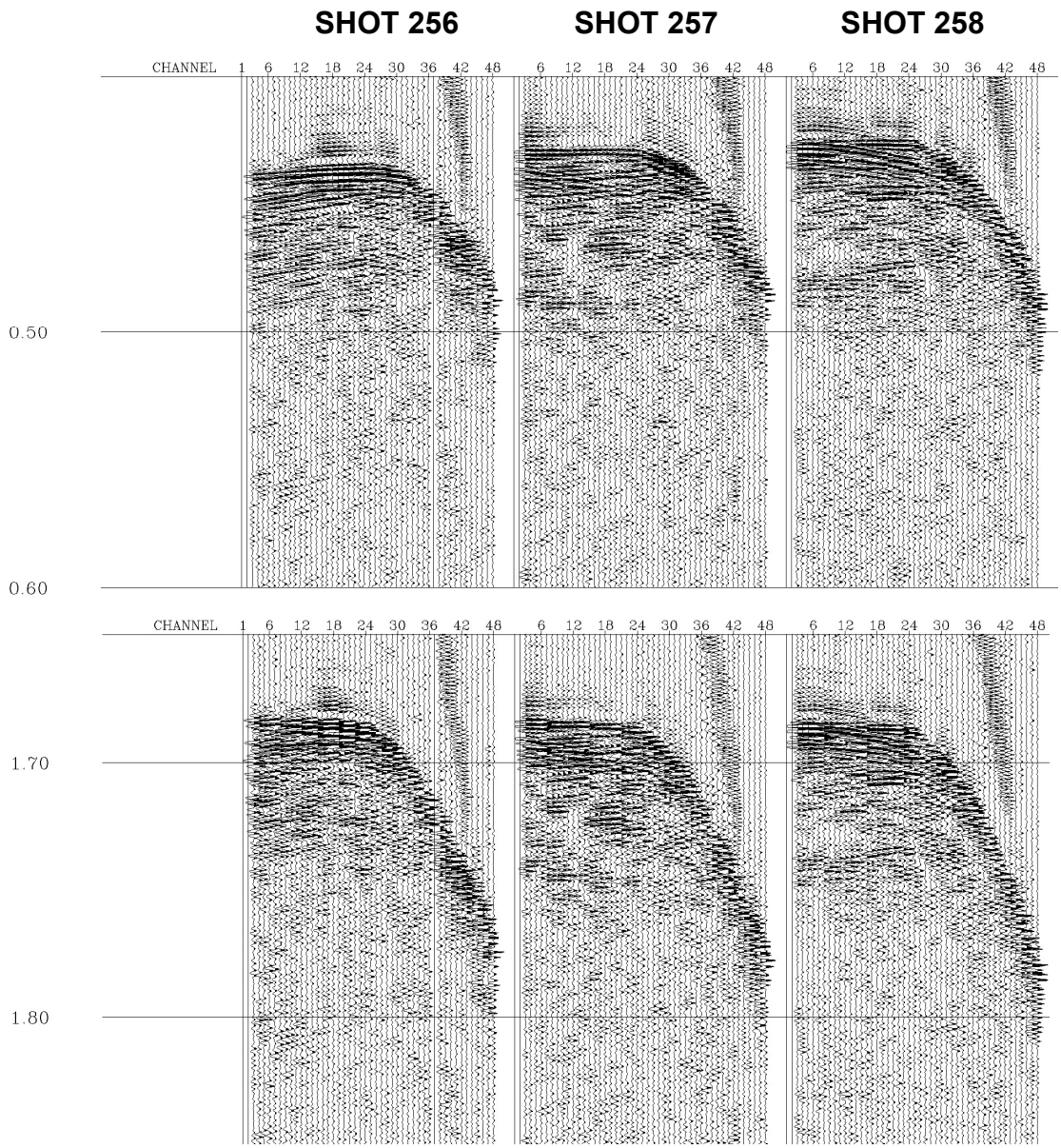

Figure 4.23 Shot gathers from the deep-tow array before (top) and after (bottom) applying time corrections for the nonlinear array tilt and shot depth variations. Note that the bottom images have been corrected to the vertical travel time from the sea surface to the seafloor, and that the traces are not equally spaced in offset: the down slope part after channel 24 corresponds to the geophysical array.

4.4 DTAGS Data Imaging

For imaging multichannel seismic data, NMO is a must-have process. However, considering the special floating datum system for the nonlinearly tilting DTAGS array, the NMO must be applied before the vertical time shifts from the datum to the sea-surface. This is because NMO time is calculated using travel time and source-receiver offset, but the travel time changes significantly while the source-receiver offset keeps constant after shifting the trace from the datum to the sea-surface. It is better to use optimal stacking velocities for NMO, but the water velocity provides an approximate NMO correction and a reasonable image, especially for seafloor alignment.

After time correcting for nonlinear cable geometries and source depth variations, NMO removal, and trace datum shifts, the DTAGS data were passed to surface-consistency statics analysis and shot image stitching. To seek consistency along a seismic reflector, the following calculations were based on cross-correlations of trace envelopes.

4.4.1 Receiver Statics

Since the maximum offset between two adjacent receivers is 15 m after cable geometry correction, the corresponding reflection point difference is 7.5 m, which is less than the Fresnel zone size of the DTAGS system. Therefore, two adjacent receiver images are in theory indistinguishable; if there is a noticeable difference between them, receiver statics should be applied to eliminate this ensemble difference. The traces were first sorted into receiver gathers and then trace envelopes were produced and exported as a Matlab binary data file in Claritas. Note that the acoustic array only has a 3-m group interval; therefore one of every 5 traces (channels 4, 9, 14, 19 and 24) of the acoustic array was selected, while all traces (channels 25-48) of the geophysical array were included. To calculate the statics value between two adjacent receiver gathers, two traces having the same shot number were cross-correlated and the lag of the maximum amplitude of the cross-correlation was picked in Matlab. Figure 4.24(a) shows typical relative lags from two adjacent receiver gathers (channels 26 and 27) of survey line DT10.

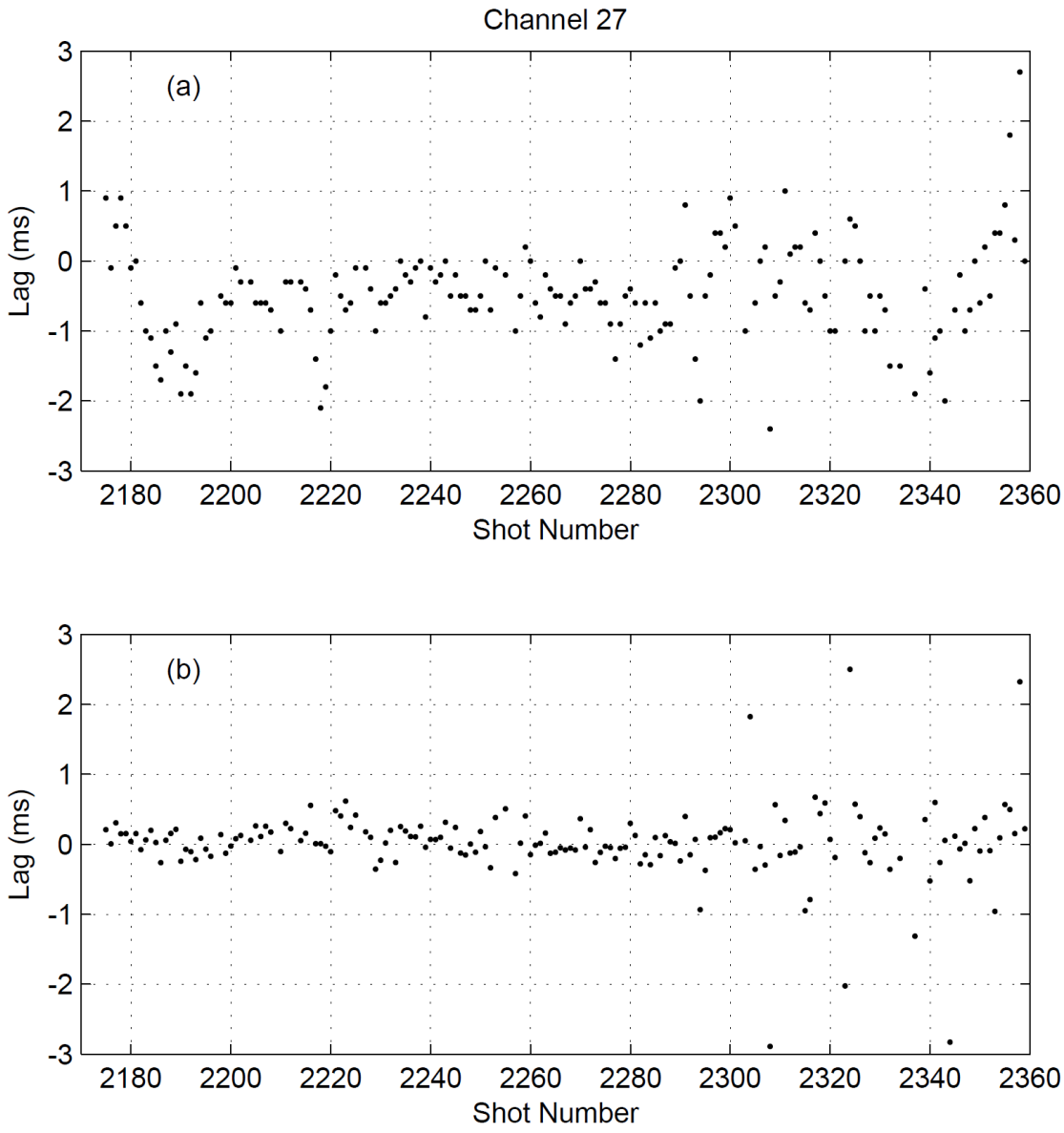

Figure 4.24 (a) The cross-correlation lags of the receiver gather for Channel 27 of survey line DT10 relative to Channel 26, showing patterns associated with local geology structures, mainly seafloor topography. (b) The lags are close to random variations after removing the geology patterns.

The cross-correlation pattern indicates that geological structures, mainly strong seafloor reflections, were included in the lags calculation, since the reflection points in a shot gather span a distance of over 200 m. To derive the geological structures, a low-pass filter was applied to shot-gather-sorted lags (e.g., Shot 2301 in Figure 4.25a). After

removing the geology information by subtracting the filtered values (red curve, Figure 4.25a) from the original lags (blue curve, Figure 4.25a), the residual lags within Shot 2301 fluctuated around 0 (black curve, Figure 4.25b). Once the geology information is removed for all shots, the residual lags of the receiver gather are close to random variations around a value of 0, such as the example of Channel 27 shown in Figure 4.24(b).

As mentioned above, the largest offset between two adjacent receivers is 15 m, and therefore only small relative lags are expected for receiver statics. After plotting observations of lag patterns from several common receiver gathers, ±1 ms was determined as the bounds for "valid" residual lags; any value outside these bounds was rejected as a "wild" point caused by the unstable nature of DTAGS signal. To calculate the final statics value for each seismic trace, the following steps are involved:

1. In a shot gather, if one channel has a residual lag outside ±1 ms bounds, the value is reset to 0; thus a set of new residual lags is produced.
2. The mean value of residual lags is calculated for the new receiver gather; the mean values should be always within the ±1 ms bounds.
3. The relative statics of traces in a shot gather is calculated by subtracting the mean values from the new residual lags according to the channel number (Figure 4.25b).
4. The final absolute statics of each trace in a shot gather is calculated by firstly accumulating the relative statics from the first channel and then shifting the whole shot gather so that the mean value of the final statics is 0.
5. Finally the absolute statics is written into the 'rec_static' trace header in the receiver gather, to be implemented using the STATIC module of Claritas.
6. The receiver-corrected DTAGS data were sorted back to shot gathers for shot statics and image stitching in the next process step.

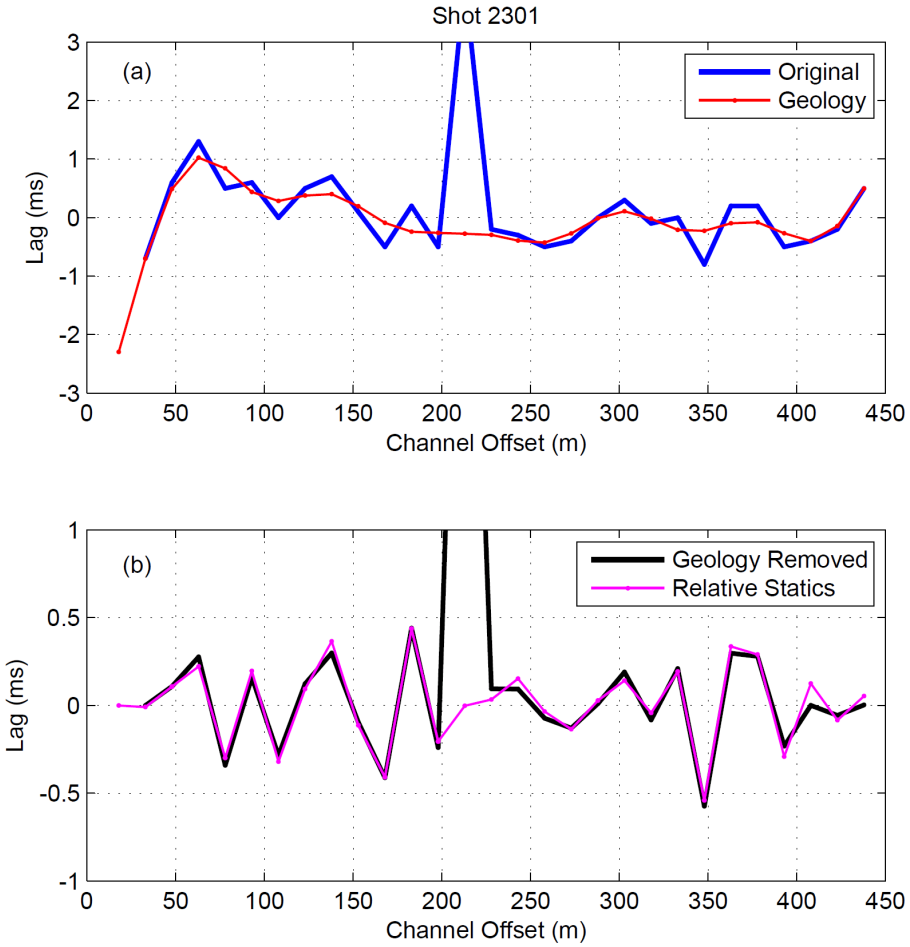

Figure 4.25 (a) Shot-gather-sorted cross-correlation lags of Shot 2301 (blue) and filtered low frequency geology structures (red). (b) Residual lags after geology information removed (black) and final statics after rejecting "wild" points larger than ±1 ms and subtracting the mean lag of each receiver gather.

4.4.2 Shot Statics and Image Stitching

The major differences between two adjacent shot images are mainly caused by variations in the source spacing and source depth. Although the ship's navigation provided estimates of ship position and speed, the source did not precisely follow the motion of the ship; as the ship's speed varied, the source, located at the end of a long tow cable, would rise or fall vertically in the water column and so the horizontal distance behind the ship would vary. To constrain this variation in source position, the large overlapping area between two adjacent shot images were used to calculate both vertical shot statics and the optimal horizontal position for image stitching.

Although the nominal ship speed is ~2 knots, the ship speed actually varied from 1.5 knots to 3 knots over most of the survey, with corresponding shot spacing variations of about 21-45 m for a shot interval of 30 s. Since the minimum hydrophone spacing of 3 m was achieved at the acoustic group, a marching distance of 3 m was used to find the best overlapping area of two adjacent shot images by comparing the overlapping areas trace-by-trace for shot spacing varying from 21 m to 45 m. For example, Shot 111 and Shot 110 are adjacent shots on survey line DT09 (Figure 4.26). The source location of Shot 110 is defined as 0 distance with coordinate $\boldsymbol{x}$ increasing along the direction of the ship's heading. If the source of Shot 111 was located at 30 m, corresponding to 3 marching windows from the minimum shot spacing of 21 m, Channel 48 of Shot 111 shared the same midpoint as Channel 46 of Shot 110 at -204 m (Figure 4.26). After checking the reflection midpoint (RMP), there were a total 36 pairs of traces with each pair having the same RMP location: Channels 13-48 of Shot 111 match Channels 3-14, 19 and 24-46 of Shot 110 one by one. All these 36 pairs of traces formed the overlapping area of Shot 111 and Shot 110 for the given shot spacing of 30 m. The two traces of each pair were cross-correlated and the results of all 36 pairs formed a cross-correlation seismogram (Figure 4.27). The lags of Shot 111 relative to Shot 110 were picked at the maximum amplitudes of the cross-correlation traces. The mean and standard deviation of the 36 lags measured the similarity of the overlapping area from the two adjacent shot images with offset of 30 m; the smaller the mean and standard deviation, the more similar was the overlapping area.

Marching Shot 111 relative to Shot 110 from 21 m to 45 m with a step of 3 m produced a series of cross-correlation seismograms for different overlapping areas, and thus a series of means and standard deviations for the picked trace lags. The combinations of means and standard deviations were used to determine the optimal shot spacing, which provides the best stitching result between the two shot images. A term "similarity tolerance" was defined to limit the reasonable deviation range. In practice the similarity tolerance was set to twice the smallest value of all standard deviations. Of the combinations having standard deviation no larger than the similarity tolerance, the one

having the smallest mean value was chosen to represent the optimal shot spacing with the most similar overlapping image between Shot 111 and Shot 110.

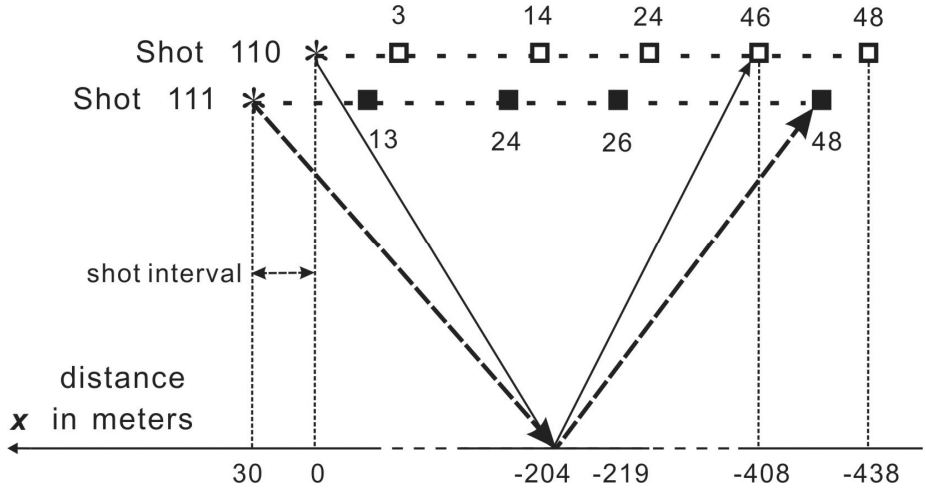

Figure 4.26 An example illustrates RMP locations when Shot 111 marching away from Shot 110 along ship heading of survey line DT09.

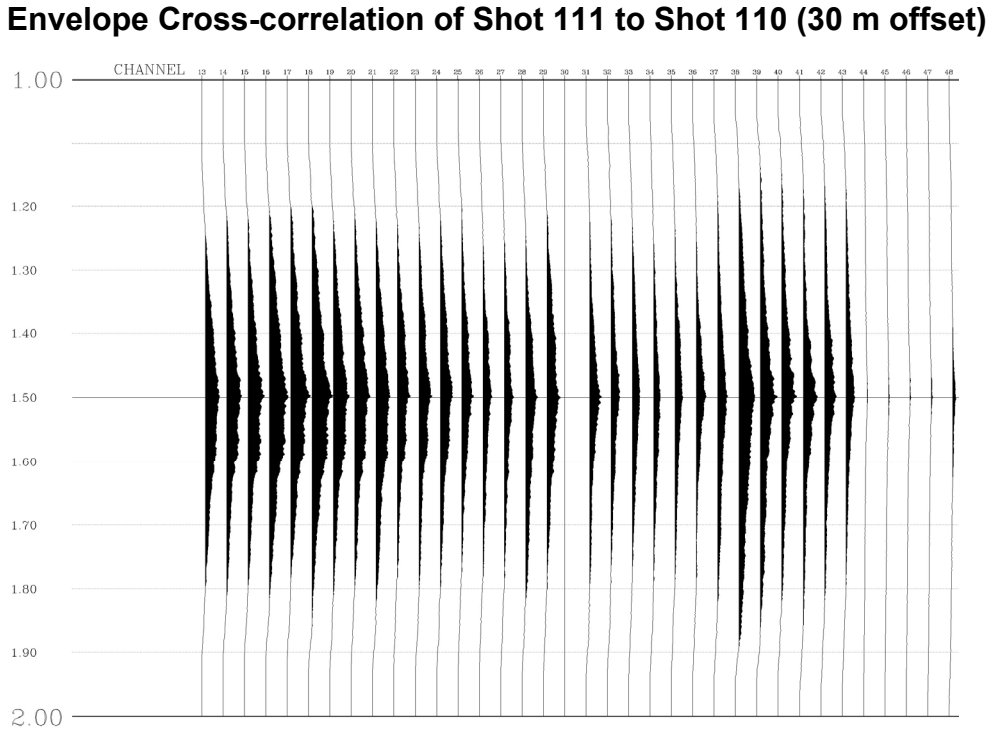

Figure 4.27 Cross-correlation seismogram of overlapping trace pairs when Shot 111 is 30 m ahead of Shot 110. Note that the cross-correlations are computed based on envelopes of real traces.

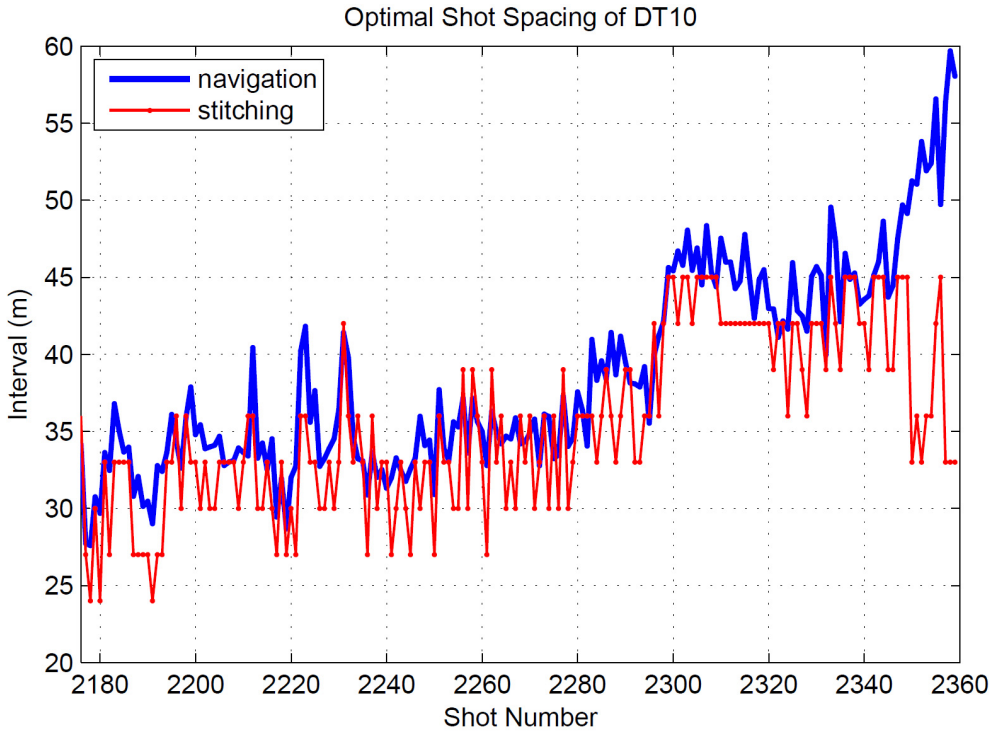

Figure 4.28 The comparison of navigation intervals (blue) to calculated optimal shot spacings (red) of survey line DT10. Note that the ship speeded up at the end of the survey line when it turned to the next survey line.

Figure 4.28 shows an example of calculated optimal shot spacings for survey line DT10. These shot spacings deviate from the corresponding navigation intervals (see section 2.2.3 for details of navigation calculation) due to the shrinking/expanding effect of the DTAGS tow cable and receiver cable geometry; however, these deviations are not large except at the end of survey line where the ship speeded up during turns onto the next track.

Table 4.1 lists the stitching results for Shots 2201-2210. For example, the best overlapping area between Shot 2204 and Shot 2203 was produced when Channel 21 of Shot 2204 aligned with Channel 1 of Shot 2203; this corresponded to an optimal shot spacing of 30 m from Shot 2204 to Shot 2203. Since the first two traces of the DTAGS2 streamer were dead, the final stitched image only used acoustic channels 3-24 and all geophysical traces were abandoned, no matter they were within or outside the overlapping area. For the acoustic traces within the overlapping area, the traces of the

current shot were removed to avoid repeating the common traces of the previous shot. For example, as indicated by the transparent yellow in Figure 4.29, the kept traces for image stitching comprised traces 3-22 of Shots 2204-2203 and traces 3-24 of Shot 2202.

Table 4.1 Example of stitching result for survey line DT10

Shot Number	2201	2202	2203	2204	2205	2206	2207	2208	2209	2210
Alignment Trace of Previous Shot	1	1	1	1	1	1	1	1	1	1
Alignment Trace of Current Shot	21	23	21	21	23	23	23	23	21	23
Optimal Shot Spacing (m)	30	33	30	30	33	33	33	33	30	33
Mean Lag (sample)	1.12	1	-0.56	-31	-10.8	-4	-11.3	-12.3	-14.7	-9
Auto-stitch Lag (sample)	-11.8	0.2	0	0	-14.6	-15.4	-15	-20.6	-15.4	-12.4
Manual-adjust Lag (sample)	0	0	0	5	0	0	0	0	-5	0
Final Lag (sample)	-11.8	0.2	0	5	-14.6	-15.4	-15	-20.6	-20.4	-12.4

* 1 sample = 0.1 ms

Figure 4.29 Images of Shots 2202-2204, showing stitching areas with yellow color in transparency.

There are two obvious advantages of this image stitching method:

1. The calculation of relative shot spacing does not rely on any positioning information (e.g., DGPS navigation, acoustic transponder net).
2. A more continuous stitched image can be achieved by removing all geophysical traces and overlapping acoustic traces from later-firing shot gathers.

Although the minimum mean value of lags can approximately represent the vertical statics correction of the current shot relative to the previous shot, it is not in practice appropriate to align the end of current shot to the head of previous shot. To stitch high resolution DTAGS shot images more accurately, the vertical shot statics were calculated by the following steps:

Step 1: Automatic Relative Lag Calculation

A Matlab routine was firstly used to automatically generate relative vertical shifts for two adjacent shots, based on cross-correlation lags of the first 3 common traces in the overlapping area. For example, the first 3 traces are Channels 23-25 for Shot 2209 and Channels 3-5 for Shot 2208. The cross-correlation was calculated between any two traces belonging to different shots; thus, a total of 9 lags were produced for two 3-trace-groups. Then the 9 lags were sorted in order of increasing value and the mean of the 5 middle values (i.e., 3-7 places) was used as the vertical shift of Shot 2209 relative to Shot 2208. The vertical shift in this case was -15.4 samples, or -1.54 ms; the minus means shifting Shot 2209 upward relative to Shot 2208 (Table 4.1).

This automatic method normally can provide sufficiently accurate statics to stitch 80-90% of the shots, and thus saves much labor in later manual readjustment work. Figure 4.30 displays the difference between the lags used for image stitching (red line) and the ones for optimal shot spacing for best overlap (blue line).

Step 2: Applying Auto-lag Shot Statics

Once the lag (x_i) of the current shot relative to the previous one is calculated in step 1, the absolute vertical statics X_i for each shot is given by Equation 4.13

$$X_i = S_i - \frac{\sum_{i=1}^{N} S_i}{N} \qquad \text{(Equation 4.13),}$$

where N is the total number of shots in the survey, i is the current shot number, and S_i is the accumulated lag relative to the first shot of the survey:

$$S_i = \sum_{1}^{i} x_i \qquad \text{(Equation 4.14).}$$

Note that the relative lag of the first shot, x_1, is 0. Figure 4.31 shows the calculated absolute statics for survey line DT10, which is converted to time (1 sample = 0.1 ms) and written into the 'source_static' trace headers. Then the STATIC module of Claritas shifted the traces according to these header values.

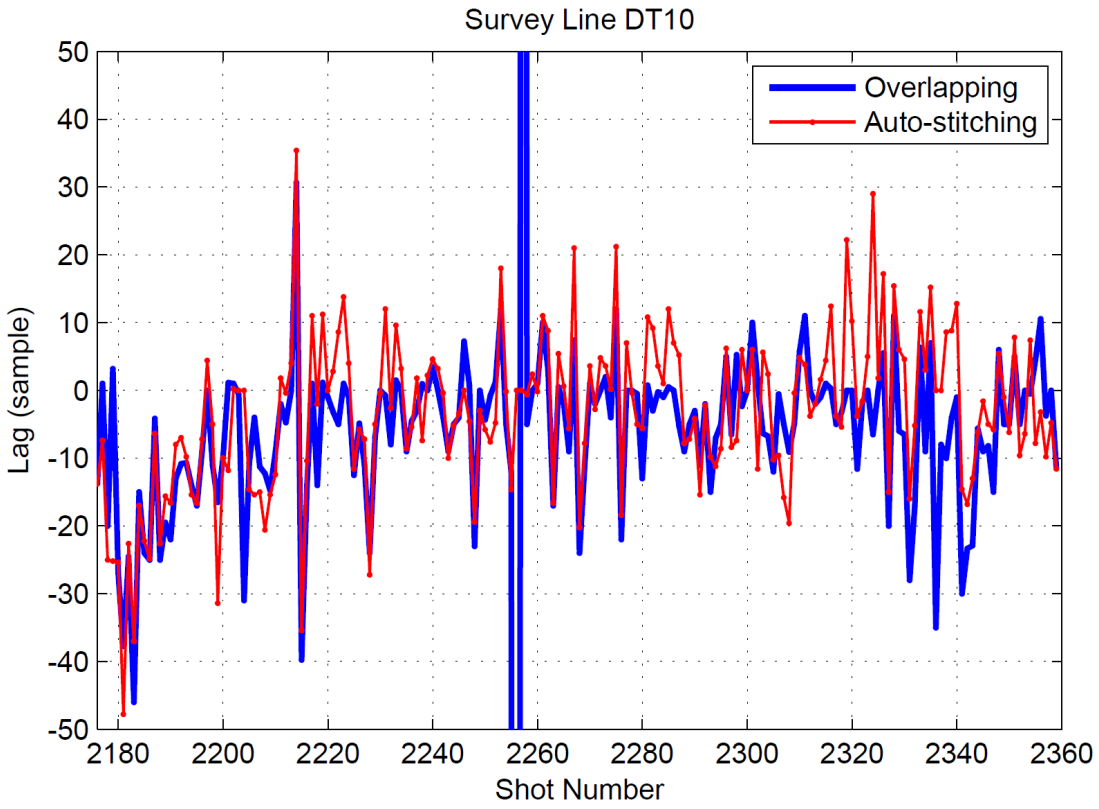

Figure 4.30 Comparison of lags for different uses: the values in blue are averaged lags over whole overlapping areas, thus suitable to find the optimal shot spacing. The values in red only average lags of head part of the overlapping area; however, they provide more appropriate alignment of two adjacent shots than the former.

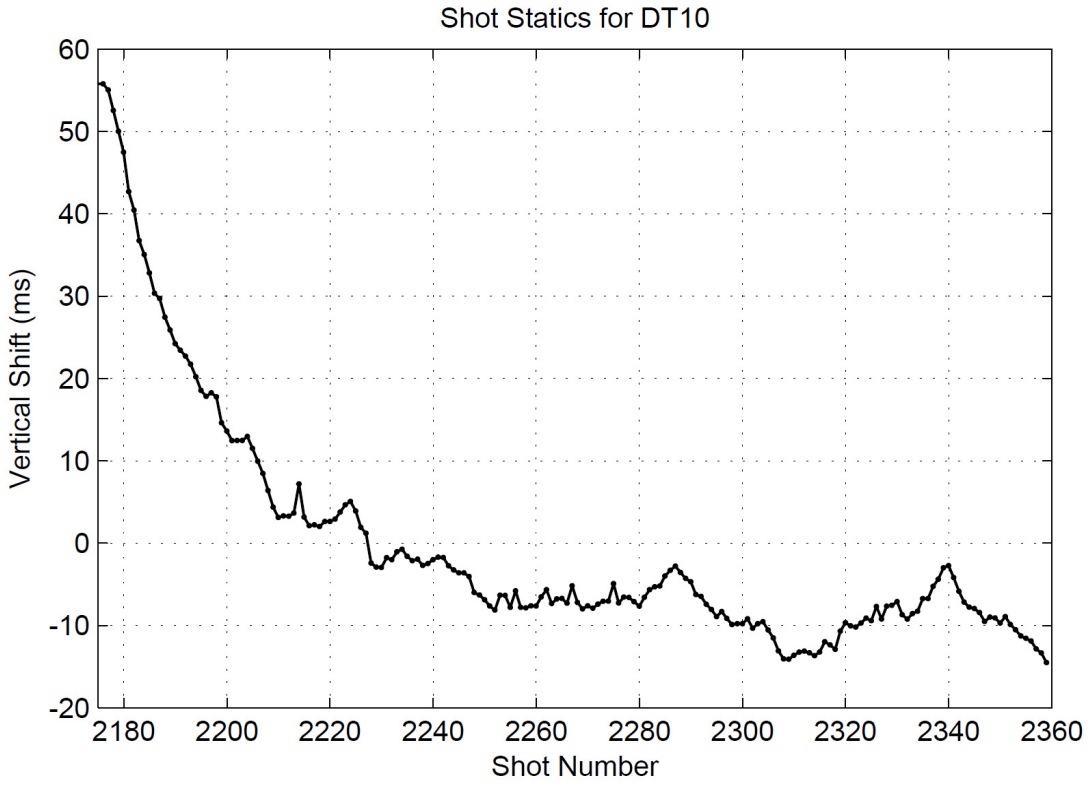

Figure 4.31 Shot statics of survey line DT10, calculated on relative lags between two adjacent shots generated previously.

Step 3: Manual Readjustment for Individual Shots

The automatic routine can not ensure 100% seamless stitching for all shots, especially for bad shots such as Shot 2203 where many empty traces exist (Figure 4.29). For such shots manual readjustment was required. The manual shifting times were measured on the first edition stitched image using automatically generated lags, and the picked values were added to the existing auto-lag to generate the final relative lag (refer to Table 4.1). After replacing the old relative lags with the new ones, the equations in step 2 will produce final absolute shot statics for stitching the whole survey. For the instance of survey line DT10, only about 14% of the shots (26 of 186) need manual readjustment; the automatic routine in step 1 saves significant labor. Figure 4.32 displays the final stitched image for Shots 2202-2204 in Figure 4.29, after removing unused traces (i.e., traces outside the yellow areas) and shifting shots vertically according to the final absolute statics.

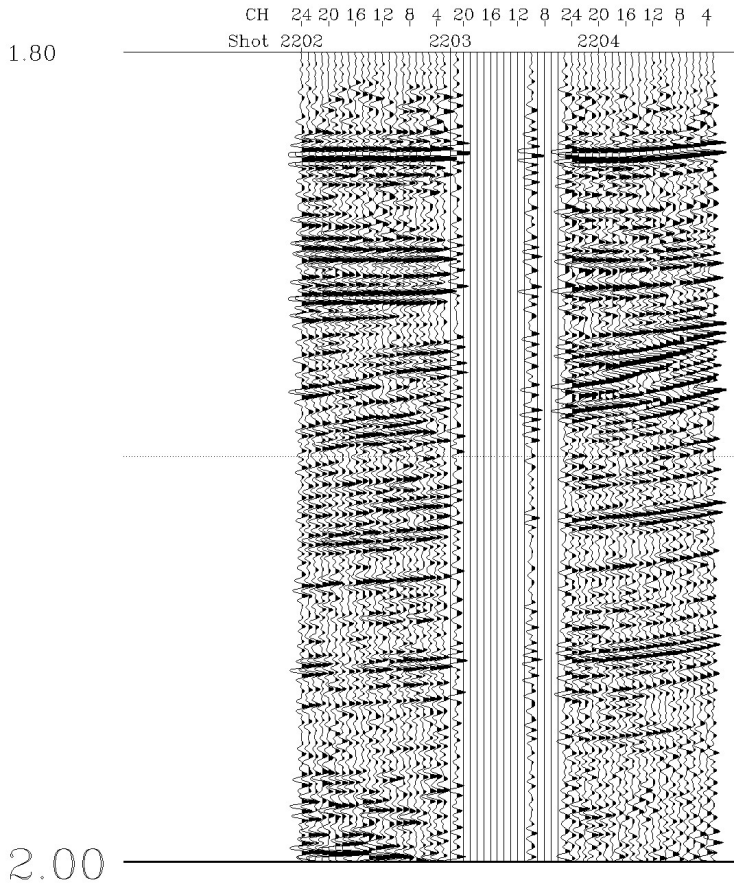

Figure 4.32 Stitched image for Shots 2202-2204 of survey line DT10.

4.4.3 DTAGS Imaging Process Summary

The imaging process for the DTAGS data is summarized in the flow chart of Figure 4.33, and the seismic imaging result for survey line DT09 is shown in Figure 4.34 using this process flow. Compared to the onboard foot-print version of Figure 4.9, the processing method developed in this study provides a more natural stitched image with smoother transition between shots; subseafloor features are positioned more reliably, and this increases the possibility of more accurate velocity analysis in later stages of the DTAGS data process. Considering the above advantages and obvious improvement in image quality, it is worthwhile to expend the extra effort to manually pick the times of the SSR and direct arrival and to measure readjustment times for a small number of inappropriately stitched shots. In any case, most data processing steps in Figure 4.33 can be accomplished efficiently by automatic routines.

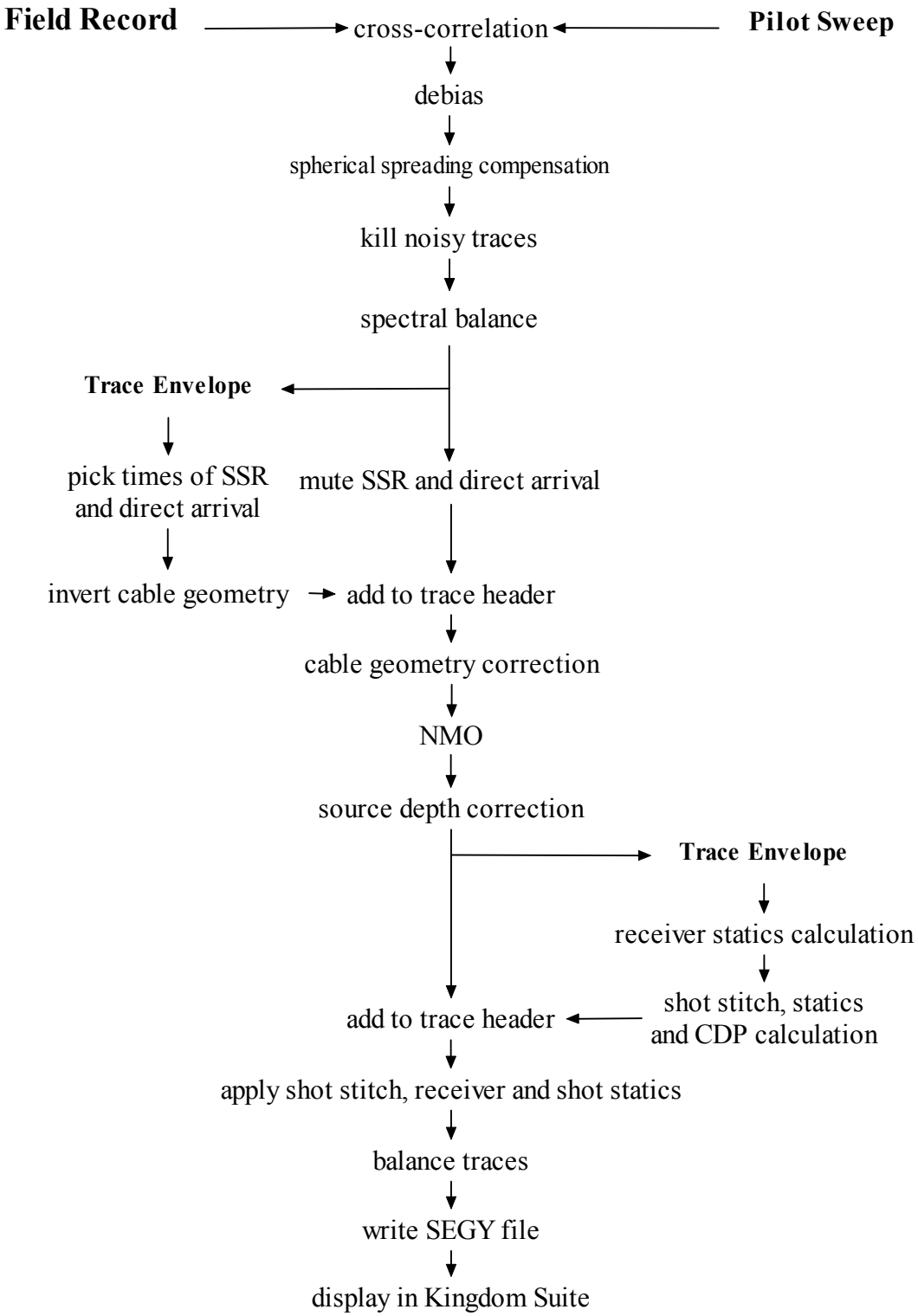

Figure 4.33 Flow chart of DTAGS data processing for imaging.

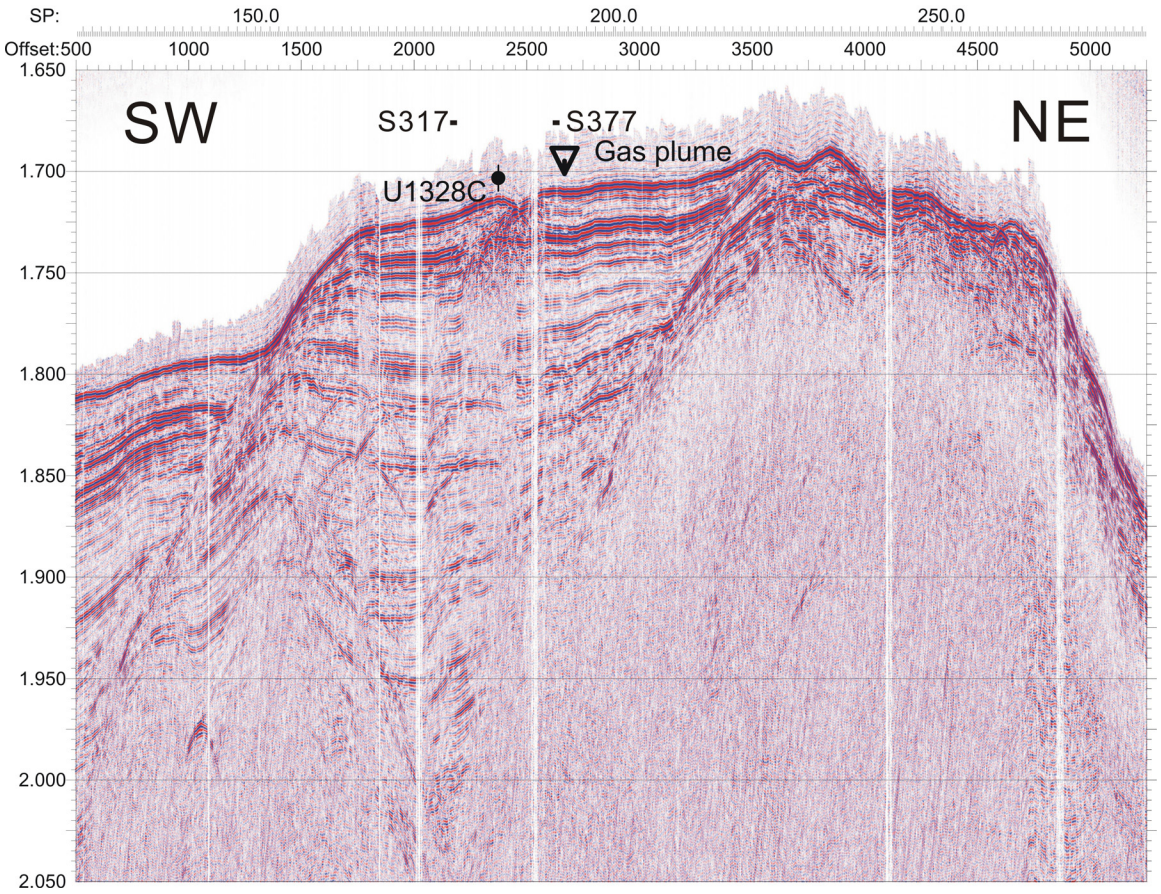

Figure 4.34 Acoustic image (100% coverage) of the survey line DT09, processed according to the flow chart in Figure 4.33. The locations of IODP drill site U1328C and a recently-recovered gas plume are labeled. S317 and S377 label two locations where conventional velocity analysis was tried in section 6.3.1.3.

4.4.4 Post DTAGS Images on Map

The stitched DTAGS images using the above method have no information on geographical coordinates. To better correlate subseafloor features to seafloor topography, these images must be posted on the bathymetry map. During the DTAGS2 survey, an acoustic transponder net was used around the Bullseye venting field, in an attempt to provide accurate navigation of the DTAGS system; however, this net can only cover a small area. Outside the Bullseye region, such as at Cucumber Ridge, the ship's DGPS system was used to estimate approximate locations of the DTAGS, assuming a constant distance behind the ship stern. Also, previous surface-towed single or multi-channel seismic lines, which have been posted on the map, can provide some constraints on the

DTAGS locations if they crossed the DTAGS2 survey lines at a sufficiently large angle. Since the map posting process is basically a navigation problem, the details are described in section 2.2.3 and 2.2.4.

4.4.5 Fine Tuning with Previous Seismic Grid

The existing surface-towed seismic survey lines can provide further corrections for DTAGS line positioning if they cross each other at sufficiently large angles. Around Bullseye venting field, a Teledyne pseudo-3D seismic grid (Tele2000, Figure 4.35) was collected in 2000. The 2002 DTAGS2 Survey line DT09, positioned with corrected rover navigation, crossed Tele2000 grid at an angle of about 30^{o} (Figure 4.35). Therefore a series of inlines from the Tele2000 grid should repeat the main features of DT09.

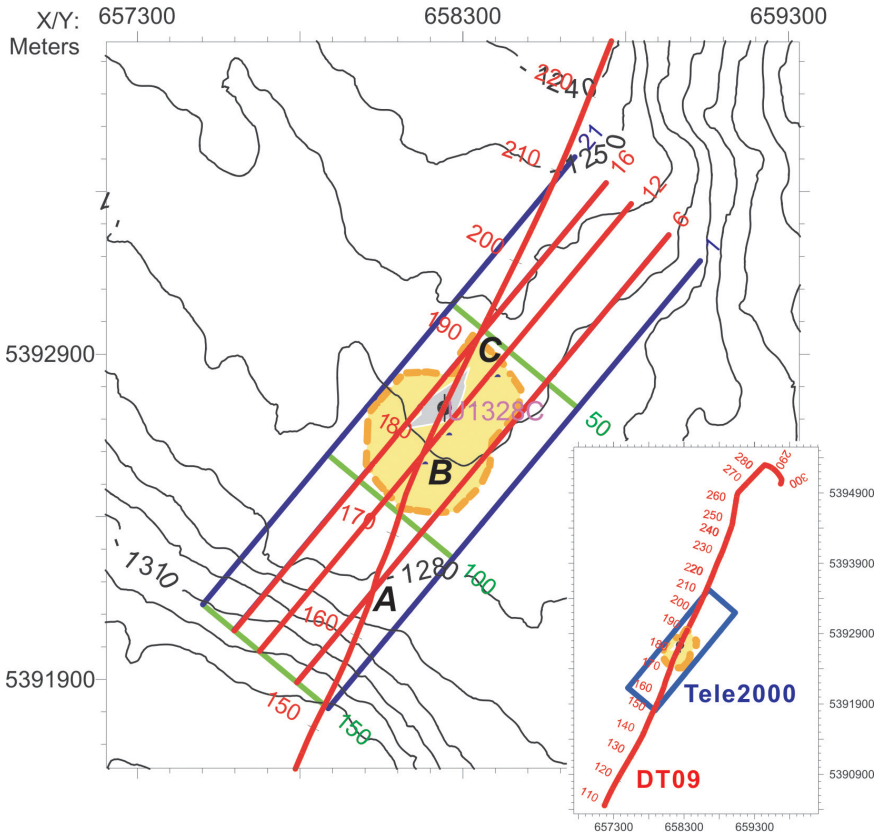

Figure 4.35 Bathymetry map showing the 2002 DTAGS2 survey line DT09 (rover corrected) crossing obliquely with Teledyne 2000 pseudo-3D grid. The characters ***A***, ***B*** and ***C*** label distinct seafloor features shown in Figure 4.36 on selected Tele2000 inlines 6, 12 and 16, respectively. The image of DT09 is bulk shifted horizontally along its rover navigation and vertically to match the same seafloor features at ***A***, ***B*** and ***C***.

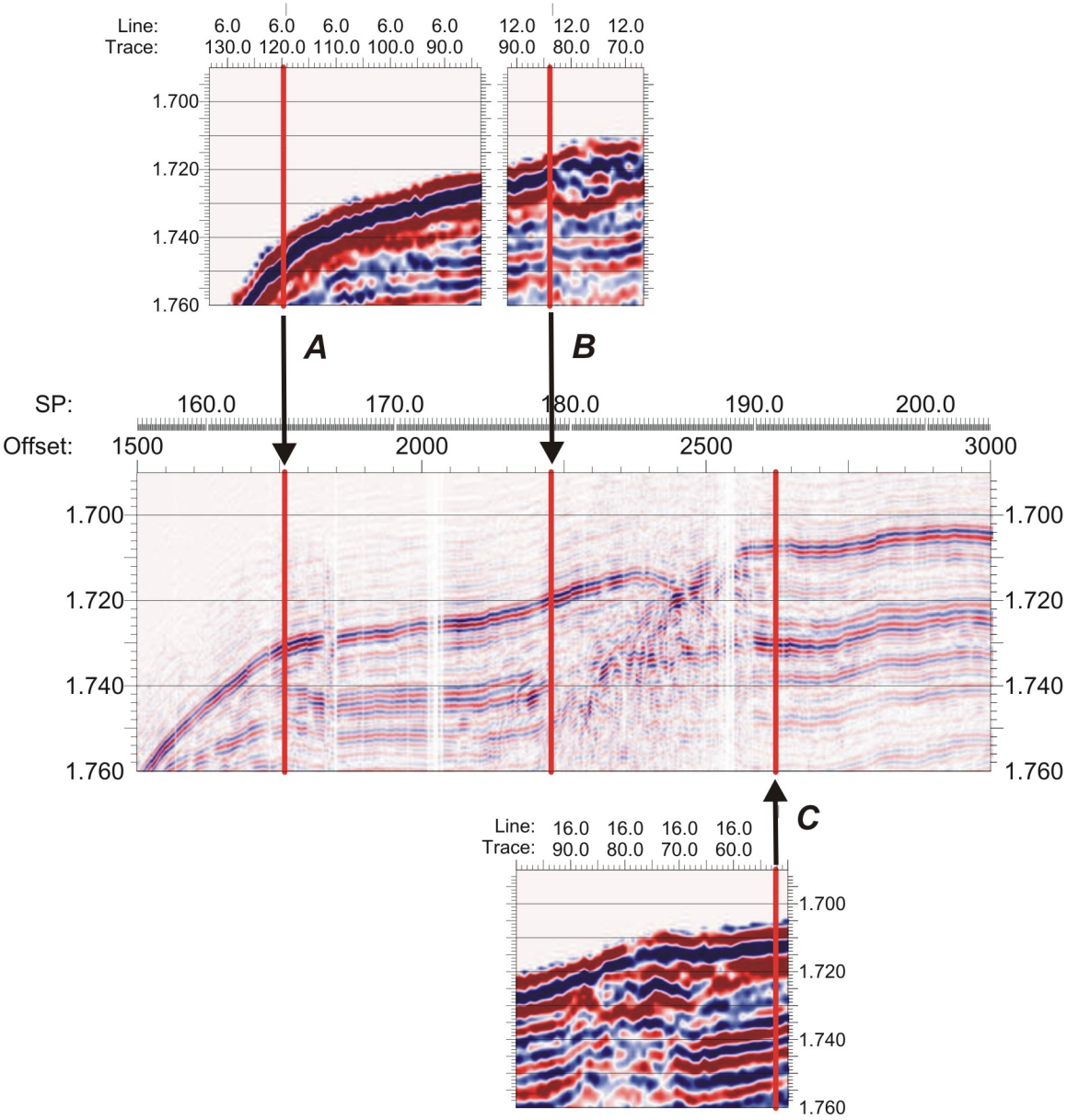

Figure 4.36 The final shift result by aligning the same seafloor features between DTAGS2 line DT09 (middle image) and selected Tele2000 inlines 6 (top left), 12 (top right) and 16 (bottom) at labels (A) start of steep slope, (B) start of strong diffraction area, and (C) end of the strong diffraction area.

For example, the steep slope around Shot 160 and a strong diffraction zone between Shots 180-190 are two distinctive seafloor features of survey line DT09 (Figure 4.34 and Figure 4.36). Although these two features are not obvious simultaneously on a single line of the Teledyne 2000 grid, different parts of them can be found on a series of

lines, such as steep slope on inline 6, and the strong diffraction zone on inlines 12 and 16 (Figure 4.36). These reference points were labeled: **A** for start of the steep slope, **B** and **C** for start and end of the strong diffraction area respectively. Then the trace positions of DT09 image were bulk-shifted vertically in time and horizontally along the corrected rover navigation track to align its A, B and C points to the corresponding reference positions on inlines 6, 12 and 16 of the Teledyne 2000 grid. In practice, the DT09 image was shifted about 100 m along the rover heading direction (i.e., North-Northeast) and about 8 ms down to match the above three reference points. Figure 4.35 and Figure 4.36 showed the final shifting results on the map and image, respectively.

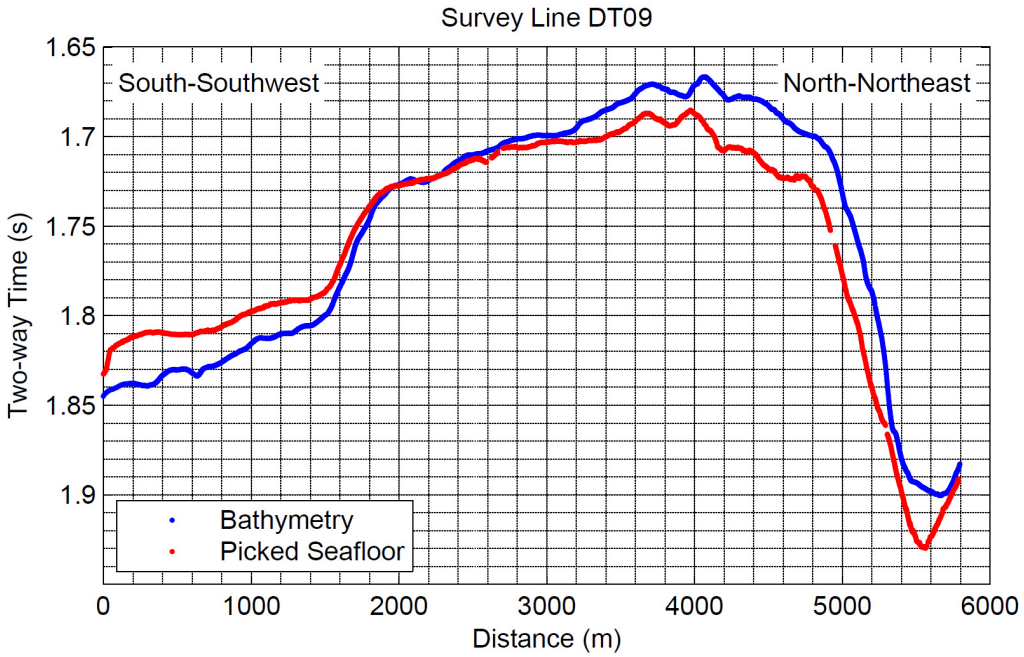

Figure 4.37 Depths comparison between the swath bathymetry (blue) and picked seafloor reflections (red) along rover track of DT09. The original bathymetry in meters was converted to two-way time using constant seawater velocity of 1482 m/s.

To further check the validity of this positioning method, the bathymetry values along the final positioned DT09 image were derived from the swath bathymetry map (Figure 4.35). After converting to two-way time using constant seawater velocity of 1482 m/s, the bathymetry was compared with the picked seafloor time from DT09 image in

Figure 4.37. It showed that the major features on the two water depth profiles matched each other well, indicating the success of this positioning method. However, the picked seafloor was tilted clockwise relative to the derived bathymetry, by as much as about 20 ms or 15 m. This tilting maybe caused by 1) the accumulated tilting of each shot from receiver and shot statics during the image stitching process, and/or 2) still existing small deviations of image trace positions from the real trace locations even after the above positioning process. In each case, this small tilting is minimal and can be ignored at the primary study location, Bullseye venting field (distance between 2000 to 3000 m in Figure 4.37).

4.4.6 Image Comparisons

Gettrust et al. (2004) posted the onboard "foot-print" of survey line DT09 (Cascadia Margin Line 9) on the map based on the ship's navigation (Figure 4.38). Imaging results for the same survey line, processed in this study, are shown in Figure 4.39. Comparison of these two figures shows 3 advantages of the method developed in this study:

1. Improved seismic image displays clearer sediment layering.
2. Seafloor depths are closer to the true bathymetry after time corrections for nonlinear cable tilting, source depth variations and vertical shot alignments.
3. Absolute map positioning is more accurate, based on the combination of corrected rover navigation and bulk readjustment according to existing seasurface-towed seismic lines. For example, Figure 4.39 shows more reliable locations of cores 5-7 (red arrows) than the ones on Figure 4.38.

DTAGS line DT09 and Teledyne 2000 inline BT14 also provide a comparison of these two different high resolution seismic imaging methods (Figure 4.40). Although the sampling rate for the Teledyne single channel data (0.5 ms) is similar to the DTAGS data, its dominant frequency is only about 80-180 Hz (e.g., Figure 3.4, section 3.2). Therefore, the DTAGS data, with its wide high frequency band (220-1000 Hz, Figure 4.4a), can resolve finer sediment layering than the Teledyne data. However, unlike the Teledyne

data, the DTAGS data cannot image the BSR, although DTAGS energy still reaches the depth of the BSR at about 2.0 s (two-way time) as shown between Shots 170-180 (Figure 4.40a). For example, at the crossing point of DT09 and BT14 (indicated by vertical red line on images), BT14 shows a clear BSR just above the 2.0 s time line, but DT09 image shows seismic blanking below time 1.95 s. This may be due to frequency effects associated with attenuation and velocity gradients in the gas hydrate layers (Fink and Spence, 1999; Chapman et al., 2002).

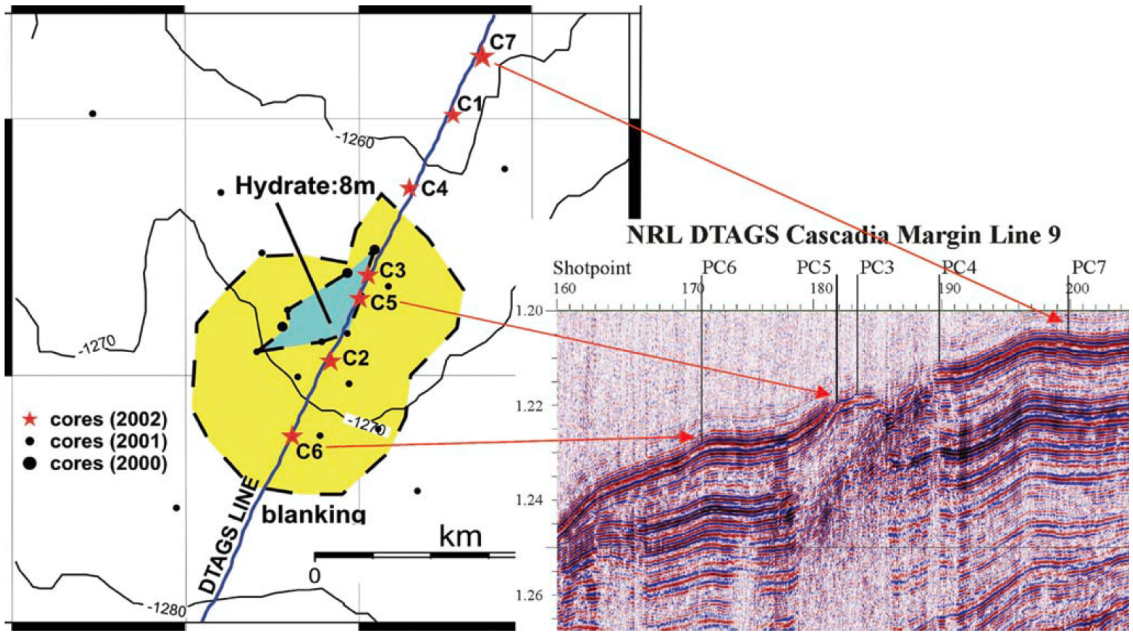

Figure 4.38 Map view of a hydrate-related pockmark (light blue) and associated seismic wipeout zone (yellow) around Bullseye venting field on the Cascadia Margin. A seismic section of the 2002 DTAGS2 survey line DT09 with core locations also is presented. (From Gettrust et al., 2004)

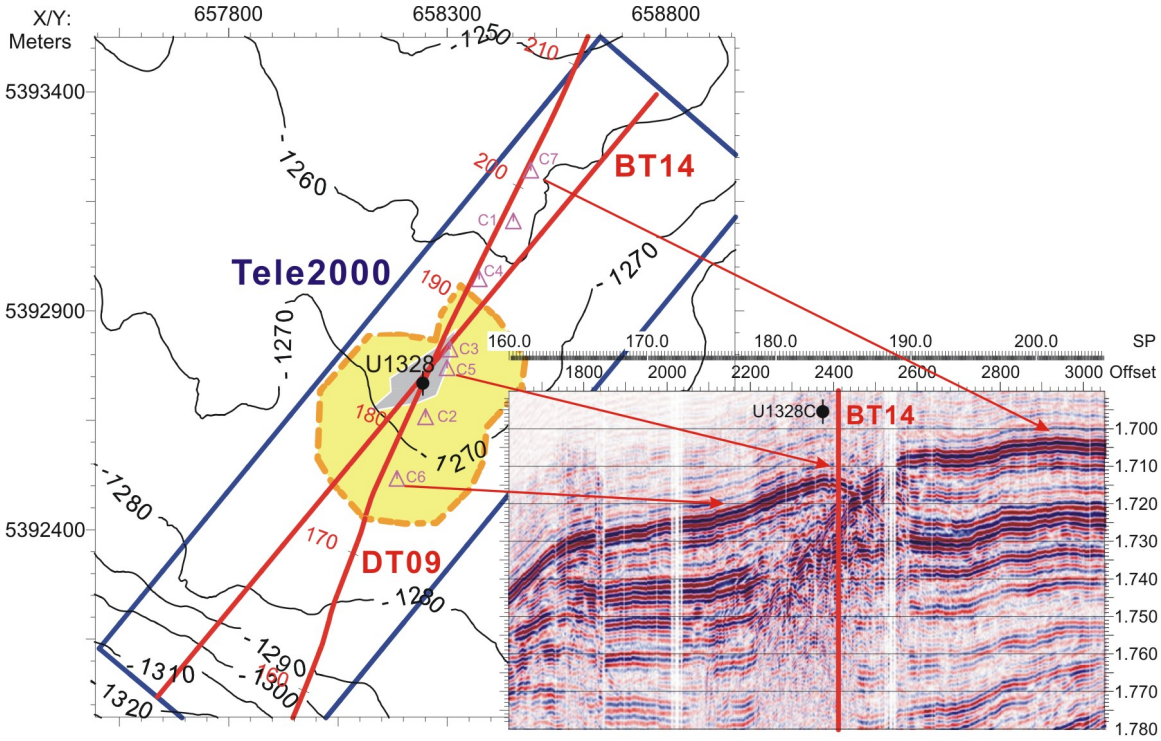

Figure 4.39 Map view and associated DTAGS seismic section with similar display as Figure 4.38. Teledyne 2000 inline grid BT14, which crossed DT09 at the location very close to IODP Site U1328, was displayed in Figure 4.40(b).

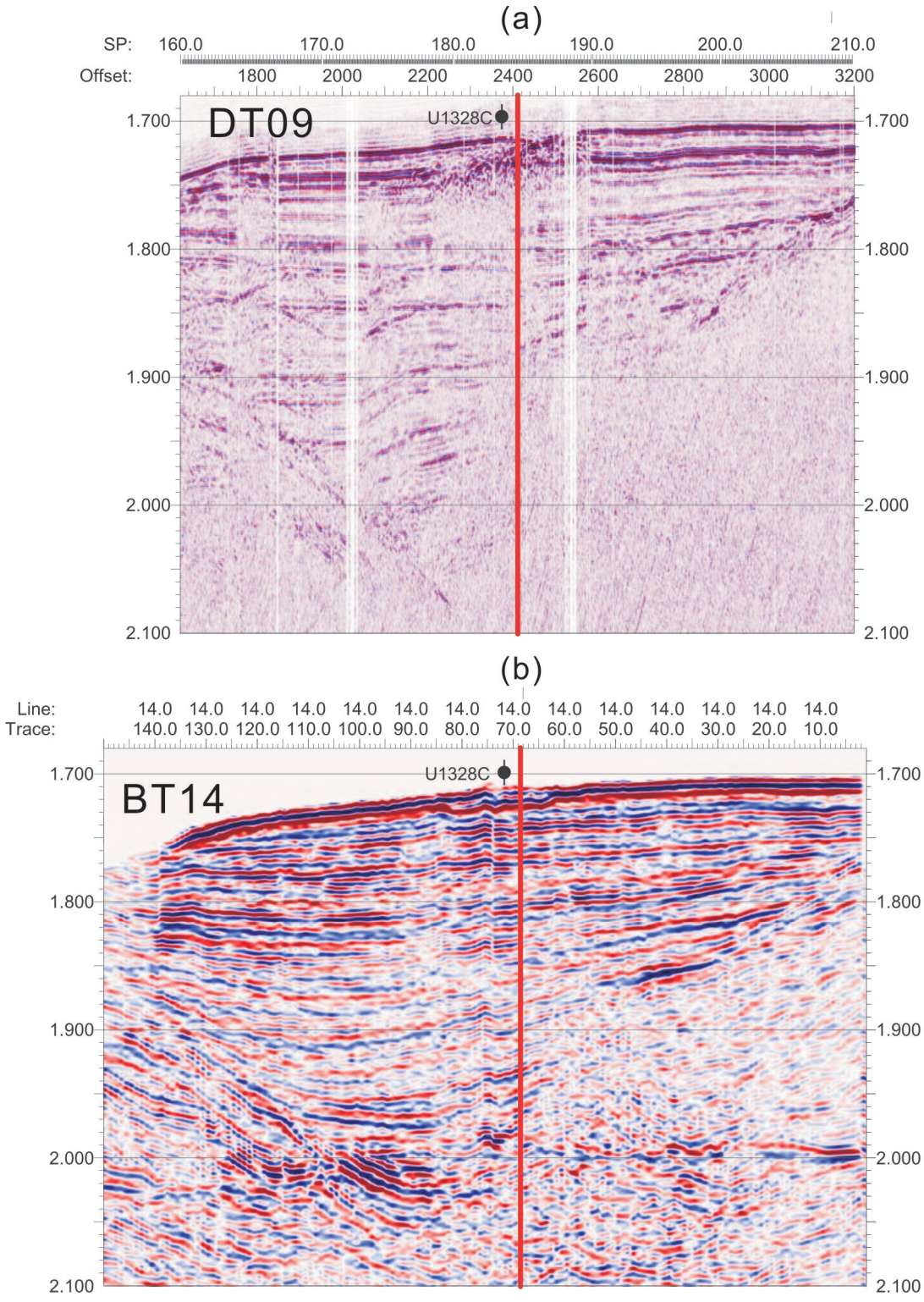

Figure 4.40 DT09 (a) of DTAGS and BT14 (b) of Teledyne 2000 crossed each other (indicated by the red vertical line) beside IODP Site U1328.

Chapter 5

Analysis and Interpretation: Cucumber Ridge

Elsewhere on the Cascadia margin, extensive seafloor carbonate cover has been observed, particularly on Hydrate Ridge (Tréhu et al., 2006); however, Cucumber Ridge is a large mud or carbonate mound formation first interpreted on this margin offshore Vancouver Island. One objective of the current study is to examine indicators of upward fluid flow at the mound Cucumber Ridge and in the surrounding region. To meet the objective, the remotely-operated submersible ROPOS was deployed on the mound during a cruise in May 2001 (Beaudet et al., 2001; Riedel, 2001), and a closely-spaced grid of high-resolution Teledyne single channel seismic lines was collected over the mound in July/August 2001 (Spence et al., 2002; see sections 2.1 and Chapter 3 for details of data collection and processing).

In this chapter, constraints on structure and fluid flow in the Cucumber Ridge region are investigated through several approaches: 1) determination of heat flow from the depth of the BSR as observed on regional seismic data; 2) examination of near-seafloor observations, including those from the ROPOS submersible, piston cores and water column measurements; 3) analyses of seismic stratigraphy and structure from single-channel, multichannel and deep-towed DTAGS sections. Note that most study results in this chapter have been published in the paper by He et al. (2007).

5.1 BSR Derived Local Variations of Heat Flow

To examine the thermal effect of possible upward fluid flow beneath Cucumber Ridge, heat flow at the mound and in the neighboring region was calculated from the depth of the BSR below the seafloor from the 2001 Teledyne data based on the theoretical temperature-pressure phase equilibrium relationship of the gas hydrate stability field. The local heat flow variations over the mound were extended over a much broader region by integrating them with comparable results determined from the 1999 COAMS multi-channel seismic data set (Riedel, 2001). Since the extended region

included ODP site 889 and IODP Site U1327, this heat flow data set was calibrated with heat flow calculated from temperature measurements at the drill sites.

5.1.1 Local Heat Flow Calculated From BSR Depths

Two-way traveltimes for the seafloor and for the BSRs were determined from the migrated versions of all originally recorded seismic sections from the single-channel Teledyne grid and the multichannel COAMS grid. Where the seafloor and BSR reflection waveforms were resolvable, the two-way travel times for the positive seafloor reflection and negative BSR reflection were picked. The BSR may result from a transition in seismic impedance over a few metres (e.g., Chapman et al., 2002), but this should not introduce significant error. The BSR is interpreted to represent the contact between overlying gas hydrate concentrations and underlying free gas concentrations. The BSR is taken to be the base of the gas hydrate stability field, and so the temperature at the BSR depth can be calculated using laboratory stability data. Using the depths to the BSR from the reflection times, velocity-depth estimates and estimates of seafloor temperature, the temperature gradient may be determined (e.g., Englezos and Bishnoi, 1988; Dickens and Quinby-Hunt, 1994; Ganguly et al., 2000). The heat flow then may be determined, using thermal conductivity estimates from regional ODP/IODP borehole core measurements and from velocity-conductivity relations. The thermal conductivity increases slightly with depth as porosity decreases. Details of these calculations, similar to Ganguly et al. (2000), are given below.

5.1.1.1 Velocity-Depth Relationship and BSR Depth Calculation

The reflection interval times from the positive seafloor to the negative BSR reflection were compiled for all seismic sections. Over short segments where the BSR is missing or hidden by background sediment layers, BSR depths were interpolated in the final plots. Because the Teledyne and the COAMS seismic lines were mainly perpendicular to each other, the interpolation errors in the overlapping region were much reduced by using identical values at the line intersection points.

A simple velocity-depth relationship (Figure 5.1a) was given by Yuan et al. (1996) to convert the travel time at the BSR to depth:

$$v = 1516 + 0.5556 \times z \qquad \text{(Equation 5.1)}$$

where v is the P-wave velocity in m/s and z is the subseafloor depth in m. This relationship is based on P-wave structure from semblance velocities and full waveform inversion of multichannel seismic data in a region of gas hydrate concentration ~2 km seaward of the ODP Site 889 and ~2 km southeast of the central mound of this study. As described by Westbrook et al. (1994), the sediments above the BSR are similar in both above locations and are a combination of slope sediments, mainly clayey silt to silty clay interbedded with silt and fine sand layers of turbiditic origin, and older accreted sediments. Previous studies (Hyndman and Spence, 1992; Singh et al., 1993) indicated that the high velocity gas hydrate layer is variable in thickness and in concentration; however, even for a strong BSR, the gas hydrate layer is generally less than 100 m thick and its average velocity is less than 1800 m/s in this region compared to a normal velocity of 1600 m/s at that depth. This velocity difference leads to only ~3% effect on the average velocity from the seafloor to the BSR, but its effect on the BSR-derived heat flow is even less (see error analysis in Section 5.1.1.4).

5.1.1.2 Temperatures at Seafloor and the BSR

A seawater temperature-depth vertical profile was determined by conductivity-temperature-depth (CTD) measurements during the 2001 cruise down to a depth of 1600 m. These data were used to calculate the seafloor temperatures as a function of depth using the following equation (Figure 5.1b):

$$T = 7.0855 \times 10^{-7} h^2 - 3.6226 \times 10^{-3} h + 5.9517 \qquad \text{(Equation 5.2)}$$

where T is the temperature in ^{o}C and h is the seawater depth in m. Only small variations of deep seawater temperatures are expected at each depth such that the associated temperature uncertainty is quite small and makes a negligible contribution to the heat flow error.

The pressure used at the BSR assumes a hydrostatic model for sediment pore pressure since substantial over-pressures are unlikely at the shallow BSR depth (e.g.,

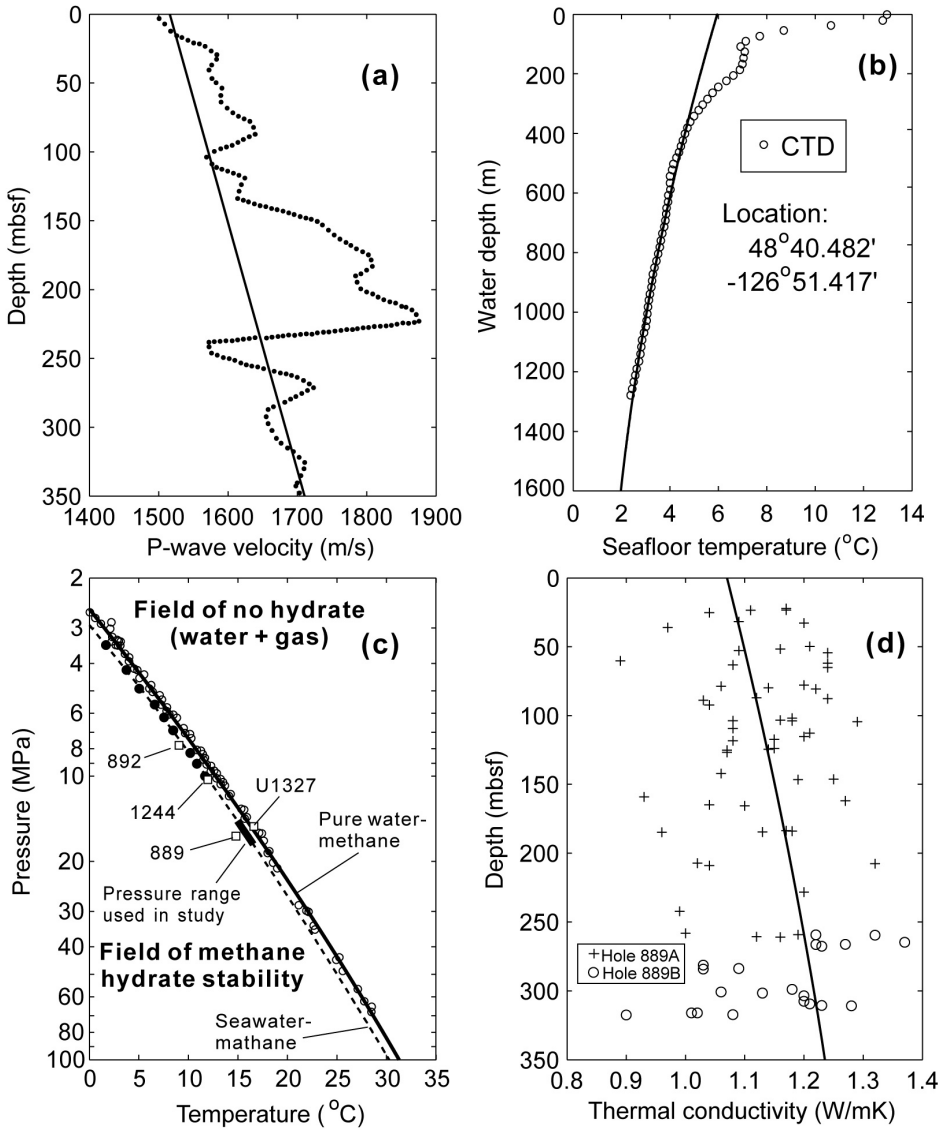

Figure 5.1 (a) A P-wave constant gradient velocity model (solid line) used to convert the travel times at the BSR to depths (Ganguly et al., 2000). The dashed curve shows the velocity profile obtained by semblance analysis and full waveform inversion of multi-channel seismic data in a nearby region of large gas hydrate concentration (Yuan et al., 1996). (b) Temperature-depth vertical profile in the seawater column based on the seawater temperature measurements (small circles) collected with a CTD near our study area during the 2001 cruise. (c) The pressure–temperature phase diagram for the methane hydrate stability field. The upper solid line is the pure water-methane curve from the compilation of laboratory data (open circles) by Sloan (1990). The dashed lower line is the seawater-methane curve from laboratory data by Dickens and Quinby-Hunt (1994) down to pressures of 10 MPa; the extrapolation to higher pressures is using the equation-of-state computation for artificial seawater by Englezos and Bishnoi (1988). The pressure range used in calculation is indicated by the small thickened part on this curve. BSR temperatures measured in some ODP/IODP drill holes on Cascadia margin are also indicated with open squares. (d) Variation of thermal conductivity with depth below seafloor from ODP Site 889 core samples (Westbrook et al., 1994). The solid line represents average conductivities from estimates of porosity and a geometric mean model for grain and fluid conductivity (Davis et al., 1990).

Hyndman et al., 1993; Zwart et al., 1996) and the predicted temperature gradient is consistent with the observed one from IODP U1327 (Riedel et al., 2006b). However, in some studies the BSR-derived heat flow assumed a lithostatic model (e.g., Ganguly et al., 2000); the difference between the lithostatic and hydrostatic BSR depth prediction was only approximately 5–10 m (Brown et al., 2006), leading to a systematic increase in heat flow of less than 1%.

The temperature at the BSR is determined from the pressure and the gas hydrate stability relationship for an assumed gas hydrate composition and pore fluid salinity. The composition of gas hydrate is assumed as dominantly methane (forms structure I) in seawater salinity pore fluid based on ODP and IODP data. One site, ODP889/IODP1327, had quite low salinity pore fluid of about 21‰ at the BSR rather than the normal 35‰ salinity of seawater (Riedel et al., 2006b). This difference could result in a heat flow error of about 6% as noted in section 5.1.1.4 below. In Figure 5.1(c) the P-T laboratory data compilation for pure methane in seawater (Dickens and Quinby-Hunt, 1994) is shown by the solid dots. For pressures beyond 10 MPa, the curve was extrapolated by the following empirical equation, which provides a close fit to 100 MPa for the equation-of-state seawater laboratory data of Englezos and Bishnoi (1988):

$$T = 0.76664x^3 - 5.0075x^2 + 28.156x - 12.136 \qquad \text{(Equation 5.3)}$$

where T is the temperature in ^{o}C, $x=log(P)$ and P is the pressure in MPa.

The calculation assumes that the BSR occurs at the theoretical base of the gas hydrate stability zone (BHSZ). However, differences between the theoretical and measured BSR temperatures have been noted at several ODP drill sites (Figure 5.1c). Recent models of BSR formation by Xu and Ruppel (1999) also predict that the BSR in regions of significant fluid flow should occur at a depth slightly shallower than the BHSZ.

5.1.1.3 Thermal Conductivity and Heat Flow Calculation

Assuming the approximation of a linear temperature gradient, heat flow was calculated with the simple conductive heat transport relationship:

$$H = k(T_{bsr} - T_{sf}) / z_{bsr} \qquad \text{(Equation 5.4)}$$

where T_{bsr} and T_{sf} are temperature at BSR and seafloor, respectively, z_{bsr} is the depth of BSR in meters measured from seafloor, and k is the average thermal conductivity in W/mK between the seafloor and the BSR. Estimated from the seismic velocity and other data (e.g., estimates of porosity and a geometric mean model for grain and fluid conductivity), an empirical expression of k has been given by Davis et al. (1990) (Figure 5.1d) for the region:

$$k = 1.07 + 5.86 \times 10^{-4} \times z_{bsr} - 3.24 \times 10^{-7} \times z_{bsr}^2 \qquad \text{(Equation 5.5)}$$

5.1.1.4 Error and Uncertainty Estimates for the BSR Method

A reflection time error originates from the difficulty in picking the onset of the negative BSR reflection. The maximum estimated errors are about one-half of the dominant seismic period, or 5-9 ms, which leads to a relative heat flow error of 3-4.5% for normal BSR depths of 200-300 ms.

The BSR-derived heat flow is not very sensitive to the velocity-depth profile chosen. An increased velocity gradient will produce a larger estimated BSR depth, but produce only a small change in the temperature gradient, since an increase in BSR depth will also cause an increase in estimated BSR temperature; e.g., Ganguly et al. (2000) showed that an increase in velocity from 1627 to 1800 m/s will produce a decrease in heat flow of only 2-3% at a depth of 200 mbsf (meters-below-seafloor). In addition, Riedel et al. (2006b) indicated that seismic velocities and gas hydrate concentrations previously calculated for ODP Site 889 may be higher than average for the region. So the heat flow error associated with BSR depth calculations may only be a maximum of 2%.

In the northern Cascadia margin at IODP Site U1327, the salinity measured at the BSR depth is unusually low, about 21‰. If this value is taken as the lower bound for salinity, Sloan's equation-of-state will predict an increased heat flow of ~6% relative to a normal salinity value of 35‰. However, the low salinity is not representative for the study region, since more normal 35‰ or slightly increased salinities are observed at other ODP/IODP sites around this region. In addition, the salinity variations below Cucumber Ridge may be very complex due to a deep-rooted fault. Since the heat flow is not calculated at a specific ODP/IODP site, normal seawater salinity is assumed. Methane

mixed with higher hydrocarbons, CO_2 or H_2S would produce a higher stability temperature, but at Sites 889 and U1327 only very minor quantities of these gases were found in pore fluids extracted from sediment cores. Thus, a gas hydrate stability curve based on pure methane in seawater was used for all calculation (Figure 5.1c).

At ODP Site 889, the observed temperature is 14.8°C at the BSR depth of 225 mbsf, whereas at nearby IODP Site U1327 the observed temperature is 16.6°C at a clearly defined BSR depth estimated to be 223 mbsf. The Site 889 value is ~1°C lower than the theoretical stability value of 15.6°C for pure methane-seawater system, whereas the Site U1327 value is ~1°C higher. At both sites the estimated error of the temperature measurements is ~1°C (Hyndman et al., 1992; M. Riedel, personal communication, 2006), and so it is uncertain if the difference is meaningful. Therefore the largest heat flow error from uncertainty in the BSR temperature should be about 8% if the hydrostatic pore pressure assumption is correct, corresponding to the 1°C temperature uncertainty relative to the average 12°C difference between the seafloor temperature of 2.7°C and BSR temperature of 14.8°C.

Another major error in heat flow calculation is the uncertainty of thermal conductivity. Compared to actual measurements from ODP sites 889/890 (Figure 5.1d), the relation predicted by Equation 5.5 is consistent with the mean values of the data. The ±10% scatter of the measurements probably represents a maximum error for the estimate of average thermal conductivity.

Based on the estimates discussed above, the sources of error in the heat flow calculation are mainly: (1) ±2% uncertainty of BSR depth from picking error and inaccurate estimate of average sediment velocity, (2) an error of 8% associated with the temperature measurements at the BSR, (3) ±10% uncertainty in estimating average thermal conductivity. Through combining the errors and allowing partial cancellation of the errors in velocity and thermal conductivity, the estimation of the absolute overall uncertainty for the BSR-derived heat flow is about ±20%. The relative accuracy among the values is much less over the region, probably about ±5%, since many of these errors are expected to be systematic and nearly constant along the profiles.

5.1.1.5 Comparison with ODP/IODP Sites 889 and U1327 Heat Flow

ODP/IODP Sites 889 and U1327 are located on a gently undulating seafloor in the mid-continental slope, ~3.5 km east of the Cucumber Ridge (Figure 1.10 and Figure 5.2) where there is a very strong BSR.

At ODP Site 889, the linear sub-seafloor temperature gradient of 54(±2) ^{o}C/km was determined by in-situ temperature measurements with the ODP water-sampling temperature probe (WSTP) and Adara probe tools. The thermal conductivity measurements on core sediment samples range from 0.88 to 1.46 W/mK and exhibit no apparent trend with depth (Figure 5.1d). Therefore, the thermal conductivity at Site 889 was assumed to be constant with a mean value of 1.15(±0.1) W/mK. With these values of temperature gradient and conductivity, Westbrook et al. (1994) estimated that the conductive heat flow at Site 889 was 62 (±8) mW/m^2.

Although very close to ODP Site 889, the data collected at IODP Site U1327 suggest a geothermal gradient of ~61°C/km, which is considerably higher than what was estimated for ODP Site 889 of ~54°C/km, and a constant thermal conductivity of 1.1W/mK (Expedition 311 Scientists, 2005). The implied heat flow, using these two numbers, is ~67 mW/m^2.

A map showing BSR-derived heat flow in this study is presented in Figure 5.2. At Site 889, the BSR-derived value is 72.5 mW/m^2, 15% higher than the heat flow determined from the drill hole measurements. Note that at Site 889 the BSR depth is determined to be ~225 mbsf, based on the sonic log and Vertical Seismic Profile velocities (Westbrook et al., 1994). However, using the parameters in the calculations of this study, the BSR depth is estimated to be 215.3 mbsf; the ~10 m difference is caused by using a slower velocity model, which is more applicable over the entire study region. Based on the calculation model in this study, an average thermal conductivity of 1.18 W/mK and an average temperature gradient of 61.4^{o}C/km are predicted with the BSR at a depth of 215.3 mbsf. The BSR-derived temperature gradient is very close to the measured values at Site U1327.

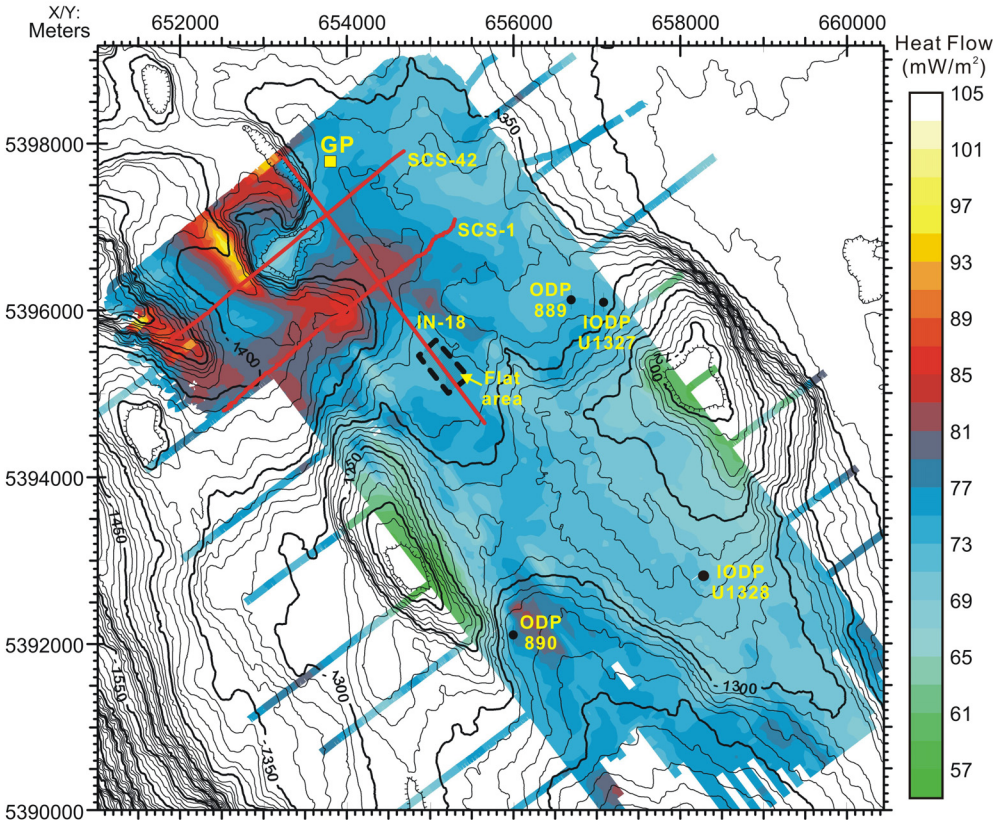

Figure 5.2 BSR-derived heat flow map superimposed on seafloor bathymetry. Except for the yellow and red local high heat flow areas due to the focusing effect of topographic valleys and/or focussed fluid flow, lower heat flow values (blue) occur over a broad region northeast and southeast of the central mound. The lowest heat flow values (light-blue to green) occur over the central mound area and the peaks of two ridges, corresponding to the defocusing effect on heat flow of convex upward topography. The flat area southeast of Cucumber Ridge in dashed rectangle was chosen for the regional background heat flow value of 74 mW/m^2. The solid yellow square with label "GP" indicates the location of verified gas plume in the water column, detected by the 12 kHz profiler during 2006 cruise of C.C.G. vessel John. P. Tully.

It is uncertain whether the BSR-derived values or the drillhole-calculated values are more representative for estimating heat flow in the region, for two reasons: (1) the gas hydrate concentrations and therefore seismic velocities at Sites 889/U1327 may be anomalously high for the region, and (2) the BSR temperature measured at the drill hole has a 1^{o}C or 8% measurement uncertainty, so that temperatures estimated from the theoretical BSR stability field may be more reliable. Because the drillhole measurements cannot be extrapolated to the rest of the region, only the BSR-derived heat flow values are used in later interpretations.

5.1.1.6 Comparison with Heat Flow from Sediment Heat Probe Measurements

Previous marine heat probe measurements in this region included the 1987 survey reported by Davis et al. (1990) who found values of 90-100 mW/m^2 along a margin-normal profile passing near ODP Site 889. Comparable values were obtained in a repeat survey in 1992 (Hyndman et al., 1994). In contrast, marine probe heat flow measured in July 2000 (Riedel et al., 2006a) and in September 2000 (H. Villinger, personal communication, 2000) indicated significantly lower values of 50-60 mW/m^2, even at stations only a few hundred meters from stations of the 1987 or 1992 surveys. This difference indicates the uncertainties in using sediment heat probe measurements extending only 3-5 m below the seafloor to estimate deeper equilibrium heat flow. Even though well-constrained linear temperature gradients were obtained in all surveys, the differences are likely caused by systematic changes with time of seafloor temperatures related to large currents. To verify this assumption, long-term bottom temperature measurements need to be made. Therefore the BSR-derived heat flow in this study is not compared to the sediment heat probe values in this study. The BSR-derived heat flow values, which are in better agreement with drillhole measurements than heat probe measurements, are taken as the most reliable regional deep heat flow estimates available on the north Cascadia margin.

5.1.2 BSR Heat flow observations

5.1.2.1 Regional Variations

The BSR-derived local heat flow map indicates a correlation between major heat flow patterns and the general seafloor bathymetry (Figure 5.2). Higher heat flow values (in yellow and red colors on the map) are observed along the foot of the steep seaward flank of the central mound, whereas lower heat flow values (in blue colors on the map) are seen over a broad region northeast and southeast of the central mound where the seafloor varies relatively little in depth. The lowest heat flow values (in green colors on the map) are over the central mound area and over two ridges in the southeast that were formed due to lateral compression and folding of accretionary wedge sediments.

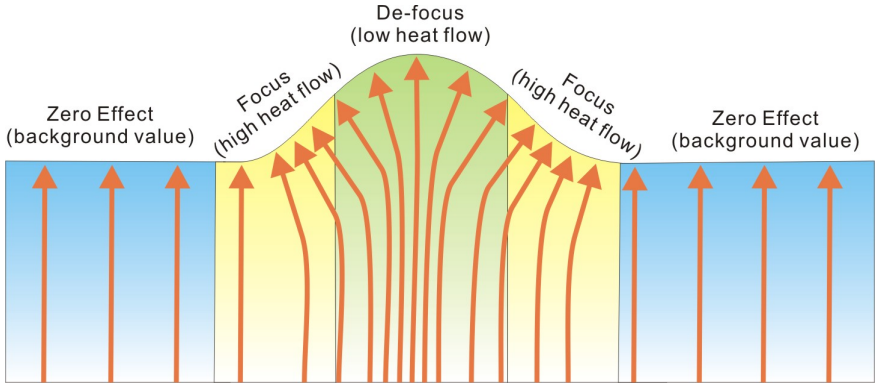

Figure 5.3 Diagram shows schematically the focusing and de-focusing effect of seafloor topography on surficial heat flow. At flat area, topographic effect is zero. At valleys, heat flow is focused, while de-focusing happens at ridges.

5.1.2.2 Topographic Effect on Superficial Heat Flow over Mound

The observed heat flow patterns may be due to the steady state topographic effects of seafloor features that focus or defocus upward heat flow. Over ridges or other convex-upward topography, refraction of upward-directed heat flow results in defocusing and reduction of heat flow, whereas the opposite occurs in valleys or regions of concave-upward topography (Figure 5.3).

By approximating the irregular topographic surface with a series of 2D plane reference surfaces, a simple 2D analytical solution provided by Lachenbruch (1968) is used to estimate the approximate magnitude and pattern of this topographic effect. For a plane slope of height H ($H>0$) and angle β (between 0 and 90°), the superficial heat flow $q(x)$ at a distance x from the brink of the slope is:

$$q(x) = G(1 + \Delta q(x)) = G\left(1 + \frac{1}{\pi}\tan\beta \ln\left|\frac{x}{x + H\cot\beta}\right|\right) \qquad \text{(Equation 5.6)}$$

where G is the regional background heat flow (see box of flat area on Figure 5.2 for G location). Figure 5.4 and Figure 5.5 show the results of applying this simple 2D analytical topographic correction along lines SCS-42 and SCS-1 (see locations on Figure 5.2), respectively.

Selection of background heat flow G. A value of 74 mW/m^2 (red horizontal line in Figure 5.4b and Figure 5.5b) is used for the background regional heat flow G. This

corresponds to the BSR-derived values at the small relatively flat area about 1500 m southeast of the central mound (Figure 5.2), where the topographic effect is close to zero. As well, this value matches the heat flow across this region predicted by Hyndman et al. (1993) for a large-scale theoretical model of the accretionary prism in which the age of the subducting lithosphere is 5 Ma and the effects of sediment thickening and delayed fluid expulsion are included.

Asymptotes at plane intersections in 2D model. Note that theoretical model heat flow values cannot be compared to the observed values at plane intersections, since there is a model singularity with the correction approaching infinity as x approaches 0. In reality, the topography varies smoothly and better approximations for the topography are required for more accurate modeling. Thus theoretical and observed values should be compared only away from the intersections of the model surfaces.

Comparison with observations. For seismic line SCS-42, the variations in heat flow due to simplified model topography (red line) account for the major variations in the observed heat flow pattern (dotted blue line): a large 20 mW/m^2 positive heat flow anomaly over steep slope seaward of the ridge, a local negative anomaly over the ridge that is ~6 mW/m^2 (±1) lower than regional heat flow value, and a return to the regional value over the flat area ~1.5 km landward of the ridge (Figure 5.4). However, for line SCS-1, the observed heat flow seaward and landward of the steep slope is systematically higher by ~8 mW/m^2 (±2) than the topography-corrected regional values (Figure 5.5).

2D assumption. It is recognized that a 3D topographic correction is needed for a more accurate representation of the topographic effect, particularly for the mound itself. However, the seismic section SCS-42 crossed the approximate midline of the central mound and, at the steep slope, the depth contour lines are locally nearly perpendicular to the profile (Figure 5.2). For SCS-1, the topography is also locally 2D across seaward of the steep slope, whereas it is nearly 1D landward of the slope where the bathymetry has only small depth variations (Figure 5.2). Over the central mound, a 3D correction would reduce even further the model negative corrections. Thus, in this area, the observed deeper heat flow may be higher than the corrected regional value.

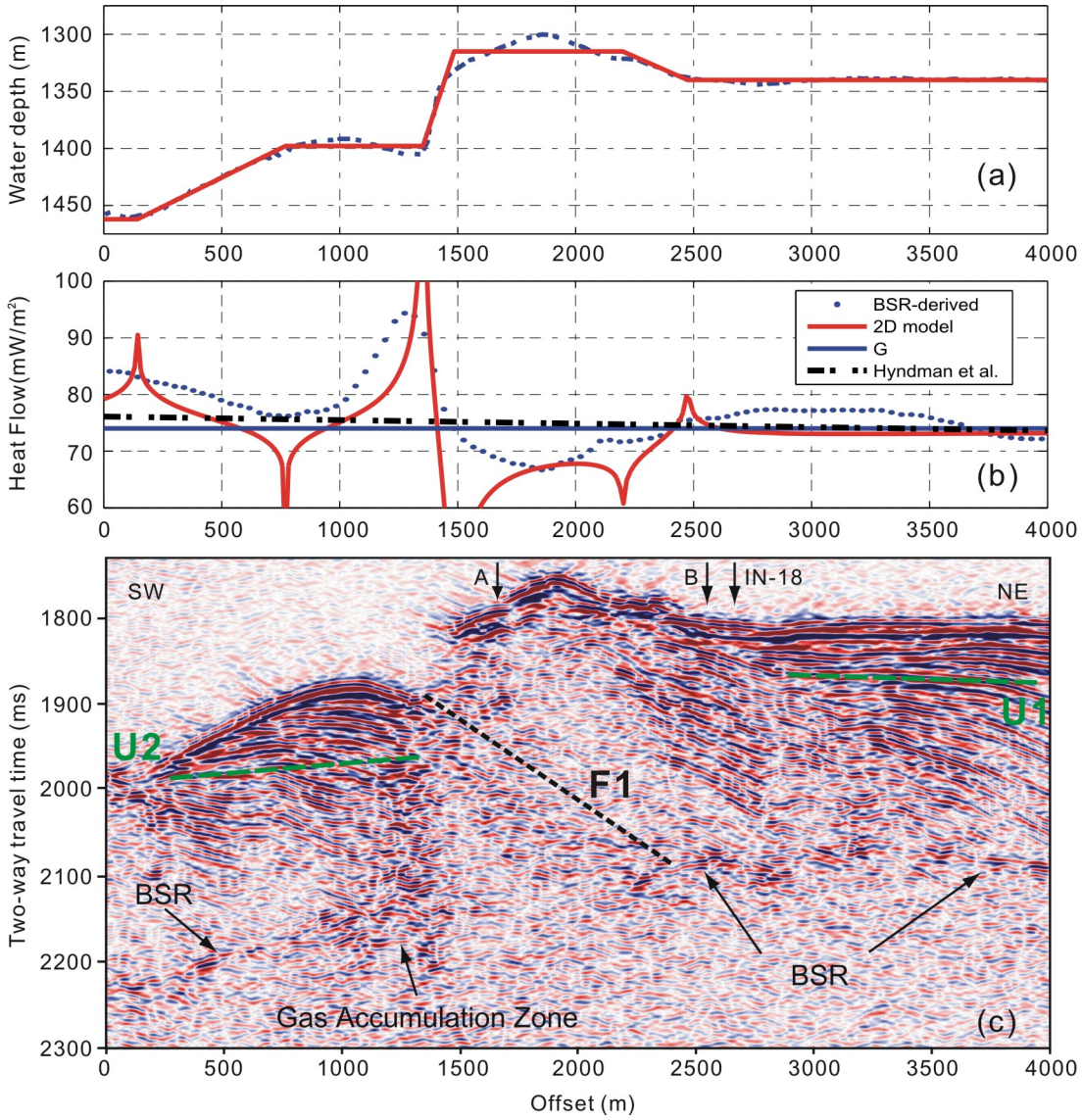

Figure 5.4 Local heat flow variations and 2D model topographic corrections along 2001 Teledyne survey line SCS-42 across peak of the central mound. (a) Seafloor topography (dashed blue line) and its 2D plane surface approximation (red line). (b) BSR-derived heat flow observations (blue dots) and 2D model topographic correction (red line) for regional heat flow value *G* of 74mW/m^2 (horizontal blue line). The thick dashed black line is the prediction from the large-scale heat flow model of Hyndman et al. (1993). (c) Migrated section of line SCS-42, showing central mound with weakened reflectors, stratified slope sediments with unconformities U1 and U2, a possible fracture zone F1, gas accumulation zone and the BSR. Locations of ROPOS pictures A and B in Figure 5.6 and intersection point with COAMS seismic grid IN-18 are indicated by arrows.

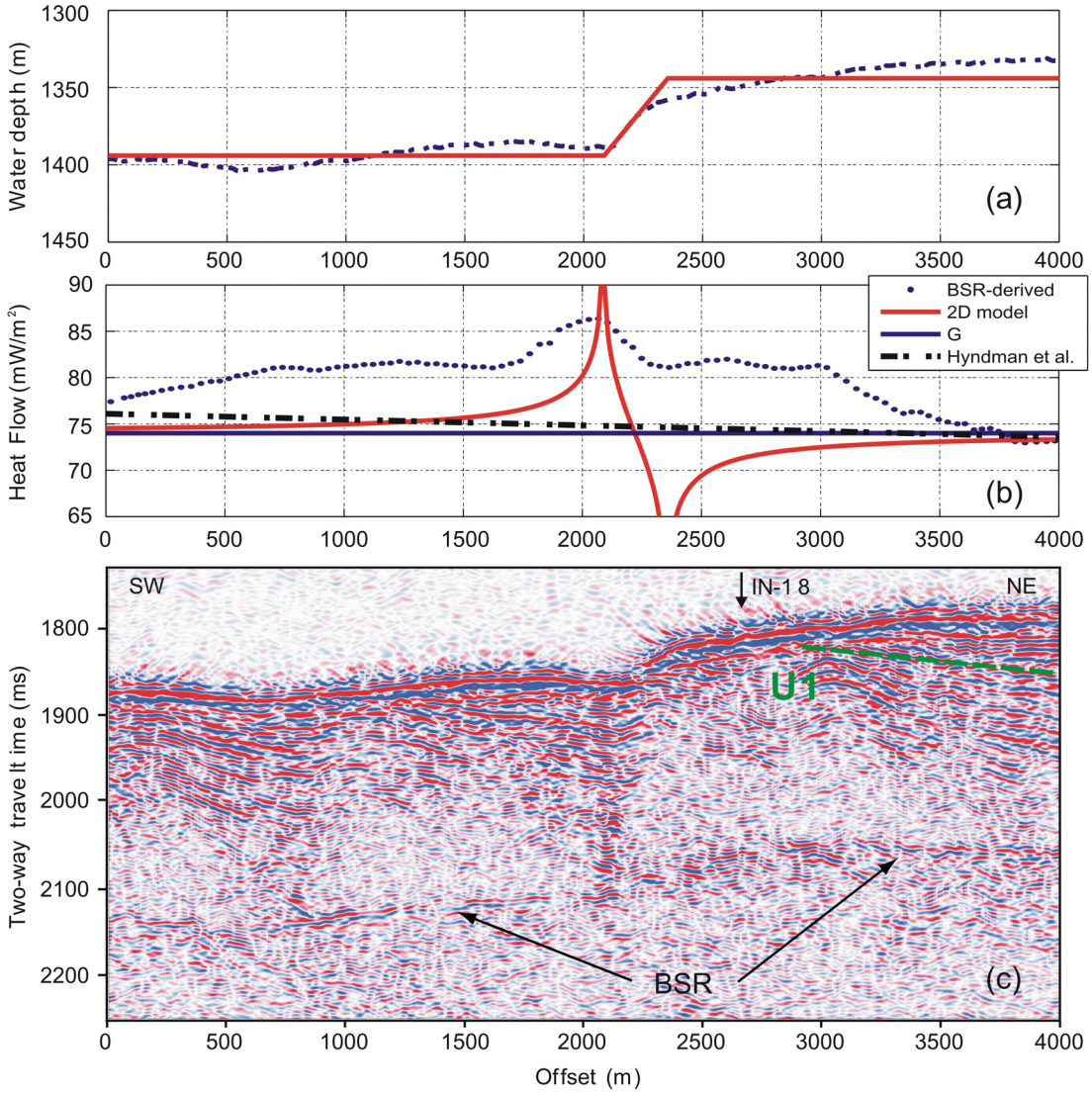

Figure 5.5 Local heat flow variations and 2D model topographic corrections along 2001 Teledyne survey line SCS-1 just south of the mound. (a) Seafloor topography (dashed blue line) and its 2D plane surface approximation (red line). (b) BSR-derived heat flow observations (blue dots) and 2D model topographic correction (red line) for regional heat flow value G of 74 mW/m^2 (horizontal blue line). The thick dashed black line is the prediction from the large-scale heat flow model of Hyndman et al. (1993). (c) Migrated section of line SCS-1, showing stratified slope sediments with unconformity U1 and the clear BSR. Location of intersection point with COAMS seismic grid IN-18 is indicated by arrow.

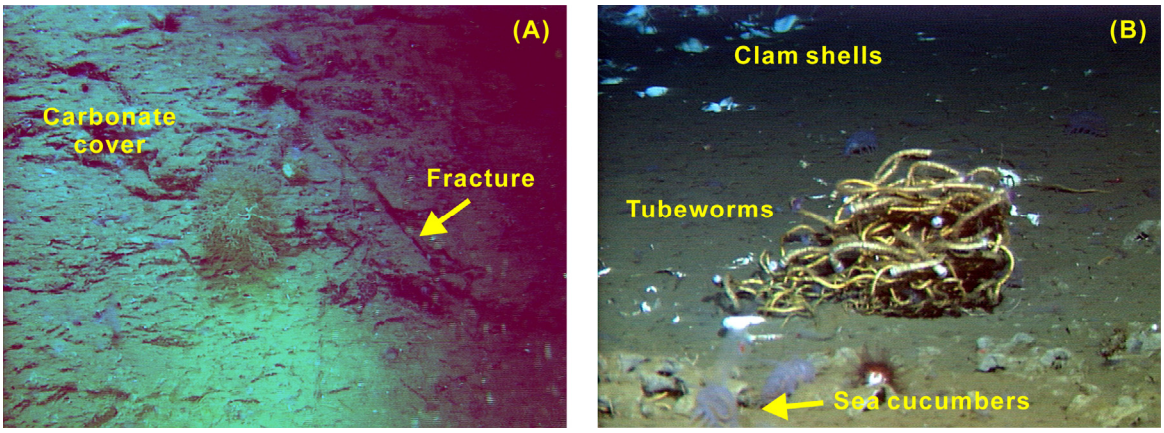

Figure 5.6 Seabed-video images over the carbonate mound structure by the remotely operated submersible (ROPOS) during cruise in May 2001. The locations are labelled in Figure 2.1. (A) Sediment-covered carbonate ridge with seafloor fracture. (B) Fauna on carbonate-covered seafloor: tubeworms (*lamellibrachia barhami*), clam shells (species unknown), and sea cucumbers (*elasiopid holothurian*).

5.2 Seafloor Observations at Cucumber Ridge

In May 2001 (two months before July/August Teledyne survey) the Canadian Scientific Submersible Facility, remotely-operated submersible ROPOS was deployed on the Cucumber Ridge and a series of seabed-video observations were recorded, showing the presence of seafloor carbonate as well as chemosynthetic communities. In the range of the ROPOS survey (Figure 1.10 and Figure 2.1), seabed-video images showed most of the ridge area near the top of the steep seaward slope of the mound to be carbonate-covered. The top surface of the carbonate has linear fractures (Figure 5.6a), possibly the surface expression of a recent fault or fracture zone. Several ROPOS sediment push cores penetrated only 15 cm into the substrate, likely because of the near-seafloor hard carbonate cover. ROPOS also observed several communities of tubeworms (basement-grown from carbonate cover, not seen at other locations like Bullseye vent site or Barkley canyon) and clams (Figure 5.6b), indicating current methane discharge.

During the 2001 Teledyne high-resolution seismic reflection cruise, 3 piston cores (Core 3-5) failed to penetrate the carbonate cover on the crest of the mound (locations labeled in Figure 2.1). CTD (conductivity-temperature-depth) and water column methane measurements were also carried out over the region at almost the same locations as core sites 3 and 5. No high temperature anomalies and no elevated methane concentrations

were found. This indicates either that (1) upward fluid flows at those sites are currently too slow to significantly disturb the sediment temperatures in the mound region, or (2) fluid flows are localized and were missed by the surveys, or are episodic with little present flow. If the latter explanation for the lack of water column anomalies is correct, the flow episodes still must be sufficiently frequent to maintain the observed biological communities. A recent survey with a narrow beam 12 kHz profiler showed gas plumes in the water near the landward edge of Cucumber Ridge (E. Willoughby, personal communication, 2006; location with "GP" labeled on Figure 5.2 and Figure 5.7) indicating probable strong localized methane expulsion.

5.3 Seismic Observations of Mound Structures

The 2001 Teledyne survey is a high-resolution single channel seismic grid with close line spacing, recording coherent reflectivity down to ~400 m beneath the seafloor. The seismic data provided acoustic images of Cucumber Ridge and of the gas hydrate BSR beneath it. Together with several seismic sections from the 1999 COAMS data set and the 2002 DTAGS2 data set (Figure 5.7), the mound structures were resolved seismically along profiles with different directions, frequency ranges and resolution scales.

Figure 5.8 shows the 2001 Teledyne line SCS33 and the 1999 COAMS reference line XL01, which crossed the mound in the SW-NE direction (Figure 5.7). On the migrated seismic section SCS33 (Figure 5.8a), the central mound appears mostly unstratified and reflections are relatively weak, probably due to (1) deformation during the mound formation or (2) scattering or interference effects associated with the hard and irregular carbonate-covered seafloor, as observed by ROPOS (refer to section 5.2). The mound topography typically traps sediments on its landward (NE) upslope flank, while its seaward side (SW) is well exposed and forms a steep slope that is ~70 m high over a lateral distance of ~500 m. On both the seaward and landward sides of the mound, the stratified slope sediment layers dip landward and the layer thicknesses also increase landward, suggesting regional landward-down tilting. Unconformities are present in the stratified flanks (e.g., U1 and U2, on Figure 5.4c and Figure 5.8), indicating differential

uplift and sedimentation. On SCS42 (Figure 5.4c) and SCS33 (Figure 5.8a), a strip of brightened reflectors extends from the foot of the seaward steep slope to a strong BSR; they terminate landward against the feature F1, which may represent a fault or fracture zone providing a pathway for fluid flow including methane. Note that above F1, near the

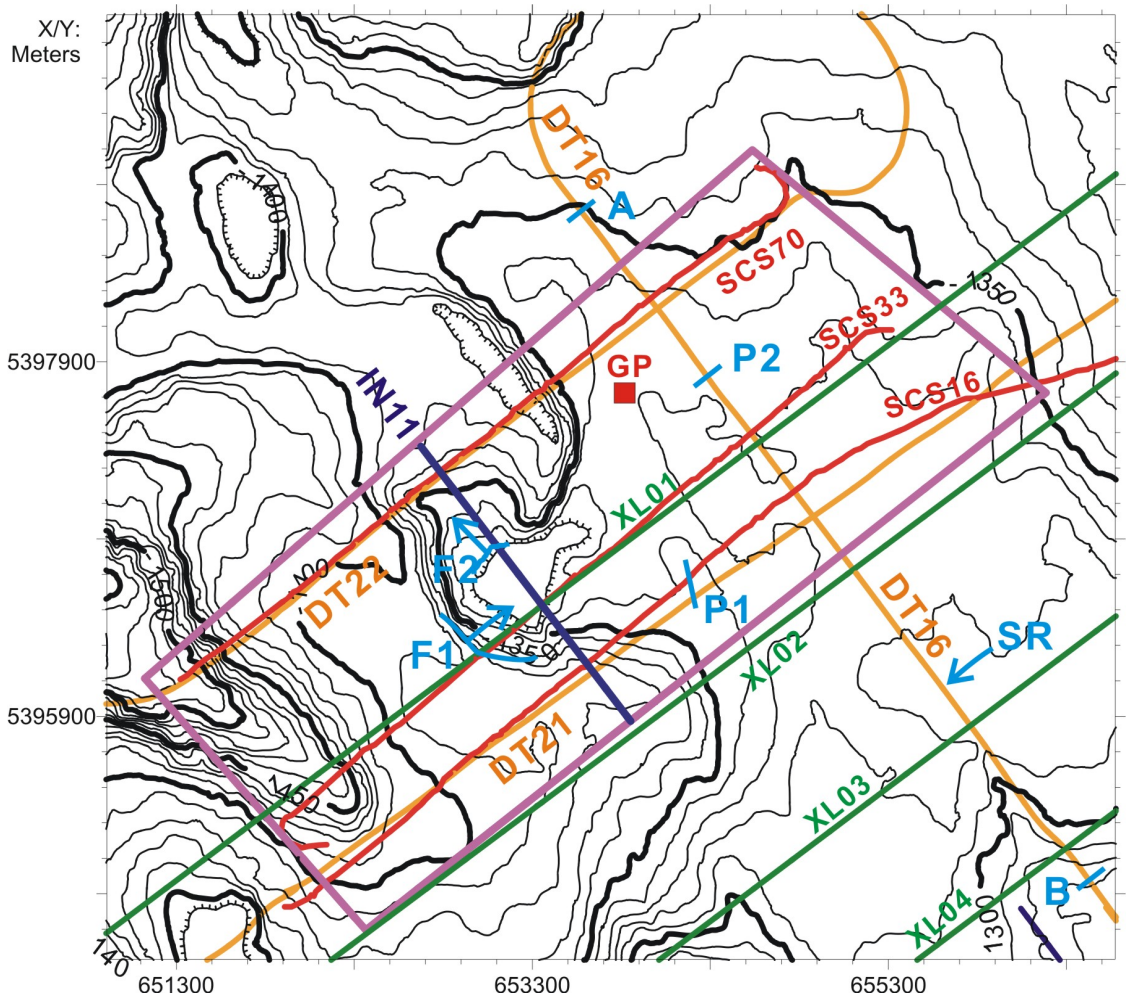

Figure 5.7 Map view of selected seismic lines to show subseafloor structures across Cucumber Ridge, including (1) the 2001 Teledyne lines SCS16, SCS33 and SCS70 (red lines); (2) the 2002 DTAGS deep-towed MCS lines DT16 (segment between A and B), DT21 and DT22 (orange lines); (3) the 1999 COAMS MCS lines XL01 (green line), IN11 (purple line) and IN26, which is coincident with DT16. The labels "F1" and "F2" indicate the possible fault/fracture zones on Figure 5.8, Figure 5.9 and Figure 5.10, with arrows indicating dip direction. The labels "P1" and "P2" indicate two possible gas plume locations on Figure 5.11 and Figure 5.12. The solid red square with label "GP" indicates the location of a gas plume observed in the water column, detected by the 12 kHz profiler during 2006 cruise of CCGS vessel John. P. Tully. The label "SR" indicates the location of the small ridge on Figure 5.12.

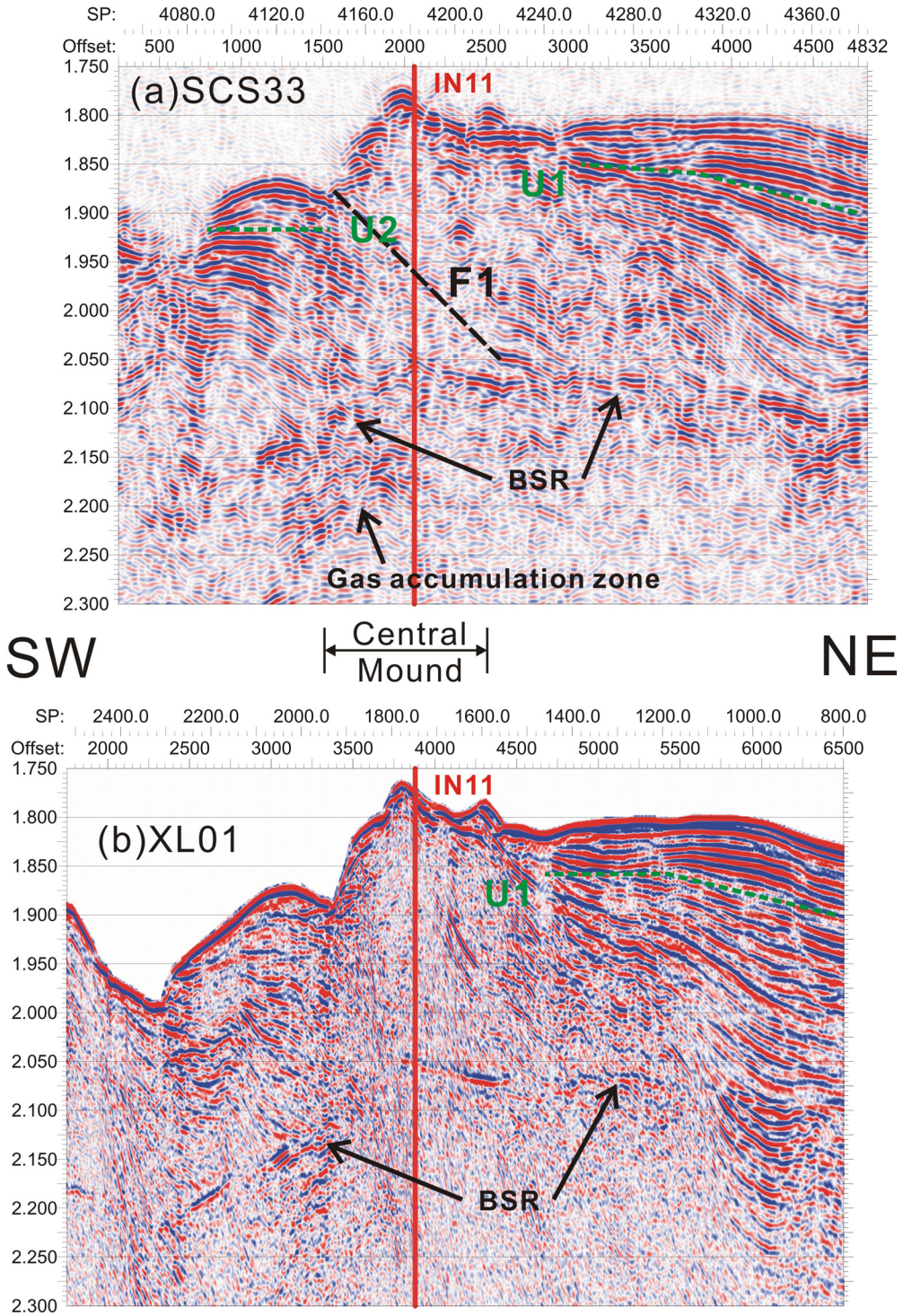

Figure 5.8 Migrated seismic images of nearly-coincident lines of the 2001 Teledyne SCS33 and the 1999 COAMS XL01, which crossed Cucumber Ridge perpendicular to the continental margin in the SW-NE direction (see line locations on Figure 5.7). U1 and U2 are sediment unconformity boundaries. The red vertical line indicates the intersection point with the 1999 COAMS grid IN11 (Figure 5.9), which is in the NW-SE direction (Figure 5.7)

steep seaward edge of the mound, ROPOS observed the carbonate-covered seafloor and possible recent fracturing (location A, Figure 2.1 and Figure 5.6). As well, beneath the BSR near its intersection with F1, a region of strong reflectors may be associated with an underlying gas accumulation zone.

In comparison, the seismic section of 1999 COAMS reference line XL01 (Figure 5.8b), almost coincident with SCS33, shows similar subseafloor structures and clear BSRs but better over-all image quality profiting from the multichannel COAMS streamer. Landward of the mound, XL01 shows more clearly the boundary between the blanking region beneath the central mound and deformed sediments. In the SW seaward of the mound, the fracture zone is still apparent; however, sediment layering near seafloor and the gas accumulation zone below the BSR are more poorly resolved for some unknown reason.

The 1999 COAMS inlines provide complementary seismic observations of mound structures from the direction perpendicular to the 2001 Teledyne grid. The north segment of inline IN11 shows seismic structures of the central mound in NW-SE direction (Figure 5.9). Sediment layering is evident at only shallow depths below the seafloor. A strong reflector R1 is present at about 20-30 ms below the seafloor, which has an apparent opposite reflection polarity compared to the seafloor in the 1999 COAMS data (e.g., on Figure 5.7 the seafloor has reflection polarity in color sequence of red-blue while the reflector R1 is blue-red). The BSR is difficult to recognize at the depths expected from intersections with perpendicular lines (e.g., around 2.07 s twt on XL01 and SCS33, Figure 5.8). A few reflectors are present just above the depth of BSR, but most of the region below the mound shows little reflectivity. An apparent large normal fault F2 is associated with a prominent NW-facing seafloor scarp and extends to the depth of BSR. This fault may indicate local extension in the NW-SE direction, consistent with the tectonic compressive stress in SW-NE direction (perpendicular to the continental margin).

At north brink of the mound (Figure 5.7), the 2001 Teledyne line SCS70 and the 2002 DTAGS2 line DT22 provide comparable information of subseafloor structures (Figure 5.10). The image quality of SCS70 is not very good since the north brink of Cucumber Ridge has complex 3D topography (Figure 5.7). In addition to sediment

layering on both seaward and landward sides of central mound as seen on all Teledyne lines, more sediment reflector segments are observed under the central mound on SCS70 (Figure 5.10a) than on lines SCS33 (Figure 5.8a) or SCS42 (Figure 5.4c). This indicates that the sediment deformation, which produces the blanking, is less extreme on the edge of the mound, possibly corresponding to the local stress release due to the normal fault F2 against the reverse fault F1. However, the continuous sediment stratification down to 300-400 mbsf make it hard to recognize the BSR, which is expected to be at a two-way time of about 2.1 s (Figure 5.10a).

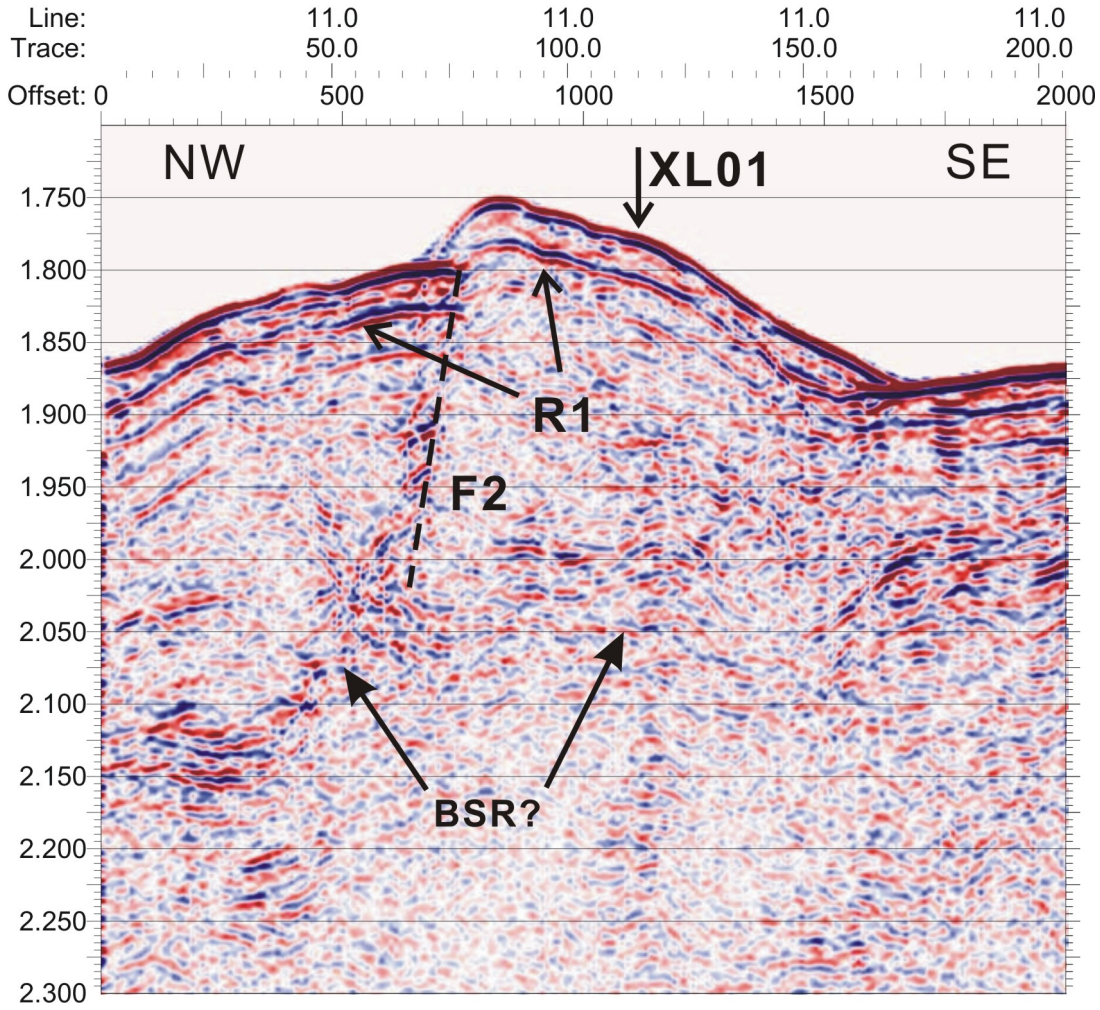

Figure 5.9 Migrated seismic image shows the NW part of the 1999 COAMS inline IN11, which crossed the central mound in the NW-SW direction. Note that the BSR locations are those expected from perpendicular line XL01 and the 2001 Teledyne lines.

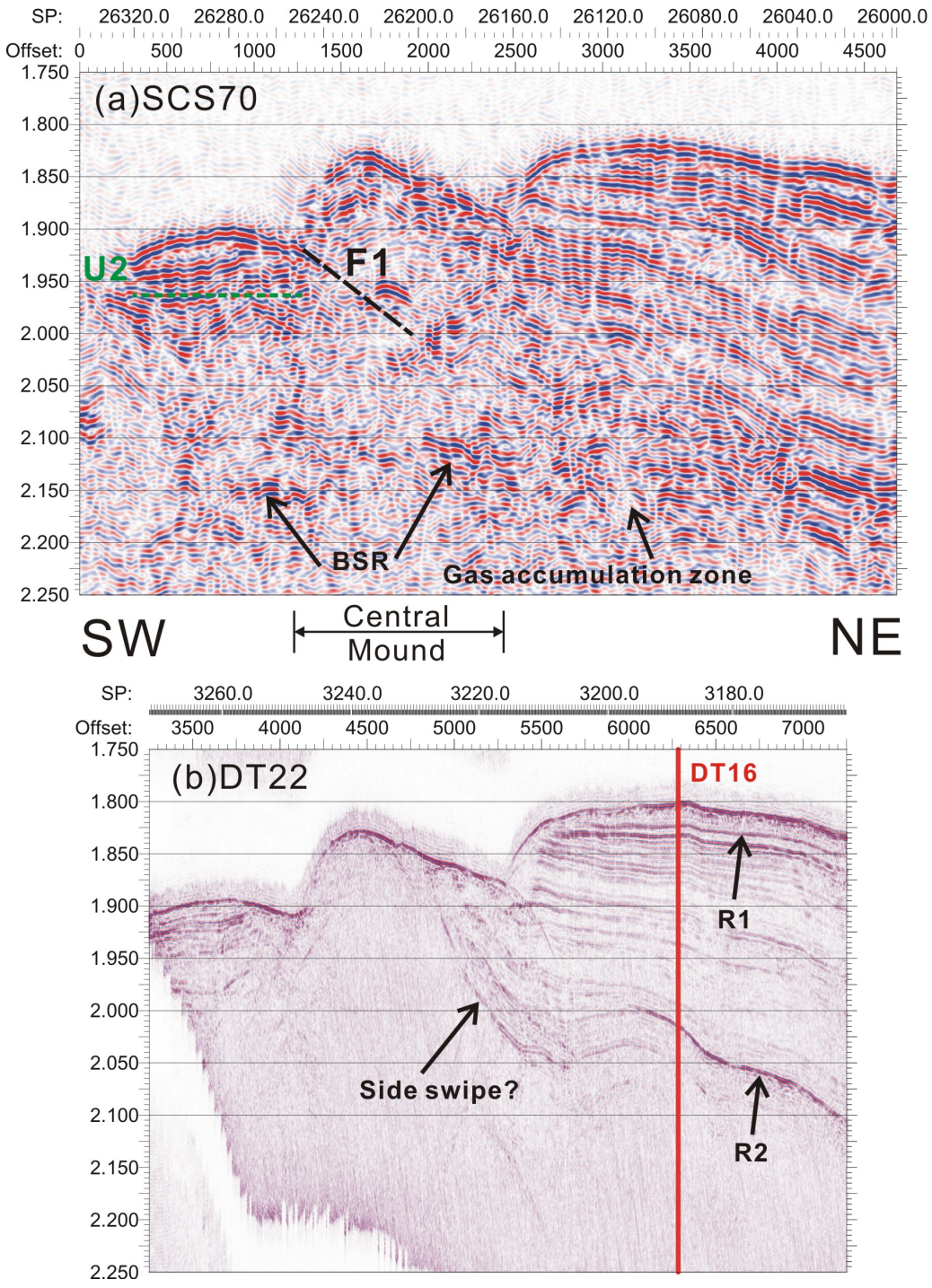

Figure 5.10 Seismic images of the 2001 Teledyne line SCS70 (migrated) and the 2002 DTAGS line DT22, which nearly coincidently crossed the north brink of the mound in the SW-NE direction (Figure 5.7). The red vertical line indicates the intersection with perpendicular lines DT16 and In26. The label "R1" indicates the same shallow strong reflector as seen on the 1999 COAMS inline IN11 (Figure 5.9). The label "R2" indicates another deeper strong reflector, which is also seen on DT16 (Figure 5.12).

Compared to the ringy image of SCS70, the nearly-coincident DTAGS2 line DT22 shows more highly resolved sediment layers between thin reflectors (Figure 5.10b). The DTAGS image also outlines more clearly the structures in the landward slope sediments, for example, the bottom large folded layer at ~2.0 s twt between offset 5500-6500 m. The strong reflector R1 is also present at about 25 ms below the seafloor. Although only occasionally seen on the 1999 COAMS data, this reflector is common on most DTAGS lines, not only in the Cucumber Ridge area but also near Bullseye vent (e.g., Figure 6.26). A previous study by Riedel (2001) suggested that this shallow reflector, with negative impedance-contrast relative to the seafloor, interfered with the seafloor reflection and thus caused frequency dependence of the seafloor reflection coefficient. Based on the velocity analysis at Bullseye vent in this study (details in section 6.3.2.4), the sediment layer above this reflector has high velocity, possibly due to the existence of carbonate.

At the south brink of the central mound, the seismic section for line SCS16 (Figure 5.11a) shows relatively simple subseafloor structures. Similar to SCS33 (Figure 5.8a) and SCS42 (Figure 5.4c), unconformities U1 and U2 occur between the uppermost sediment layers and landward-dipping stratified slope sediment layers. The layer thicknesses of slope sediments beneath the unconformities also increase landward, indicating a growth feature. The BSR is more continuous on SCS16 (Figure 5.11a) than on line SCS33 (Figure 5.8a). For the coincident DTAGS line DT21 (Figure 5.11b), the image shows most of the same subseafloor structures as SCS16, but the sediment layers are much better resolved and the boundaries are defined more clearly. However, no BSR is observed. The DTAGS image also shows greater contrast between the highly deformed regions (HDR) below and less deformed regions (LDR) above (Figure 5.11b), but the base of the less deformed slope sediments is poorly defined due to limited penetration of the DTAGS when compared to the Teledyne signal (Figure 5.11a). The low reflectivity region between offset 3500-4000 m on DT21 or 2500-3000 m on SCS16, marking the zone with high deformation sediments, is probably continuous beneath the slope with the highly deformed Cucumber Ridge to the north. There is a small seafloor depression on both images of DT21 and SCS16 (P1 label, Figure 5.11). There is also a strong

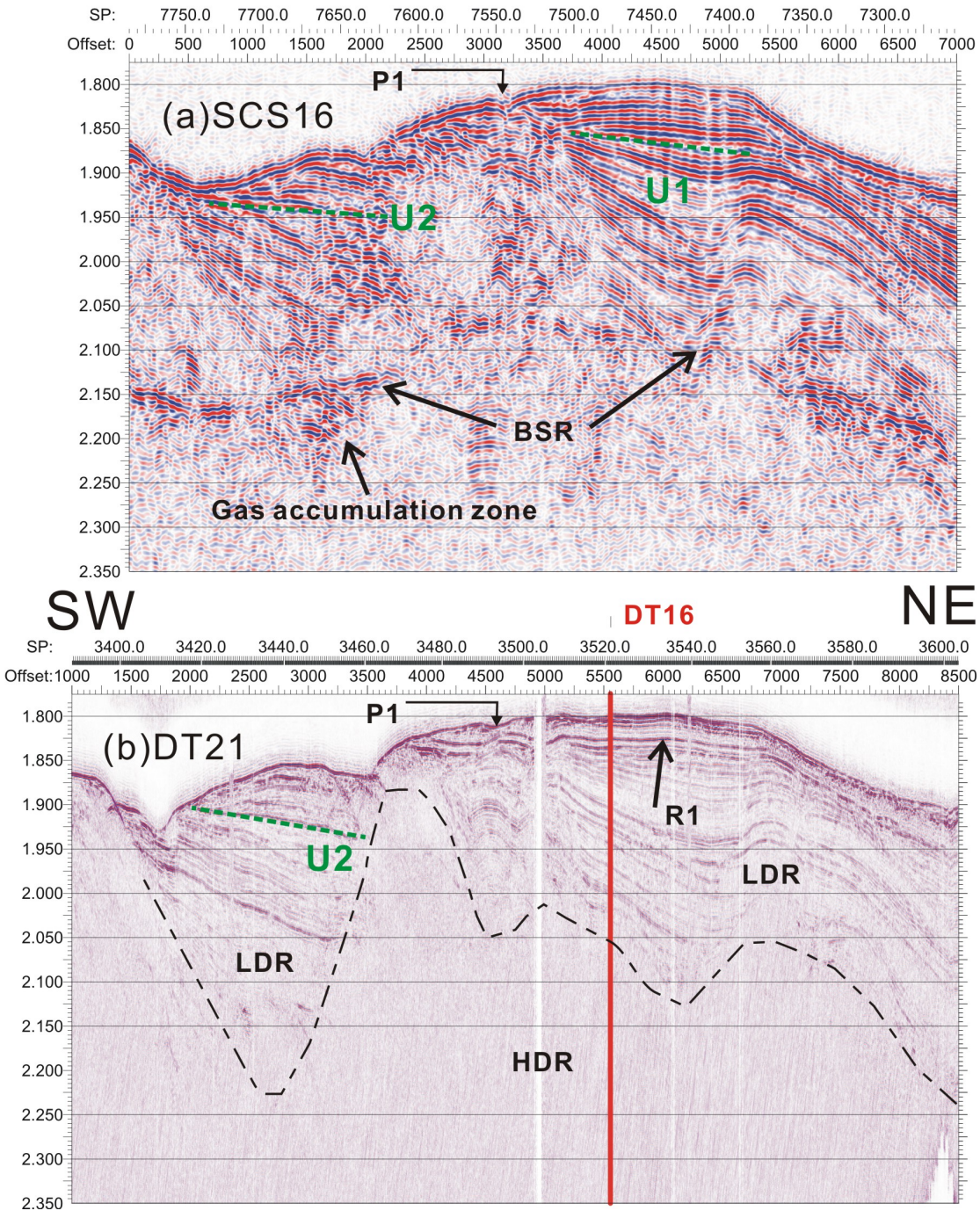

Figure 5.11 Seismic images of the 2001 Teledyne SCS16 (migrated) and the 2002 DTAGS line DT21, which nearly coincidently crossed the south brink of the mound in SW-NE direction (Figure 5.7). The black dashed line separates the sediment regions with lower deformation above (LDR) and higher deformation below (HDR). The label "P1" indicates the location of a possible gas conduit, with an associated small seafloor depression. U1 and U2 are sediment unconformity boundaries. The red vertical line indicates the intersection point with perpendicular DTAGS line DT16 and COAMS line IN26.

reflectivity strip beneath the BSR at almost the same location on Teledyne image (Figure 5.11a). This P1 feature is located in the local high heat flow region derived from BSR depths (Figure 5.7, Figure 5.2), and thus probably presents the seafloor expression of a small fault, providing a vertical conduit for fluid flow to carry gas to the seafloor.

The third DTAGS line across Cucumber Ridge area is a NW-SE segment of DT16 (Figure 5.12b), located in the relatively flat area east of the central mound (Figure 5.7). Compared to the coincident seismic segment from the 1999 COAMS inline IN26 (Figure 5.12a), the DTAGS image better defines the approximate base of less deformed slope sediments. However, the DTAGS image only shows deformed sediment layering ~50 ms twt below the strong reflector R2 to a maximum depth of 2.1 s twt (Figure 5.12b), while the COAMS IN26 shows strong sediment layering to depths greater than 2.15 s twt (Figure 5.12a). The shallow reflector R1 on IN26 is only seen below the small ridge (label "SR, Figure 5.12a) in the SE side, but R1 is much stronger over a much broader region on DT16 (Figure 5.12b). The deeper strong reflector R2 dipping in the SE direction is clearly seen on DT16 just above 2.05 s twt (Figure 5.12b); a series of similar strong reflectors occur at shallower depths on IN26 (Figure 5.12a). Since this abnormal reflector is dipping in the NE direction as seen at the same depth on the perpendicular line DT22 (Figure 5.10b), the true regional dip for this reflector is approximately in the east direction. This reflector probably indicates an impermeable cover trapping gas locally. On COAMS IN26 (Figure 5.12a) an adjacent seismic blanking zone is present just to the SW of the location of R2, vertically extending from the seafloor with an obvious manifestation P2 down to depths below the BSR. This seafloor manifestation P2 is also seen at the almost same location on DT16 (Figure 5.12b), and is only ~400 m east of the location of an identified gas plume (label "GP", Figure 5.7), where massive hydrate-coated methane bubbles were injected into water column and observed by a 12 kHz profiler (E. Willoughby, personal communication, 2006). Thus this vertical seismic blanking zone may indicate a vertical channel for gas to escape from this small reservoir and may produce another gas plume, which is waiting to be verified.

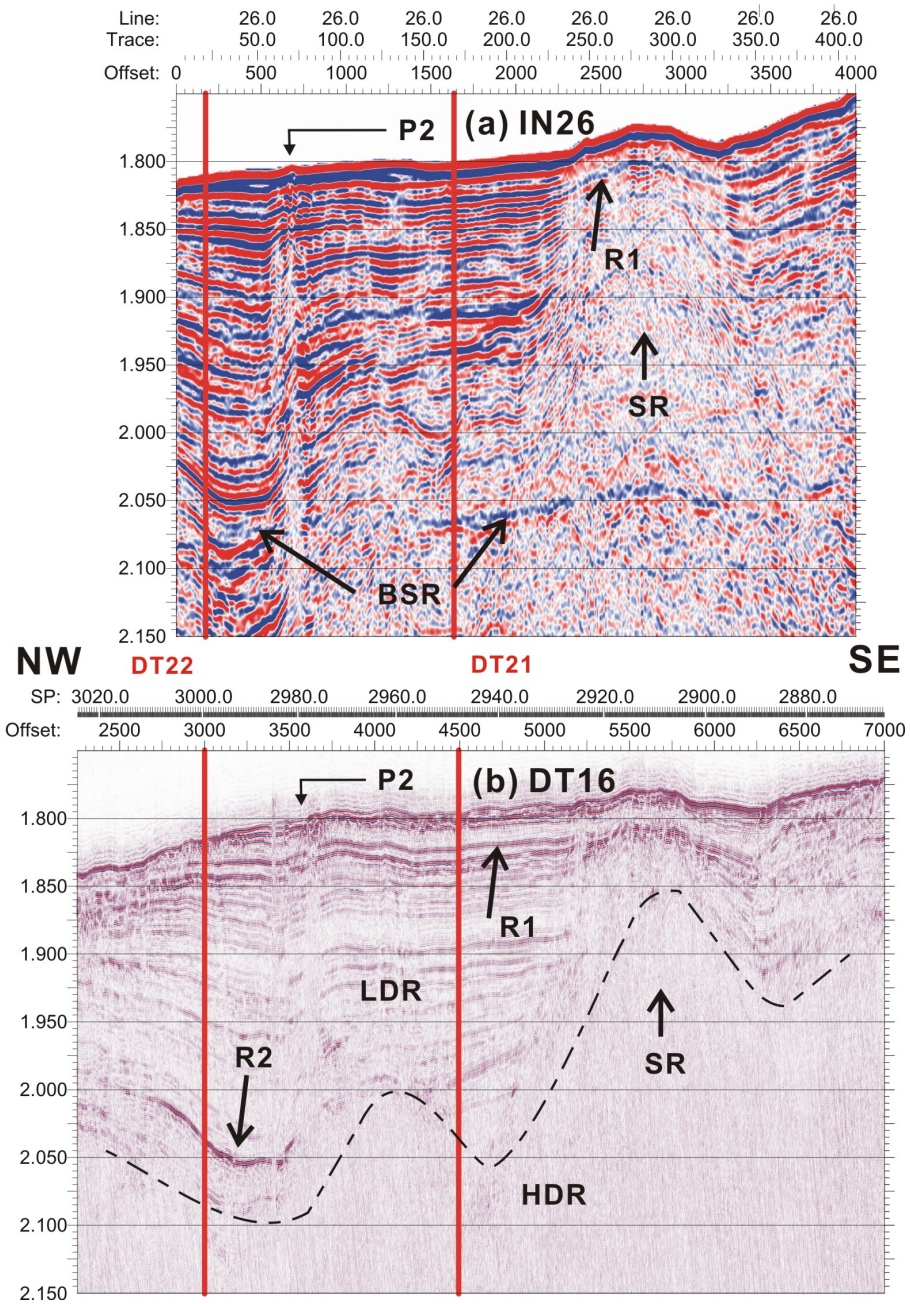

Figure 5.12 NW seismic sections of the 1999 COAMS inline IN26 (migrated) and the 2002 DTAGS line DT16, which crossed the relatively flat area east of Cucumber Ridge (Figure 5.7) and intersected with the two SW-NE DTAGS lines of DT21 and DT22 (indicated by the red vertical lines). The black dashed line separates the sediment regions for lower deformation above (LDR) and higher deformation below (HDR). The label "P2" indicates the location of a seafloor manifestation related with a seismic blanking zone below, probably related with another gas conduit and perhaps with a water-column gas plume. The label "R2" indicates the same strong reflector as on DT22 (Figure 5.10).

Chapter 6

Analysis and Interpretation: Bullseye Vent

As the first direct evidence on the north Cascadia margin for focused fluid/gas flow, the recently discovered vent field is located on an uplifted sediment block near Site 889/890 of ODP Leg 146 (Riedel 2001; Riedel et al., 2002), offshore Vancouver Island. Since 1999 intensive geophysical and geochemical studies have been carried out at the main vent site, which is up to 500 m in diameter, and referred to as the Bullseye vent. High concentration of gas hydrate was recovered at this vent within the upper 2–8 m by piston coring (Riedel, 2001) and at depths from about 5-35 m below the seafloor by IODP U1328 drill logging (Riedel et al., 2006b).

The objectives of this thesis for Bullseye vent are to obtain high resolution structural details, including the extent of associated gas hydrate and underlying gas, and to determine the associated seismic velocities. Part of these objectives are to compare the seismic results with drillhole data from the new IODP Site U1328, to determine if the seismic information can help to extend models of structure, velocity and gas hydrate concentration into the region surrounding the drillhole.

6.1 Seismic Observations at Bullseye Vent

There are two data sets used in the study: the Teledyne 2000 single channel 3-D grid (light blue box, Figure 6.1) and the 2002 DTAGS2 deep-towed multichannel lines (deep blue and red lines, Figure 6.1).

Within Bullseye vent (yellow area on Figure 6.1; also on Figure 4.38 and Figure 4.39) the hydrate cap is an eye-catching feature on seismic images (e.g., Figure 6.2). The hydrate cap was first identified during the cruise in July 2000, from both physical evidence of piston cores and from later-processed Teledyne SCS images. The piston cores recovered massive hydrate at depths of 3-8 m below the seafloor (small patch within the yellow Bullseye vent area on Figure 4.38 and Figure 4.39). Crossline XL75 from the Teledyne 2000 grid shows a shallow reflector in cap shape formed by the

hydrate (Figure 6.2; see Figure 6.3 for location). Figure 6.3 shows the depth map (two-way time below sea surface) of the hydrate cap picked from seismic sections of the Teledyne 2000 pesudo-3D grid, while Figure 6.4 shows the mapped hydrate cap reflectors in a 3D display. As described by Riedel (2001), the depth of the hydrate cap dips away from the center of the vent (Figure 6.2 and Figure 6.3), and corresponds well to the depth of the hydrate recovery at the four piston core sites.

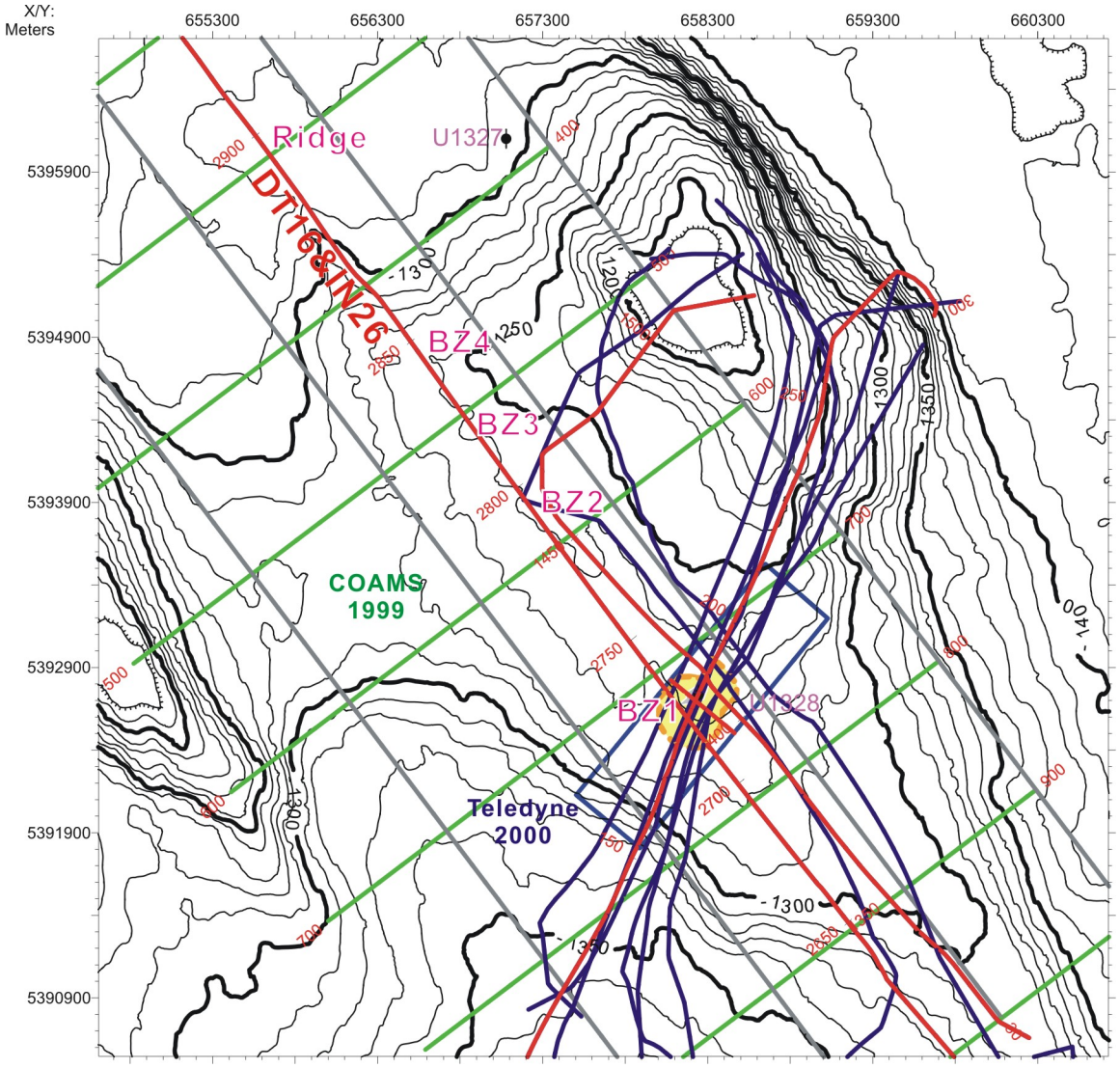

Figure 6.1 Location of 2002 DTAGS2 lines, Teledyne 2000 single channel 3-D grid (blue box) and COAMS 1999 multichannel grid (green lines) around Bullseye vent (yellow area). The locations of four seismically blanking zones are also labeled with BZ1-4 as well as on Figure 6.9 and Figure 6.10. The bathymetry is 10 m contours.

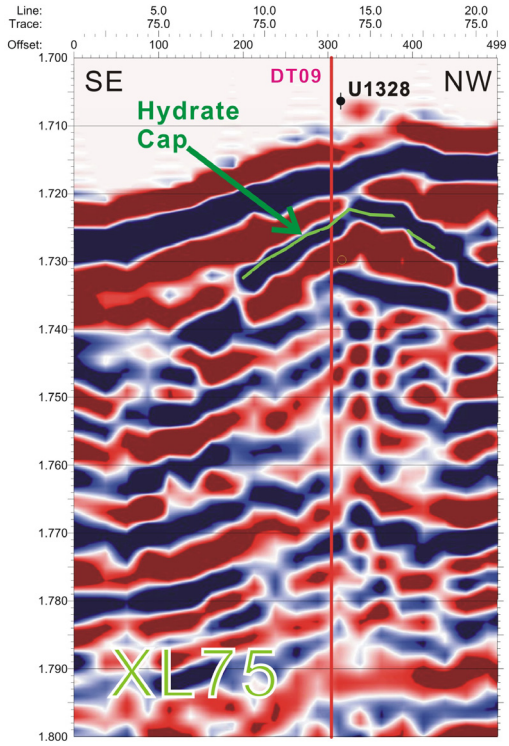

Figure 6.2 SE-NW seismic section showing hydrate cap details from Teledyne 2000 crossline XL75. Note reduced seismic amplitudes obviously below hydrate cap (center of the vent).

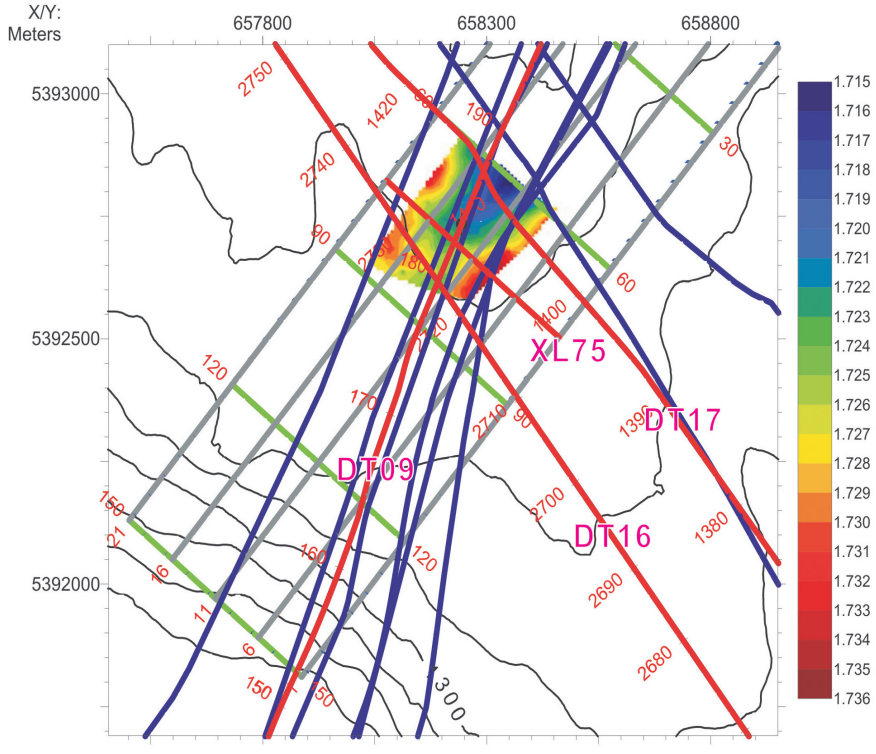

Figure 6.3 Depth map of hydrate cap (two-way time in seconds below sea surface) picked from seismic sections of Teledyne 2000 3-D grid (e.g., crossline XL75 in Figure 6.2).

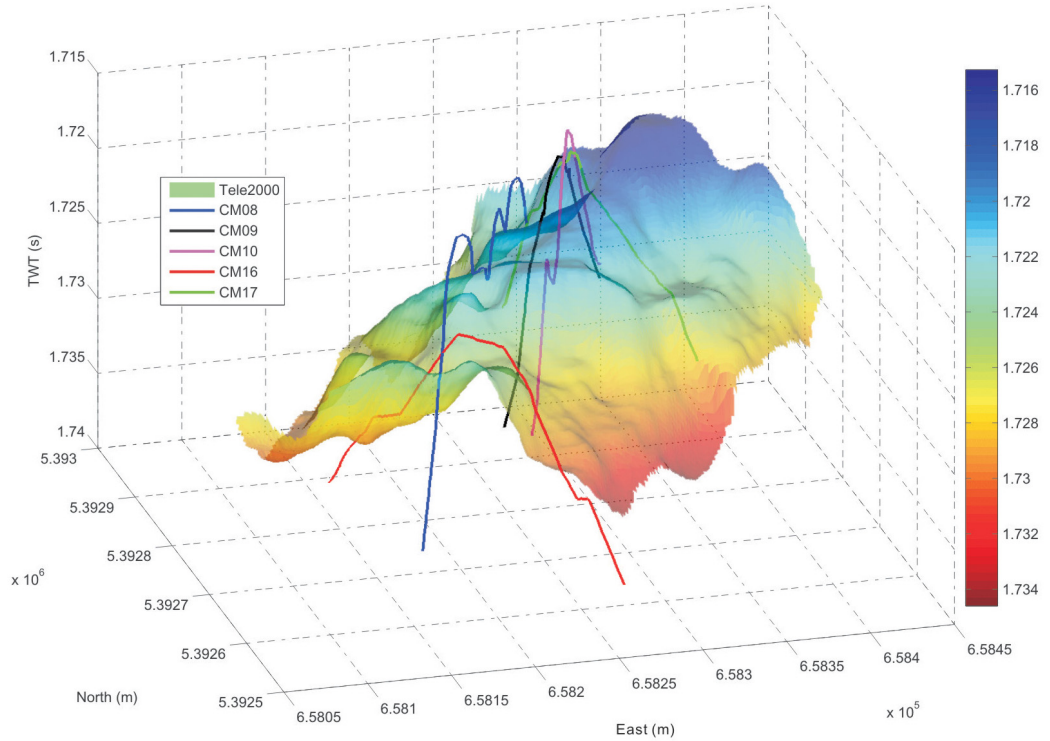

Figure 6.4 3D display of depth map (two-way time in seconds) of the same hydrate cap from Teledyne 2000 grid and from DTAGS lines, indicating the top of the hydrate layer around the center of the Bullseye vent.

The hydrate cap reflector is also seen on the 2002 DTAGS2 lines. DT16 and DT17 are two DTAGS lines across Bullseye vent oriented approximately SE-NW, close to the direction of the Teledyne 2000 crossline XL75 but offset by 50-100 m (locations on Figure 6.3). Also, DTAGS lines DT08, DT09 and DT10 cross the centre of the vent in the SW-NE direction (Figure 6.3). On the images of these DTAGS lines, the top of the hydrate cap is indicated by a yellow curve (e.g., Figure 6.5, Figure 6.6 and Figure 6.7), inferred from individual images and from intersections with other DTAGS lines. For comparison, the hydrate cap locations inferred from the Teledyne 2000 grid are plotted in green. There are obvious depth differences of the hydrate cap between the DTAGS and the Teledyne lines (e.g., 2D images of Figure 6.5, Figure 6.6 and Figure 6.7 and 3D view of Figure 6.4). The maximum depth difference is only 5-6 ms in two-way time (e.g., DT09 on Figure 6.7). Considering the different dominant frequency for Teledyne (~120 Hz) and DTAGS (~400 Hz), this inconsistency may be due to frequency effects associated with attenuation and velocity gradients in the gas hydrate layers.

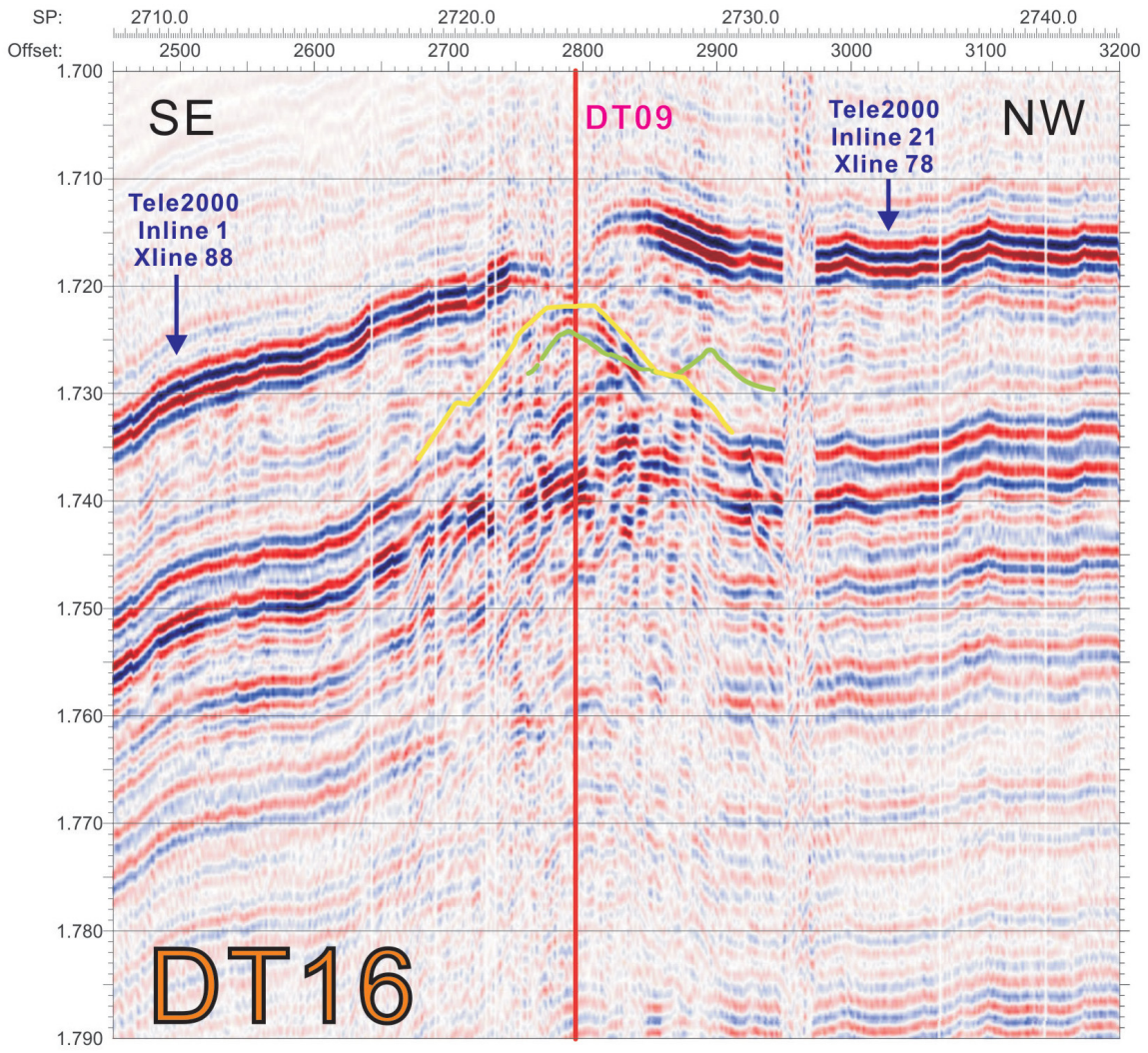

Figure 6.5 SE-NW seismic sections showing hydrate cap details from DT16. The green color curve is the hydrate cap location indicated from the Teledyne 2000 grid, while the yellow one is from the DTAGS line.

Of those DTAGS lines, DT09 is a special one in that the IODP Site U1328 was drilled almost on this line (see "U1328" label on Figure 4.39 for detailed location) within Bullseye vent. DT09 also provides an excellent seismic image of Bullseye vent in the direction perpendicular to Teledyne 2000 crossline grid XL75. The main vent is indicated by the seismic blanking zone between DT16 and XL75 (Figure 6.7). This blanking zone disrupts the second coherent layer, but leaves the seafloor untouched. However, there is a

high reflectivity zone dipping southwest from a seabed depression, where the hydrate cap nearly intersects the seafloor, down to a depth of 20-25 ms TWT (~15-20 mbsf) where it disrupts a prominent reflector in the blanking zone (Figure 6.7). This high reflectivity feature may be a fracture zone that provides an oblique pathway for fluid flow in the main vent of the blanking zone to bring the gas and/or hydrate-coated bubbles to very near the seafloor.

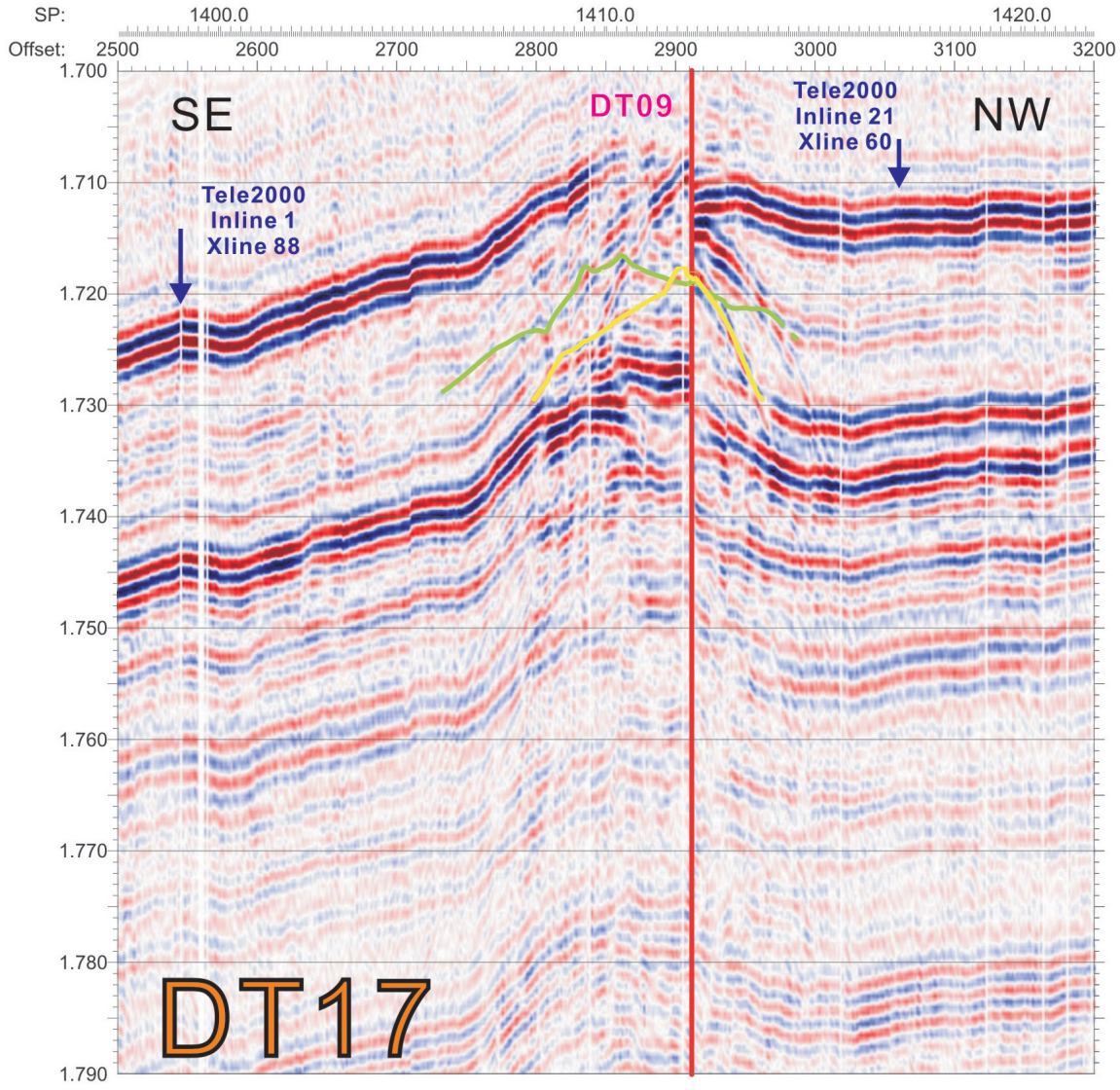

Figure 6.6 SE-NW seismic sections showing hydrate cap details from DT17. The green color curve is the hydrate cap location indicated from the Teledyne 2000 grid, while the yellow one is from the DTAGS line.

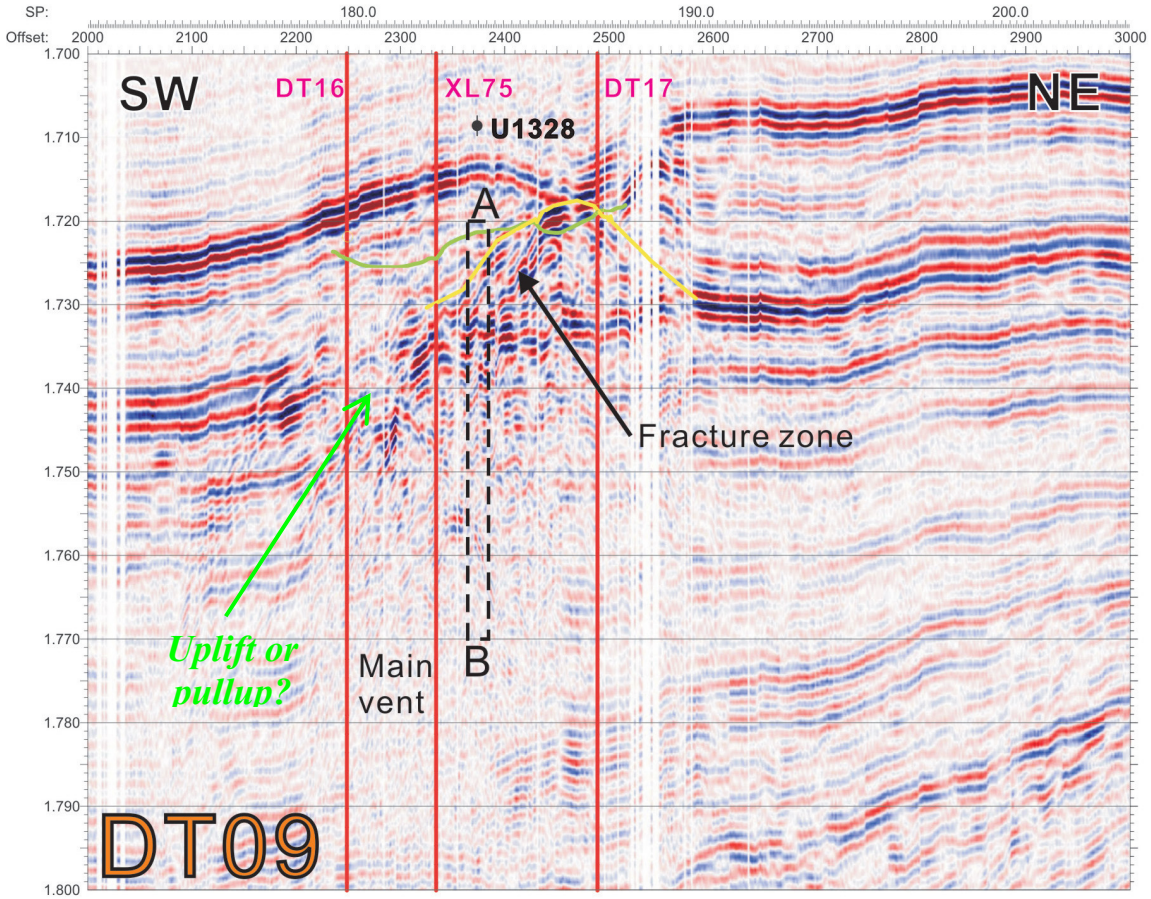

Figure 6.7 SW-NE seismic section from DTAGS2 line DT09. The green color curve is the hydrate cap location indicated from the Teledyne 2000 grid, while the yellow one is from the DTAGS line. The dashed rectangle box indicates a layer with high hydrate concentrations from about 5-35 mbsf revealed by IODP Site 1328 on this line (Figure 6.8). The top of this layer corresponds to the hydrate cap location at A. Maximum hydrate concentrations (~60%) correspond to a high reflectivity fracture zone that projects to the seafloor.

Figure 6.8 shows the summary of the logging data recorded at IODP Site U1328 on the line DT09. In the resistivity and water saturation columns (indicated by blue circles), the very high values between 5-35 mbsf of dashed lines A and B are caused by the shallow region of massive methane hydrate with the upper line likely corresponding to the top of the hydrate cap. This high hydrate concentration section based on in-situ observations is indicated with a narrow dashed box on DTAGS image DT09 and is consistent with the high reflectivity zone of 10-25 m in thickness, extending from the seafloor to a depth of ~25 m (Figure 6.7).

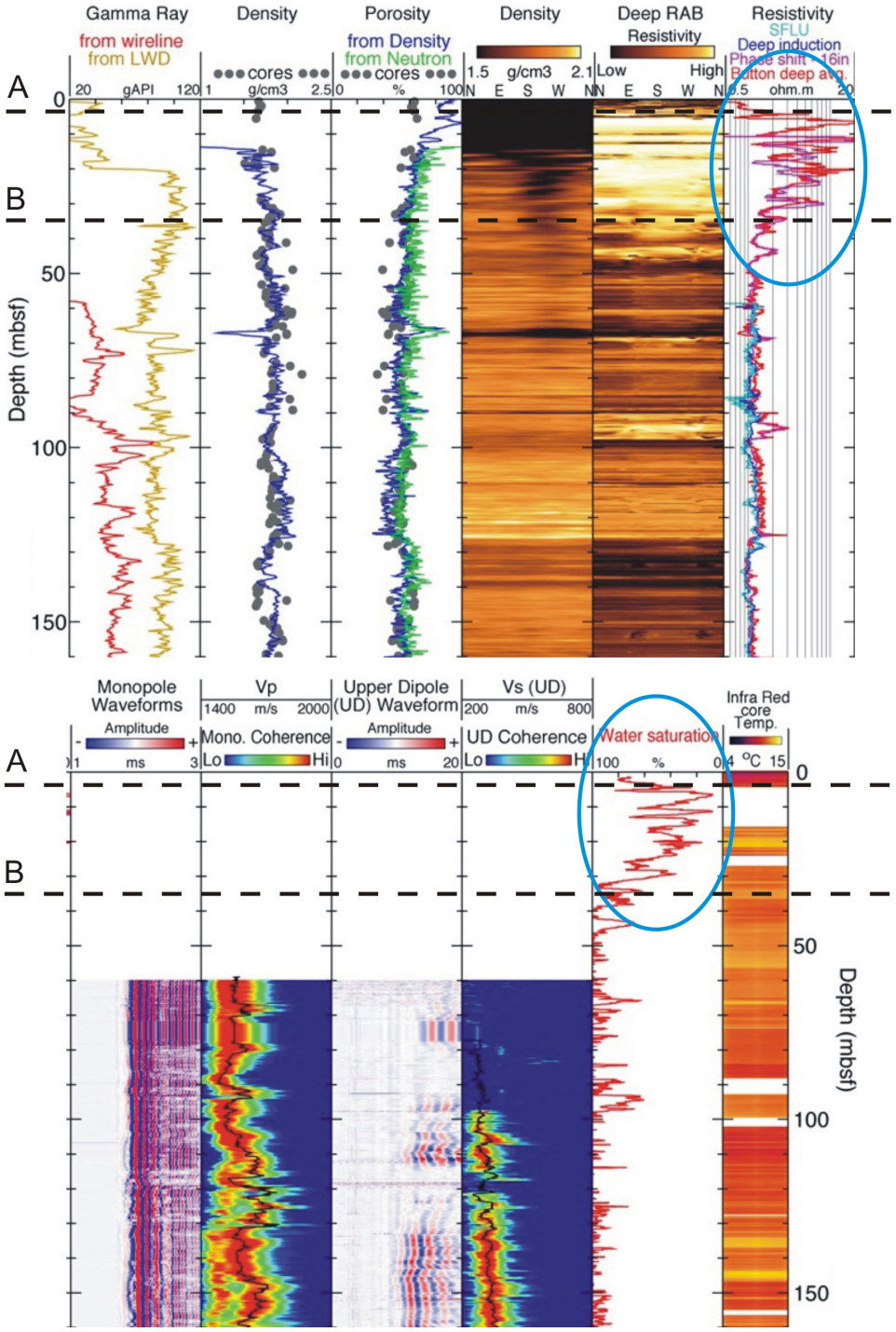

Figure 6.8 Summary of the logging data recorded at Site U1328 in the upper 150 m. In the resistivity column, the Deep Induction and SFLU (Spherically Focused Log Unfiltered) curves were recorded with the wireline tools, the others with LWD. The last column on the right is a compilation of the Infra Red (IR) images recorded on the core liner of the recovered sections to detect gas hydrate. The A and B dashed lines correspond to the top (A) and bottom (B) of the dashed box in Figure 6.7. (After Expedition 311 Scientific Party, 2006)

6.2 Blank Zones on the 2002 DTAGS2 Transit Line DT16

Line DT16, collected during the 2002 DTAGS2 experiment, is a transit line from Bullseye cold vent in the south to Cucumber Ridge in the north. This line initially was designed to repeat the track of the 1999 DTAGS survey, on which 4 blanking zones were identified within a sediment block that was uplifted by about 45 m. The 1999 COAMS grid inline IN26 is coincident with DT16 on the map (Figure 6.1), providing a good comparison of a conventional surface-towed multichannel seismic image with the deep-towed high resolution multichannel seismic image.

The high quality seismic image of DT16 shows very detailed shallow sediment layers (Figure 6.9b), compared to the conventional multichannel seismic image of IN26 (Figure 6.9a). The IN26 image resolves 4 seismic blanking zones as labelled in the slope sediments, likely representing fluid vent sites or proto-vents, since not all of them extend upwards to the seafloor. However, on the DT16 image, small diffractions were observed at the seafloor for blanking zones BZ2, BZ3 and BZ4, indicating the surface expressions of these vent-like features. The surface expression of the largest blanking zone (BZ1) on DT16 is similar to a pockmark with a depression in the middle (Figure 6.5); however, this line does not cross the blanking zone on a diameter (e.g., Figure 6.2, Figure 6.7). The second coherent interface at about 20 ms twt below seafloor seems an apparent upward barrier for blanking zone 2, indicated by the small prominent high amplitude reflector with a cap shape, but blanking zones 3 and 4 partially cross this layer. The flanks of the blanking zones show small-scale diffractions and an apparent increase in seismic reflectivity in case of blanking zone 3 (Figure 6.9b).

The entire region from BZ2 to just northwest of BZ4 (Figure 6.9b) is a structural high. At the high frequency range of DTAGS2, the amplitude pattern in this region also contrasts with the surrounding area with some reflectors (about 1.8-1.85 s twt) having enhanced amplitude, while the deepest reflector with similar amplitude (~1.95 s twt) between BZ1 and BZ2 is not present beneath the structural high. The entire structural high region may contain greater amounts of hydrate than the surrounding area. Such an interpretation is consistent with the observations from controlled-source EM measurements (Schwalenberg et al., 2005), in which electrical resistivity beneath the

entire BZ2 to BZ4 region is higher than that in the no-hydrate reference area (Figure 6.10).

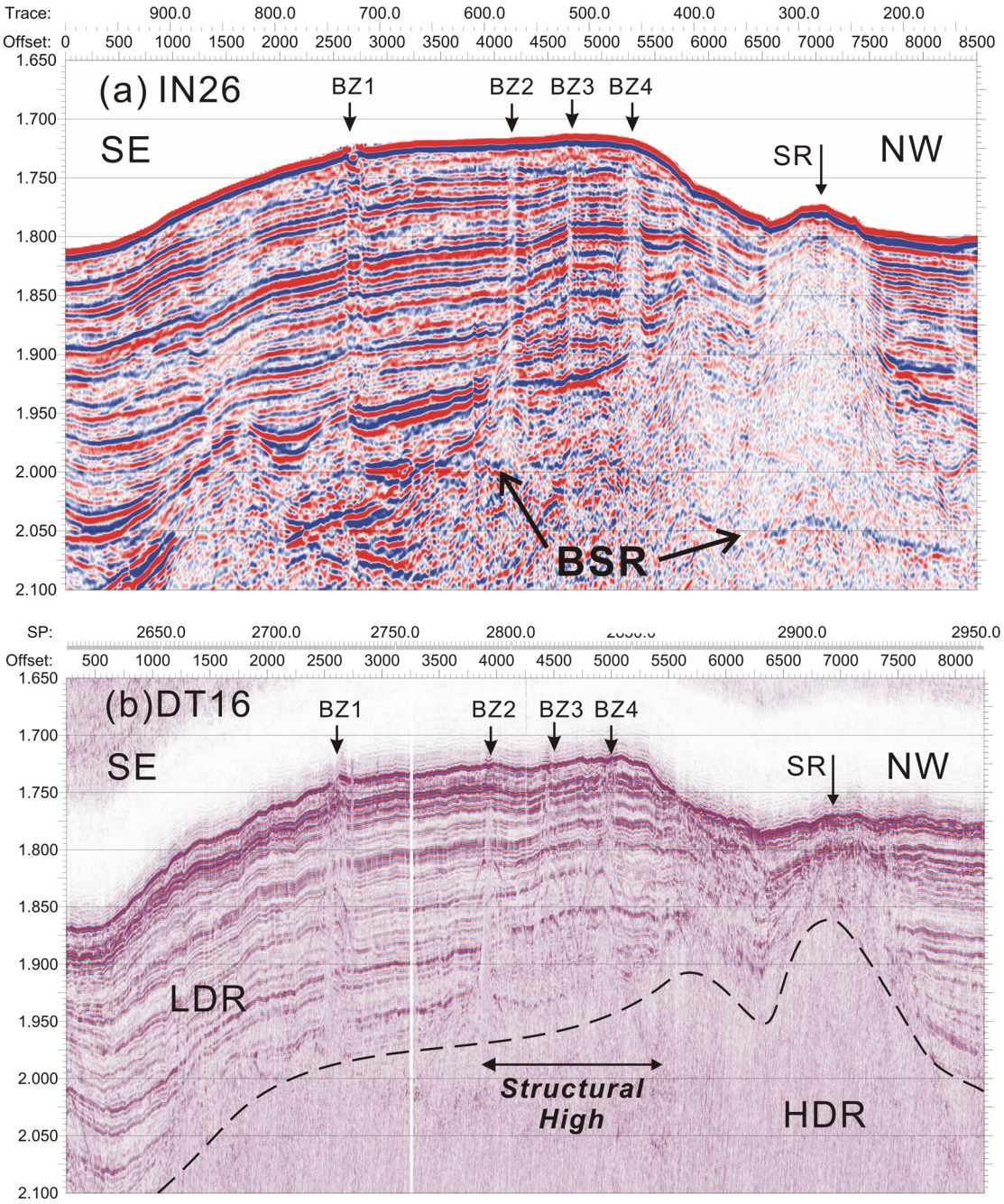

Figure 6.9 (a) Conventional multichannel seismic image of the 1999 COAMS grid inline IN26, providing a good comparison to the coincident DTAGS transit line DT16. (b) Acoustic image (100% coverage) of the 2002 DTAGS2 transit line DT16, showing fine layering of slope sediments with relatively clear boundary for highly and less deformed region (dashed line), four seismic blanking zones BZ1-4 and a small ridge (SR) of accreted sediments, possibly diapiric.

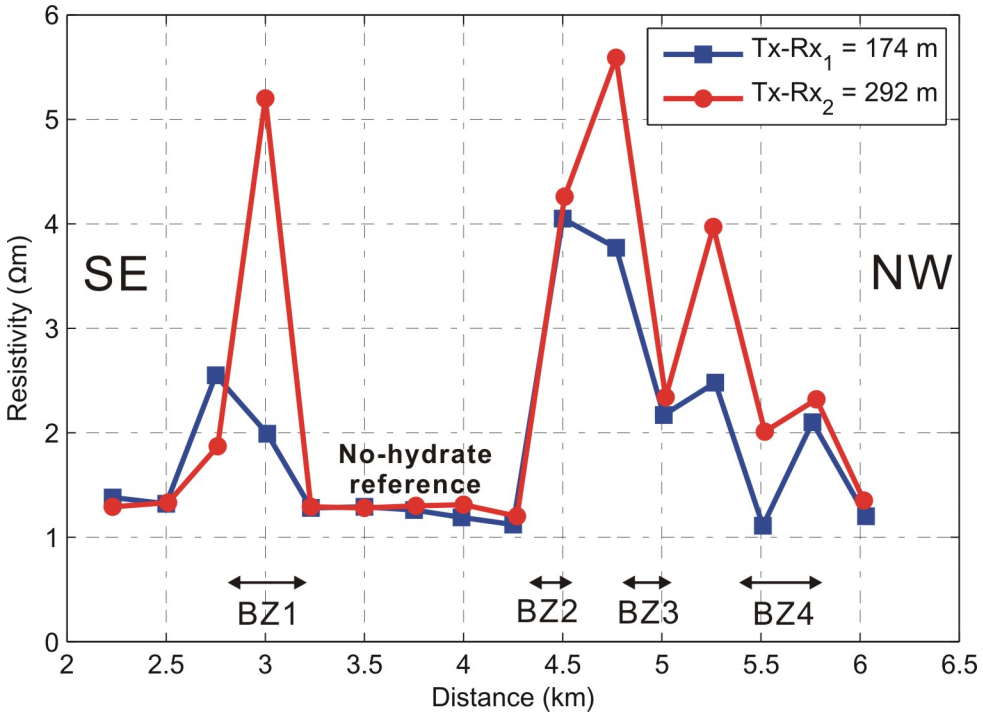

Figure 6.10 CSEM resistivities (background values ~1.1-1.5 Ωm) showing local high-resistivity anomalies >5 Ωm spatially correlated with blank zones 1 to 4. (After Schwalenberg et al., 2005)

In the lower frequency COAMS data of IN26, most of the sedimentary layers can be traced through the blank zones. Especially at blanking zone 1, the uppermost sediment layers, down to ~250 ms twt below the seafloor, are pulled up by about 5-10 ms (Figure 6.9a). Riedel (2001) proposed 3 suggestions for this observation: 1) higher velocities due to large hydrate concentration in the sediments, 2) real deformation of sediment layers, or 3) seafloor topographic effects. Strong reflectivity, just below the depth of the BSR, is observed directly below blanking zone 1 between 2.0 and 2.1 s, indicating a possible gas accumulation zone (Figure 6.9a).

There is also a prominent small ridge at the foot of the slope ~1500 m northwest of the blanking zone BZ4. It is interpreted as the result of accreted sediments based on IN26, since the COAMS image shows widespread seismic blanking below the ridge and the neighboring region (Figure 6.9a) (Riedel, 2001). However, the DTAGS image DT16 shows a clear second coherent interface and a diapiric structure with uplifted sediments on both sides below the ridge. Therefore it is confirmed that this ridge is composed of highly-deformed sediments, and not gas-charged or hydrate-filled sediments.

During the 1999 COAMS survey, 3.5 kHz data were also collected simultaneously with other seismic data. Due to severe weather conditions, part of the 3.5 kHz data was lost on the main grid line IN26, and thus only blanking zones 1 and 2 were covered (Figure 6.11b). The 3.5 kHz subbottom profiler on the CCGS J. P. Tully gave a high-resolution image of the uppermost 30-40 m of the sediment column, which is compared to the DTAGS data (220-1k Hz) also in high-resolution. Since the 3.5 KHz data were displayed with amplitude envelope without processing, the DTAGS data were converted to amplitude envelope too (Figure 6.11a).

The 3.5 kHz data have a penetration depth of about 60 m around the vent area, much shallower than the DTAGS data. However, in contrast to DTAGS data, blanking zones BZ1 and BZ2 are clearly asymmetric on the 3.5 kHz data: the SE sides widen with depth, whereas the NW flanks appear as sharp vertical boundaries (Figure 6.11b). Riedel (2001) suggested that the asymmetric shape of the blank zones may indicate the tilt of the underlying fault. Blanking zone BZ1 has a distinct surface expression as seen on the DTAGS and 3.5 kHz data. On the DTAGS data, blanking zone BZ2 seems to extend no shallower than the strong reflectors at ~20 ms twt below seafloor, which indicates that the interface is an apparent barrier for upward migrating fluids at this blanking zone. However, the 3.5 kHz data show upward doming above the equivalent strong reflector and a small topographic mound (less than 2 m in height). There is a weak indication of blanking above the reflector as well. That is, the interface is a barrier to most fluid flow, but it appears to have some permeability.

6.3 Velocity Analysis across Bullseye Vent

One of objectives of the 2002 DTAGS2 survey was to investigate the properties of gas hydrate and associated BSRs. The solid ice-like form of gas hydrate may result in high interval velocities >2000 m/s, depending upon the fraction of pore space that they occupy. In contrast, non-hydrated sediments at these depths have velocities of ~1600 m/s. Since DTAGS data have much higher frequency wavelet than conventional seismic data, they in theory can provide fine-scale velocity information for thin sediment layers containing gas hydrate.

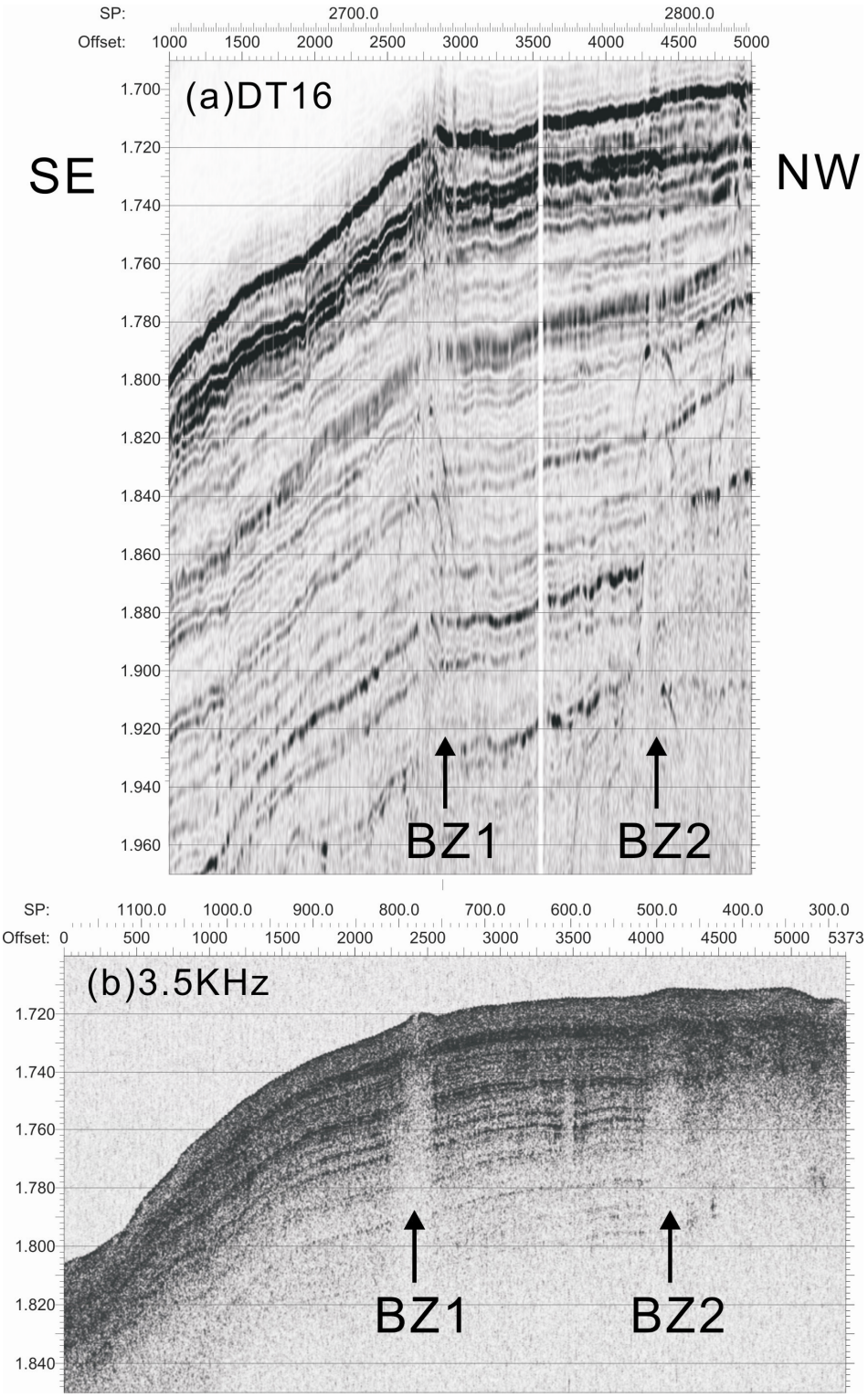

Figure 6.11 (a) Part of 2002 DTAGS2 line DT16 showing blanking zones 1 and 2 in amplitude envelope. (b) Part of 1999 COAMS inline grid IN26 over blanking zones 1 and 2 recorded on 3.5 kHz subbottom profiler, displayed in amplitude envelope.

6.3.1 Standard Stacking Velocity Analysis

6.3.1.1 CMP Binning, CDP Sorting and Super-CDP Gathering

If the ship speed keeps constant at a nominal speed of 2 knots, the 30 s shot interval will produce ~30 m shot spacing, which is twice the 15 m group spacing of the geophysical array. However, the variable ship speed and the variable array geometry resulted in irregular shot spacing and trace spacing for the whole survey, and this complicated the CMP binning of the DTAGS data.

To apply CMP binning, all traces of a DTAGS survey were assigned RMP locations. As illustrated by Figure 4.26 in section 4.4.2, the horizontal axis ***x*** is defined along the direction of the ship heading, with the 0 coordinate assigned to the source location of the first shot gather of a survey line. As an example, for traces in Shot 110 along line DT09, RMP locations on the axis are easily calculated: from -4.5 m to -39 m spaced by 1.5 m corresponding to the receiver coordinates from -9 m to -78 m with a group interval of 3 m for the acoustic array, and from -46.5 m to -219 m spaced by 7.5 m corresponding to the receiver coordinates from -93 to -438 m with a group interval of 15 m for the geophysical array. If the next shot, Shot 111, has an optimal distance of 30 m ahead of Shot 110, then the source of Shot 111 is at 30 m and the last receiver Channel 48 is at -408 m. Therefore traces in Shot 111 have RMP coordinates from 25.5 m to -9 m for the acoustic array, and from -16.5 m to -189 m for the geophysical array.

Iteratively aligning shot gathers according to their optimal shot spacings will assign each trace an RMP coordinate in the whole survey line. Since the optimal spacing between two adjacent shots is always a multiple of 3 m (stepping interval), all RMP coordinates are multiples of 1.5 m and each RMP location can take several traces within its bin area. Thus the CMP binning process is summarized as below:

1. Select a CMP bin spacing of 7.5 m and a bin size (half width) of 3.75 m since the largest group spacing of the DTAGS array is 15 m.
2. Sort all RMP coordinates of a survey in increasing order and assign the centre of first CMP bin (CMP 1) to the smallest RMP coordinate, i.e., -219 m in the case of Figure 4.26.

3. Calculate other CMP coordinates of bin centre locations starting at CMP 1 with a CMP spacing of 7.5 m.
4. If a trace falls into a CMP bin, i.e., its RMP coordinate lies within the range of 3.75 m from the bin centre, the trace will be assigned to the corresponding CMP number.
5. Write CMP numbers and CMP coordinates into the appropriate trace header positions ('cdp' and 'xcmp', respectively, for the Claritas processing system).

Flow chart in Figure 6.12 summarizes full data flow for standard velocity analysis and CDP-stacked image. To limit the influence of cable correction for velocity analyses, a single reference datum for a CDP/Super-CDP gather is chosen, and no depth shifting to sea surface is needed (compare to the flow chart for imaging purpose in Figure 4.33). The process flow for velocity analysis and CDP-stacked image must use the inverted cable geometry and the calculated CDP/CMP number and coordinates as prior information.

Once the cable geometry and CDP information are merged into the trace header, the DTAGS data can be sorted from shot gathers into CDP gathers with secondary sorting by increasing offset. To do velocity analysis, adjacent CDPs are normally grouped into a super-CDP gather that has increased offset resolution to as many offsets in the CDP gathers as there are in the shot. Since the nominal shot interval is 30 m and the CDP space between two successive geophysical hydrophones are 7.5 m, the 4 adjacent CDPs are grouped to form super-CDP gather for the case of the 2002 DTAGS2 experiment.

6.3.1.2 Time Corrections for Cable Geometry

Similar to the image process, time corrections for cable tilting and source depth variations are applied to shift the sources and receivers within a CDP/Super-CDP gather to a reference datum; however, this datum is a fixed value since the source depth varied by only a small amount over several successive shots. The datum depth is the average value of mean depths of each source-receiver pair.

Once the cable geometry is corrected, the CDP/Super-CDP gather can be treated approximately as a conventional seismic data set and passed to standard seismic analysis.

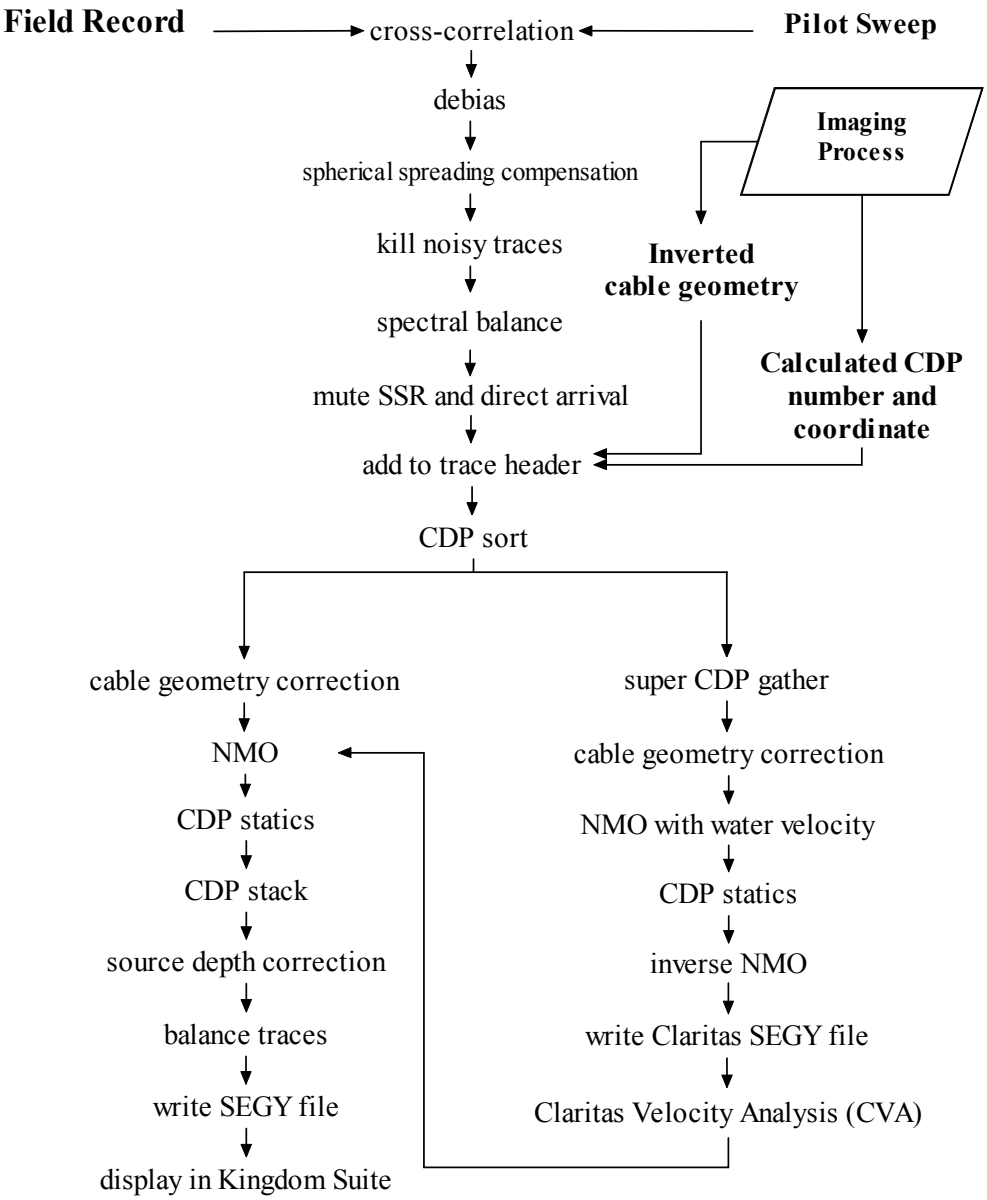

Figure 6.12 Flow chart showing DTAGS data flow for CDP sort, stack image and velocity analysis.

6.3.1.3 Velocity Analysis

Super-CDPs S317 and S337 of DTAGS2 survey line DT09 were selected as targets, since they contained strong reflectors which were nearly horizontal (Figure 6.13 and Figure 6.14). They are located on the SW and NE sides of the prominent seafloor pockmark associated with Bullseye vent (Figure 4.34). The reflection points for the super-CDPs span about 25 m, from 2175 m to 2200 m for S317 and from 2620 m to 2645 m for S337.

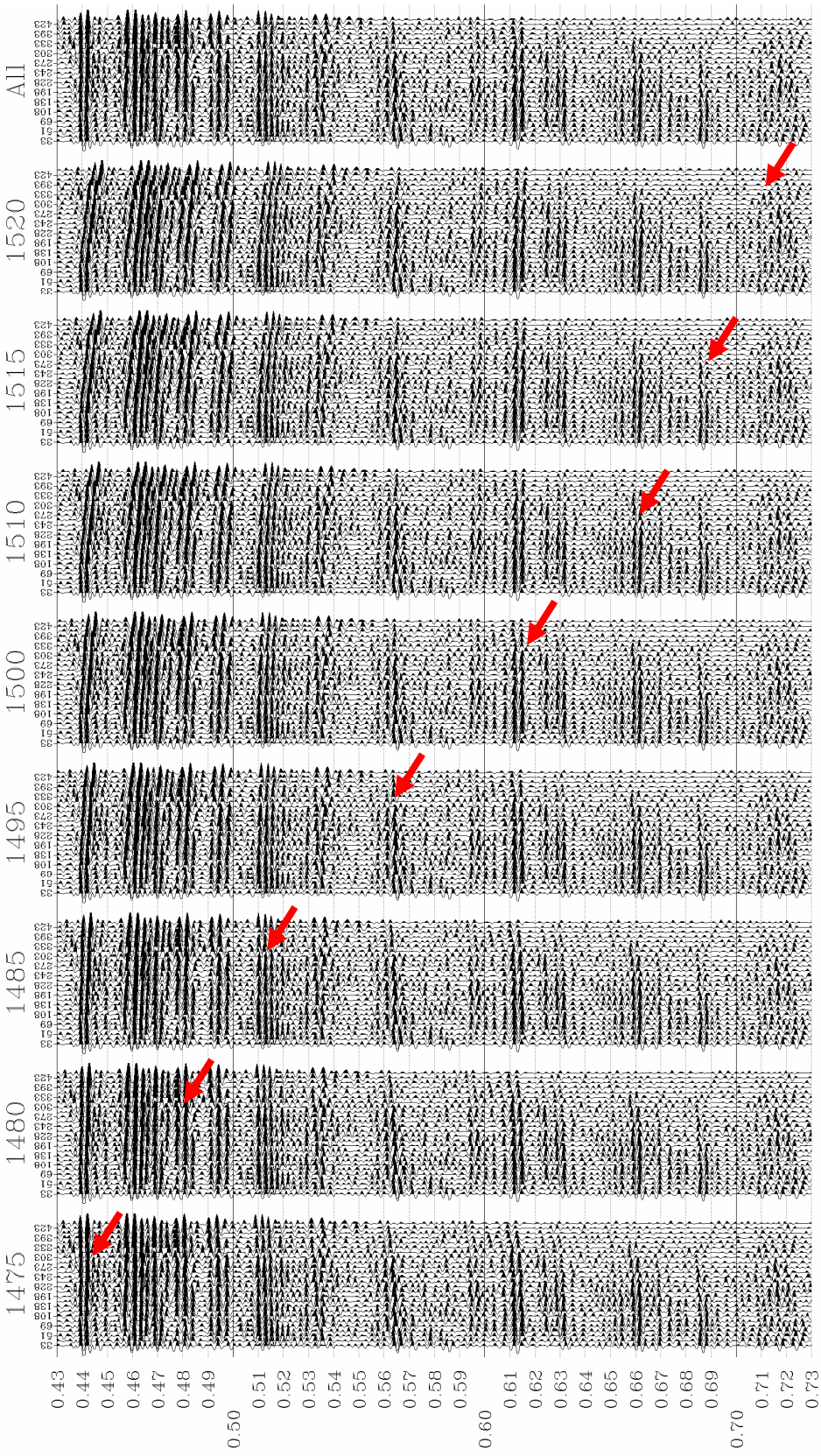

Figure 6.13 Constant velocity gathers (CVG) at super-CDP S317 on DTAGS2 survey line DT09. Top of the panels, the first line is the RMS velocity for NMO correction with specific event indicated by arrow, and the second line is the trace offset in meters. The "All" panel shows the resulting image after normal move out with the determined RMS velocity profile (Figure 6.15).

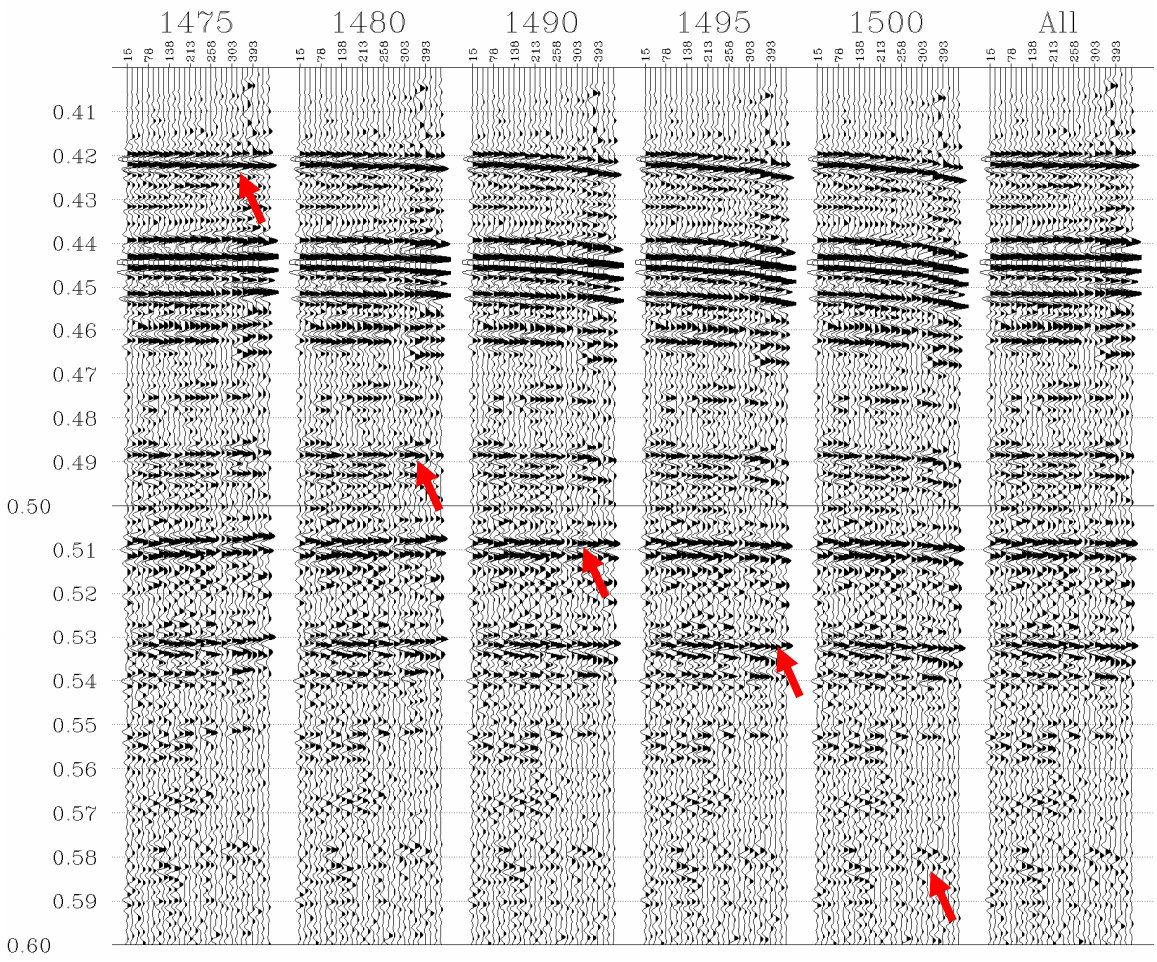

Figure 6.14 Constant velocity gathers (CVG) at super-CDP S377 on DTAGS2 survey line DT09. Top of the panels, the first line is the RMS velocity for NMO correction with specific event indicated by arrow, and the second line is the trace offset in meters. The "All" panel shows the resulting image after normal move out with the determined RMS velocity profile (Figure 6.16).

Panels in Figure 6.13 show pre-stack images of the constant-velocity-gathers for super-CDP S317; for a given stacking or RMS (root-mean-squared) velocity, the flattening results for different reflectors are evaluated. Thus a RMS velocity profile can be determined by picking the time-velocity pair which best flattens the reflector at that time and that velocity. After applying NMO to the data with this RMS velocity profile, the final pre-stack image in the last panel shows all flattened reflectors. From the monotonically increasing RMS velocity profile, the corresponding interval velocities can

be calculated using the Dix equation (Figure 6.15). There are no distinct reflectors around the previously determined BSR depth of ~210 m to resolve velocities of the low-velocity gas layer beneath the BSR.

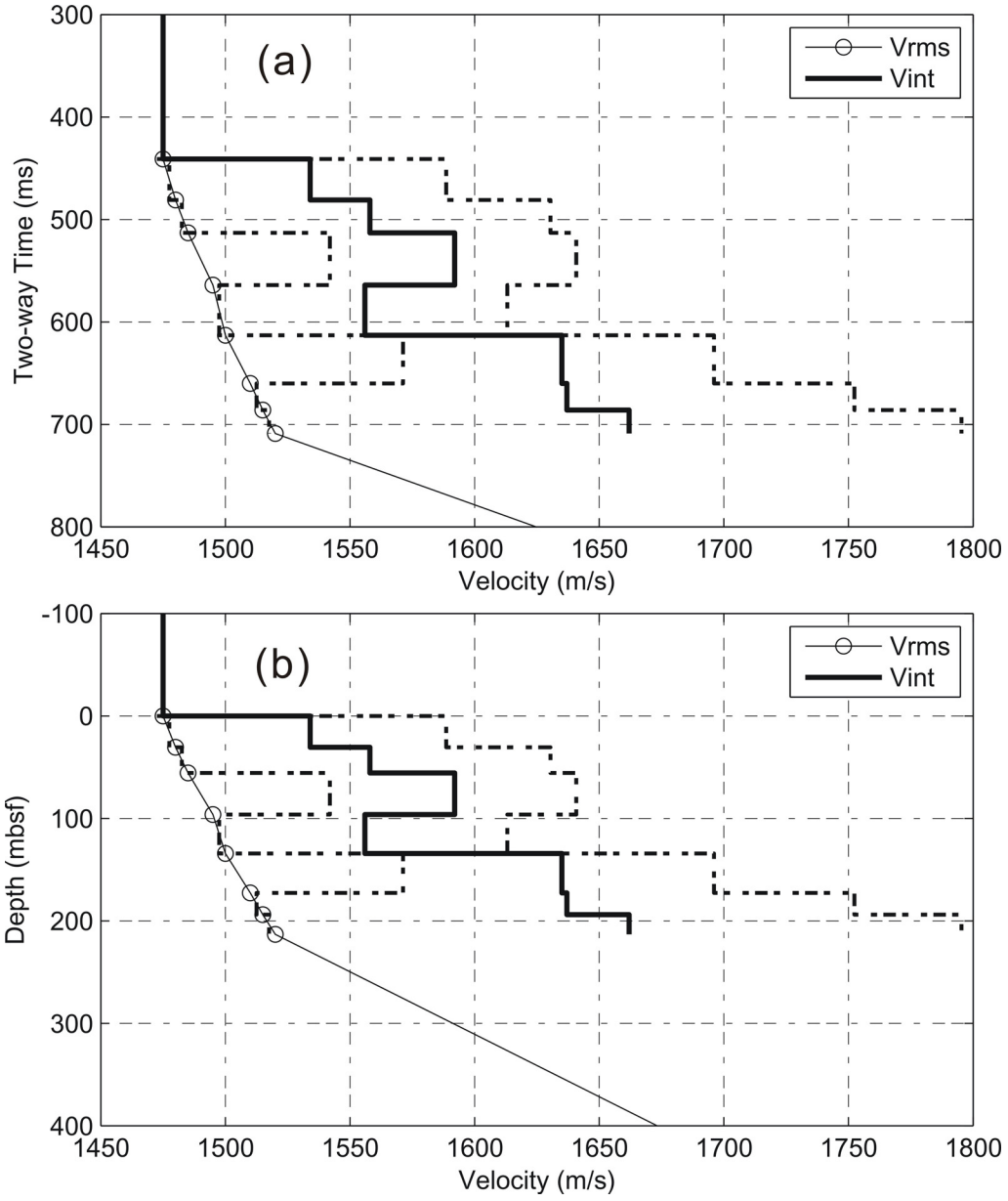

Figure 6.15 Root-mean-squared velocity (Vrms) and corresponding interval velocity (Vint) in two-way travel time (a) and depth below seafloor (b), determined from constant velocity gathers on super-CDP S317 in Figure 6.13. The estimated error bounds for Vint are indicated by dashed lines.

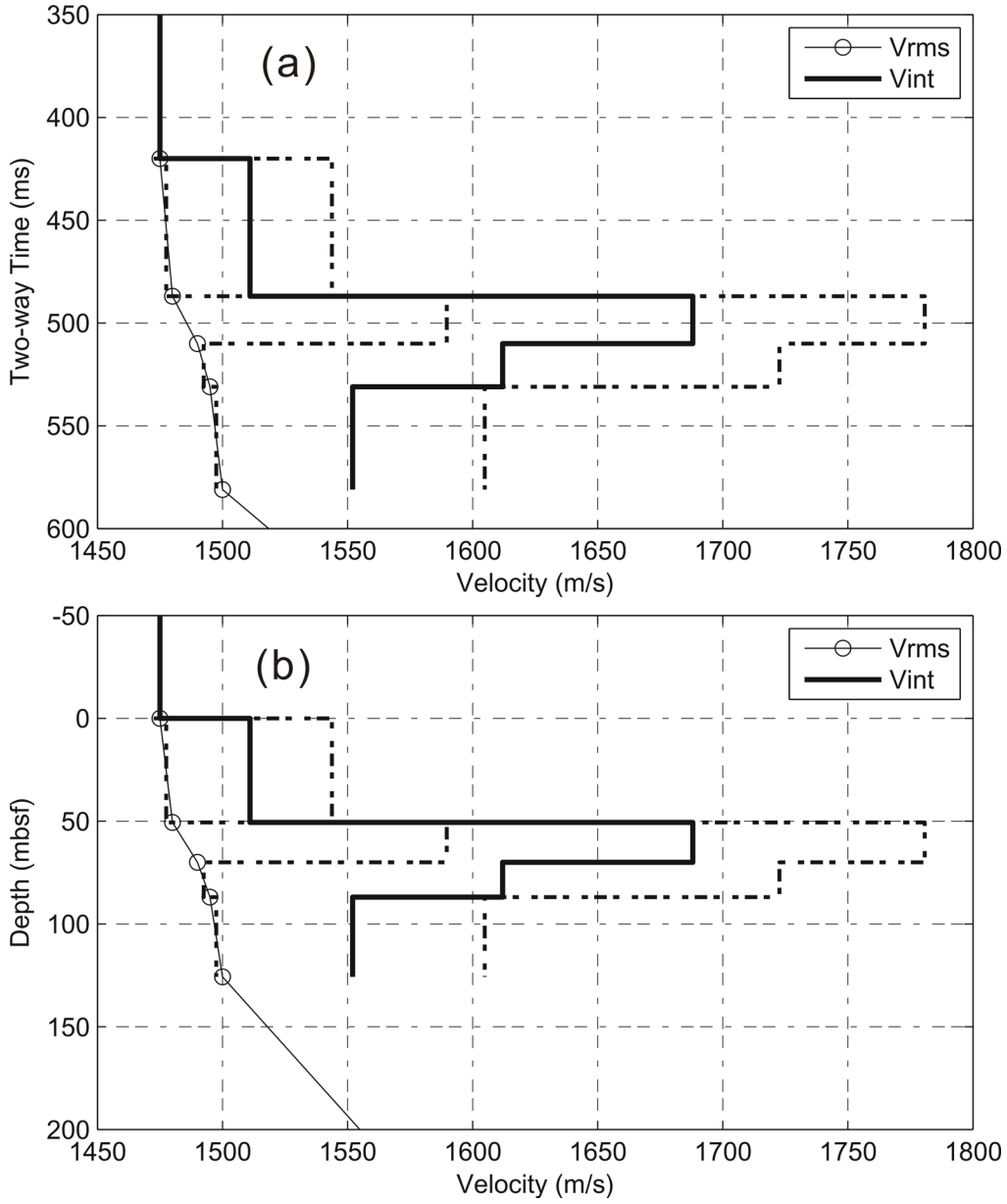

Figure 6.16 Root-mean-squared velocity (Vrms) and corresponding interval velocity (Vint) in two-way travel time (a) and depth below seafloor (b), determined from constant velocity gathers on super-CDP S377 in Figure 6.14. The estimated error bounds for Vint are indicated by dashed lines.

The calculated interval velocity between 50 to 100 mbsf has a value of 1590 m/s, higher than the normal slope sediment velocities at these depths (refers to Equation 3.1, section 4.3.3.3). Velocities are also higher than normal at the depth just above BSR.

Although high velocities are consistent with the presence of hydrate, the error bounds are large and evidence for high velocities is weak.

For super-CDP S377, similar NMO velocity panels were generated and interval velocities were calculated (Figure 6.14 and Figure 6.16). The velocity analysis was limited to the upper 125 m due to weaker reflectors. The calculated velocity between 50 to 90 mbsf is even higher than S317, although the associated errors are very large.

6.3.1.4 Uncertainty Estimation

As the spatial extent of reflection points in super-CDP gathers is ~25 m, the velocity analyses averaged over this distance will provide velocity information at a much finer scale and with less horizontal smearing than the previous DTAGS velocity study of Rowe and Gettrust (1993), which was based on shot gathers, with the reflection points extending over a distance of more than 200 m.

The uncertainties of RMS velocities from the constant velocity gathers were about ±2.5 m/s given the analysis stepping of 5 m/s. The associated uncertainties for interval velocities (dashed lines in Figure 6.15 and Figure 6.16) are significantly larger (±50 m/s to >100 m/s), particularly for thin sediment layers. These uncertainties are related to limitations in the ability to flatten a given reflector. Part of the limitation is due to random picking errors, and part is due to incorrect source/receiver geometry or to errors associated with the datum correction, which is intended to "correct" the array geometry so that all sources and receivers are at the same depth.

Reflector stacking requires that the depth differences between the source and receivers are less than half the wavelength of the signal. Thus, for the high resolution DTAGS with a mid-frequency of 500 Hz, the positions of the source and receivers must be known to within ~1.5 m vertically. The errors in the array geometry correction are difficult to quantity. Thus, a forward simulation was used to estimate the effects of array geometry correction on conventional velocity analysis. Figure 6.17(a) shows the model configuration: the inverted cable geometry of Shot 196 on Line DT09, a 100-m-thick homogeneous sediment layer with velocity of 1550 m/s between the horizontal seafloor and reflector 1, and seawater velocity of 1480 m/s. The travel times for the seafloor

reflection and reflector 1 were calculated using straight raypaths with Snell's law (Figure 6.17b). Using the same water speed and sediment velocity, a time correction was applied using the method in section 6.3.1.2, and the corrected travel times followed hyperbola-like curves. However, the NMO velocity for the time-corrected reflector 1 was determined as ~1500 m/s, corresponding to an interval velocity of ~1570 m/s for layer 1, which was 20 m/s larger than the true value of 1550 m/s.

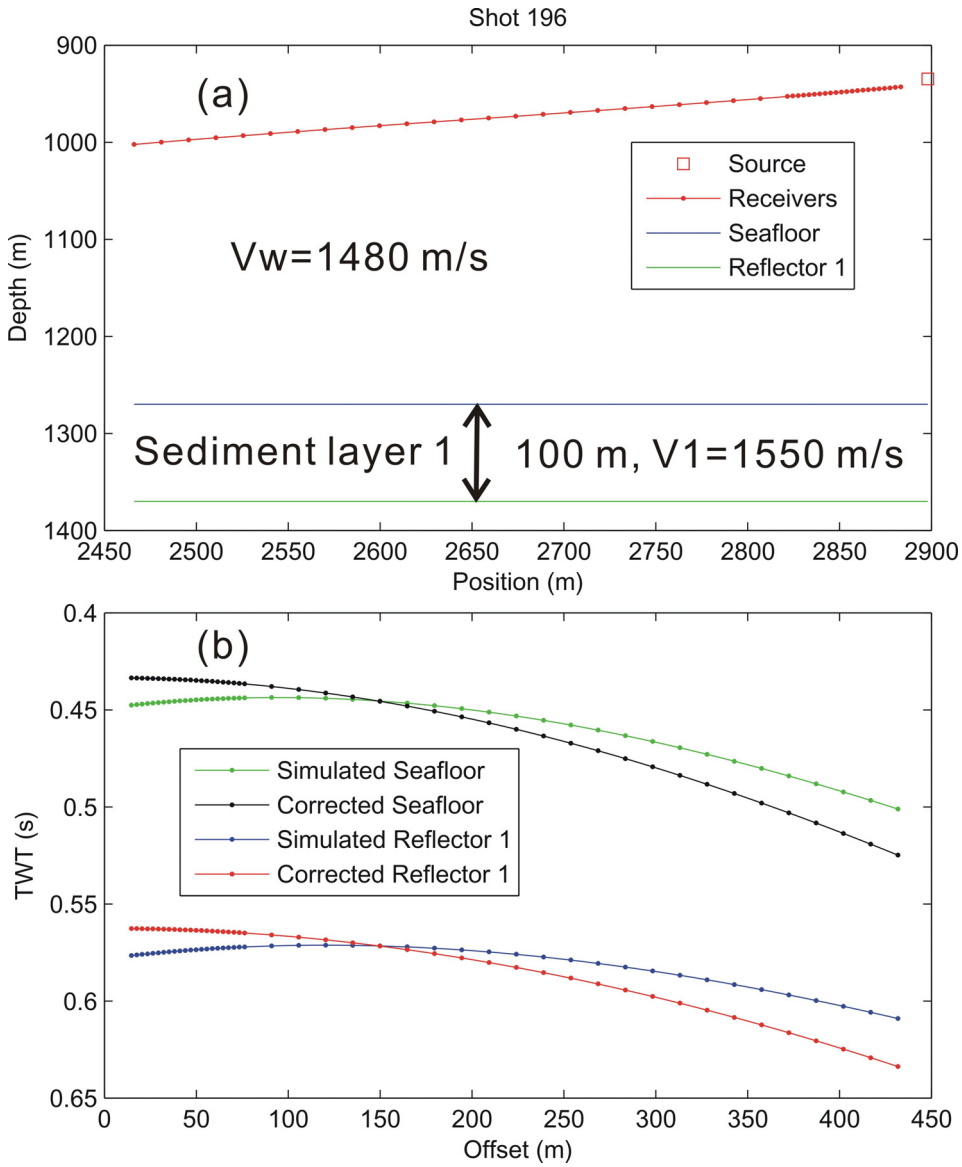

Figure 6.17 The simplest one-layer model simulating travel times for nonlinear cable geometry and associated time corrections for horizontal datum. (a) Illustration of model configuration. (b) Calculated travel times before and after cable geometry correction.

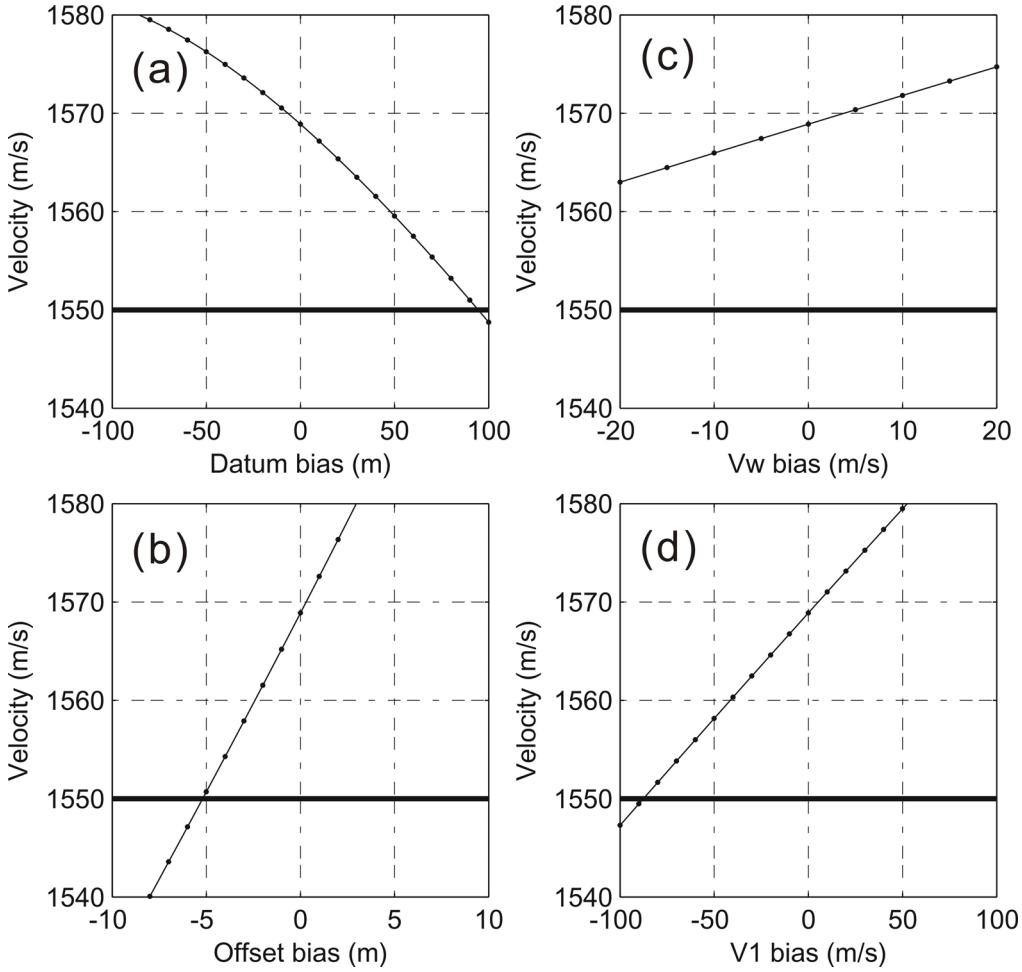

Figure 6.18 Sensitivity test for interval velocity of sediment layer 1 by calculating travel time corrections for varying parameter values: (a) depth bias for selected datum to shift the source and receivers, (b) seawater acoustic speed bias for seafloor depth, (c) uncertainties of horizontal source-receiver offset for inverted cable geometry, and (d) bias of assumed constant sediment velocity to calculate layer 1 thickness. The true model value of 1550 m/s is indicated by the thick line.

The cause of this velocity shift is complex. However, the datum correction calculation is a likely source of error, particularly the assumption of a straight-line path through the sediments (refer to Figure 4.21). A simple sensitivity analysis was applied to examine the relationship between the calculated interval velocity and 4 parameters used in cable geometry correction: datum selection, water speed, inverted horizontal source-receiver offset and assumed sediment velocity. The test calculated interval velocities for

layer 1 by adding a bias value to one parameter in its possible range while keeping other parameters fixed at the same values as used in the forward model. The results are shown in Figure 6.18. The water speed has only a small effect on the interval velocity (Figure 6.18c): the interval velocity cannot be shifted back to its true value of 1550 m/s in the reasonable water speed range of 1460-1500 m/s. Compared to water speed, the interval velocity has a larger sensitivity to the assumed sediment velocity V1; however, the true interval velocity can still be obtained at extreme case of ~1450 m/s due to the large varying range of V1 (Figure 6.18d). This also indicates that the real velocity profile can be replaced with a good estimation of constant sediment velocity for shallow depths. The selected datum has an intermediate but opposite effect on interval velocity (Figure 6.18a) since the 100 m of source depth variation is commonly seen over the entire survey line, and the source-receiver depth difference can reach this number sometimes. Thus, the floating datum system used in this study can efficiently reduce the datum-related errors. The most sensitive parameter is the inverted horizontal source-receiver offset (Figure 6.18b): only 5 meters difference of the over-400-m-length cable will cause a large interval velocity change of 20 m/s. The effect of cable geometry will also be seen in later velocity inversion section of 6.3.2.4 (Figure 6.35 and Figure 6.36). However, the combined effect of all 4 parameters is still an open question at this stage and the complexity for multiple sediment layers is another challenge.

6.3.2 Velocity Analysis Using Inverse Method

Rather than applying hard-to-interpret conventional velocity analysis associated with traveltime corrections for the nonlinearly streamer geometry, a better solution for the DTAGS data may be to model traveltimes along rays from the best-determined source position to the streamer with its best-determined geometry. That is, observed traveltimes are picked for specific reflectors, and a line-ray-trace method is used to invert model velocity.

6.3.2.1 Inverse Assumptions

There are some basic assumptions for this velocity inverse method proposed here:

1) The previously determined cable geometry in section 4.3.3 is accurate within the shot gather; a systematic depth error only occurs from shot-to-shot, and this error can be corrected by a vertical shift.
2) The accuracy of image stitching between two adjacent shot gathers is ~30 m, i.e. the size of a super-CDP used in field data.
3) The target reflectors are representative of large localized changes in reflectivity due to impedance contrast or interference from fine layers, while the travel times are controlled by the average layer velocity between target reflectors. Therefore, stable average layer velocities and reflector depths can be inverted without knowing detailed velocity variations at the interface itself. That is, the target reflectors are similar to the "floating reflectors" of Zelt et al. (1992).
4) Within each layer, the sediments are divided into locally homogeneous columns, i.e., the layer velocity within a column is the constant average velocity of the sediments. However, this average velocity may vary from column to column along the layer.
5) When a ray hits the layer interface, the slope at the incident point is 0, i.e., the local area around the incident point is always horizontal. This is a safe option for smooth variations in interface depth where the subseafloor structure is unknown in detail.

6.3.2.2 Inverse Algorithm

Given a specific reflector ***T(x, t)*** with picked travel time ***t*** at horizontal offset ***x***, there is a best ray path $\boldsymbol{r_i}$ for each trace, which has the end point at coordinate $\boldsymbol{(x_i, y_i)}$ closest to the receiver $\boldsymbol{R_i}$ for the given travel time $\boldsymbol{t_i}$:

$$r(x_i, y_i) = f\left[h(x, y), v(x, y); t_i(x, t)\right] \qquad \text{(Equation 6.1)},$$

where ***h(x, y)*** is the reflector depth function, ***v(x, y)*** is the average velocity function of sediments associated with ***h(x, y)***. Since ***v(x, y)*** between two interfaces can be estimated from the layer thickness ***d(x, y)*** and the one-way vertical travel time ***dt(x, y)***

$$v(x, y) = d(x, y) / dt(x, y) \qquad \text{(Equation 6.2)},$$

the optimization problem is to find best reflector depths ***h(x, y)***, which minimize the average bias b_i of the ray path end point r_i relative to the corresponding receiver location R_i; the objective function Φ is

$$\Phi = \frac{\sum_{i=1}^{M} b_i}{M} = \frac{\sum_{i=1}^{M} [R_i(X_i, Y_i) - r_i(x_i, y_i)]}{M} \quad \text{(Equation 6.3),}$$

where ***M*** is the number of "good' traces out of the total number of traces ***N***. To select ***M***, a test objective function Φ' is first calculated using all traces ***N***

$$\Phi' = \frac{\sum_{i=1}^{N} b_i}{N} = \frac{\sum_{i=1}^{N} [R_i(X_i, Y_i) - r_i(x_i, y_i)]}{N} \quad \text{(Equation 6.4),}$$

and then the standard deviation β of the bias b_i is calculated,

$$\beta = \sqrt{\frac{1}{N-1} \sum_{i=1}^{N} (b_i - \Phi')^2} \quad \text{(Equation 6.5),}$$

thus a trace ***i*** is good if its bias b_i satisfies the following equation

$$b_i < \Phi' + 2 \cdot \beta \quad \text{(Equation 6.6).}$$

The inverse algorithm essentially tries to find the best layer thickness and average velocity simultaneously. The near-offset acoustic vertical times can only constrain the layer thicknesses by linking velocity changes to the layer thickness changes. The wide-angle travel times constrain both the velocities and the layer thicknesses.

Figure 6.19 illustrates a simple example of ray path through a model of two homogeneous sediment layers with seawater above. Since the inversion proceeds downward from layer to layer, for inversion of layer 2, the depths of interface 1 (***h1***) and associated layer velocity ***v1*** have been fixed. During each iteration, the inverse process will select a depth for interface 2 (***h2***), and thus produce a layer thickness ***d2*** and an average sediment velocity ***v2***. For a given receiver ***i*** and picked travel time t_i from the source to the reflector and then to the receiver, the inversion searches for the best ray path SAB with the smallest error in distance between the end point B and the receiver ***R***. When the depth changes from ***h2*** to ***h2'***, the average velocity will change correspondingly from ***v2*** to ***v2'***, since the one-way vertical travel time ***dt*** between the two

interfaces is an independent constant. The velocity variation results in the best raypath changing from SAB to SCD. When the inverse process finished, the determined depths of interface 2 should minimize the average errors of all traces, whose reflection points are on the interface 2.

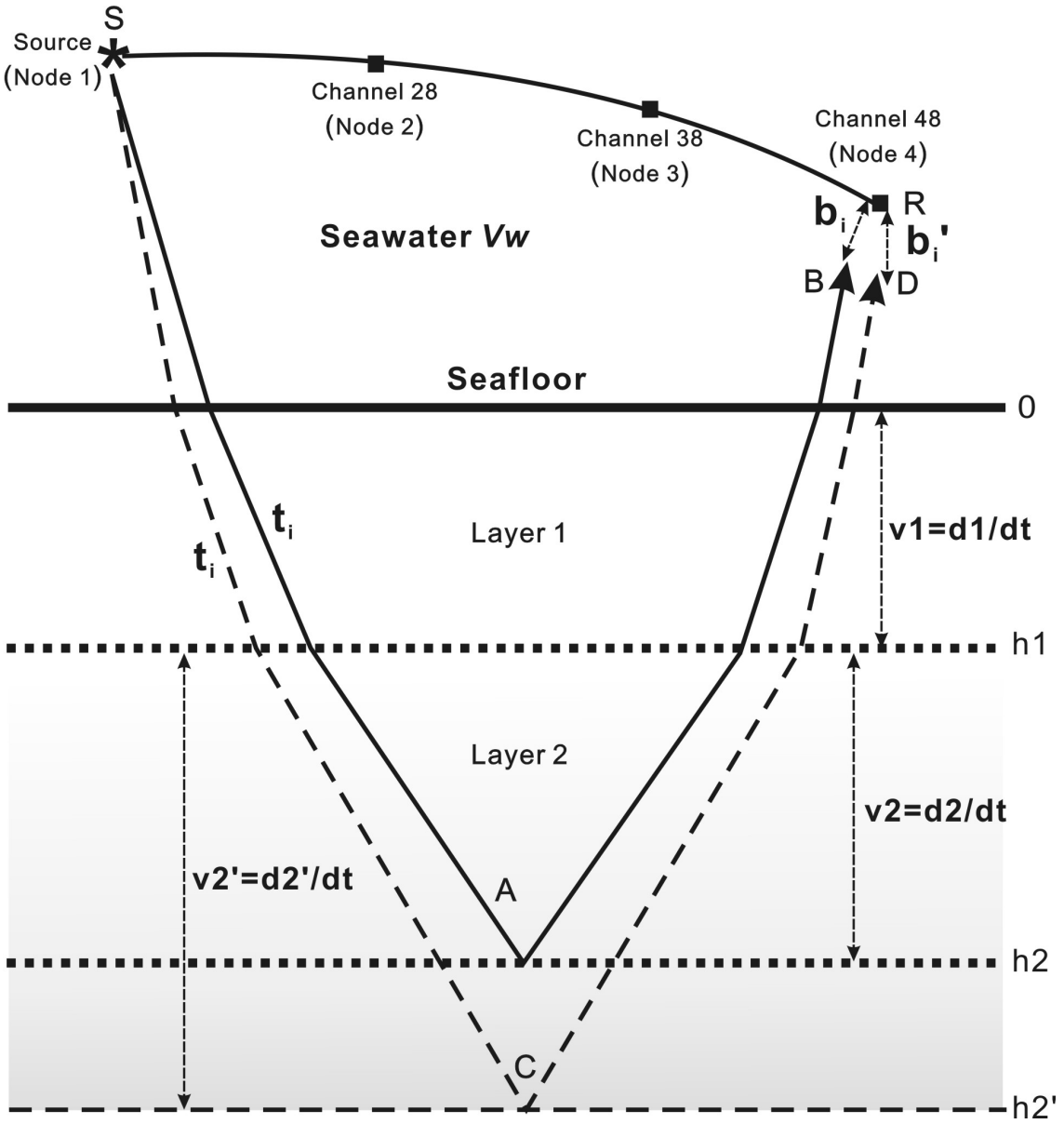

Figure 6.19 Model illustration of the ray path through 2 sediment layers. When layer 2 depth increases from ***h2*** to ***h2'***, the average velocity correspondingly increases from ***v2*** to ***v2'*** since the vertical travel time difference ***dt*** between the picked reflector 1 and reflector 2 is fixed.

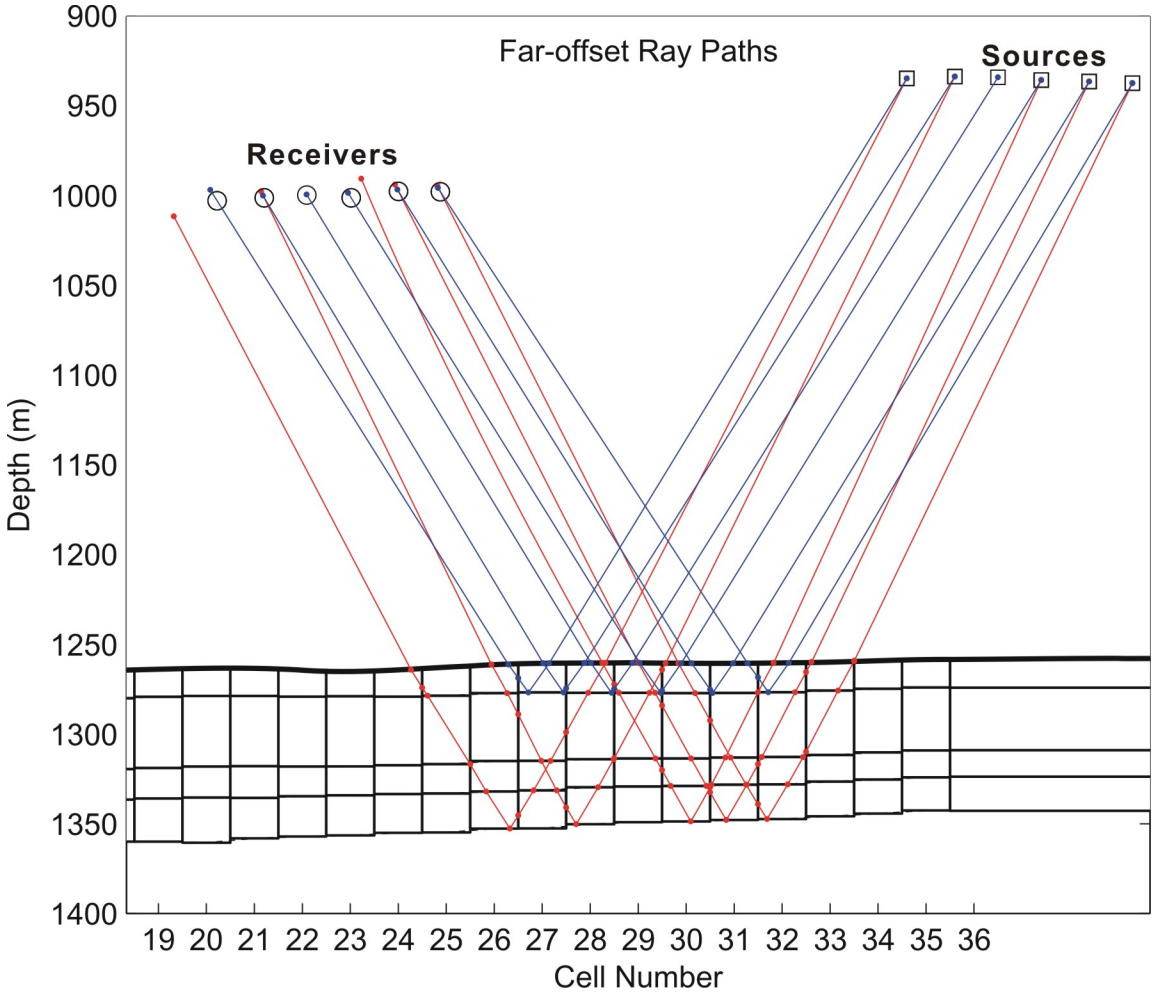

Figure 6.20 Example of ray paths to the farthest trace Channel48 for the first shallow reflector (blue lines) and for the deeper reflector (red lines) during the inverse process. The centers of sediment cells are spaced at 30 m, with top/bottom boundaries determined by inverse method. The dots on the ray path indicate the location where Snell's law is applied. Note that the bias between the ray end point and the target receiver can increase when ray goes deeper.

For the inversion, the sediment section is divided horizontally into cells of 30-m spacing, with reflection interfaces as top/bottom boundaries (Figure 6.20). Within a cell the one-way vertical time is a constant value, averaged from the acoustic traces through this cell. For the cells in the current inverse layer, the top depths have been fixed during previous inverse process for the upper layer; thus, selecting the bottom depth of each cell fixes the layer thickness, as well as the average velocity of the sediment in this cell by dividing the layer thickness by the constant vertical time. When the inversion proceeds downward from layer to layer, a velocity function is produced that varies laterally along

the layer from one cell to the next and vertically from layer to layer. Given a velocity function, the best ray path of each geophysical trace is fixed with smallest bias $\boldsymbol{b_i}$ of the ray end point with the corresponding receiver location. As shown in Figure 6.20, the DTAGS streamer is about 300 m above the seafloor. For the first sediment interface as shallow as ~15-20 mbsf, the ray for the largest source-receiver offset of ~436 m may pass through a maximum of 2 columns (blue lines, Figure 6.20); however, for deeper interface (~100 mbsf), the ray can easily pass through 4 adjacent 30-m-wide columns (red lines, Figure 6.20). Thus, full ray tracing is used to compute refraction angles at layer interfaces and vertical cell boundaries (the small dots on the ray path, Figure 6.20). Figure 6.20 also shows that the bias level increases for deeper sediment interfaces. For example, the first and third red ray paths have much larger distances between their end points and the corresponding receiver locations compared to the blue ray paths.

To obtain stable inversion results, the sediment cells must be sampled several times by different ray paths. Figure 6.21 shows ray paths for the Reflector4 at about 100 mbsf, whose reflections points fall into 3 adjacent cells 24-26. Cell26 is a "hot" cell, where as many as 15 red rays hit the cell bottom. In contrast, Cell24 is a "cold" cell with only 4 reflection points from blue rays; however, another 2 green rays pass through this cell after reflection from adjacent Cell25. Not counting possible rays for Cell23, "cold" Cell24 is still sampled by at least 6 times, which is adequate for acceptable inversion quality. For a given shot, 2-3 adjacent sediment cells are coupled together (Figure 6.21) in a running average sense with weighting factor decreasing from the center cell to the outside cells. Thus, when the source marches from one side to the other side of the model area, the inversion results are stable over most of the region, except the 2 edges (4-5 cells at each edge).

The model area is between offset 1800-2850 m and is equally divided into 36 columns; thus, the column width is 30 m, the same as the nominal shot spacing in the 2002 DTAGS2 survey. Corresponding to the model area, the shot number of survey line DT09 ranges from 170 to 200. Since the far-offset geophysical subarray contains 24 receivers, a maximum of 744 ray paths may be required to compute any change of velocity function due to the depth change of any sediment cell. Thus the computation of

the whole inversion process is very intensive even for this small scale model. To reduce the computation time, the ray paths and cell depths are inverted using the Matlab built-in "patternsearch" module.

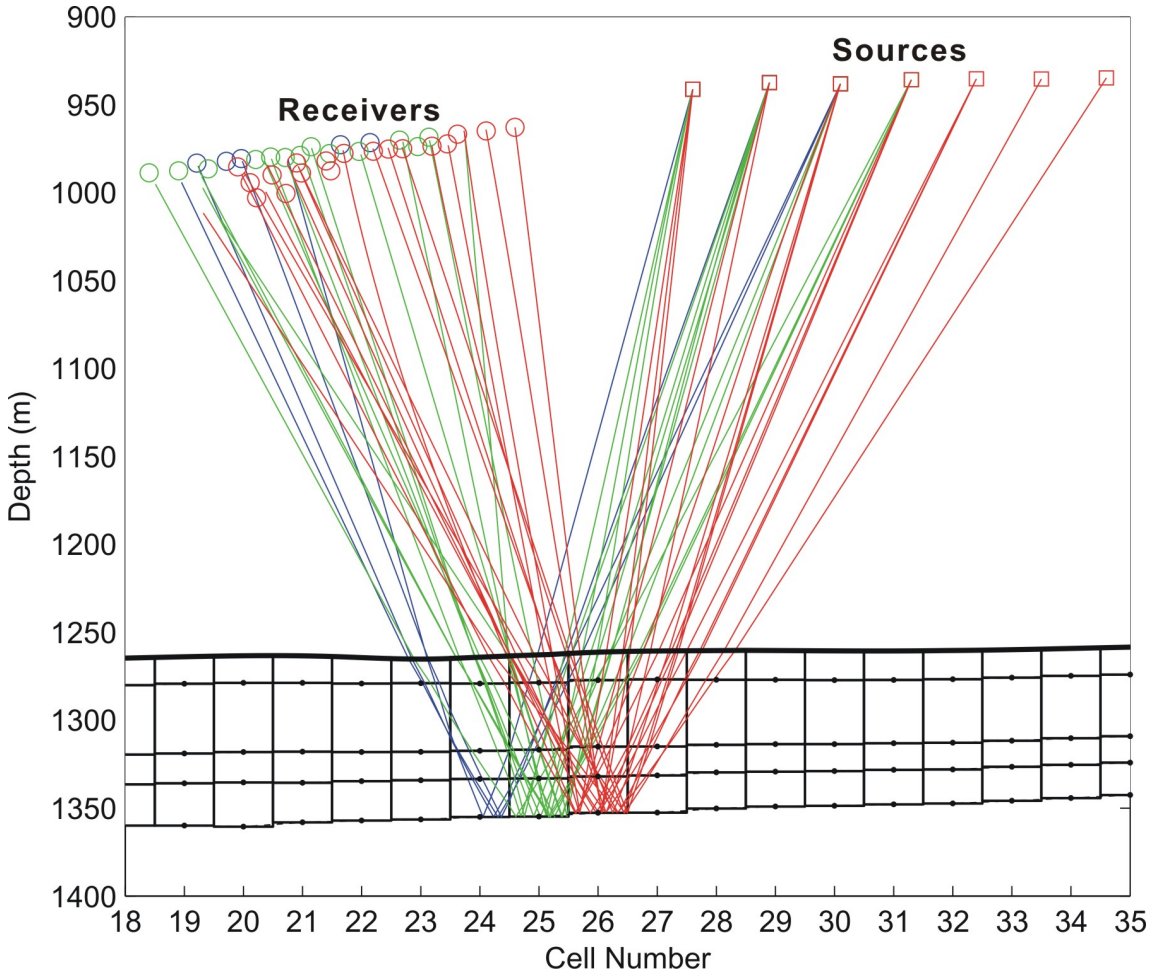

Figure 6.21 Ray paths showing sampling rate for a segment of Reflector4, with reflection points falling into 3 adjacent cells 24 (blue), 25 (green) and 26 (red). Note that the cells are sampled not only by the rays reflected within them but also by those passing through them.

The pattern search algorithm (PSA) was first proposed by Hooke and Jeeves (1961) to make a locally direct search for solving optimization problems that do not require any information about the gradient of the objective function. A "pattern" is a set of vectors that the pattern search algorithm uses to determine which points to search at each iteration. The set of vectors ***P*** is defined by the number of independent variables in the objective function and the positive basis set. The pattern search begins at the given

initial point ***x0***, the current point, and mesh size ***m0***. At each step, the algorithm forms a set of searching points around the current point ***x0*** by adding ***x0*** to a mesh, which is obtained by multiplying ***m0*** by ***P***. The pattern vector $\boldsymbol{P_i}$ that produces a mesh point ***i*** is called its direction $\boldsymbol{d_i}$. Then the algorithm polls the points in the current mesh by computing their objective function values from different directions. If the algorithm finds a point ***x1*** whose objective function value is less than that of the current point ***x0***, the poll is called successful and the point it finds becomes the current point at the next iteration. At the next iteration, the pattern ***P*** is updated with the direction $\boldsymbol{d_1}$ and the mesh size is increased by multiplying ***m0*** by a given expansion factor ***e*** (the default value is 2). Thus a larger mesh forms along the direction which has been proven to reduce the objective function value. If none of the mesh points has a smaller objective function value than the value at ***x0***, the poll is unsuccessful. In this case, the algorithm does not change the current point at the next iteration; however, the algorithm reduces the mesh size by multiplying the current mesh size ***m0*** by contraction factor ***c*** (the default value is 0.5). Thus the algorithm polls points in a smaller variable space around the previous successful point. Iteratively changing the mesh size and the search direction, the PSA computes a sequence of points that get closer and closer to the optimal point.

The pattern search algorithm actually used a version specifically developed for Matlab, called Augmented Lagrangian Pattern Search (ALPS), which can provide a global convergence to the optimal point for nonlinear constraint problems with simple bounds. This is just the case of the inversion problem in this study: the reflector depth in each cell varies nonlinearly but has simple bounds corresponding to some estimation for the average sediment velocity (between typical values of 1450 m/s and 2450 m/s). The ALPS was first proposed by Conn et al. (1991, 1997) and then developed by Lewis and Torczon (2002). A simple description of this algorithm is given below. The ALPS separates bounds and linear constraints from nonlinear constraints and forms a series of subproblems by combining the objective function and nonlinear constraint function using the Lagrangian and the penalty parameters, which is an approximation of the original problem. Then a sequence of such optimization problems are approximately minimized using a pattern search algorithm (PSA) such that the linear constraints and bounds are

satisfied. When the subproblem is minimized to a required accuracy and satisfies feasibility conditions, the Lagrangian estimates are updated. Otherwise, the penalty parameter is increased by a penalty factor. This results in a new subproblem formulation and minimization problem. These steps are repeated until the stopping criteria are met. The algorithm stops when any of the conditions below occurs; the parameter values used for the velocity inversion are given in parentheses.

- The mesh size is less than **Mesh tolerance** (1e-12).
- The distance between the points found in two consecutive iterations and the mesh size are both less than **X tolerance** (1e-6).
- The change in the objective function in two consecutive iterations and the mesh size are both less than **Function tolerance** (1e-12).
- The number of iterations performed by the algorithm reaches the value of **Max iteration** (+inf).
- The total number of objective function evaluations performed by the algorithm reaches the value of **Max function evaluations** (+inf).
- The computation time, in seconds, reaches the value of **Time limit** (+inf).

Compared to Genetic algorithm (GA), another global optimization method, the PSA (or ALPS) using the generalized pattern search (GPS) method has following advantages:

1) Repeatable results. The selection of variable values is not as random as in GA; the mesh forming and pattern searching algorithm is fixed for the PSA given a set of initial values and parameters.
2) Efficient computation time. If the initial values are appropriate, the PSA can quickly find the approximate pattern and search direction toward the optimal point, and thus greatly reduces iterations.
3) Easy use. The parameters for PSA are more comprehensible than those of GA. For different optimization problems, GA requires experience to set parameters specifically to balance the speed and the results.

The PSA with GPS method may not produce results as close to the optimal point as ones from GA given the same objective function, since the GPS searches a finite mesh space with somewhat fixed pattern for step length variation, while GA tries to search all variable space. However, there is typically a 20 times saving in computation time with only a very subtle quality loss. In fact the PSA still can provide inversion results as accurate as GA, if the mesh adaptive search (MADS) method is used; however, MADS will result loosing the first advantage as listed above. The computation time for all 744 ray paths at one iteration is about 50-60 seconds on a desktop with Intel® Core Duo 3.4 GHz CPU, and the inversion time for a sediment layer is about 5-10 hours depending on the total iteration numbers.

6.3.2.3 Model Test

To justify our inverse assumptions and verify the inversion algorithm, a one-layer model simulation test was run to determine the depth of the layer bottom using its average velocity. Figure 6.22 shows a hypothetical one-layer model with 4 sub-layers, simulating a possible high velocity column below a hydrate cap near IODP Site U1328 located at 2370m offset. Note that the default location of U1328 refers to drillhole C without any other explicit statement in the following text. The first sub-layer is seawater with velocity of 1473 m/s down to the seafloor at a depth of 1265 m. A 15-m-thick sub-layer (1265-1280 m depth) occurs just beneath the seafloor and contains high concentration gas hydrate with velocity increasing from 1520m/s to 1800m/s over a horizontal scale of 100 m (2250-2350 m offset). The third sub-layer is a relatively thick layer from 1280 m to 1340 m depth with a high velocity zone below hydrate cap. The bottom sub-layer is a thin 30-m-thick layer with normal velocity of 1650 m/s. However, in this one-layer model, it is assumed that only the seafloor and the reflector at a depth of 1370 m (the bottom of the 4th sub-layer) can be picked since reflectors of other sub-layer interfaces are discontinuous and/or too weak to be recognizable.

Prepare Synthetic Travel Time Data

Shots 170-195 of survey line DT09 were selected for the test section, with the positions of sources and receivers determined from the previous map-posting process for

the stitched DTAGS image (refer to sections 2.2.3 and 2.2.4). For a far-offset source-receiver pair (channel 25-48), the travel time corresponding to the reflector at 1370 m was computed using a forward ray tracing method, and thus the "picked" travel time for this trace is produced. The two-way time of the seafloor reflection for each trace can be directly calculated from simple raypath geometry with constant water velocity. The one-way vertical time from the seafloor to the target boundary can be determined from the model directly.

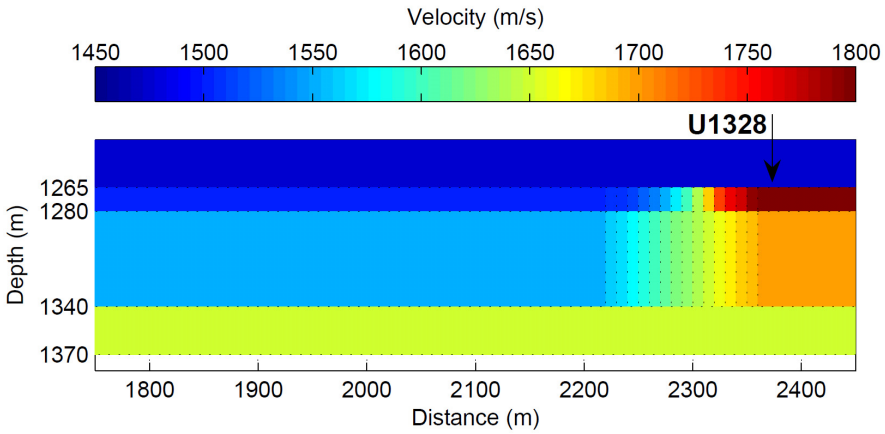

Figure 6.22 Illustration of a hypothetical one-layer model consisting of 4 sub-layers, simulating a high velocity column below the hydrate cap near IODP Site U1328. Note that the default location of U1328 refers to drillhole C without any other explicit statement in the following text.

Noise-free Results

Figure 6.23 shows the inverse result using the original travel times from forward ray tracing. Although the inverse model cannot reconstruct the detailed velocity zones of the complex model in Figure 6.22, the depths of the target layer are resolved with an accuracy of ±1 m. Also the average velocity of sediment cells shows a large increase near U1328, indicating the existence of a high velocity zone there, which in turn causes the large biases and scatter in the ray tracing results.

Noise-added Results

The above inverse result is noise free (i.e., the originally computed travel time is reused as "picked" time). To test the robustness of the inverse method, noise was added to the reflector's travel time to simulate the actual errors in data collection and time

picking. Since the DTAGS2 system has a wide frequency band source of 220-1k Hz, the dominant period is about 2.5 ms (for a dominant frequency of 400 Hz), and picking errors are on the order of 1 ms. For the far offset geophysical subarray, the difference of reflectors' travel time between two adjacent receivers is in the range of about 1-4 ms, which is the magnitude of signal resolution. Therefore a large noise fluctuation was added to the original computed travel time by multiplying the time differences of two adjacent traces by a random series uniformly distributed between -10 and 10 (a 10 times noise level).

Figure 6.24 shows the inverted results for the noisy data set. Compared to the noise-free inverted results (Figure 6.23), the reflector depths and the distribution of average velocities do not change much, although the bias level is increased by about 10 times.

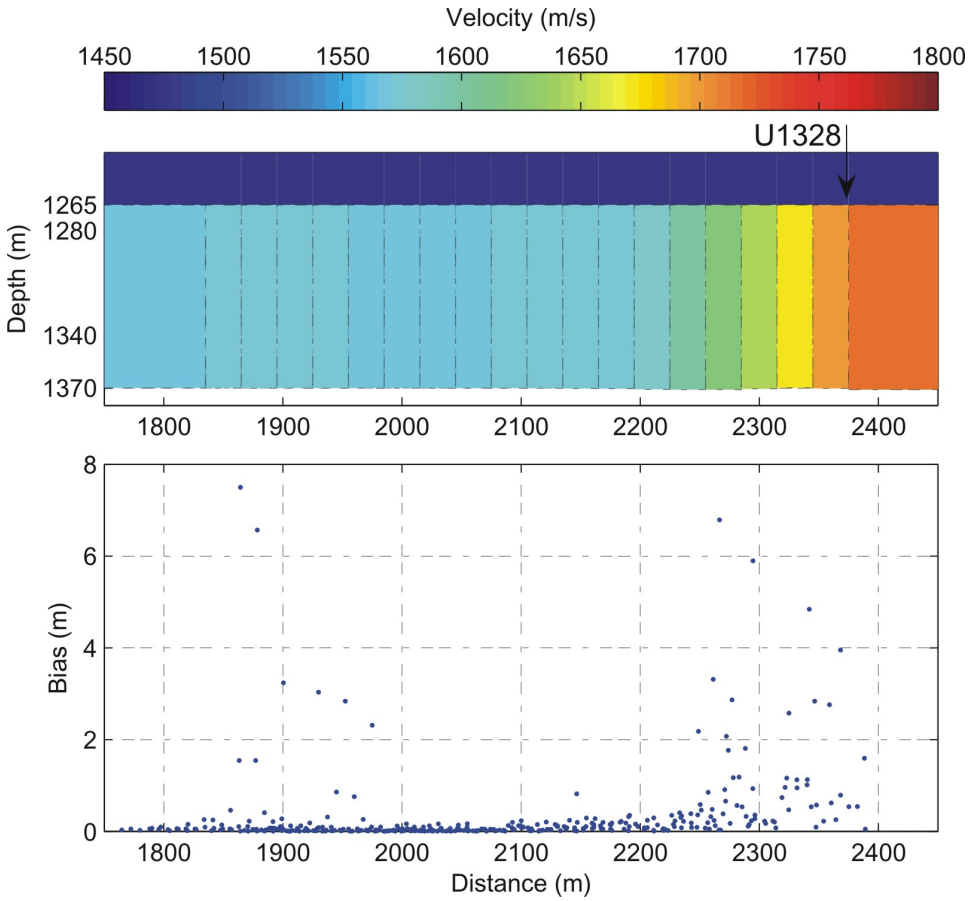

Figure 6.23 Velocity distribution of the result for inverting the hypothetical model in Figure 6.22 (top) and the corresponding bias of each trace at the location of the reflection point (bottom).

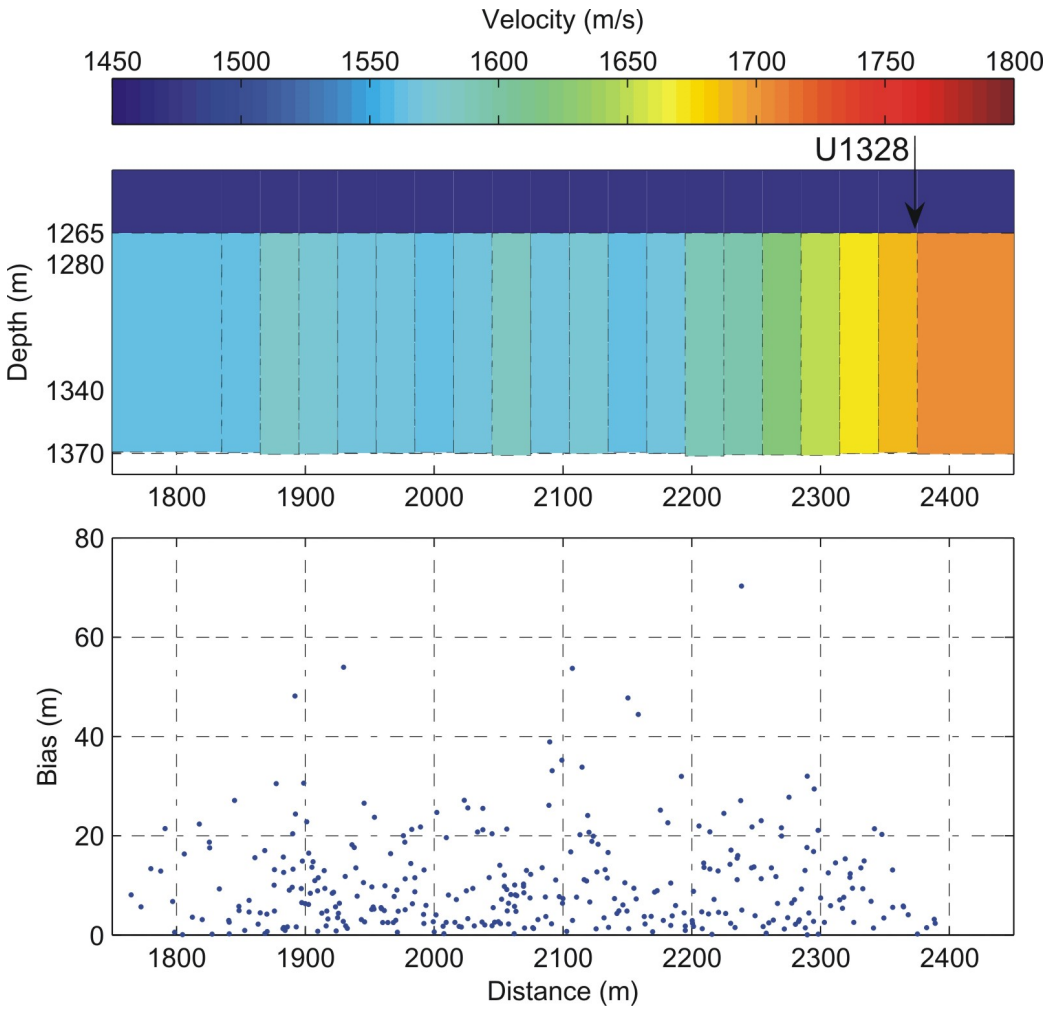

Figure 6.24 Inverted model results after adding a 10 times level noise to the synthetic observed travel times: (top) distribution of average velocities and (bottom) the corresponding bias of each trace at the location of reflection point.

How Well the Model Fits

Figure 6.25 provides detailed comparisons of the true model, the inverted noise-free model and the inverted noisy model. It shows that the biases of reflector depths are hardly over ±1m even when a 10 times level noise is added, or the relative uncertainties for this 105-m-thick layer are about 1%. The average velocities show a maximum fluctuation of ±20 m/s for absolute values, however, the relative velocity uncertainties are as small as those of layer thickness, since the average velocities are calculated by dividing layer thickness by a constant one-way travel time in that layer. These biases provide a sense of possible inversion errors, although they are not statistical uncertainties.

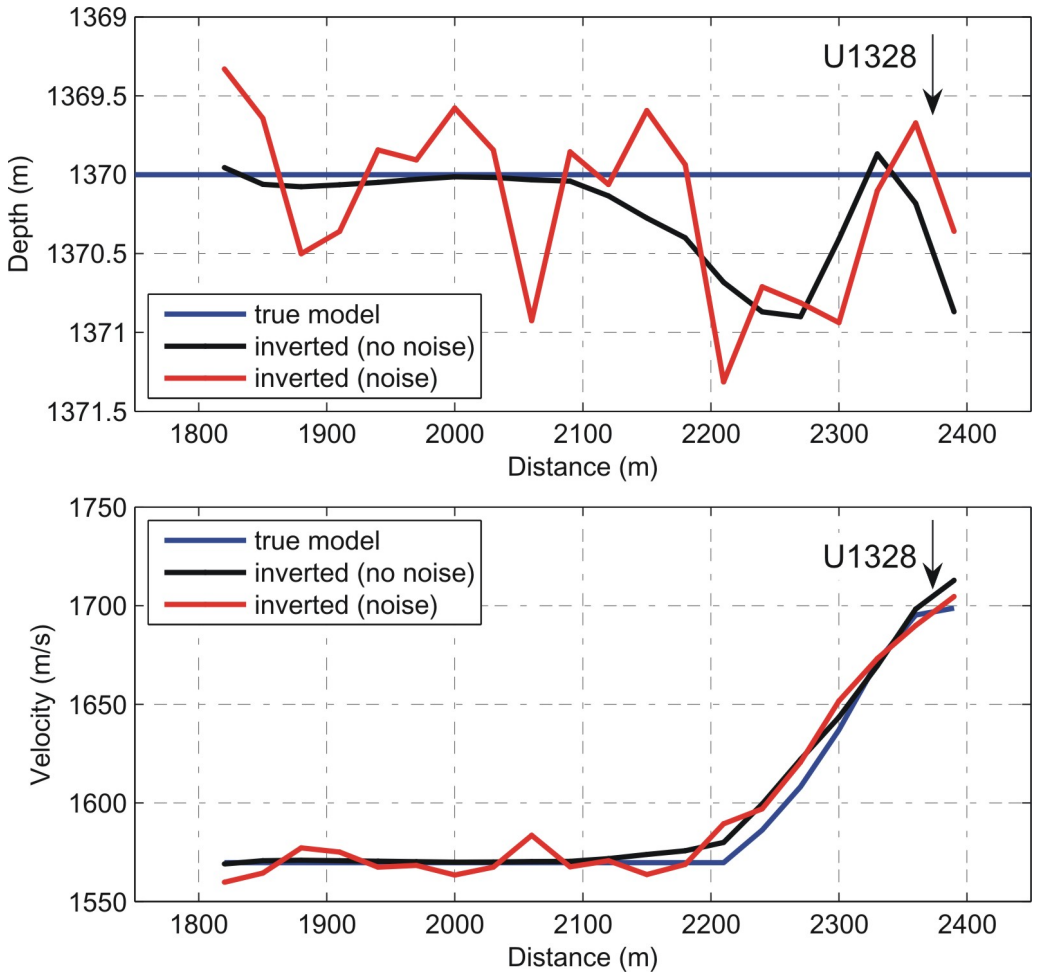

Figure 6.25 The comparisons of true model (blue line), inverted noise-free model (black line) and inverted model with 10 times level noise added (red line): (top) reflector depths and (bottom) average velocities of sediment column from seafloor to the reflector.

6.3.2.4 Invert Field Data – Example of DT09 Segment across Bullseye Vent

1. Pick Target Reflectors

Shot gathers from 170 to 200 on DTAGS2 survey line DT09 are selected for inversion. On the acoustic image of Figure 6.26(a), the reflection points of these shots approximately span model offset 1800-2900 m, over a section of gently varying seafloor. The seismic segment crossed Bullseye vent and the IODP Site U1328.

4 reflectors are identified as target layers for inversion (Figure 6.26b); the travel times of these 4 layers and the seafloor are picked. The acoustic image was formed using

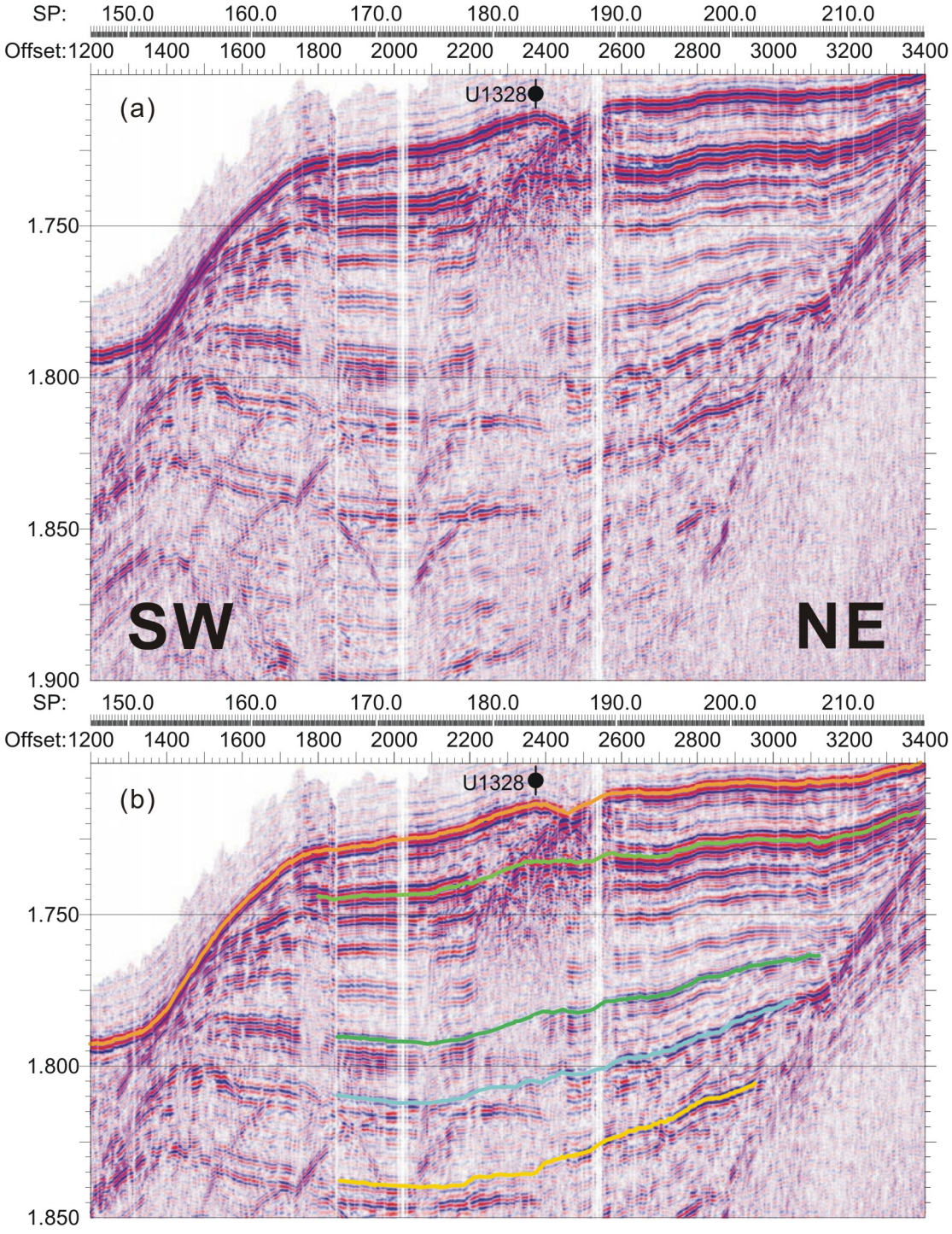

Figure 6.26 (a) Part of acoustic image of DTAGS2 survey line DT09, showing sediment layering across Bullseye cold vent and location of IODP Site U1328. (b) Picked specific reflectors for model inversion, including seafloor (orange), layer1 (light green), layer2 (deep green), layer3 (cyan) and layer4 (yellow).

constant water velocity for the NMO correction. The times picked from the acoustic image can be treated as two-way vertical time from the seasurface, since the near-offset acoustic traces (Channel 3-24 with largest source-receiver offset of 78m) are not very sensitive to NMO or to the cable geometry correction. Thus the average velocity within a sediment cell can be determined using the time differences between reflectors for selected layer thicknesses, especially for the situation of relatively deep sediments.

However, only the far-offset geophysical subarray (Channel 25-48) can carry possible velocity information for the sediment layers. Guided by the previous picks from the acoustic image, the target layers 1-4 were picked for each shot gather on the acoustic and geophysical channels (e.g., Shot 179 in Figure 6.27). These picked times were the reflector travel times for the inversion.

2. Inversion Results and Error Estimation

The inverted reflector depths and associated average velocity structure are shown in Figure 6.28. The details of the 4 sediment layers are presented in Figure 6.29 to Figure 6.32, respectively. Note that for all figures, the inverted results at SW edge of the reflector are not reliable due to the effect of the steep slope to the SW (refer to Figure 6.26) and due to an edge effect, indicated by a relatively high level of fitness error (e.g., Figure 6.29d). Figure 6.33 shows the histograms of the reflection point distribution among sediments cells for the 4 reflectors. These histograms can provide a minimum estimation whether a cell is well sampled or badly sampled. As shown in Figure 6.21, however, the rays may pass through the cell but hit the reflector in the adjacent cells. Thus, the actual sampling rate for each cell must be higher than the number of reflection points within the cell. For example, Cell23 at reflector4 is empty for reflection points but may still be sampled by rays passing through it.

Since the layer thickness is constrained from both near-offset and far-offset travel times, the inverted reflector depths are relatively stable. Based on the experience from model test, an accuracy of ~1% can be expected for inverted reflector depths, and the corresponding error of layer thickness is maximally ~1 m. The accuracy of layer thicknesses is also implied from the smooth variation of reflector depths (Figure 6.28).

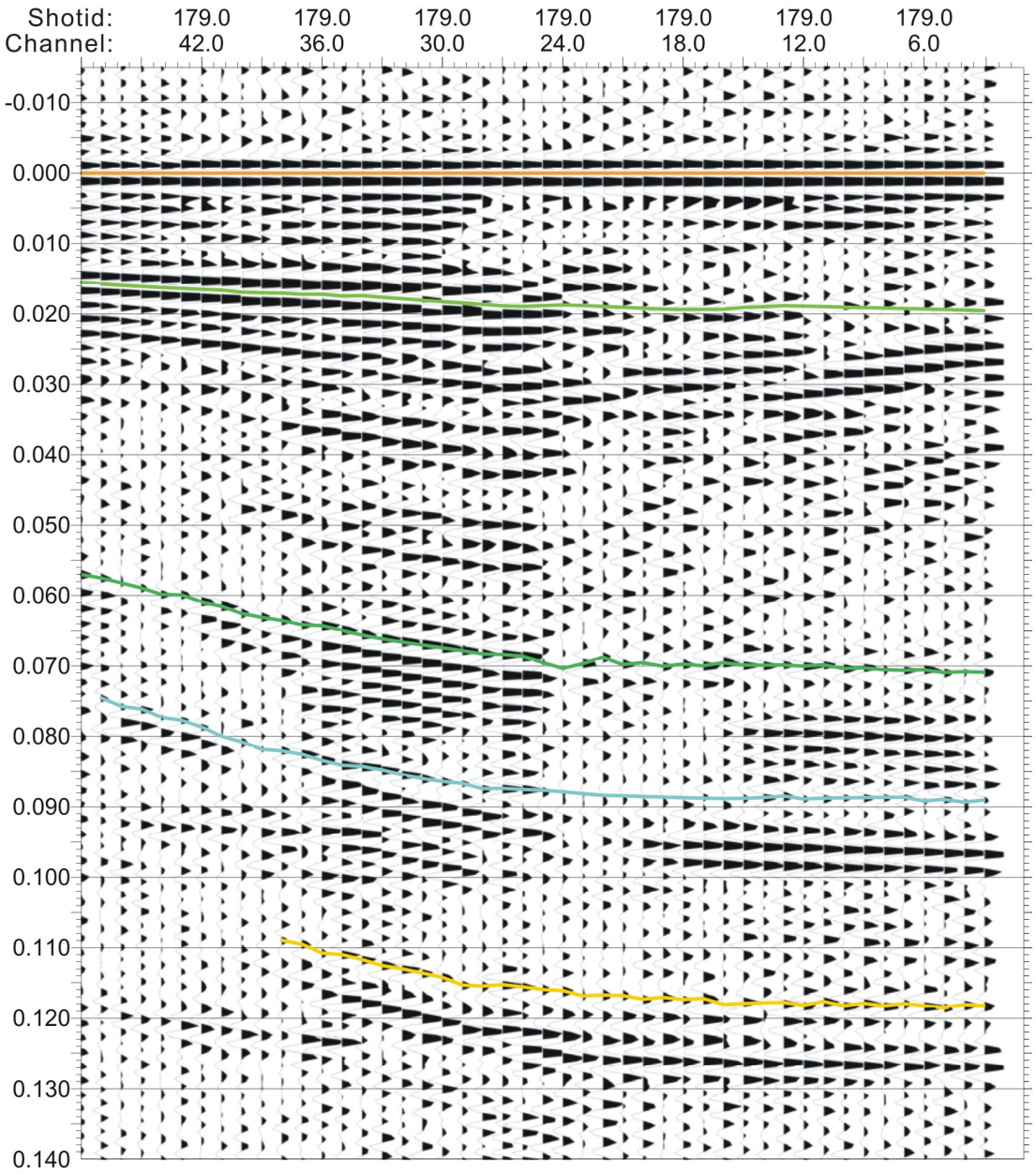

Figure 6.27 After flattening the seafloor reflection, target layers 1-4 (same colors as Figure 6.26) are more easily recognized within a shot gather (in this case, Shot 179), especially for DTAGS far-offset geophysical subarray (Channel 25-48), which carries possible layer velocity information.

Compared to reflector depths, the absolute value of average velocities associated with layer thickness can vary over a large range since they are mainly constrained by the far-offset travel times. The errors affecting velocity can be subjectively divided into two categories: random or systematic. The random errors come from reflector picking in a

shot gather and trace localization during the previous process of shot stitching. Since reflection points from different source-receiver pairs are divided into sediment cells during the inversion process, the errors from the above random sources can be simulated by random noise added during model test, which showed corresponding velocity errors in sediment cells mostly cancelled each other. The model test implied that the derived average velocity undulated with an accuracy of 10-20 m/s (Figure 6.25) due to random noise.

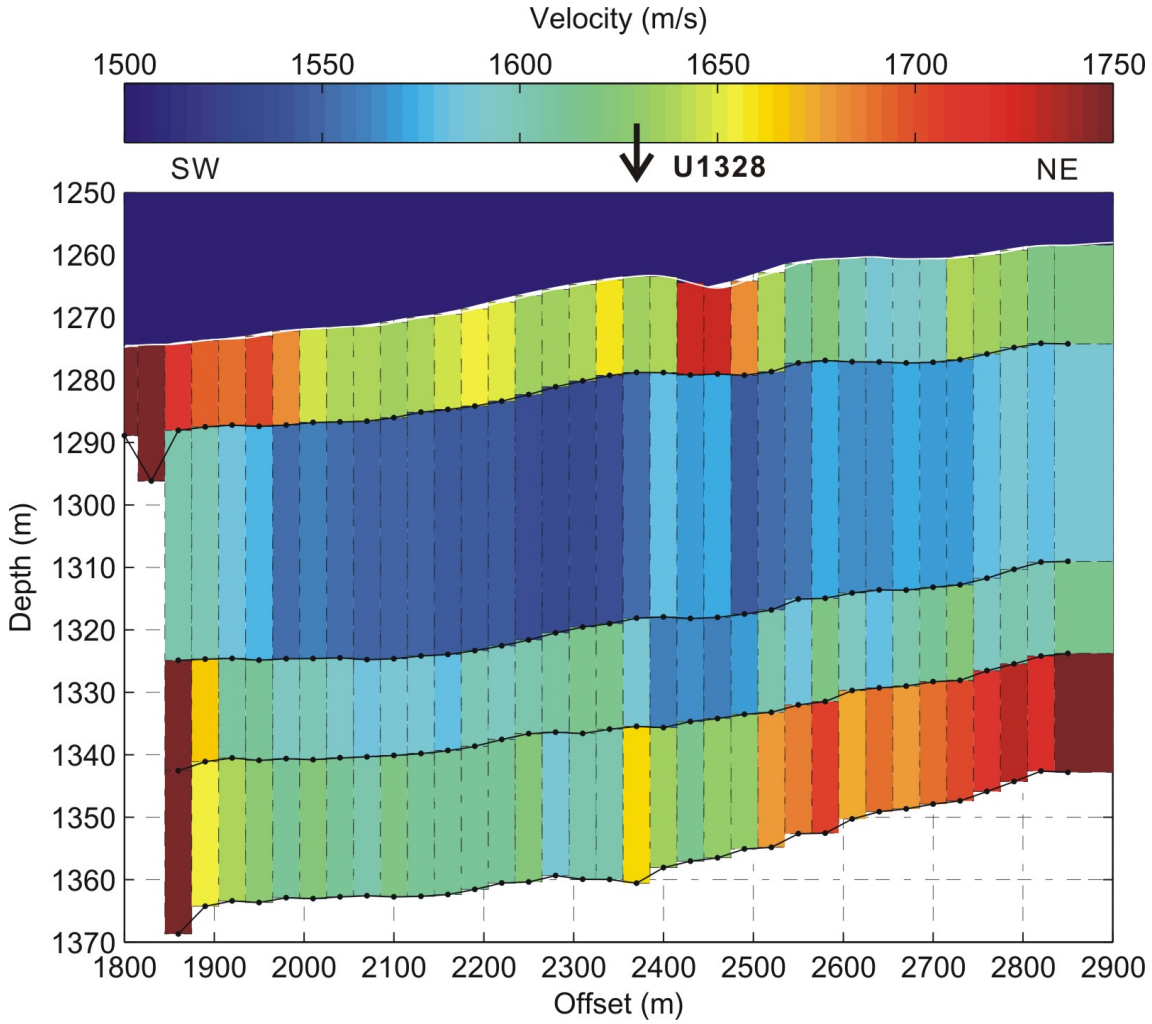

Figure 6.28 Inverted depths (black line with dots indicating the locations of cell centers) of picked reflectors in Figure 6.26(b) and corresponding average velocity distribution in color coded patches. The seafloor is outlined with white line. Note that a constant seawater velocity of 1474.4 m/s was used for model inversion, which is averaged over all shot gathers from 170 to 200. The location of IODP Site U1328 is also labeled.

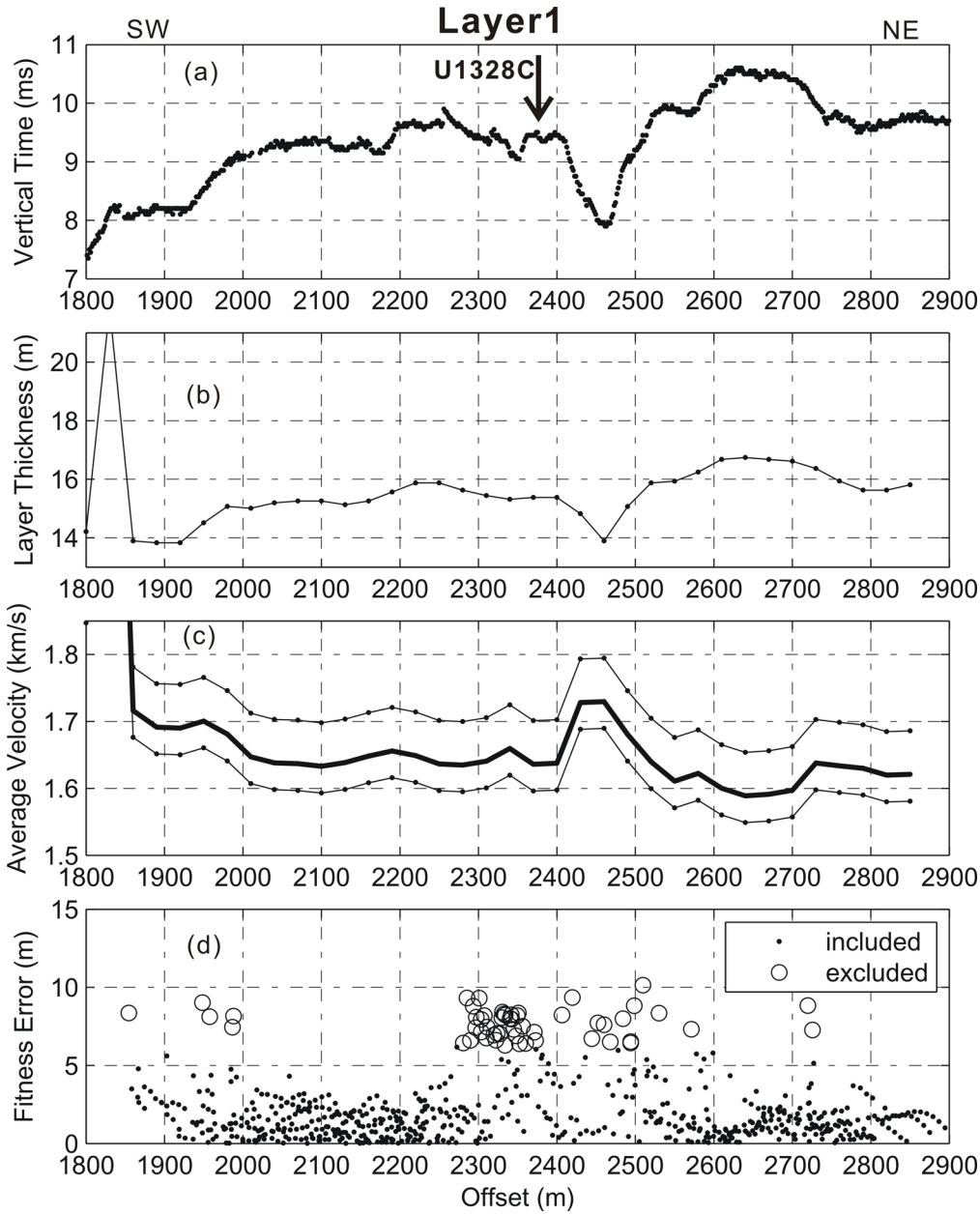

Figure 6.29 Details of inversion results for layer1. (a) One-way vertical time of layer1, half of the time differences from seafloor to reflector1 picked on acoustic image of Figure 6.26(b). (b) Layer1 thickness, the depth difference of seafloor and inverted reflector1 at cell centers (indicated by dots). (c) Average sediment velocity (thick line) and associated uncertainty band (thin lines) from the sensitivity test in Figure 6.34. (d) Fitness error of each trace, the distance between ray end point and the receiver. Note that only "good" traces (indicated by the dots) were used to calculate mean fitness error during inverse process, and the final mean fitness error is 1.57 m for layer1. The location of IODP Site U1328C is also labeled.

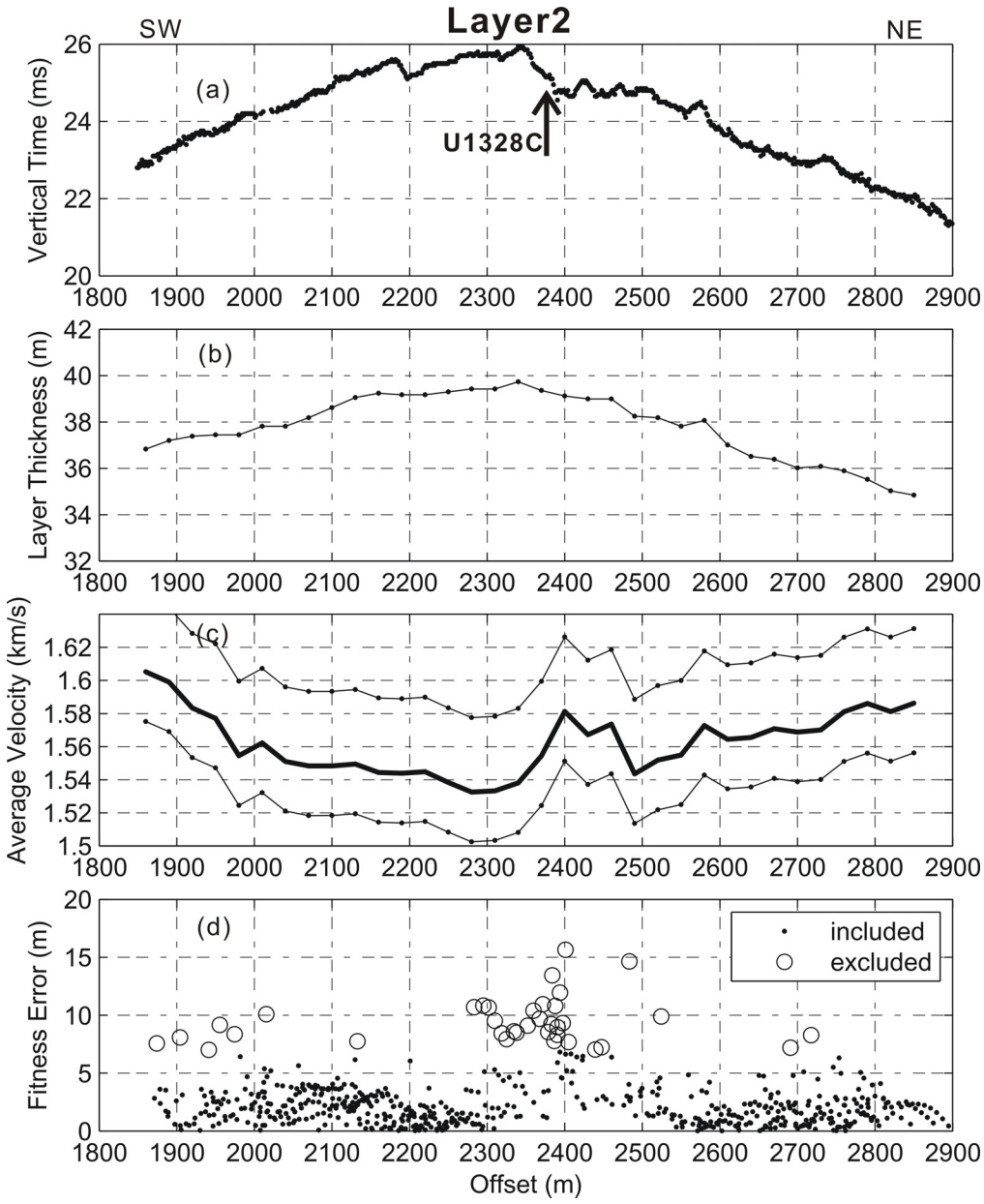

Figure 6.30 Details of inversion results for layer2. (a) One-way vertical time of layer2, half of the time differences from reflector1 to reflector2 picked on acoustic image of Figure 6.26(b). (b) Layer2 thickness, the depth difference of inverted reflector1 and inverted reflector2 at cell centers (indicated by dots). (c) Average sediment velocity (thick line) and associated uncertainty band (thin lines) from the sensitivity test in Figure 6.34. (d) Fitness error of each trace, the distance between ray end point and the receiver. Note that only "good" traces (indicated by the dots) were used to calculate mean fitness error during inverse process, and the final mean fitness error is 1.97 m for layer2. The location of IODP Site U1328C is also labeled.

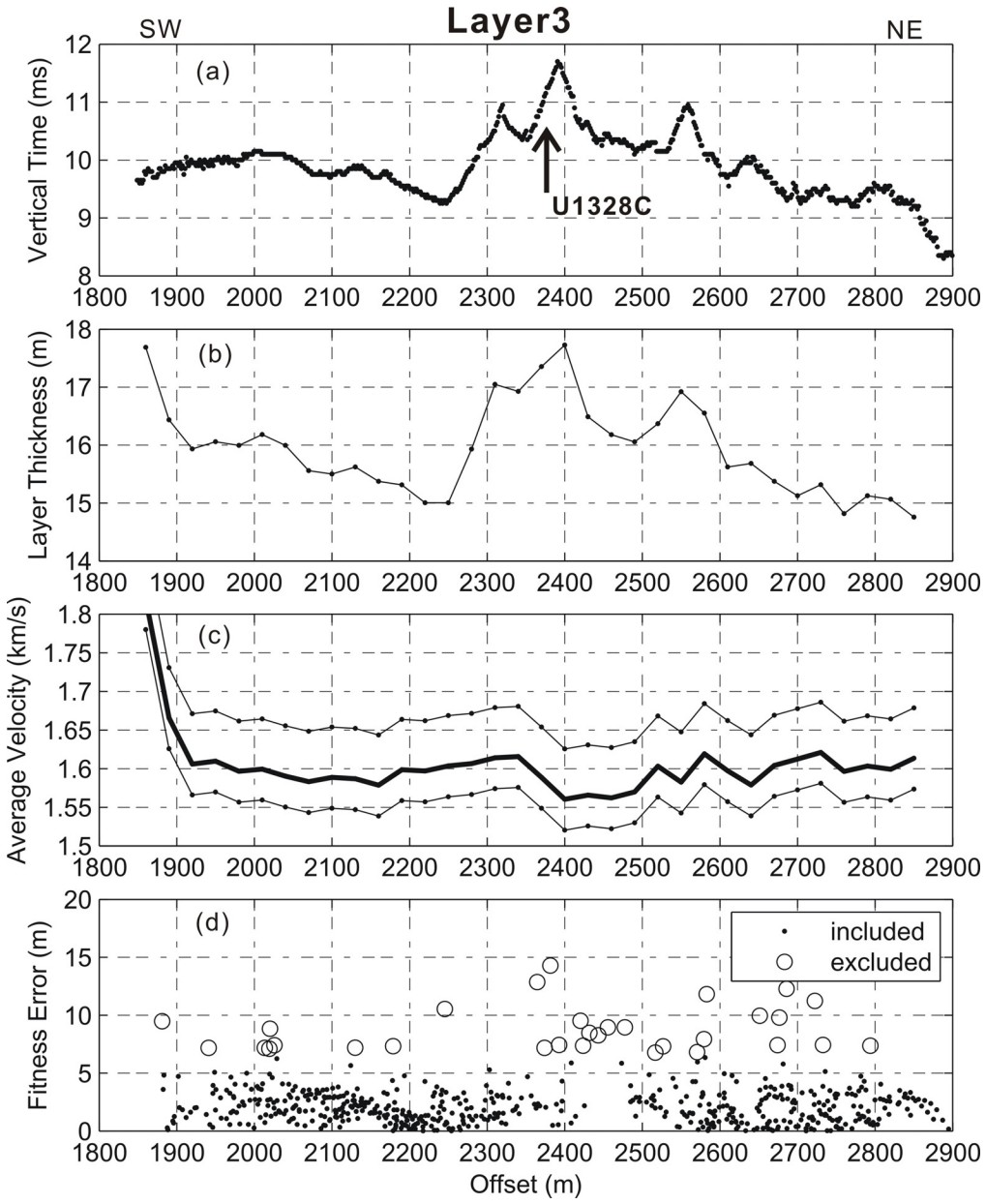

Figure 6.31 Details of inversion results for layer3. (a) One-way vertical time of layer3, half of the time differences from reflector2 to reflector3 picked on acoustic image of Figure 6.26(b). (b) Layer3 thickness, the depth difference of inverted reflector2 and inverted reflector3 at cell centers (indicated by dots). (c) Average sediment velocity (thick line) and associated uncertainty band (thin lines) from the sensitivity test in Figure 6.34. (d) Fitness error of each trace, the distance between ray end point and the receiver. Note that only "good" traces (indicated by the dots) were used to calculate mean fitness error during inverse process, and the final mean fitness error is 2.01 m for layer3. The location of IODP Site U1328C is also labeled.

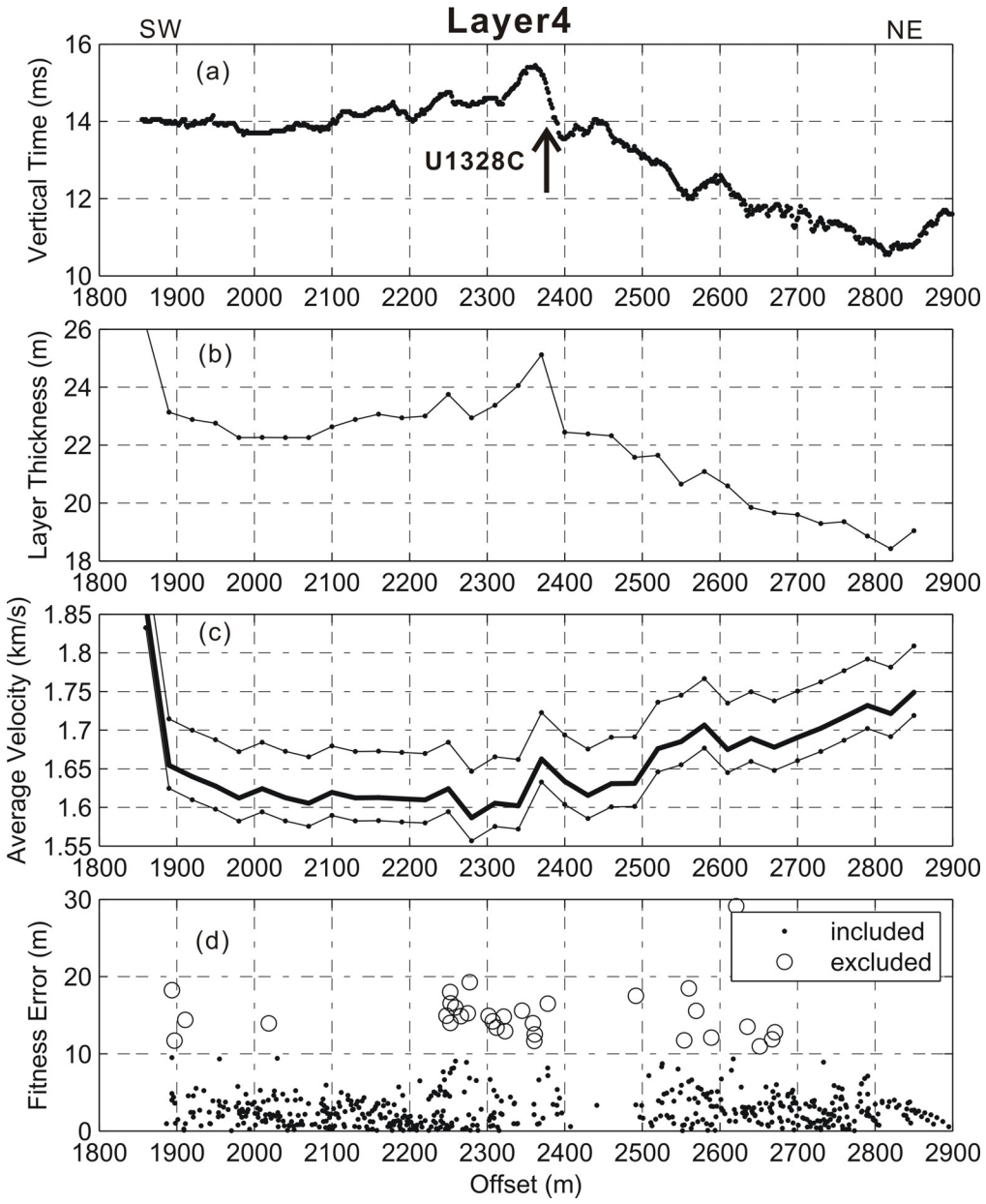

Figure 6.32 Details of inversion results for layer4. (a) One-way vertical time of layer4, half of the time differences from reflector3 to reflector4 picked on acoustic image of Figure 6.26(b). (b) Layer4 thickness, the depth difference of inverted reflector3 and inverted reflector4 at cell centers (indicated by dots). (c) Average sediment velocity (thick line) and associated uncertainty band (thin lines) from the sensitivity test in Figure 6.34. (d) Fitness error of each trace, the distance between ray end point and the receiver. Note that only "good" traces (indicated by the dots) were used to calculate mean fitness error during inverse process, and the final mean fitness error is 2.63 m for layer4. The location of IODP Site U1328C is also labeled.

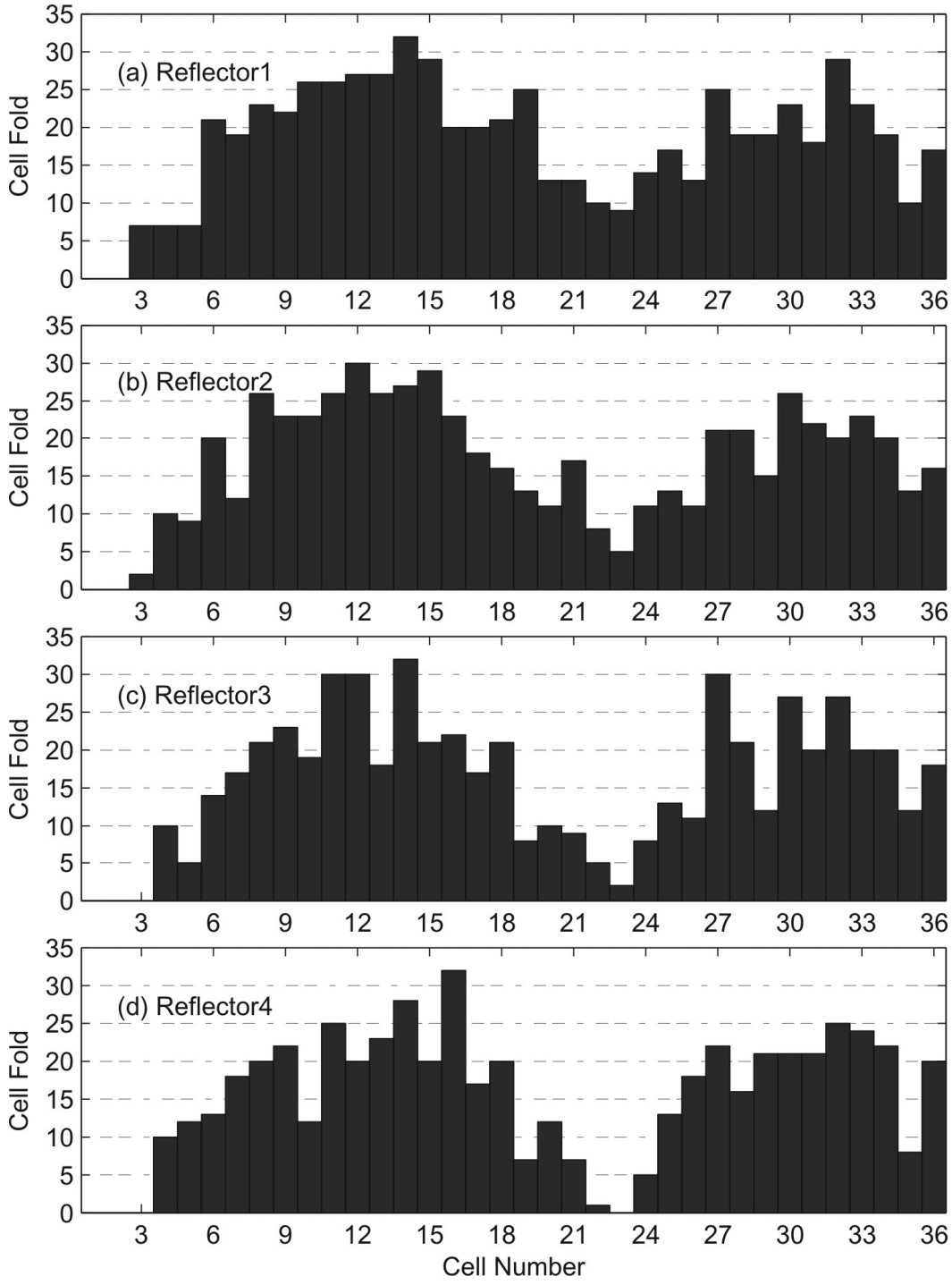

Figure 6.33 Histograms of the reflection point distribution among sediments cells for the 4 reflectors. Note that the actual sampling rate for each cell is much higher than the number of reflection points within this cell since the rays may pass through this cell but hit the reflector in the adjacent cells (Figure 6.21). Thus, Cell23 at reflector4 is empty for reflection points but may still be sampled by rays passing through it.

In contrast, the systematic error comes mainly from the reflector picking issue; this occurs at locations where the reflector's phase changes due to the DTAGS data nature of unstable cross correlation. When picking jumped from peaks to troughs (or vice versa), an ambiguity of ~2 ms (half wave length) was produced, corresponding to a one-way vertical time error of ~1 ms for the sediment layer. Since the layer thickness is tens of meters, a one-way vertical time change as small as 1 ms will cause a large average velocity change.

To estimate the combined effect of the random and systematic errors on inverted average velocities, a simple sensitivity test was applied. This test assumed that inverted reflector depths represented the real subseafloor structures, and added a series of constant velocity biases to the inverted velocities. Then forward ray tracing was used to calculate the fitness error of distance bias between the raypath end point and corresponding receiver position. The average fitness error is plotted against velocity biases in Figure 6.34. A qualitative estimate of error can be obtained from these curves. That is, the flat area around lowest point of each curve, where the average fitness values have no significant differences, represents the insensitive range of velocities, and thus a minimum estimate of velocity error. Since the true error must be larger than this, a velocity range that was approximately twice the width of the "flat area" for each curve was somewhat arbitrarily selected as an estimate of the velocity error (arrow area in Figure 6.34).

The lower and upper bounds of the average velocities are determined by adding the velocity error estimates to the inverted values; these are plotted in Figure 6.29(c) to Figure 6.32(c). Note that the simple error estimation only is only applied for an individual layer, while the actual errors could have a cumulative effect when passed from one layer to the next during the top-down inversion process. This is indicated by the fitness error levels (Figure 6.29d to Figure 6.32d): mean fitness error is 1.57 m for layer1, and then increases to 1.97 m for layer2, 2.01 m for layer3, and 2.63 m for layer4, even after rejecting some "bad" traces with large fitness errors.

It was also noticed that the cable geometry has a large effect on the inversion results as previously seen in conventional velocity analysis. An extreme example is linear cable geometry, which has the largest maximum horizontal source-receiver offset for a

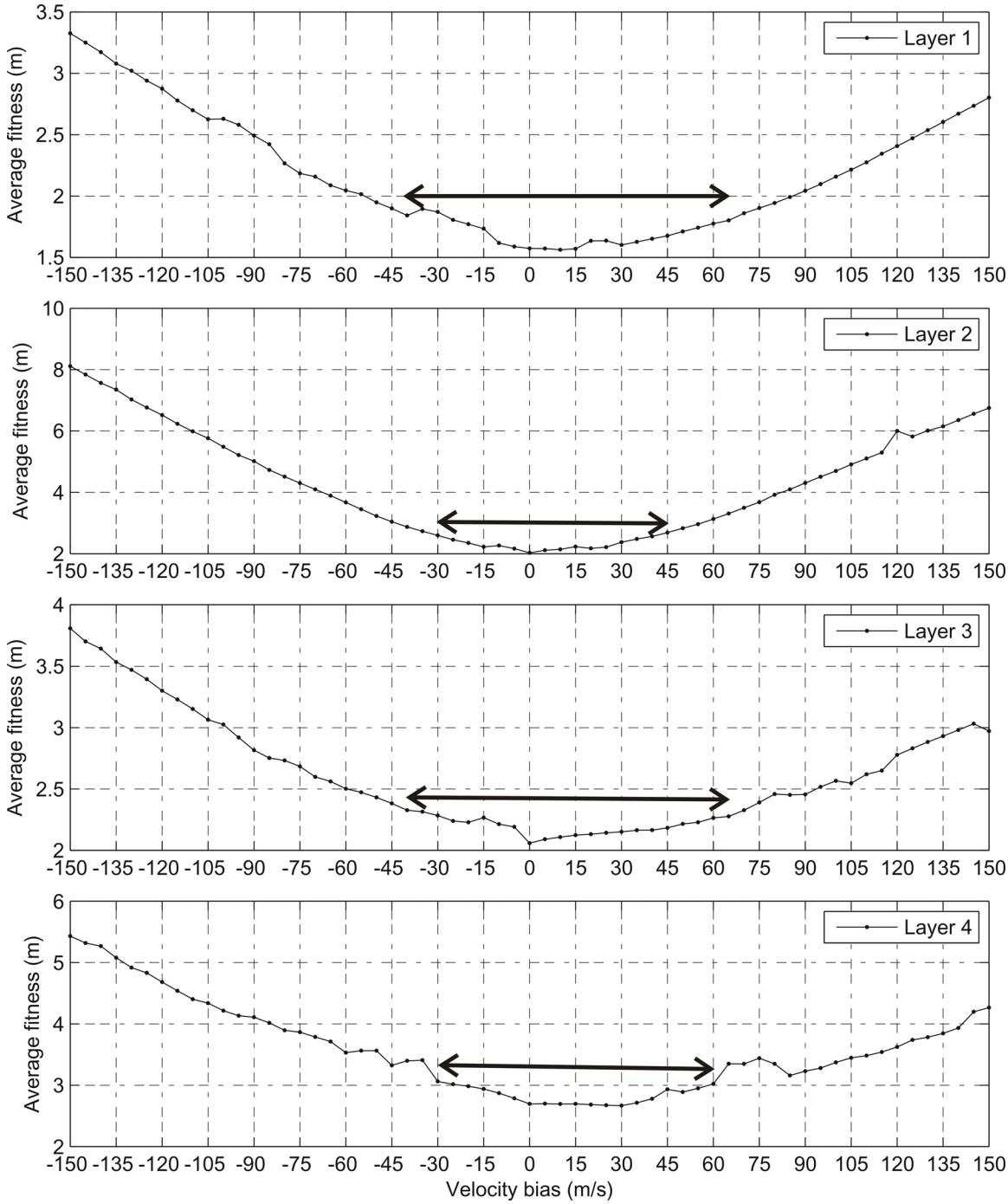

Figure 6.34 Results for sensitivity of average sediment velocity for a specific layer while keeping other layers untouched. A constant velocity bias was added to the current inverted average layer velocity, and then the average fitness error was calculated from forwarding ray tracing using inverted layer thickness.

given shot since the cable segments are straight between depth nodes. Compared to the inverted cable geometry in the model area, the linear cable geometry is ~2 m larger in maximum horizontal source-receiver offset (Figure 6.35). Using the same picked times, the inverse process was repeated for the linear cable geometry with results shown in Figure 6.36. Although the inverted reflector depths do not differ much, the associated average velocities for linear cable geometry (Figure 6.36) are significantly different than the ones for the inverted cable geometry (Figure 6.28). Since the former has unusual high velocities in layer1 and unusual low velocities in layer2, which cannot be supported by lithological samples from the local IODP drilling, it inferred that the inverted velocities for linear cable geometry are not very meaningful, especially for the absolute values. Thus, the correct cable geometry is the most important prior information for DTAGS data processing, not only in seismic imaging, but also in velocity analysis.

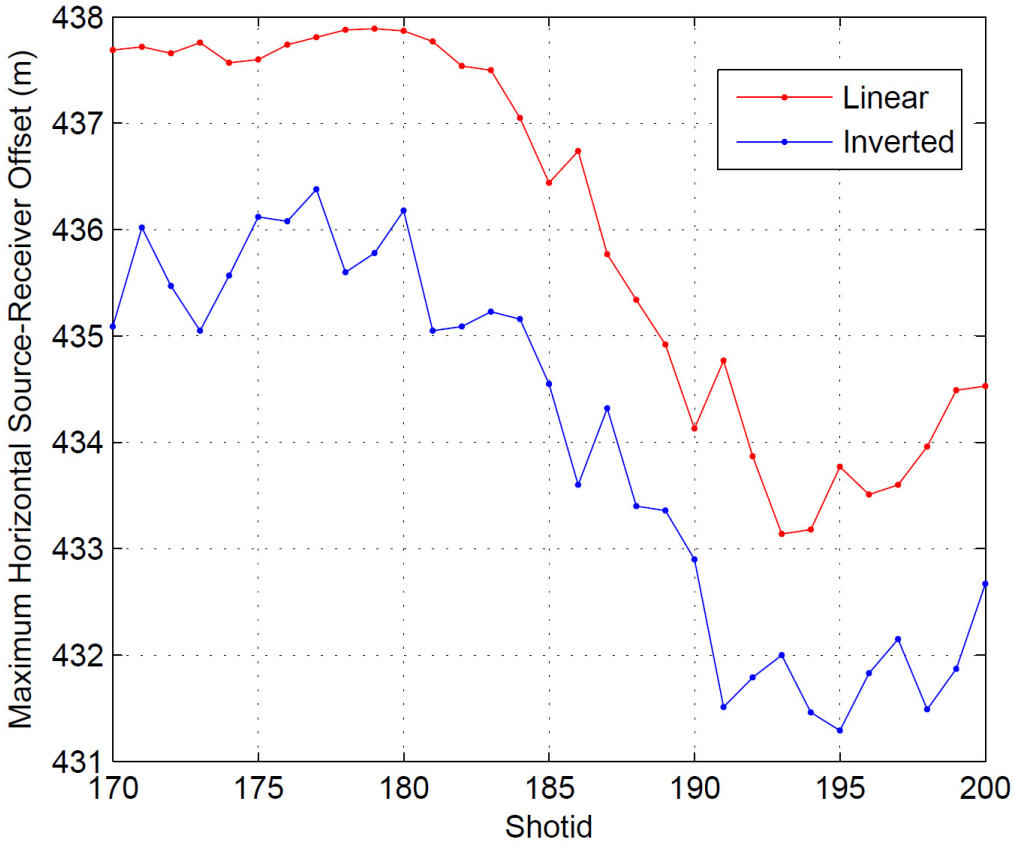

Figure 6.35 Shot-to-shot comparison of maximum horizontal source-receiver offsets between linear cable geometry (red line) assuming straight line between nodes and inverted cable geometry (blue line) best fitting the picked SSR times.

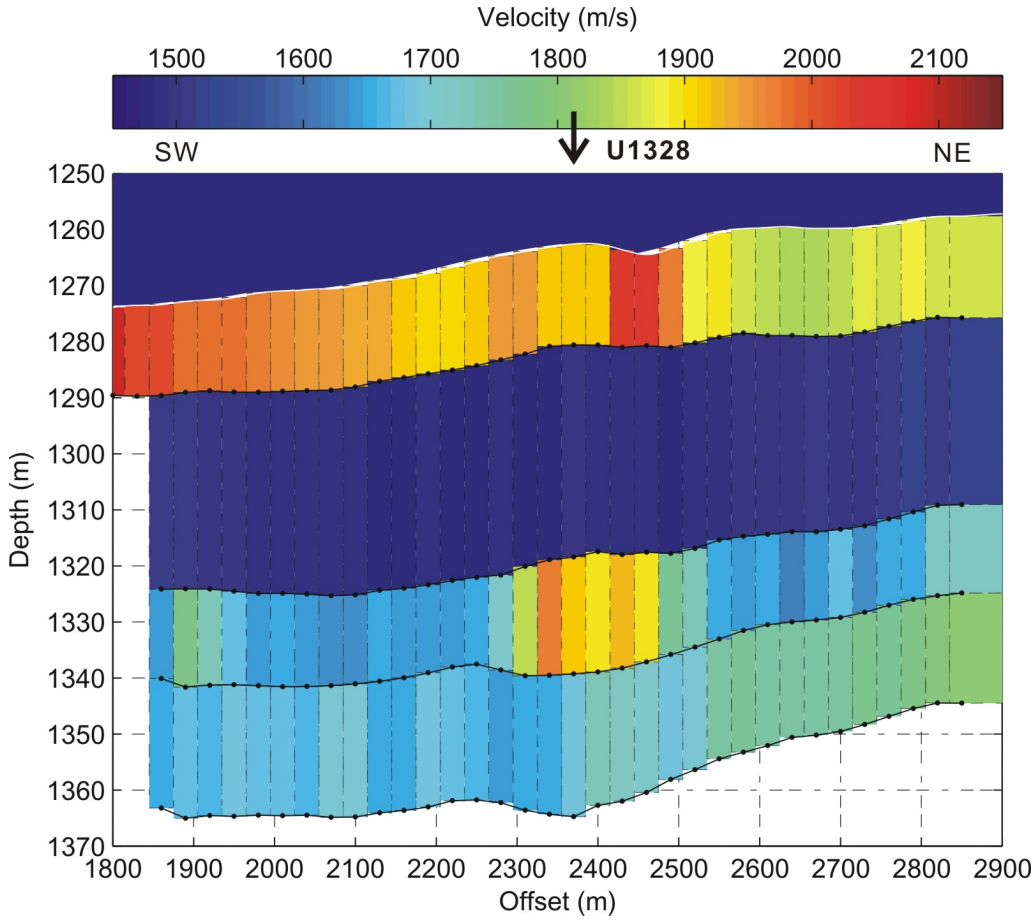

Figure 6.36 Inverted depths (black line with dots indicating the locations of cell centers) of picked reflectors in Figure 6.26(b) and corresponding average velocity distribution in color coded patches using linear cable geometry (red line, Figure 6.35). The seafloor is outlined with white line. Note that a constant seawater velocity of 1473.5 m/s was used for model inversion, which is averaged over all shot gathers from 170 to 200. The location of IODP Site U1328 is also labeled.

3. Interpretation

Compared to the normal under-consolidated seafloor sediments with velocities around 1500 m/s, layer1 is a high velocity layer with values that undulate around 1650 m/s (Figure 6.28; Figure 6.29c). This thin layer has thicknesses of 14-17 m (Figure 6.29b) and may indicate the hard cover of carbonate pavement (Fink and Spence, 1999). The lowest value of ~1600 m/s occurs over the distance range 2600-2700 m (Figure 6.29c). Also, the velocity increases slightly from ~1640 m/s to ~1720 m/s between offset 2400-

2500 m (Figure 6.29c), corresponding to the seafloor depression within Bullseye vent (Figure 6.26 and Figure 6.28). Since the fitness errors in this range are not obviously different from those between offset 2300-2400 m (Figure 6.29d), this variation of velocity may be true, and is consistent with a massive concentration of gas hydrate recovered by the piston coring within this seafloor pockmark feature. However, the ~80 m/s anomaly is small and equivalent in magnitude to the velocity errors.

Compared to layer1 above and layers 3-4 below, layer2 is a low velocity layer (Figure 6.28) with layer thickness of 35-40 m (Figure 6.30b). The velocity mainly varies between 1540-1580 m/s over offset 1900-2800 m. This low velocity may indicate that the concentration of gas hydrate in layer2 is decreasing rapidly with depth. The low velocity could also be the result of under-consolidated sediments. The IODP drilling results at Site U1328 shows that the ratio of shear strength to overburden pressure is lower than 0.25 from 8-220 mbsf (Figure 6.37), indicating layers 2-4 are all in the under-consolidation environment. Possibly the above hard layer1 becomes an impermeable cover for the upward fluid low along the fractures revealed in this area (e.g., vertical blanking zone and diffractions on the acoustic image of Figure 6.26), and thus sediments are enriched with fluid flow. Fluid flow may also carry gases which can further reduce sediment velocity. Under the seafloor depression feature, there is also a small high velocity zone between offset 2350-2450 m. Although the trace fitness errors in this zone are obviously higher, the "good" traces may roughly control the inversion quality (Figure 6.30d). The ~40 m/s positive anomaly is only half of the one at layer1, probably indicating a small scale concentration of gas hydrate.

Layer3 is a thin layer with thickness between 15-18 m. In this layer the average velocity of ~1550 m/s over the distance range 2350-2500m is slightly lower than the velocity of ~1600 m/s outside this range (Figure 6.31c). This small velocity anomaly zone corresponds to the acoustic blanking zone below the pockmark feature, where the continuity of reflector3 is hard to identify on the acoustic image (Figure 6.26) and on the far-offset channels within these shot gathers. Thus the inversion process has reduced control due to fewer picking points over this segment, indicated by sparse fitness error points with relatively high values (Figure 6.31d) and low frequency of sampling rate by

rays (Figure 6.33c). Outside the uncertainty area, a small velocity increase occurs from layer2 (~1560 m/s) to layer3 (~1600 m/s). This may indicate the normal trend of sediments consolidation that increases with depth.

For layer4, the velocity seaward of U1328 is mostly 1600-1620 m/s (Figure 6.32c), almost the same as the layer3 velocity, indicating the very similar lithology of these two layers. Landward of U1328, the velocity slowly increases to 1750 m/s at distance ~2850 m (Figure 6.32c). This may be caused by further increase in sediment consolidation when approaching the accreted small ridge (Figure 6.26).

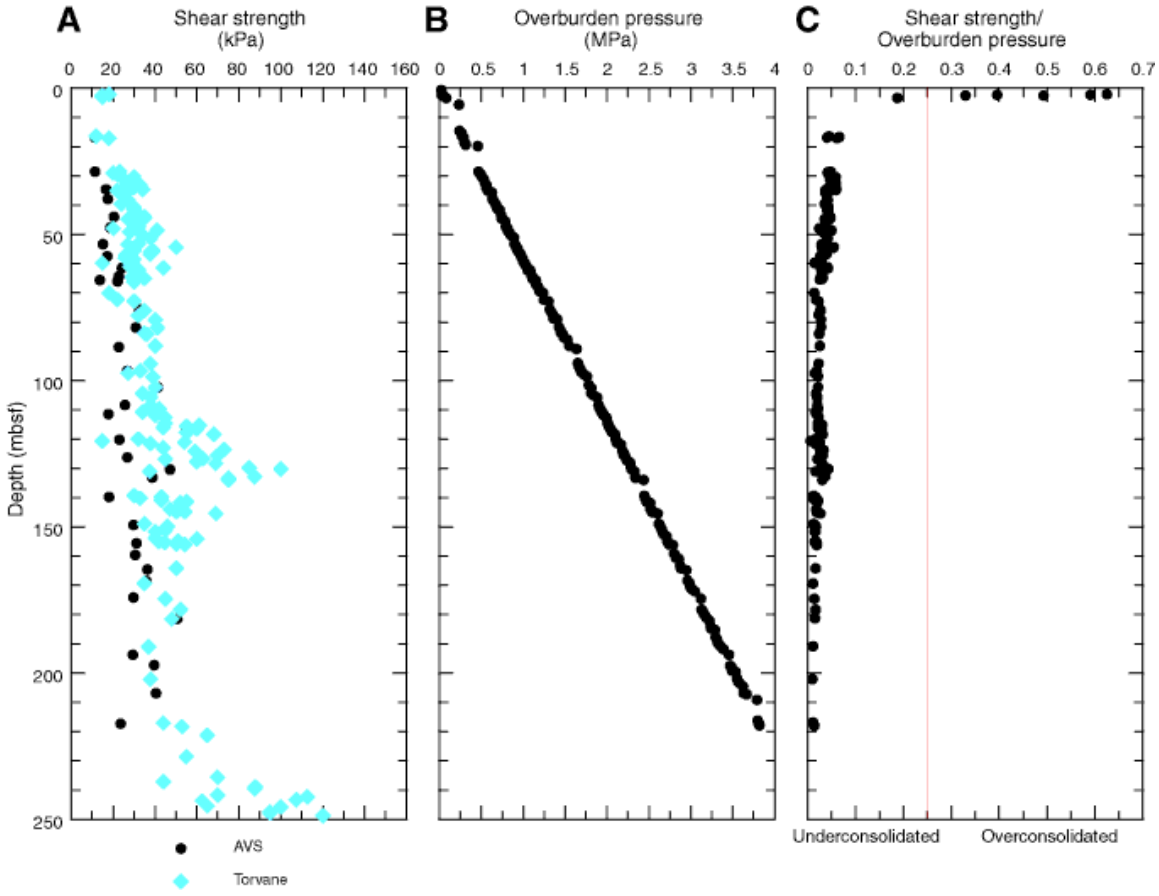

Figure 6.37 Shear strength measurements throughout Holes U1328B and U1328C using the handheld Torvane and the automated vane shear (AVS) system. **A.** Comparison between AVS and handheld Torvane shear strength measurements. **B.** Overburden pressure calculated from MAD bulk density data. **C.** Ratio of Torvane shear strength to overburden pressure. The thin red line at 0.25 separates the degree of sediment under-consolidation or over-consolidation. (From Expedition 311 Scientists, 2006b)

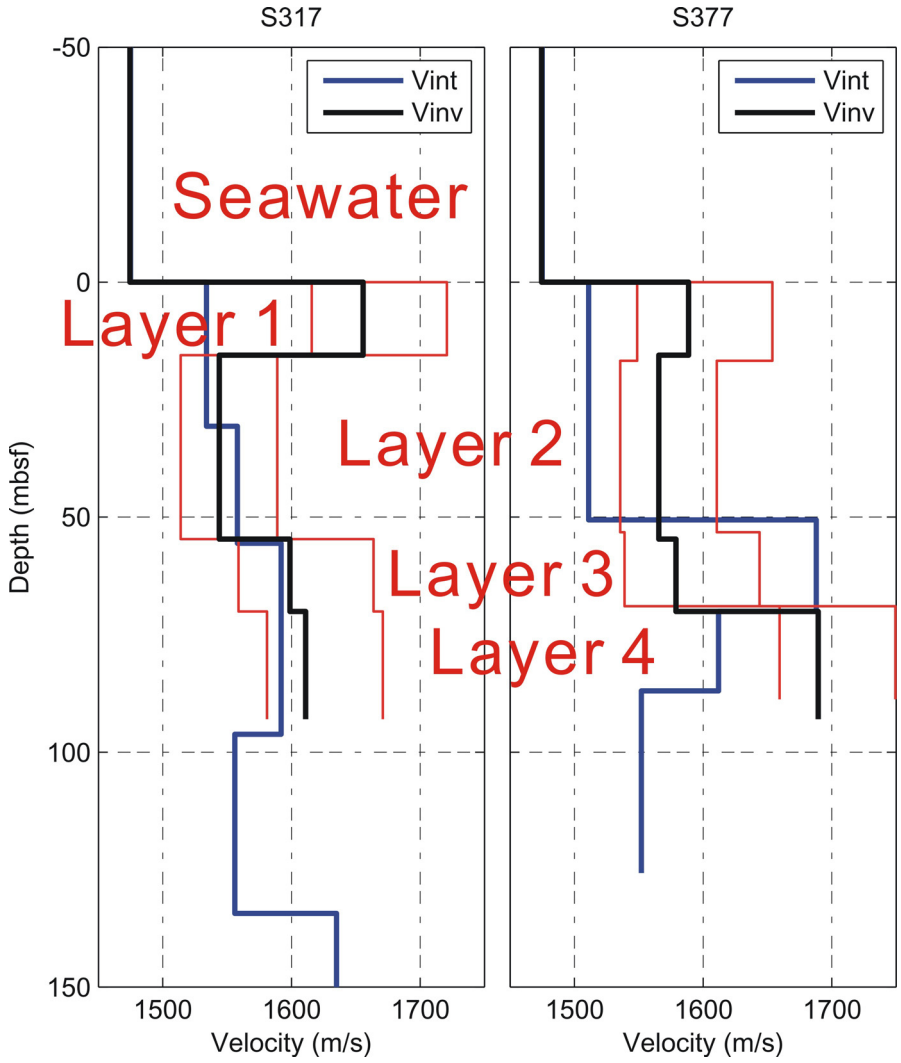

Figure 6.38 Comparison of inverted average velocities (thick black line Vinv) and interval velocities (thick blue line Vint) from NMO analyses at super-CDPs S317 and S318 (see Figure 4.34 for locations; see Figure 6.15 and Figure 6.16 for the error bounds of interval velocities). The possible error bounds for the inverted velocities are indicated by thin red lines.

4. Comparison

Figure 6.38 compares the inverted average velocities and the interval velocities from the previous stacking velocity analyses for the upper ~100 m of sediments at the locations of super-CDPs S317 and S377, on the SW and NE side of the Bullseye seafloor pockmark respectively. At S317, no reflector was picked for NMO analysis at the depth of inverted-layer 1 (~15 mbsf), since the small layer thickness produced large uncertainties in the conversion of NMO velocity to interval velocity. The first sub-

seafloor interface for NMO analysis was at ~30 mbsf (Figure 6.38), corresponding to the depth of hydrate cap diffractions at this position (Figure 4.34; Figure 6.26). The interval velocities for upper 55 m sediments were within the uncertainty bounds of inverted average velocity for layer 2. The inverted velocities for layers 3 and 4 were very similar, and the corresponding interval velocity between 55-95 mbsf was within the uncertainty bounds of the inverted values.

At S377 on the NE side of the seafloor pockmark, the interval velocity for the upper ~50 m sediments was significantly lower than the inverted velocities for layers 1 and 2, although the error bounds for the two methods overlapped (refers to Figure 6.16 for the error bounds of interval velocities). Similarly, error bounds for layers 3 and 4 also overlapped, although the calculated interval velocities themselves showed opposite variations compared to the inverted values: within layer 3 the interval velocity was ~110 m/s higher, while within layer 4 it was ~90 m/s lower. This inconsistency may be due to the stronger reflector dips at this position (Figure 4.34; Figure 6.26).

Also logging data from IODP Site U1328 drilled on this line could provide valuable calibration for the velocity inversion results. Although no velocity measurements could be obtained for the upper 60 m sediments beneath seafloor, other logging (e.g., porosity, density, resistivity) still can recover parts of information for this segment (Figure 6.39). The inverted high velocity layer1 of ~16 m in thickness is supported by the high resistivity values over this depth range (Figure 6.39). These high resistivities at the drill site were interpreted as evidence for massive hydrate with saturations of 60-80% of the pore space (Figure 6.8). Here the high velocities of layer1 are not interpreted as massive hydrate everywhere within this layer, but rather as evidence for widespread carbonate, which has been discussed using reflectivity study (Fink and Spence, 1999). However, only small amount of carbonate was observed within the vent area on bottom images from ROPOS (Beaudet et al., 2001) and other seismic studies using conventional velocity analysis do not support widespread carbonate presence (e.g., Riedel, 2001; this study, Figure 6.15 and Figure 6.16). On the other hand, the local high velocities (~1700 m/s) in layer1 beneath the pockmark (thick red line, Figure 6.39) indicate that the broadest concentrations of massive gas hydrate are beneath

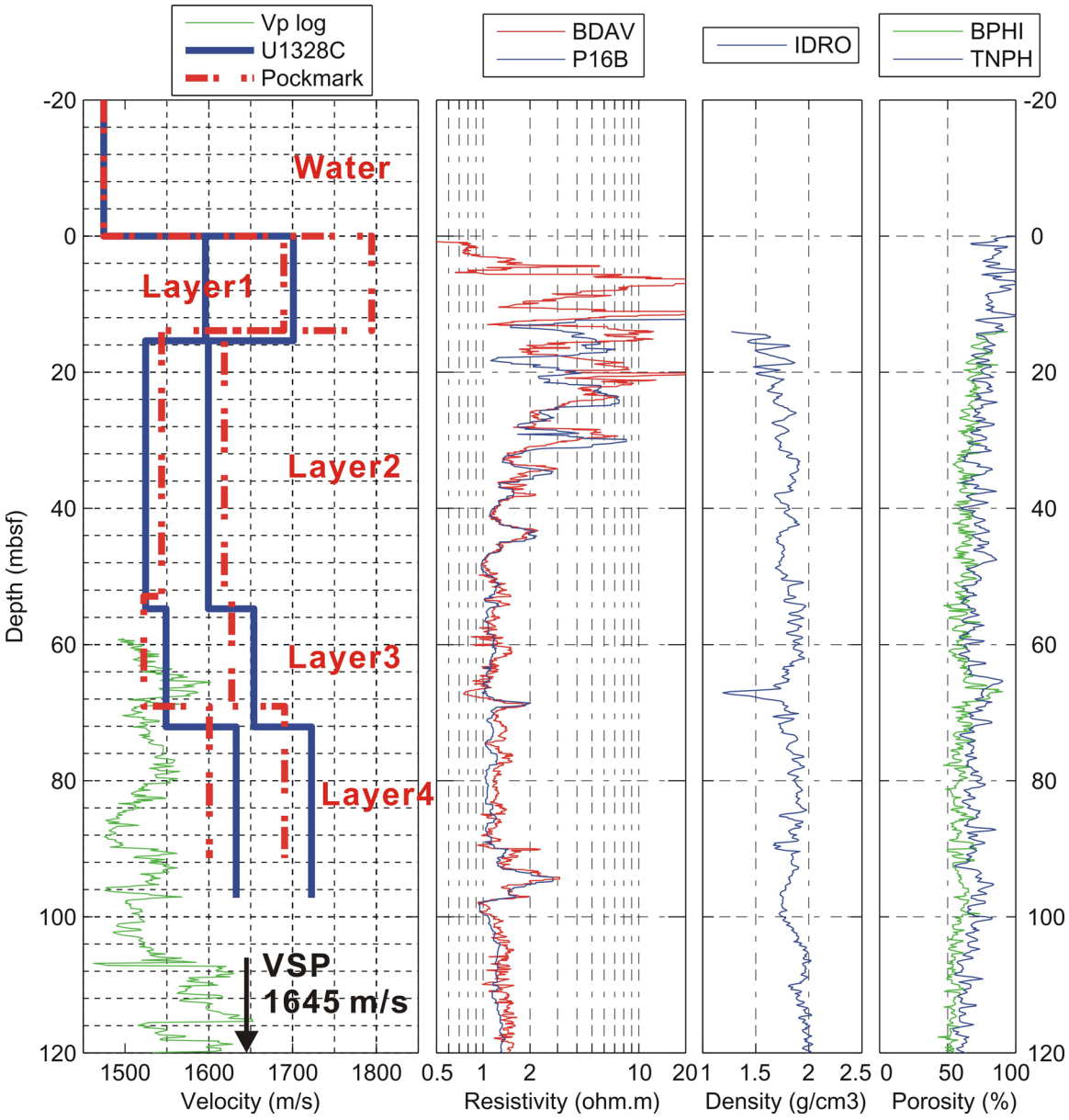

Figure 6.39 Comparisons of the inversion results with the U1328 drillhole logs: (Velocity Panel) inverted sediment velocities as uncertainty band at the locations of drillhole U1328C (thick blue line, offset 2370 m) and nearby seafloor pockmark (thick red dashed line, offset 2460 m), the sonic log (green line), and a constant average interval velocity of 1645 m/s from vertical seismic profile (VSP) (black arrow; refers to Figure 6.40); (Resistivity Panel) Phase Shift Resistivity Blended, 16 in. (P16B, blue line) and Deep Resistivity Average (BDAV, red line); (Density Panel) Image Derived Bulk Density (IDRO, blue line); (Porosity Panel) Best Thermal Neutron Porosity, Average (BPHI, green line) and Thermal Neutron Porosity (TNPH, blue line). Note that except for the sonic log and VSP which were recorded in the Hole U1328C, all other logs came from nearby drillhole U1328A.

the pockmark. This observation is consistent with the high resistivities at the drill site over the upper ~35 mbsf. It is also consistent with the physical evidence of piston cores (see locations on Figure 4.38 and Figure 4.39) during the cruise in July 2000, which recovered massive hydrate at depths of 3-8 m below the seafloor. For the local high velocity region (~1575 m/s) across U1328 in the inverted "low" velocity layer2 (16-56 mbsf, thick blue line), it is probably still associated with the upper high resistivity segment (~16-30 mbsf, Figure 6.39) in this layer.

Compared to velocities of ~1590 m/s in layer3 from 55 to 72 mbsf, the Vp log at U1328 shows a localized high velocity region from 60-70 mbsf, with a maximum value of ~1600 m/s; over this region, the inversion result and the Vp log are consistent, within the about ±50 m/s error of the inversion (Figure 6.39). In addition, the inversion result also shows a small velocity depression in layer3 over model distance 2400-2500 m, just northeast of U1328 (Figure 6.31). This lateral change perhaps relates to the corresponding abnormally high porosity and low density values at ~68 mbsf (Figure 6.39).

In layer4 at 72-96 mbsf, the inverted velocity is around 1650 m/s and apparently higher than the Vp logging of 1500-1550 m/s (thick blue line, Figure 6.39). Although this discrepancy may be caused by abnormal high velocity within the single cell at U1328 (yellow color cell in layer4 beneath the arrow of U1328, Figure 6.28), the velocities beneath pockmark (thick red line, Figure 6.39) and around these two locations (Figure 6.28; Figure 6.32c) are still obviously higher than the Vp log. This low Vp log segment might be caused by the well mud, or it might reveal the velocity structure in this seismically "blank" area, since the low velocity values and a very low variability are consistent with the low seismic reflectivity (Expedition 311 Scientific Party, 2006). However, the inverted layer4 velocities match the Vp log and an average interval velocity of 1645 m/s from vertical seismic profile (VSP) within error bounds by extending the inverted values to a depth of 106 mbsf (Figure 6.39 and Figure 6.40). In any case, the Vp log or VSP only represents velocity at one location of tens cm in diameter, so it still is not directly comparable to the inverted velocity which average velocities over tens of meters horizontally and vertically. As shown in Figure 6.39, the inverted velocity profile directly

beneath the pockmark feature shows a different variation pattern from the one at U1328 only 90 m away. The localization of sediments may be caused by steeply dipping fractures that act as conduits feeding the near surface gas hydrate accumulation (Expedition 311 Scientific Party, 2006), and thus make it difficult to extend the knowledge at the drill hole over a broader region.

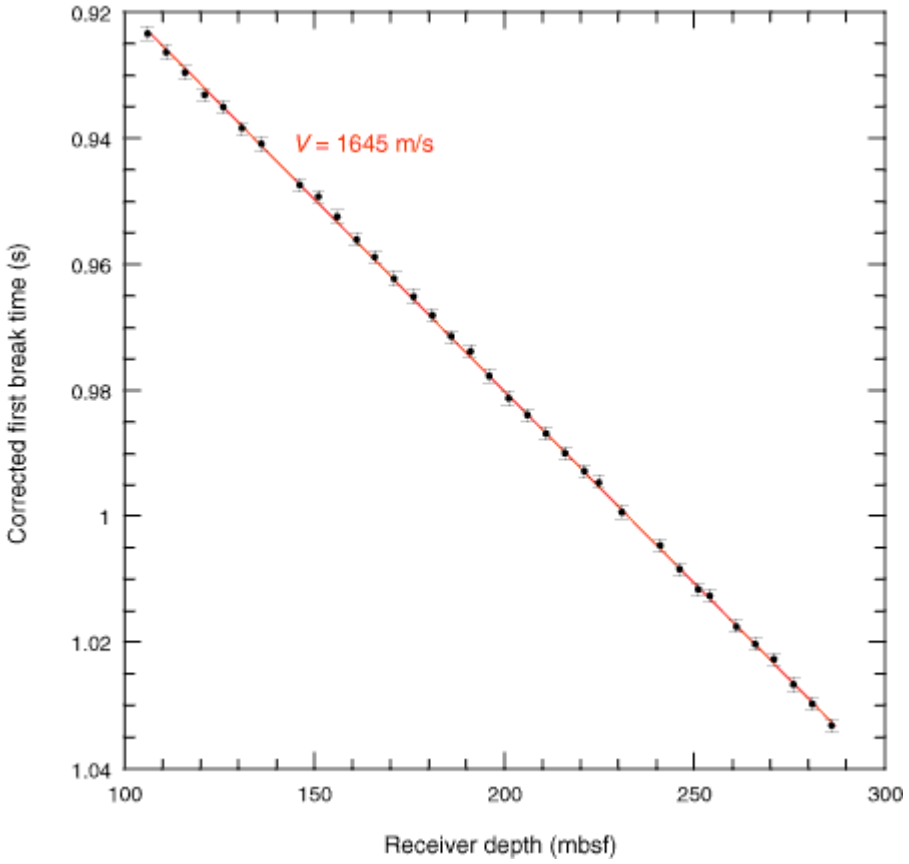

Figure 6.40 Time vs. depth plot of first break times in the Hole U1328C vertical seismic profile. The best-fit straight line indicates an average interval velocity (V) of 1645 m/s. The error bars show combined uncertainty in the picked first break times of ±1 ms. (From Expedition 311 Scientists, 2006b)

Chapter 7

Discussions

7.1 Do Heat Flow Variations Indicate Fluid Flow?

For seismic profile SCS-42 (Figure 5.2 and Figure 5.4) across the central mound of Cucumber Ridge, there is no direct answer whether the BSR-based heat flow variations indicate localized fluid flow, since most of the variations are explained by the simple 2D topography model (Figure 5.4b). A 3D model is required for more accurate modeling, as noted in previous section 5.1.2.2. However, the heat flow anomaly northwest of the mound along its steep seaward slope Figure 5.2) is even larger than that modeled along SCS-42 (25-30 mW/m^2 vs. ~20 mW/m^2), while the steepness of the slope is about the same or smaller. Therefore it tentatively can be concluded that much of this prominent heat flow anomaly is due to localized fluid flow. Upward flow rates of the order of 1 mm/yr are required for disturbance to the thermal regime of this magnitude (e.g., Hyndman et al., 1993).

Profile SCS-1 was chosen to present heat flow variations just south of the central mound where high heat flow also is found (Figure 5.5). The topography-corrected heat flow matches the observed values only over a limited eastern portion of the line (Figure 5.5b). The highest observed heat flow values occur at the scarp where the predicted values also have a maximum. The topographic effect due to the scarp is quite limited in lateral extent. Over a distance range of ~500 m both seaward and landward of the slope, the topographic effect should reduce heat flow by up to 12 mW/m^2 relative to heat flow near the scarp. However, the observed heat flow in the region is only ~5 mW/m^2 lower than the values at the scarp. There is thus a positive heat flow anomaly of at least 7 mW/m^2 on both sides of the scarp, which cannot be explained by a simple 2D topographic effect. This anomaly is probably not due to complex 3D topographic effects, especially for landward side, because the surrounding seafloor is relatively flat (Figure 5.2). The fresh water (low salinity) from a deep source or from hydrate formation could

elevate BSR depths and produce such a small positive heat flow anomaly (7 mW/m^2), however, there is little direct evidence around Cucumber Ridge to support this argument.

Warm fluids may produce the localized high heat flow, with faults or fracture zones providing migration channels. Figure 7.1(c) shows COAMS seismic section IN-18, which crosses the SCS-1 high heat flow area and perpendicularly intersects seismic sections SCS-42 and SCS-1 (Figure 2.1 and Figure 5.2). The seafloor near SCS-1 forms a shallow valley with only small slopes. The 2D model topography-corrected values are close to the regional background heat flow southeast of the valley. However, observed heat flow over the valley itself has a positive anomaly as large as 6 mW/m^2 (± 2) higher than the theoretical value, with the observed peak located near SCS-1 (Figure 7.1b). On the seismic image, the central portion of this section appears uplifted relative to the flanks, particularly to the northwest where strong reflectors are observed. Seismic blanking zones occur in this central segment. A prominent blank zone is present just to the southeast of SCS-1; this zone extends to the surface, and is underlain by a particularly bright BSR that may be associated with a large gas accumulation. The blank zone may indicate faults or fracture zones, providing pathways for warm fluids and producing a local high in heat flow.

7.2 Genesis of Cucumber Ridge Carbonate Mound

Worldwide, most carbonate mounds originated either as bioherms (e.g., in the north-eastern Orphan Basin and on the Orphan Knoll offshore Newfoundland, Figure 1.7) or as mud volcanoes formed as a result of the rise of fluidized mud along faults and fractures (e.g., Mound Culebra offshore Nicoya Peninsula, Costa Rica, Figure 1.8) (Milkov, 2000). However, analyses of seismic data and submersible observations indicate that Cucumber Ridge is different from the above two types and is more representative of a structural topographic high cemented by authigenic carbonates.

It is noted that the original layering is present beneath portions of the mound and that these layers are deformed by compressive deformation (e.g., Figure 5.4c, Figure 5.8a, Figure 5.11a). The steep seaward slope of the mound is interpreted to represent the region of deformation in the hanging wall of a major reverse fault. Significant seismic blanking

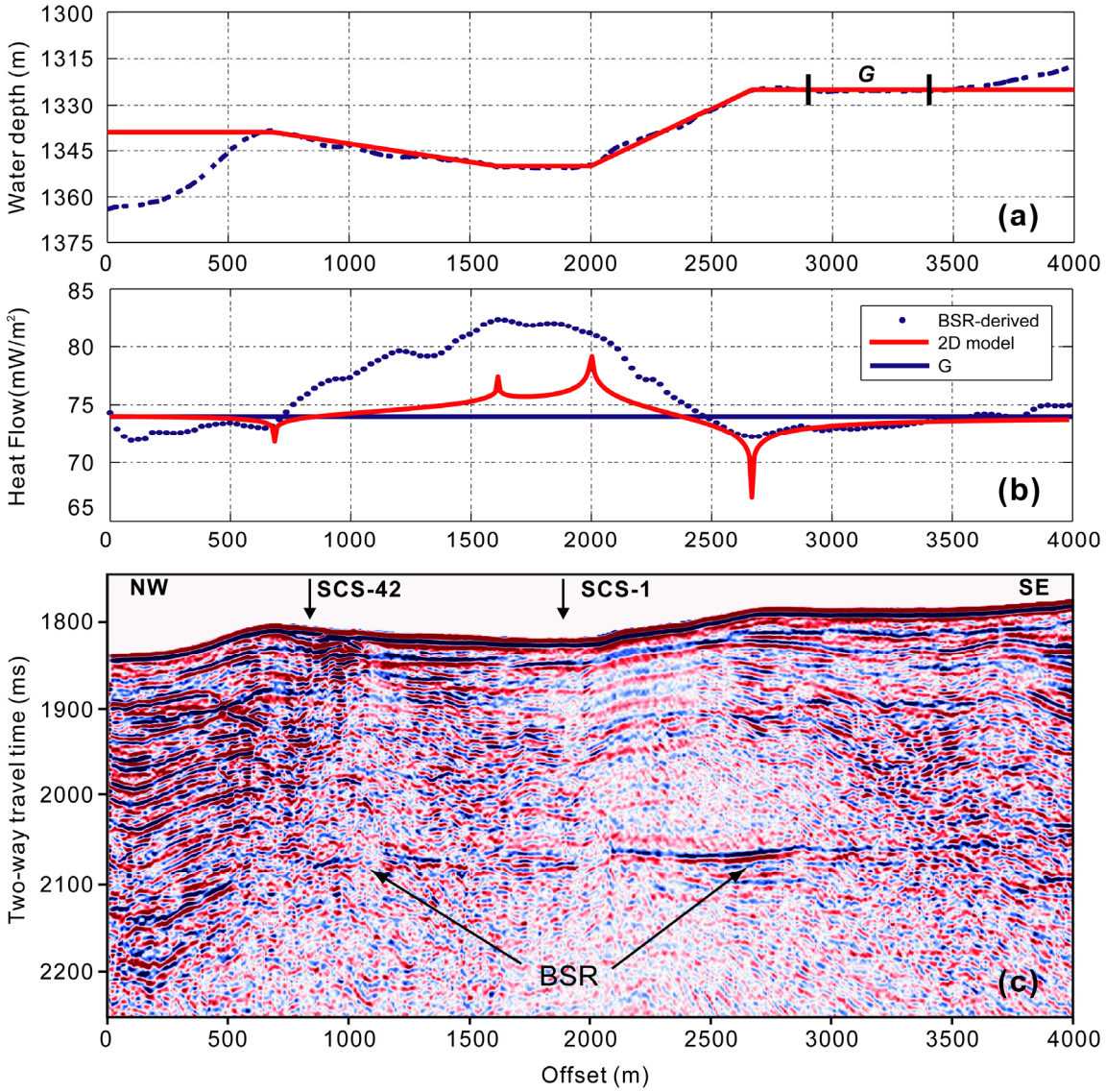

Figure 7.1 Local heat flow variations and 2D model topographic corrections along the 1999 COAMS grid inline IN-18 across flat area east of the central mound (see Figure 2.1 and Figure 5.2 for locations). (a) Seafloor topography (dashed blue line) and its 2D plane surface approximation (red line). The flat area (also shown in Figure 2.1 and Figure 5.2) used to set regional background heat flow is also labelled with *G*. (b) BSR depth derived heat flow observations (blue dots) and 2D model topographic correction (red line) for regional heat flow value *G* of 74 mW/m^2 (horizontal blue line). (c) Seismic section of IN-18, showing the complex uplifted sediments, seismic blanking zone, and strong BSR segment. Intersections with lines SCS-1 and SCS-42 are indicated by the arrows.

is present beneath the central portion of the mound, which is an indicator of extensive deformation and may imply that vents and associated fractures are located throughout the blanking region (Figure 5.4c and Figure 5.8a). The origin for the seismic blanking is likely similar to that proposed for vents in the Bullseye region just to the south of Cucumber Ridge. In detail, however, the nature of the blanking is subtly different beneath Cucumber Ridge compared to Bullseye vent. Below the mound, the seismic blanking is observed from both low frequency signals (e.g., airgun, Figure 5.10a) and high frequency signals (e.g., DTAGS, Figure 5.10b). The blanking is probably produced by attenuation due to either (1) scattering from highly-deformed sediments (e.g., Figure 5.10), or (2) absorption by sediments mixed with fluid, gas and hydrate. In addition, a portion of the seismic blanking can be attributed to absorption and scattering by the seafloor carbonate cover. In contrast, the sediment layers below the seafloor pockmark of Bullseye vent can commonly be traced through seismic blanking zones on low frequency seismograms (e.g., Figure 6.9a), while diffractions are more likely present on high frequency seismograms (e.g., Figure 6.9b). This observation is consistent with a more diffuse fluid flow system and a hydraulic fracture zone in shallow sediments (Tréhu et al., 1999; Zühlsdorff and Spiess, 2004). These near-vertical hydraulic fractures are small fluid conduits and thus do not disrupt sediment layering much; however, free gas bubbles and hydrate nodules within those hydraulic fractures will produce scattering and diffractions, particularly for high frequency signals. With a higher degree of seismic blanking at Cucumber Ridge, this would suggest that fracturing is more extensive and fluid flow is more vigorous beneath Cucumber Ridge than below Bullseye vent. However, it is noticed that the stronger BSR beneath Cucumber Ridge than beneath Bullseye vent may not be consistent with more vigorous fluid flow beneath Cucumber Ridge.

Visible fractures associated with faulting on the seafloor are observed by the submersible ROPOS at Cucumber Ridge (Figure 5.6a). In the seismic images, a fault zone (e.g., F1 in Figure 5.8a) is observed extending from the seafloor to the depth below BSR, where brightened reflectors are present and might indicate a gas accumulation zone. The fault zone provides pathways for fluids including gas to migrate from BSR depths to the seafloor. Near the seafloor the methane is subject to oxidation and bacterial action,

and diagenetic carbonate forms and cements the near-surface soft sediments. The venting also provides nutrients around the active vent area to feed local biological communities (deep-water coral, clams, sea cucumbers, tubeworms, etc.; Figure 5.6b). ROPOS observed that the vent biota at Cucumber Ridge are more diverse and densely populated than at Bullseye vent, and this is an additional evidence that fluid flow is more vigorous beneath Cucumber Ridge than below Bullseye vent. As well, carbonate appears to be more widespread at Cucumber Ridge than at Bullseye vent; piston coring at Cucumber Ridge was completely unsuccessful probably due to hard carbonates, while abundant piston cores at Bullseye vent indicated that near-surface soft sediments were common. The more widespread hard carbonate-cemented sediment cover at Cucumber Ridge may indicate that fluid flow has been longer-lived at Cucumber Ridge than at Bullseye vent.

Cucumber Ridge may be a small-scale version of Hydrate Ridge, located on the Southern Cascadia margin, offshore Oregon. The seafloor morphology of Hydrate Ridge likely developed through uplift along thrust faults within accreted sediments and associated fluid flow cemented near-surface sediments through formation of authigenic carbonates. Also, the north-to-south variation in venting activity from Cucumber Ridge to the vent field around Bullseye vent may be similar to the variations observed by Tréhu et al. (1999) along Hydrate Ridge. Around the north peak of Hydrate Ridge, there are abundant indicators of focused fluid flow, including massive carbonates and communities of vent-dependent organisms, upward deflection of the BSR, and vigorous streams of methane bubbles; in contrast, the southern part of Hydrate Ridge has soft sediments with massive shallow gas hydrate, but shows less evidence for focused fluid flow on the sea floor. Thus, Tréhu et al. (1999) proposed that that the northern part of Hydrate Ridge is more mature than the southern part. Similarly, Cucumber Ridge in the north is more mature than the venting field in the south.

7.3 Focused Fluid Flow Venting – Mounds vs. Pockmarks

Worldwide, some vents produce large seafloor structures with positive topography, while others produce seafloor depressions. The two different seafloor morphologies for seafloor mounds and pockmarks can be related to the fluid expulsion

rate. Roberts et al. (2006) suggested three qualitative ranges in the rates of fluid and gas expulsion in the northern Gulf of Mexico continental slope, corresponding to three gas-hydrate domains and associated geologic-biologic responses at the seafloor (Figure 7.2):

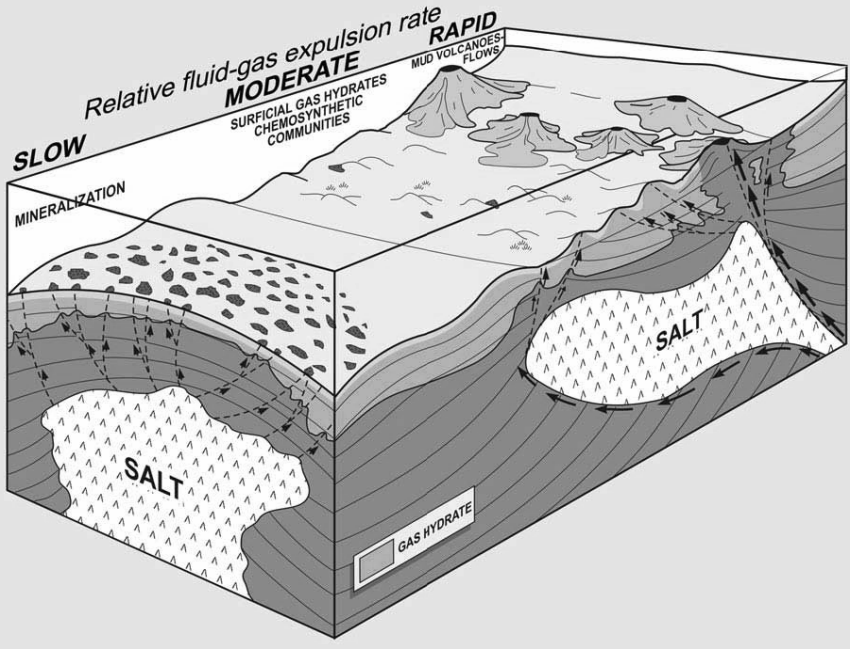

Figure 7.2 Block diagram schematically illustrating the three deepwater types of seafloor responses proposed by Roberts et al. (2006), corresponding to rapid-to-slow fluid and gas expulsion (see text). In this study area Cucumber Ridge and Bullseye vent both belong to the regime of moderate fluid-gas expulsion rate, which exhibits productive chemosynthetic communities, extensive carbonate formation and locally massive gas hydrate in shallow sediments. (From Roberts et al., 2006)

1. Rapid flux or venting may be associated with deep-cutting faults that intersect an overpressured gas reservoir. Fluid and associated gas migrate along these pathways and fluidize sediments. If mud flows in sufficient volumes, mud volcanoes can be created. The hydrocarbons within the mud flow are subject to oxidation and bacterial action, and thus carbonate forms and cements the mud volcanoes into carbonate mounds. During this process, considerable heat can be brought by deep-sourced fluid to the shallow sediments, which may disrupt the gas-hydrate stability zone or dramatically shift it toward the seafloor along the migration pathways. Gas hydrates can form in mud vents that are inactive or in flank sediments.

2. Slow flux, or seepage, may be associated with short migration routes. These systems eject hydrocarbons over a widespread region. Cementation of surficial sediments is commonly associated with microbial communities and authigenic carbonates. Gas hydrate may occur in the subsurface, but never at the seafloor. At Gulf of Mexico a seafloor camera showed that slow-flux and rapid-flux environments do not support well-populated and diverse chemosynthetic communities.
3. Moderate flux may supply gas at such a rate that seafloor-exposed and shallow-subsurface gas-hydrate deposits are maintained and rebuilt after hydrate instability and dissociation due to very low gas concentrations in the water column. Moderate flux may produce optimal conditions for vent biota, with gas hydrates created in the very shallow subsurface and some hydrate being exposed as localized outcrops.

Based on above definitions, in this study area Bullseye vent may be representative of moderate fluid rates, since massive hydrate was recovered in the shallow subsurface, and extensive carbonate pavement is observed on the seafloor, although only few chemosynthetic communities occur. Cucumber Ridge is likely also representative of moderate fluid rates. It should be emphasized that Cucumber Ridge is a structural high associated with large faults, and was not formed as a mud volcano associated with rapid fluid flow rates. Compared to Bullseye vent, however, fluid flow could be more vigorous and longer-lived at Cucumber Ridge, with evidence of more well-populated and diverse vent biota and a more widespread hard sediment cover cemented by authigenic carbonate. No hydrates have been recovered at Cucumber Ridge, but there have been only two submersible observations by ROPOS in 2001 (Beaudet et al, 2001) and 2002 (N.R. Chapman, personal communication, 2007), respectively, and deeper piston coring was unsuccessful due to carbonate. It is possible that hydrate might be observed either by additional submersible operations or perhaps through shallow drilling that could penetrate the carbonate.

Chapter 8

Summary

8.1 A Methodology for Optimal DTAGS Data Processing

Since significantly nonlinear variations of the source depths and receivers locations occurred during the entire DTAGS2 survey, a specific process routine was developed in this study for DTAGS data processing, including cable geometry estimation, floating datum time correction, acoustic image stitching and mapping, and velocity analysis from wide-angle travel time inversion.

As the basis of this procedure, cable geometry estimation is the first and the most critical step since all later processes, including data imaging and velocity analysis, are highly sensitive to source and receivers positions. A Genetic Algorithm inversion method was developed to find positions of the sources and receivers, using the known node depths and manually picked direct arrivals and the reflections from the sea surface. This method is an improvement of the method developed by Walia and Hannay (1999) and determines the cable geometry much better for stitching high resolution images.

To achieve high quality seismic images, a source-receiver pair is first corrected to its average depth, using a linear velocity function to calculate time shifts. Since the average depths form a floating datum, the traces can then be easily corrected to vertical incidence from the seasurface by applying NMO and vertical time shifting with water velocity. By defining reflection midpoint (RMP) locations for the entire receiver array, a series of overlapping areas is carefully examined to find the optimal shot position by using the redundant data between 2 adjacent shot gathers. Then a 100% coverage acoustic image is formed by stitching acoustic array data from neighbouring shot gathers.

The conventional stacking velocity analysis is challenging for the high resolution DTAGS data because of (1) unknown errors from datum corrections for nonlinear cable geometry, and (2) large uncertainty of interval velocities for those shallow thin layers. Thus a ray-trace-based inverse method, using the optimal source and receivers positions,

was developed in this study to implement the DTAGS velocity analysis. Using both the acoustic and geophysical arrays of the streamer, the method simultaneously inverts traveltimes for both vertical incidence and wide-angle reflections for a series of sub-bottom events. The 2D method inverts for reflector depths and average layer velocities using a nonlinear pattern search algorithm that examines the global parameter space through a series of expanding and contracting grid selections.

Using the ship's DGPS locations and/or partly corrected transponder net navigation, the absolute positioning of the DTAGS image on a bathymetry map is determined. Thus the final processed images and inverted sediment velocities can be analyzed with bathymetry information and compared to nearby seismic data sets and IODP drill holes.

8.2 Evolution Model for Cucumber Ridge

A large carbonate mound, Cucumber Ridge, was previously identified on the mid-slope region offshore Vancouver Island by seismic data and seafloor observations. Cucumber Ridge has a steep slope (~70 m high) seaward of the central mound, and a broad relatively flat plateau is present landward of the central mound. Thus the seafloor morphology of Cucumber Ridge is different from base-rooted giant bioherms or many diapiric mud domes for which slopes are relative steep in all directions. However, the internal structures of Cucumber Ridge show that it is distinct from either a bioherm or a diapiric mud dome.

A conceptual model for the evolution of Cucumber Ridge was developed based on seismic observations and the local tectonic setting. During an initial phase, under lateral tectonic compressive stress, large reverse faults formed at the base of the current steep seaward slope of the ridge. These faults provided pathways for fluids including methane to migrate from BSR depths (or even deeper) to the seafloor. Weakened by the fluid, sediment layers near the steep slope were subject to compression and deformation, and the hanging-wall block ascended along reverse faults to form a mound. Fluid flow is focused beneath the mound, where severe sediment deformation produces a loss of seismic stratigraphy. At the mound crest, the released methane is subject to oxidation and bacterial action, and diagenetic carbonate forms and cements the original soft mud.

8.3 Local High Fluid Flow over a Regional Heat Flow Map

The pervasive existence of BSRs at Cucumber Ridge and in the surrounding region provides the opportunity to investigate the relation between focused fluid flow and the formation of a mud/carbonate mound. Through quantitative assessment of topographic corrections on a BSR-derived heat flow map, possible high fluid flow regions are identified at the same locations where abnormal high heat flow occurs.

The heat flow derived from the depth of the BSR shows a 20 mW/m^2 positive heat flow anomaly around the mound and a ~6 mW/m^2 local negative anomaly over the mound. Heat flow within the flattest portion of the surrounding 4 km by 8 km region averages ~74 mW/m^2. Taking this value to represent the regional or background heat flow, a simple 2-D analytical method was used to calculate theoretical heat flow variations due to topography. Most of the variability along the mound midline is explained by topographic effects.

However, in a 2-km-long band just south of the mound including a region of flat seafloor, a 6-7 mW/m^2 positive anomaly remains even after the 2D topographic correction. Thus, this anomaly is significant and is likely due to warm fluid flow along faults or fracture zones. On both the Teledyne SCS image and DTAGS deep-towed MCS image, a possible fault or conduit for warm fluid flow and gas is indicated by the strip of strong reflectivity along a zone extending from BSR depth to near the seafloor, where a seafloor depression occurs.

Furthermore, a positive heat flow anomaly to the northwest of mound is even larger than that along the mound midline, although the steepness of the slope is about the same or smaller. Thus, this may be another indication that this prominent heat flow anomaly may be due, at least in part, to localized fluid flow.

8.4 Seismic Observations around Bullseye Vent

Because of high frequency range of the DTAGS signals (220-1k Hz) compared to the conventional surface-towed MCS (e.g., COAMS) and SCS (e.g., Teledyne) data sets, the DTAGS system provides high resolution images of subseafloor sediment layering and geologic structures. Although DTAGS does not resolve BSRs in the Northern Cascadia

margin, it better defines the boundary between highly and less deformed sediment regions over the study area.

Multiple seismic blanking zones were resolved within a slope sediment block that was uplifted by about 45 m. The blanking zones likely represent fluid vent sites or proto-vents, since not all of them extend upwards to the seafloor. At the largest vent in the region, Bullseye vent, Teledyne SCS images show a single reflector representing the top (or cap) of a region of massive hydrate. On DTAGS seismic sections, the massive hydrate appears as a ~10-m-thick high reflectivity zone, extending from the seafloor to a depth of ~30 m and dipping seaward (SW) at a small angle of ~7^{o}. This likely corresponds to the upper portion of the massive methane hydrate layer (~35 m in thickness) that was encountered at IODP Site U1328. This high reflectivity zone is interpreted as a complex near-surface hydraulic fracture system filled by hydrate and associated with steeply dipping faults below it.

The 2D velocity structure was obtained for a segment of line DT09, which crossed Bullseye vent and passed through IODP Site U1328. For sediments within the upper 100 mbsf, picked traveltimes were inverted for average layer velocities within a 4-layer model. Although the inversion results are highly sensitive to the DTAGS streamer geometry, the inverted sediment velocities in this study fall within reasonable ranges as expected for shallow sediments. This is the first time that meaningful sediment velocities are obtained from a DTAGS data set.

Compared to the normal under-consolidated seafloor sediments with velocities around 1500 m/s, layer1 is a high velocity layer with values that undulate around 1650 m/s. This thin layer has thicknesses of 14-17 m and is thought to be due to the presence of carbonate-cemented sediments. For example, if a 3-m-thick carbonate layer with velocity of 3000 m/s (see Fink and Spence, 1999; Hamilton, 1978) is interbedded in a 15-m-thick normal sediment layer with velocity of 1500 m/s, the average velocity for this sediment/carbonate layer will be ~1650 m/s. This layer, with a very strong reflector at its base, appears to be common on most DTAGS lines from Bullseye vent in the SE to Cucumber Ridge in the NW; thus it might imply that there was pervasive high fluid flow over the entire study area, or localized high fluid flow regions occurred episodically over large portion of the area. However, the widespread carbonate presence was not supported

by other seismic velocity analysis (e.g., Figure 6.15 and Figure 6.16) or piston coring results, and only observed within the vent area by ROPOS. Layer2 has layer thickness of 35-40 m with relatively low velocities mainly varying between 1540-1580 m/s. Low sediment velocities are consistent with sediment shear strength measurements at IODP Site U1328, which indicate that all of layers 2-4 are in the under-consolidation environment. In the vicinity of a prominent seafloor pockmark, inverted velocities are higher than outside for both layer1 and layer2; this is consistent with high concentrations of gas hydrate over depth range of about 5-35 m as indicated by the high resistivity values from nearby IODP drill hole U1328. Seaward of U1328, a small velocity increase occurs from layer2 (~1560 m/s) to layer3 (~1600 m/s). This may indicate that sediment consolidation increases with depth by a small amount. Layer4 seems have very similar lithology to layer3, since its velocities are also mostly around 1600-1620 m/s.

8.5 Suggestions for Future Work

8.5.1 DTAGS Cable Geometry Control and Data Recording

Because of the great sensitivity of velocity inversion and subseafloor structure imaging to DTAGS cable geometry, it is essential that better controls should be considered to determine DTAGS cable geometry more accurately.

As a minimum, another 3 depth sensors should be added on channels 24, 34 and 44. Also the data recording should start from 0 time, thus the direct arrivals can be picked on all channels, not limited to the last 2-4 traces. Gain controls will likely be needed to balance the reflection energy and direct arrivals; these effects can be removed by reverse operations. Ideally, “birds” or depth control sensors should be added to the DTAGS cable to keep it horizontal during the survey.

With the information of full direct arrivals and more node depths, the DTAGS cable might be estimated in 3D, not current 2D which must have the source and all receivers at a same vertical plane. However, to more directly address 3D cable geometry, compasses could be added to cable nodes.

8.5.2 Optimal Inversions for Cable Geometry and Sediment Velocity

In the current process for cable geometry estimation, water velocity is directly calculated based on the depths of the source and the last channel averaged over a shot interval of 30 s, and these are used to invert for the positions of the remaining channels. Although this works well for most DTAGS segments, in some segments these averaged depths may not be representative of the actual depths if rapid changes occur, which would result in bad cable geometry predictions. For example, on transit line DT16 many seismic segments showed artificial curved sediment layering. To reduce potential depth reading errors, small vertical shifts for the depth readings may be introduced as four additional inversion variables.

In the velocity inversion test at Bullseye vent, the algorithm freezes the previous layer when it proceeds downward from layer to layer. Thus the shallower layers cannot obtain feedback from rays passing through them to deeper reflectors. To provide better constraints on inversion results, a possible improvement is to invert all wide-angle traveltimes together for different layers and reflectors.

Another approach for DTAGS imaging and velocity analysis is using Kirchhoff prestack depth migration, which can derive tomographic migration velocity and image the DTAGS data directly from the actual source and receivers depths. Thus, the need is eliminated that time-shift the DTAGS data to a constant depth in order to proceed with conventional time processing (D. Lawton, personal communication, 2007).

8.5.3 Interesting Targets for Later Cruise Project

To expand the current knowledge over the study area, some predictions from seismic images and heat flow map should be verified by scientific cruise. As discussed in section 5.3, the possible gas plume locations of P1 and P2 are two interesting targets. Also several sediment heat probe measurements should be arranged in the high heat flow region of P1; perhaps the difference between the shallow heat-probe measurements and the deeper BSR-derived values could be used to calculate local fluid flow rate.

The structural high from blanking zone BZ2 to BZ4 implies high concentration of gas hydrate within deeper sediments. Simple drilling using a seafloor-mounted shallow drilling rig might be able to obtain hydrate samples from sediments about 20 mbsf.

References

Ashi, J., Saito, S., Aoike, K., Toki, T., Kuramoto, T., and Henry, P., 2002. Seafloor manifestations of fluid venting and shallow gas hydrate BSRs at the outer ridge of the eastern Nankai Trough. ***Eos*** (Transactions, American Geophysical Union), v. 83, no. 47, Fall meeting supplement, abstract T11B-1248.

Bailey, W., Shannon, P.M., Walsh, J.J., Unnithan, V., 2003. The spatial distributions of faults and deep sea carbonate mounds in the Porcupine Basin, offshore Ireland. ***Marine and Petroleum Geology***, 20, 509-522.

Bangs, N., Sawyer, D., Golovchenko, X., 1993. Free gas at the base of the hydrate zone in the vicinity of the Chile triple junction. ***Geology***, 21, 905-908.

Beaudet F., Riedel, M., and Chapman, R., 2001. ROPOS gas hydrate 2001: A seafloor survey at methane cold seeps offshore Vancouver Island, April 30-May 7, 2001. ***CEOR report 2001-2***, University of Victoria, Canada.

Ben-Avraham, Z., Smith, G., Reshef, M., Jungslager, E., 2002. Gas hydrate and mud volcanoes on the southwest African continental margin off South Africa. ***Geology***, 30, 927-930.

Brown, H.E., Holbrook, W.S., Hornbach, M.J., Nealon, J., 2006. Slide structure and role of gas hydrate at the northern boundary of the Storegga Slide, offshore Norway. ***Marine Geology***, 229, 179-186.

Chapman, N.R., Gettrust, J.F., Walia, R., Hannay, D., Spence, G.D., Wood, W.T., and Hyndman, R.D., 2002. High-resolution, deep-towed, multichannel seismic survey of deep-sea gas hydrates off Western Canada. ***Geophysics***, 67(4), 1038-1047.

Chen, M., Riedel, M., Hyndman, R.D., and Dosso S.E., 2007. AVO inversion of BSRs in marine gas hydrate studies. ***Geophysics***, 72(2), 31-43. (doi:10.1190/1.2435604)

Cita, M.B., Camerlenghi, A., Erba, E., McCoy, F.W., Castadrori, D., Cazzani, A., Guasti, G., Gambastiani, M., Lucchi, R., Nolli, V., 1989. Discovery of Mud diapirism on Mediterranean Ridge. A preliminary report. ***Bollettino della Società Geologica Italiana***, 108, 537-543.

Clennell, M.B., Hovland, M., Booth, J.S., Henry, P., and Winters, W.J., 1999. Formation of natural gas hydrate in marine sediments 1: Conceptual model of gas hydrate growth condition by host sediment properties. ***Journal of Geophysical Research***, vol. 104, B10, 22985-23003.

Clowes, R.M., Yorath, C.J., Hyndman, R.D., 1987. Reflection mapping across the convergent margin of western Canada. ***Geophysical Journal of the Royal Astronomical Society***, 89, 79–84.

Coppens F., and Mari J.L., 1984. L'égalisation spectrale: un moyen d'améliorer la qualité des données sismiques (Spectrum equalization as a tool for improving the quality of seismic data). ***Geophysical Prospecting***, vol 32, 258-281.

Conn, A.R., Gould, N.I.M., and Toint, Ph.L., 1991. A Globally Convergent Augmented Lagrangian Pattern Search Algorithm for Optimization with General Constraints and Simple Bounds. ***SIAM Journal on Numerical Analysis***, 28(2), 545-572.

Conn, A.R., Gould, N.I.M., and Toint, Ph.L., 1997. A Globally Convergent Augmented Lagrangian Pattern Search Algorithm for Optimization with General Constraints and Simple Bounds. ***Mathematics of Computation***, 66(217), 261-288.

Currie, C., Eaton, D. Bloomer, S., Chapman R. and Hyndman, R. 1999. A Seismic Study of Deep Sea Gas Hydrate in the Cascadia Accretionary Prism, Offshore Vancouver Island. ***Canadian Geophysics Union Annual Scientific Meeting***, Banff, May 9-13.

Davis, E.E., Currie, R.G., Sawyer, B.S., 1987. Marine geophysical maps of western Canada: regional SeaMARC II acoustic image mosaics and Sea Beam bathymetry. ***Geological Survey of Canada Maps***, 2-1987 to 17-1987.

Davis, E.E., and Hyndman, R.D., 1989. Accretion and recent deformation of sediments along the northern Cascadia subduction zone. ***Geological Society of America Bulletin***, 101, 1465-1480.

Davis, E.E., Hyndman, R.D., and Villinger, H., 1990. Rates of fluid expulsion across the northern Cascadia accretionary prism: constraints from new heat flow and multichannel seismic reflection data. ***Journal of Geophysical Research***, 95, 8869-8889.

Dickens, G.R. and Quinby-Hunt, M.S., 1994. Methane hydrate stability in seawater. ***Geophysical Research Letters***, 21, 2115-2118.

Edwards, R.N., 1997. On the resource evaluation of marine gas hydrate deposits using a seafloor transient electric dipole-dipole method. ***Geophysics***, 62, 63-74.

Egorov, V.N., Luth, U., Luth, C, Gulin, M.B., 1998. Gas seeps in the submarine Dnieper Canyon, Black Sea: acoustic, video and trawl data. In: Luth U, Luth C, Thiel H (eds), ***Methane gas seep explorations in the Black Sea (MEGASEEBS), Project Report***. Ber Zent Meeres Klimaforsch, Univ Hamburg, Hamburg, pp 11–21.

Enachescu, M.E., 2004. Conspicuous deepwater submarine mounds in the northeastern Orphan Basin and on the Orphan Knoll, offshore Newfoundland. ***The Leading Edge***, 23, 1290-1294.

Englezos, P., and Bishnoi, P.R., 1988. Prediction of gas hydrate formation in aqueous solutions. ***American Institute of Chemical Engineers***, 34, 1718–1721.

Expedition 311 Scientists, 2005. Cascadia margin gas hydrates. ***IODP Preliminary Report, 311***. (doi:10:2204/iodp.pr.311.2005)

Expedition 311 Scientific Party, 2006. Cascadia margin gas hydrates. ***USIO Logging Summaries, IODP Expedition 311***.

Expedition 311 Scientists, 2006a. Expedition 311 summary. *In* Riedel, M., Collett, T.S., Malone, M.J., and the Expedition 311 Scientists. ***Proceedings of the Integrated Ocean Drilling Program, 311***: Washington, DC (Integrated Ocean Drilling Program Management International, Inc.). (doi:10.2204/iodp.proc.311.101.2006)

Expedition 311 Scientists, 2006b. Site U1328. *In* Riedel, M., Collett, T.S., Malone, M.J., and the Expedition 311 Scientists. ***Proceedings of the Integrated Ocean Drilling Program, 311***: Washington, DC (Integrated Ocean Drilling Program Management International, Inc.). (doi:10.2204/iodp.proc.311.101.2006)

Fink, C.R. and Spence, G.D., 1999. Hydrate distribution off Vancouver Island from multifrequency single-channel seismic reflection data. ***Journal of Geophysical Research***, vol. 104, No. B2, 2909-2922.

Ganguly, N., Spence, G.D., Chapman, N.R., and Hyndman, R.D., 2000. Heat flow variations from bottom-simulating reflectors on the Cascadia margin. ***Marine Geology***, 164, 53-68.

Gettrust, J., Chapman, R., Walia, R., Wood, W., Hannay, D., Lindwall, D., Spence, G., Louden, K., and Hyndman, R., 1999. High resolution seismic studies of deep sea gas hydrate using the DTAGS deep towed multichannel system. ***EOS*** (Transactions, American Geophysical Union), vol. 80, No. 38, 439-440.

Gettrust, J.F., Wood, W.T., and Spychalski, S.E., 2004. High-resolution MCS in deepwater. ***The Leading Edge***, 23(4), 374-377.

Grevemeyer, I., Kopf, A.J., Fekete, N., Kaul, N., Heesemann, M., Gennerich, H.H., Müller, M., Spieß, V., Wallmann, K., Weinrebe, W., 2004. Fluid flow through active mud dome Mound Culebra offshore Nicoya Peninsula, Costa Rica: evidence from heat flow surveying. Marine Geology 207, 145-157.

Hamilton, E.L., 1978. Sound velocity-density relations in sea-floor sediments and rocks. ***Journal of the Acoustical Society of America***, 63, 366-377.

He, T., Spence, G.D., Riedel, M., Hyndman, R.D., and Chapman, N.R., 2007. Fluid flow and origin of a carbonate mound offshore Vancouver Island: Seismic and heat flow constraints. ***Marine Geology***, 239, 83–98.

Hedberg, H., 1974. Relation of methane generation to undercompacted shales, shale diapirs and mud volcanoes. ***American Association of Petroleum Geologists Bulletin***, 58, 661-673.

Hensen, C., Wallmann, K., Schmidt, M., Ranero, C.R., Sahling, H., Suess, E., 2003. Fluid expulsion related to mud volcanism at Costa Rica continental margin – a window to the subducting slab. ***Geology***, 32, 201-204.

Hobro, J.W., Singh, S., and Minshull, T., 1998. Tomographic seismic studies of the methane hydrate stability zone in the Cascadia margin. ***Geological Society of London, Special Publication***, 137, 133-140.

Hooke, R., and Jeeves, T.A., 1961. "Direct Search" solution of numerical and statistical problems. ***Journal of the Association for Computing Machinery***, 8(2), 212-229.

Hovland, M., Judd, A.G., Burke, Jr. R.A., 1993. The global flux of methane from shallow submarine sediments. ***Chemosphere***, 26, Nos. 1-4, 559-578.

Hunt, J.M., 1979. ***Petroleum Geochemistry and Geology***. W.H. Freeman, San Francisco.

Hyndman, R.D., and Davis, E.E., 1992. A mechanism for the formation of methane hydrate and seafloor bottom-simulating reflectors by vertical fluid expulsion. ***Journal of Geophysical Research***, 97, 7025-7041.

Hyndman, R.D., Foucher, J.P., Yamano, M., Fisher, A., 1992. Deep sea bottom-simulating reflectors: calibration of the base of the hydrate stability field as used for heat flow estimates. ***Earth and Planetary Science Letters***, 109, 289-301.

Hyndman, R.D. and Spence, G.D., 1992. A seismic study of methane hydrate marine bottom simulating reflectors. ***Journal of Geophysical Research***, vol. 97, No. B5, 6683-6698.

Hyndman, R.D. and Wang, K., 1993. Thermal constraints on the zone of major thrust earthquake failure: the Cascadia subduction zone. ***Journal of Geophysical Research***, 98, 2039-2060.

Hyndman, R.D., Wang, K., Yuan, T., Spence, G.D., 1993. Tectonic sediment thickening, fluid expulsion, and the thermal regime of subduction zone accretionary prism: The Cascadian margin off Vancouver Island. ***Journal of Geophysical Research***, 98, 21865-21876.

Hyndman, R.D., Spence, G.D., Yuan, T., Davis, E.E., 1994. Regional geophysical and structure framework of the Vancouver Island margin accretionary prism. ***Proceedings of the Ocean Drilling Program, Initial Reports***, 146, 399-419.

Hyndman, R.D., 1995. The Lithoprobe corridor across the Vancouver Island continental margin: the structural and tectonic consequences of subduction. ***The Canadian Journal of Earth Sciences***, 32, 1777-1802.

Hyndman, R., and Dallimore, S., 2001. "Natural Gas Hydrate Studies in Canada". The Recorder. ***Canadian Society of Exploration Geophysicists***, Vol. 26.

Hyndman, R.D., Spence, G.D., Chapman, N.R., Riedel, M., and Edwards, R.N., 2001. Geophysical Studies of Marine Gas Hydrate in Northern Cascadia. In: C.K. Paull and W.P. Dillon (eds.), ***Natural gas Hydrates, Occurrence, Distribution and Detection***, Geophysical Monograph Series No. 124, pp. 273 – 295, American Geophysical Union (AGU).

Kopf, A.J., 2002. Significance of mud volcanism. ***Reviews of Geophysics***, 40(2), 1005.

Kvenvolden, K. A., 1993. Gas hydrates as a potential energy resource - a review of their methane content. In: D. G. Howell (ed.), ***The Future of Energy Gases*** - U.S. Geological Survey Professional Paper 1570: Washington, United States Government Printing Office, p. 555-561.

Lachenbruch, A.H., 1968. Rapid estimation of the topographic disturbance to superficial thermal gradients. ***Reviews of Geophysics***, 6, 365-400.

Lee, J.H., Baek, Y.S., Ryu, B.J., Riedel, M., and Hyndman, R.D., 2005. A seismic survey to detect natural gas hydrate in the East Sea of Korea. ***Marine Geophysical Researches***, 26, 51-59.

Lewin and Assocoaites Inc., 1983. ***Handbook of gas hydrate properties and occurrence***, 243 pp., Report for US Department of Energy, Office of Fossil Energy, Morgantown Energy Technology Center, contract DE-AC21-82MC19239, Washington, D.C.

Lewis, B.T.R., Cochrane, G.C., 1990. Relations between the location of chemosynthetic benthic communities and geologic structure on the Cascadia subduction zone. ***Journal of Geophysical Research***, 95, 8783-8793.

Lewis, R.M. and Torczon V., 2002. A Globally Convergent Augmented Lagrangian Pattern Search Algorithm for Optimization with General Constraints and Simple Bounds. ***SIAM Journal on Optimization***, 12(4), 1075-1089.

MacDonald, I.R., Guinasso, N.L., Jr., Sassen, R., Brooks, J.M., Lee, L., Scott, K.T., 1994. Gas hydrate that breaches the sea floor on the continental slope of the Gulf of Mexico. ***Geology***, 22, 699-702.

MacKay, M.E., Jarrard, R.D., Westbrook, G.K., Hyndman, R.D., and the Shipboard Scientific Party of ODP Leg 146, 1994. Origin of bottom simulating reflectors:

Geophysical evidence from the Cascadia accretionary prism. ***Geology***, 22, 459-462.

McIver, R.D., 1982. Role of naturally occurring gas hydrate in sediment transport. ***American Association of Petroleum Geologists Bulletin***, vol. 66, 789-792.

Mi, Y., 1998. Seafloor sediment coring and multichannel seismic studies of gas hydrate, offshore Vancouver Island. ***MSc thesis***, University of Victoria.

Milkov, A.V., 2000. Worldwide distribution of submarine mud volcanoes and associated gas hydrates. ***Marine Geology***, 167, 29-42.

Milkov, A.V., 2004. Global estimates of hydrate-bound gas in marine sediments: how much is really out there? ***Earth-Science Reviews***, vol. 66 (3-4), 183-197. (doi:10.1016/j.earscirev.2003.11.002)

Nouzé, H., Henry, P., Noble, M., Martin, V., Pascal, G., 2004. Large gas hydrate accumulations on the eastern Nankai Trough inferred from new high-resolution 2-D seismic data. ***Geophysical Research Letters***, 31(13), L13308. (doi: 10.1029/2004GL019848)

Novosel, I., Spence, G.D., and Hyndman, R.D., 2005. Reduced magnetization produced by increased methane flux at a gas hydrate vent. ***Marine Geology***, 216, 265–274. (doi:10.1016/j.margeo.2005.02.027)

Riedel, M., 2001. ***3D seismic investigations of northern Cascadia Marine Gas Hydrates***, PhD dissertation, University of Victoria, Victoria, British Columbia.

Riedel, M., Hyndman, R.D., Spence, G.D., and Chapman, N.R., 2002. Seismic Investigations of a Vent Field Associated with Gas Hydrates, Offshore Vancouver Island. ***Journal of Geophysical Research***, 107 (B9), 2200. (doi: 10.1029/2001JB000269)

Riedel, M., Novosel, I., Spence, G.D., Hyndman, R.D., Chapman, N.R., Lewis, T., 2006a. Geophysical and geochemical signatures associated with gas hydrate–related venting in the northern Cascadia margin. ***Geological Society of America Bulletin***, 118 (1), 23-38.

Riedel, M., Collett, T.S., Malone, M.J., and the Expedition 311 Scientists, 2006b. ***Proceedings of the Integrated Ocean Drilling Program, Volume 311***: Washington, DC (Integrated Ocean Drilling Program Management International, Inc.). (doi:10.2204/iodp.proc.311.2006)

Ritger, S., Carson, B., Suess, E., 1987. Methane-derived authigenic carbonates formed by subduction-induced pore-water expulsion along the Oregon/Washington margin. ***Geological Society of America Bulletin***, 98, 147-156.

Roberts, H., Hardage, B., Shedd, W., and Hunt J.Jr., 2006. Seafloor reflectivity–an important seismic property for interpreting fluid/gas expulsion geology and the presence of gas hydrate. ***The Leading Edge***, 25(5), 620–628.

Rowe, M.M., and Gettrust, I.F., 1993. Fine structure of methane hydrate-bearing sediments on the Blake outer ridge as determined from deep-tow multichannel seismic data. ***Journal of Geophysical Research***, 98(B1), 463–474.

Scholl, D.W., and Cooper, A.K., 1978. VAMPs – possible hydrocarbon bearing structures in Bering Sea Basin. ***American Association of Petroleum Geologists Bulletin***, 62, 2481-2488.

Schwalenberg, K., Willoughby, E., Mir, R., and Edwards, R.N., 2005. Marine gas hydrate electromagnetic signatures in Cascadia and their correlation with seismic blank zones. ***First Break***, 23, 57–63.

Shipboard Scientific Party, 1998. 1. Introduction: Background, scientific objectives, and principal results for Leg 175 (Benguela current and Angola-Benguela upwelling systems), in Wefer, G., Berger, W.H., et al., ***Proceedings of the Ocean Drilling Program, Initial reports, Volume 175***: College Station, Texas, Ocean Drilling Program, p. 7–23.

Shine, K.P., 1990. Climate change. In: J.T. Hougthon, G.J. Jenkins and J.J. Ephrams (eds.), ***The IPCC Scientific Assessment***, Cambridge Univ. Press, New York.

Singh, S.C., Minshull, T.A., Spence, G.D., 1993. Velocity structure of a gas hydrate reflector. ***Science***, 260, 204-207.

Sloan, E.D., Jr., 1990. ***Clathrate hydrates of Natural Gases***, Marcel Dekker, Inc., New York, 641 pp.

Spence, G.D., Minshull, T.A., and Fink, C.R., 1995. Seismic studies of methane hydrate, offshore Vancouver Island. ***Proceedings of the Ocean Drilling Program, Scientific results***, vol. 146, 163-174.

Spence, G.D., Hyndman, R.D., Chapman, N.R., Riedel, M., Edwards, N., and Yuan, J., 2000. Cascadia Margin, Northeast Pacific Ocean: hydrate Distribution from Geophysical Investigations. In: ***Natural Gas Hydrate in Ocean and Permafrost Environments*** (ed. M.D. Max, Kluwer Academic Publisher).

Spence, G., Coffin, R., and Hoehne, J., 2002. ***VENTFLUX2: Report of PGC01-03, C.C.G. vessel John P. Tully, 23 July–12 August 2001, cruise report***: Victoria, Canada, University of Victoria, 135 p.

Suess, E., Bohrmann, G., von Huene, R., Linke, P., Wallmann, K., Lammers, S., and Sahling H., 1998. Fluid venting in the eastern Aleutian subduction zone. ***Journal of Geophysical Research***, v. 103, no. B2, p. 2597–2614.

Suess, E., Torres, M.E., Bohrmann, G., Collier, R.W., Rickert, D., Goldfinger, C., Linke, P., Hauser, A., Sahling, H., Heeschen, K., Jung, C., Nakamura, K., Greinert, J., Pfannkuche, O., Tréhu, A., Klinkhammer, G., Whiticar, M.J., Eisenhauer, A., Teichert, B., and Elvert, M., 2001. Seafloor methane hydrates at Hydrate Ridge, Cascadia margin. In: Paull, C.K., Dillon W.P. (Eds.), ***Natural Gas Hydrates: Occurrence, Distribution and Detection***, Geophysical Monograph, vol. 124, American Geophysical Union, pp. 87-98.

Tréhu, A.M., Torres, M.E., Moore, G.F., Suess, E., Bohrmann, G., 1999. Temporal and spatial evolution of a gas hydrate-bearing accretionary ridge on the Oregon continental margin. ***Geology***, 27(10), 939-942.

Tréhu, A.M., Bohrmann, G., Torres, M.E., and Colwell, F.S. (Eds.), 2006. ***Proceedings of the Ocean Drilling Program, Scientific Results, 204***: College Station, TX (Ocean Drilling Program). (doi:10.2973/odp.proc.sr.204.2006)

Vogt, P.R., Gardner, J., Crane, K., Sundvor, E., Bowles, F., Cherkashev, G., 1999. Ground-truthing 11- to 12-kHz side-scan sonar imagery in the Norwegia-Greenland Sea: Part I: Pockmarks on the Vestnesa Ridge and Storegga slide margin. ***Geo-Marine Letters***, Vol. 19(1-2), 97-110. (doi:10.1007/s003670050098)

Walia, R., and Hannay, D., 1999. Source and receiver geometry corrections for deep towed multichannel seismic data. ***Geophysical Research Letters***, vol. 26, No. 13, 1993-1996.

Westbrook, G.K., and Smith, M.J., 1983. Long decollements and mud volcanoes: Evidence from the Barbados Ridge Complex for the role of high pore-fluid pressure in the development of an accretionary complex. ***Geology***, 11, 279-283.

Westbrook, G.K., Carson, B., Musgrave, R.J., and Shipboard Scientific Party of ODP Leg 146, 1994. ***Proceedings of the Ocean Drilling Program, Initial Reports***, Vol. 146 (Part 1).

Willoughby, E.C., and Edwards, R.N., 1997. On the resource evaluation of marine gas-hydrate deposits using seafloor compliance methods. ***Geophysical Journal International***, 131, 751-766.

Willoughby, E.C., and Edwards, R.N., 2000. Shear velocities in Cascadia from seafloor compliance measurements. ***Geophysical Research Letters***, 27(7), 1021–1024.

Willoughby, E.C., Schwalenberg, K., Edwards, R.N., Spence, G.D., and Hyndman, R.D., 2005. Assessment of marine gas hydrate deposits: a comparative study of seismic,

electromagnetic and seafloor compliance methods. ***Fifth International Conference of Gas Hydrates***, 3:802–811.

Wood, W.T., Gardner, J., Hagen, R.A., Coffin, R.B., Pohlman, J.W., Hart, P.E., and Hutchinson, D.R., 2004. Modeling Heat and Fluid Flux of Seafloor Mounds in the Gulf of Mexico (Abstract). *In*: Proceedings, 85(47), AGU Fall Meeting, San Francisco, Ocean Sciences General Contributions: Gas Hydrates I OS34B-08.

Worrall, D.M., Snelson, S., 1989. Evolution of the northern Gulf of Mexico, with emphasis on Cenozoic growth faulting and the role of salt. In: Bally, A.W., Palmer, A.R. (Eds.), The Geology of North America, vol. A: The Geology of North America – An Overview. ***Geological Society of America***, Boulder, CO, pp. 97-138.

Xu, W., and Ruppel, C., 1999. Predicting the occurrence, distribution, and evolution of methane gas hydrate in porous sediments. ***Journal of Geophysical Research***, 104, 5081-5095.

Yilmaz, Ö., 2001. ***Seismic Data Analysis: Processing, Inversion, and Interpretation of Seismic Data***, 2nd edition, Society of Exploration Geophysicists: Stephen M. Doherty (Ed.).

Yorath, C.J., Clowes, R.M., MacDonald, R.D., Spencer, C., Davis, E.E., Hyndman, R.D., Rohr, K., Sweeney, J.F., Currie, R.G., Halpenny, J.F., and Seemann, D.A., 1987. ***Marine multichannel seismic reflection, gravity and magnetic profiles—Vancouver Island continental margin and Juan de Fuca Ridge***. Open File Report, Geological Survey of Canada.

Yuan, T., and Edwards, R.N., 2000. Towed seafloor electromagnetics and assesment of gas hydrate deposits. ***Geohysical Reserch Letters***, 27, 2397-2400.

Yuan, T., Spence, G.D., and Hyndman, R.D., 1994. Seismic velocities and inferred porosities in the accretionary wedge sediments at the Cascadia margin. ***Journal of Geophysical Research***, 99, 4413-4427.

Yuan, T., Hyndman, R.D., Spence G.D., and Desmos, B., 1996. Seismic velocity increase and deep-sea gas hydrate concentration above a bottom-simulating reflector on the northern Cascadia continental slope. ***Journal of Geophysical Research***, vol. 101, No. B6, 13665-13671.

Yuan, T., Spence, G.D., Hyndman, R.D., Minshull, T.A., and Singh, S.C., 1999. Seismic velocity studies of a gas hydrate bottom-simulating reflector on the northern Cascadia continental margin: Amplitude modelling and full waveform inversion. ***Journal of Geophysical Research***, vol. 104, No. B1, 1179-1191.

Yuan, J., and Edwards, N., 2001. Towed seafloor electromagnetics and assessment of gas hydrate deposits. ***Geophysical Research Letters***, 27(16), 2397-2400.

Zelt, C.A., and Smith, R.B., 1992. Seismic travel-time inversion for 2-Dcrustal velocity structure. ***Geophysical Journal International***, 108, 16–34.

Zühlsdorff, L., Spiess, V., Hübscher, C., and Breitzke, M., 1999. Seismic reflectivity in sediments at the eastern flank of the Juan de Fuca Ridge: Evidence for fluid migration? ***Journal of Geophysical Research***, vol. 104, No. B7, 15351-15364.

Zühlsdorff, L., Spiess, V., Hübscher, C., Villinger H., and Rosenberger, A., 2000. Implications for focused fluid transport at the northern Cascadia accretionary prism from a correlation between BSR occurrence a d near-sea-floor reflectivity anomalies imaged in a multi-frequency seismic data set. ***Journal International Journal of Earth Sciences***, 88, 655-667. (doi: 10.1007/s005310050295)

Zühlsdorff, L., and Spiess, V., 2004. Three-dimensional seismic characterization of a venting site reveals compelling indications of natural hydraulic fracturing. ***Geology***, v. 32, no. 2, p. 101–104. (doi: 10.1130/G19993.1)

Zwart, G., Moore, J.C., and Cochrane, G.R., 1996. Variations in temperature gradients identify active faults in the Oregon accretionary prism. ***Earth and Planetary Science Letters***, 139, 485-495.

Zykov, M.M., and Chapman, N.R., 2004. 3-D velocity model of hydrocarbon vent site in Cascadia region offshore Vancouver Island. ***AAPG Hedberg Research Conference: Gas Hydrates: Energy Resource Potential and Associated Geologic Hazards***, Vancouver, 12–16 September, 2005.

Appendix A

Excluded Process from the 2001 Teledyne SCS Data

The 2001 Teledyne survey originally planed using two streamers to achieve uniform spatial sampling in both horizontal directions – suitable for psudo-3D migration. Although the second streamer was caught in ship's screw and lost at the beginning of the survey, attempts still were made for psudo-3D of seismic grid and associated trace interpolation for empty bins and 2.5D time migration. However the image result is not satisfactory, due to resolution problems associated with the extensive trace interpolation required to fill empty bins from missing shots or ship track deviations; all these processes were excluded from the final processing flow.

A.1 Psudo-3D Binning and Trace Interpolation

The psudo-3D binning process was finished with GEOMETRY application of Claritas, based on midpoints of shot and receiver positions. Although the nominal ship track separation was 25 m, the streamer was not deployed on the ship mid line and the ship often deviated the ideal course when navigating with variable wind and wave conditions, leading to irregular midpoints pattern on the survey map (Figure A.1). To utilize the midpoints in inline direction and expand the resolution in crossline directions, the bin was set as spacing of 15 m in both directions. The summary of this psudo-3D gathering is listed in Table A.1. Due to missed shots or ship track deviations and relative small bin size in crossline direction, there were many empty bins in the pseudo-3D grid (Figure A.1; Table A.1).

To achieve continuous data set, new traces were interpolated among the existing ones. Figure A.2(a) and Figure A.3(a) show typical inline and crossline seismic sections after pseudo-3D gathering, respectively. It is apparent that inline grid has much larger gap (continuous empty bins) than crossline grid. Therefore, filling the empty bins with traces interpolated was done in crossline direction. In Claritas the trace interpolation was done in the log-frequency domain, such that the amplitude and phase were interpolated

separately. In practice, a process of spherical divergence compensation is applied before trace interpolation to achieve a stable and consistent output. Figure A.2(b) and Figure A.3(b) show the seismic images after traces interpolated. Although the amplitudes of new traces seem reasonable and improve the image quality in crossline grid of Figure A.3(b), the interpolated traces in inline grid are somewhat noisier and weaker in amplitude at previous gap positions when compared to neighboring original traces (Figure A.2).

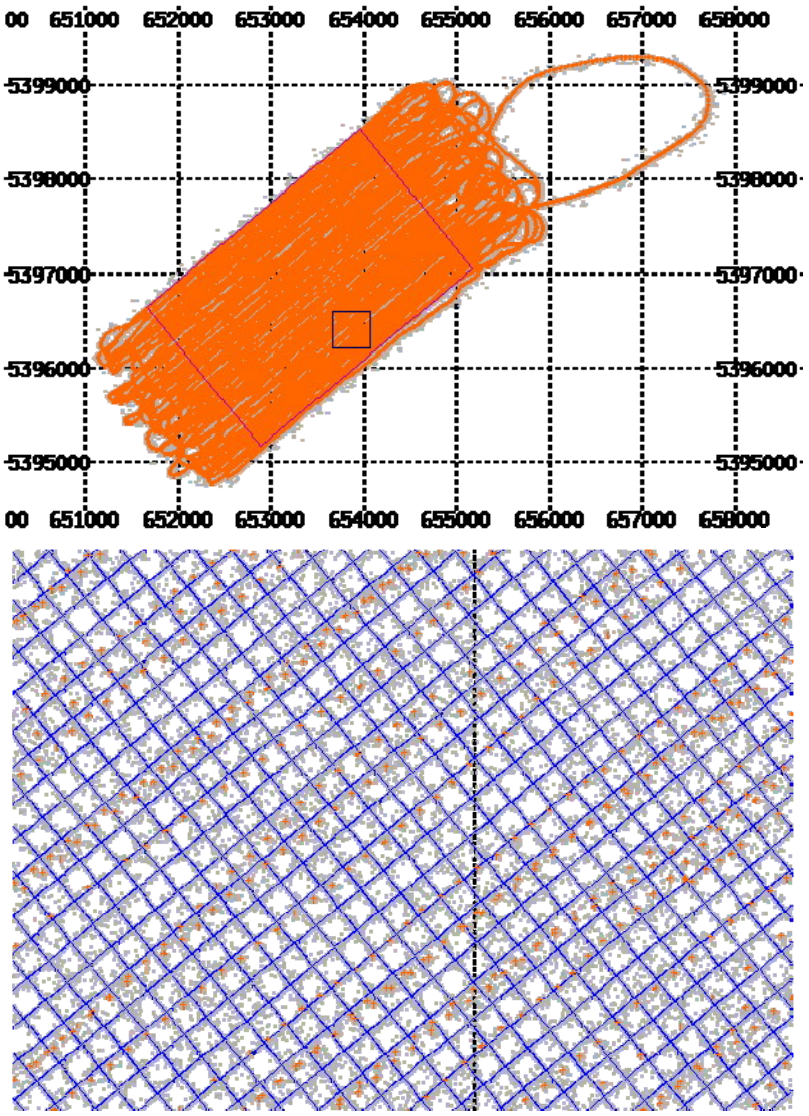

Figure A.1 The top small print shows the psudo-3D binning area (red box) for the 2001 Teledyne SCS data and selected area (black box) to blow out in the below big print, which shows the irregular midpoint (cross in orange color) pattern of the survey and empty bins (blue boxes).

Table A.1 Summary of 3D Binning Result For 2001 Teledyne Data

Geometry database file : cr_total1.geom
Gather type : 3-D grid

CDP numbers : 10001000 to 11281198 (increment 1)
Inline number: 1000 to 1128
Crossline number: 1000 to 1198
First bin co-ordinate : 652877.00 5395158.00
Last bin co-ordinate : 653955.88 5398526.00
In-line bin spacing : 15.00
Cross-line bin spacing : 15.00
Bin size along line : 7.50
perpendicular to line : 7.50
(Bin sizes are half-widths, from bin centre to the edge)

Each trace only allowed in one CDP bin
Minimum offset included : -10000000.00
Maximum offset included : 10000000.00

Total number of CDP bins : 25671
Maximum no. of traces in any CDP bin : 5
Total number of traces used in gather : 16398
Number of LIVE traces not in any CDP : 155 (1%)

Reasons for lost traces :
Traces not in a bin (in-line) : 125
Traces not in a bin (perpendicular) : 30
Total : 155

Histogram of no. of traces in each CDP bin (CDP fold) :

CDP Fold	No of bins
0	13267
1	9039
2	2787
3	529
4	47
5	2

Empty bin ratio: 51.68%(=13267/25671)
Statistics for number of bins for any one trace :
0 traces were dead
10806 traces did not fall in any bins
16398 traces fell in one bin

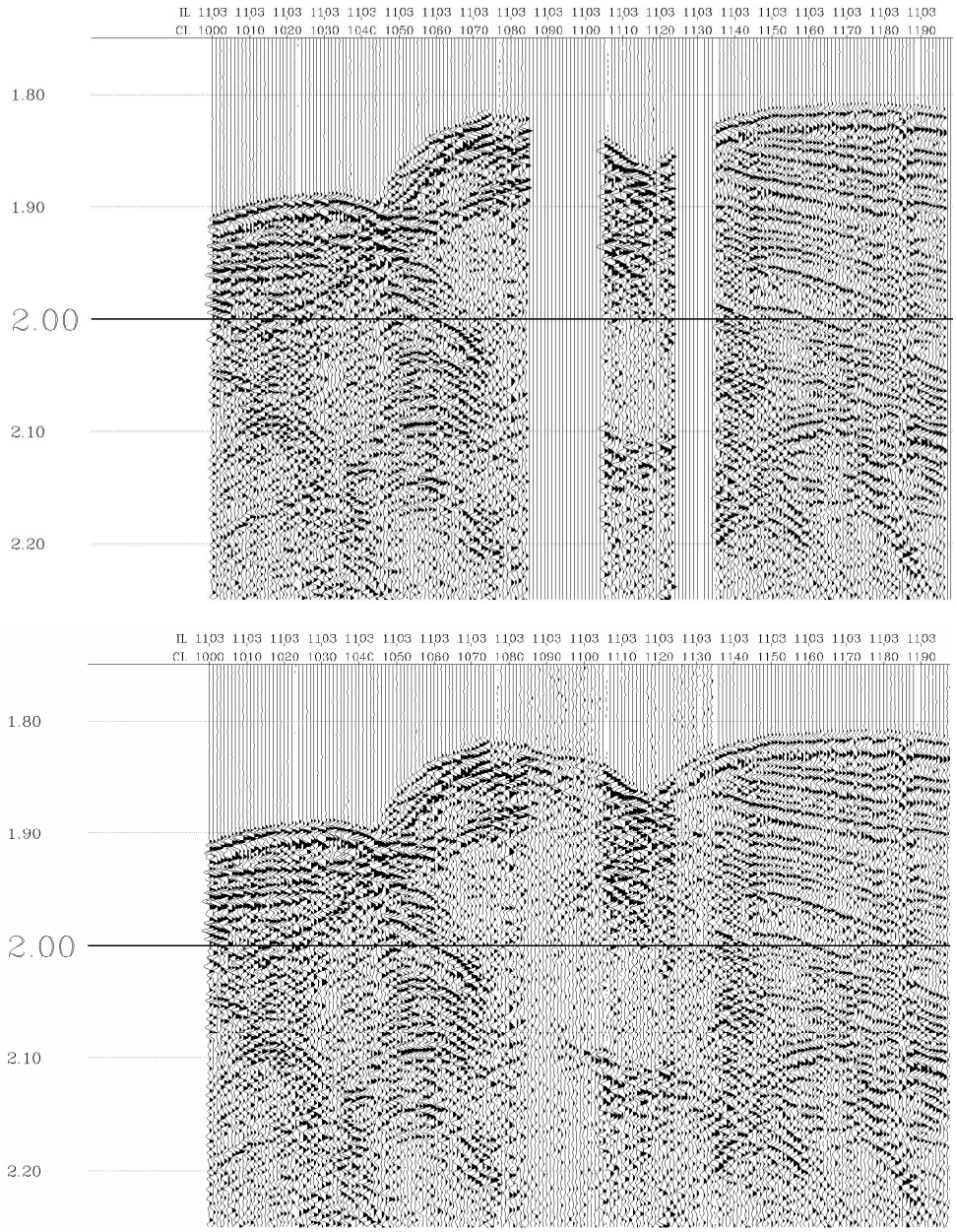

Figure A.2 (a) Original pseudo-3D grid inline IL-1103 showing typical inline seismic section with empty bins. (b) Interpolated seismic section of IL-1103. Spherical divergence compensation with factor *t* and zero-phase Butterworth band-pass filter with frequency limits of 15-40 to 150-220 Hz also were applied to both images.

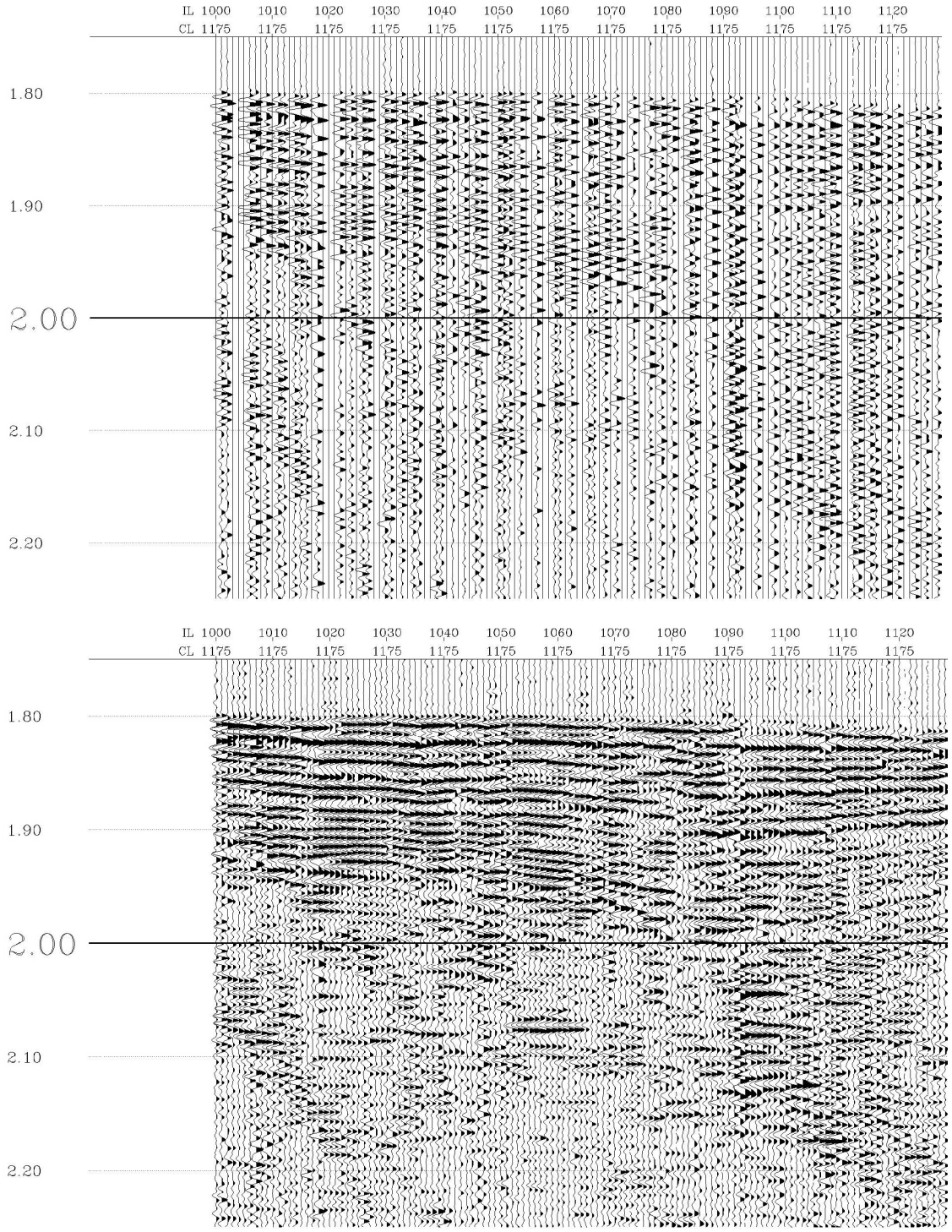

Figure A.3 (a) Original pseudo-3D grid crossline CL-1175 showing typical cross-line seismic section with empty bins. (b) Interpolated seismic section of CL-1175. Spherical divergence compensation with factor *t* and zero-phase Butterworth band-pass filter with frequency limits of 15-40 to 150-220 Hz also were applied to both images.

A.2 Images after 2.5D Migration

One of the main advantages of pseudo-3D processing is to make time slices. Figure A.4 shows seismic structures below the Cucumber Ridge after finite time migration at time slice of 1934 ms and two reference lines: inline section MI-61 and crossline section MX-88. The inline image MI-61 shows unstratified central mound, stratified slope sediments, deformation, unconformity, BSRs, possible fracture zone and gas accumulation zone. However, the image quality is not satisfactory in the inline direction because the extensive trace interpolation produced images with reduced resolution rather than the opposite should have happened. For images of time slice and crossline direction, it is hard to distinguish meaningful seismic events. Therefore, psedudo-3D processing of this case is not helpful to improve seismic image or find seismic features. It is better not to include psedudo-3D and associated 2.5D migration into final data processing for the 2001 Teledyne data set.

(a)

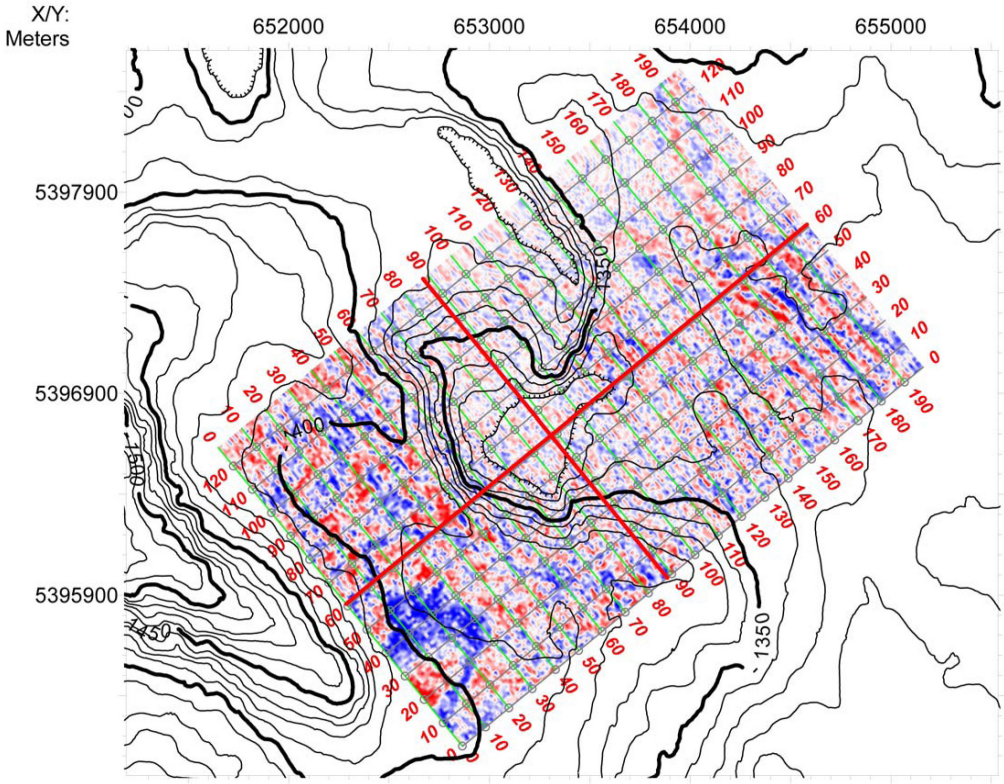

(b)

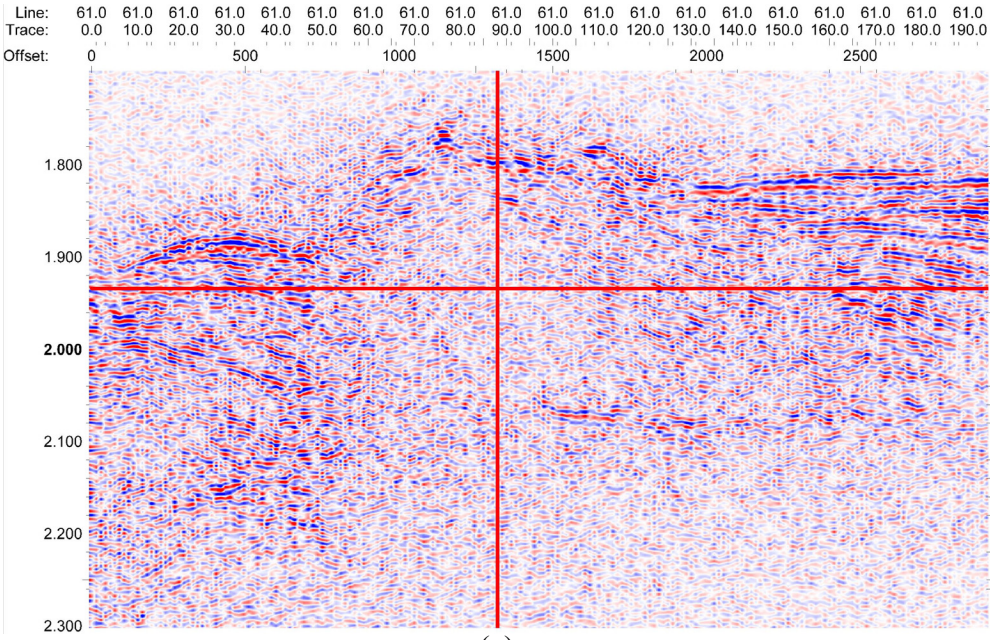

(c)

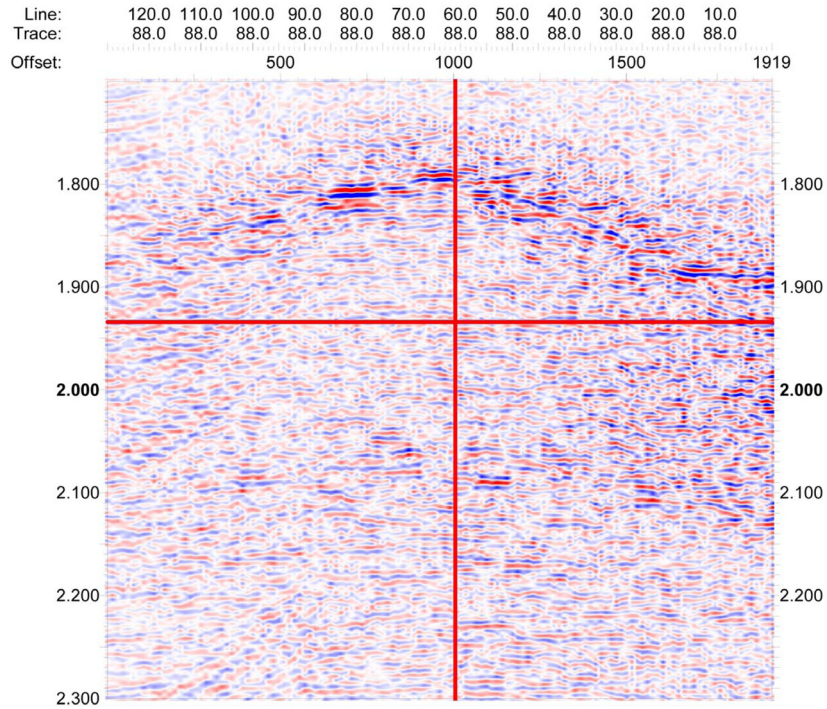

Figure A.4 Seismic structures below the carbonate mound. (a) Time slice at 1934 ms. (b) Inline section MI-61 across the central mound, showing unstratified central mound, stratified slope sediments, deformation, unconformity, BSRs, possible fracture zone and gas accumulation zone. (c) Cross-line section MX-88 across the central mound.

Appendix B

Frequency-Matching Method Used to the 2004 Teledyne Data

The 2004 Teledyne seismic survey used the same hydrophone streamer (Teledyne Ltd.) as in 2001 experiment, but the seismic source was a 120 cu. in. single airgun instead of the 40 cu. in. sleeve airgun in 2001.

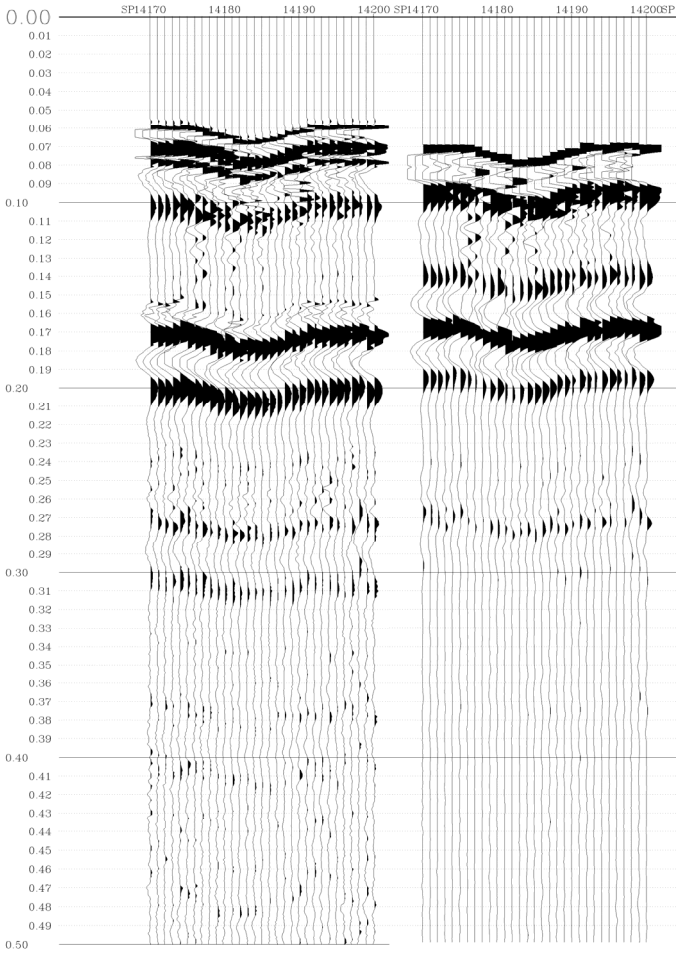

Figure B.1 (left) Typical direct arrivals of the 2004 Teledyne single channel seismic data after the spherical divergence correction. (right) Corresponding autocorrelation function with time shift to approximately match bubble events.

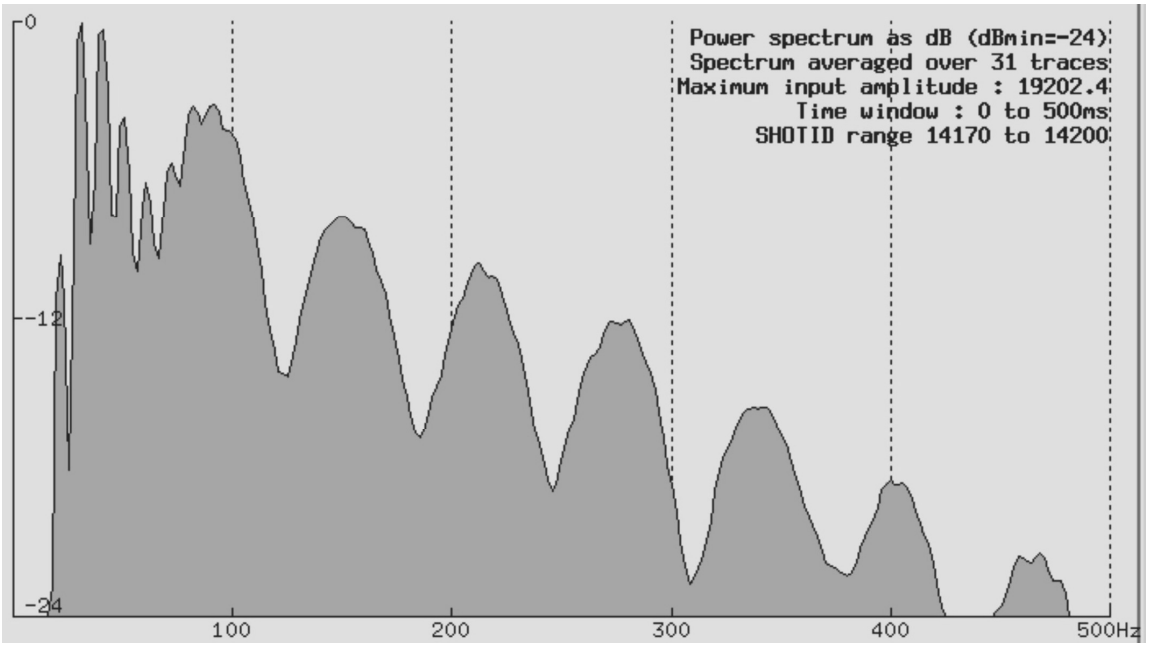

Figure B.2 Ringy power spectrum of direct arrivals (Figure B.1), from left to right showing 25 Hz lowcut (Preamplier filter), harmoniousness of 10 Hz bubble period, dominant frequency of 80-90 Hz, and other harmoniousness of this dominant frequency to the tail. Therefore, the bandwidth of direct signals is about 25-125 Hz.

Crossing track 4 of Nootka survey was selected as the test data. The primary release of the compressed air and the first 2 obvious bubbles are presented in the direct arrivals, separated by ~100 ms (Figure B.1). The power spectrum of direct arrivals has a ringy pattern, showing modulations of 10 Hz bubble period, dominant frequency of 80-90 Hz, and other modulations of this dominant frequency (Figure B.2). Therefore, the bandwidth of direct signals is about 25-125 Hz. Obvious bubble events also occurred in sediment reflections (Figure B.3).

The design window from 3.35 to 4.5 s for the Frequency-Matching method was chosen from the seafloor to depths well below the BSR. Figure B.4 and Figure B.5 show the extracted wavelet and corresponding computed amplitude spectrum for the test data of Figure B.3. The excellent signal-noise ratio (Figure B.5) implied that the extracted wavelet was statistically successful and ready for signature deconvolution.

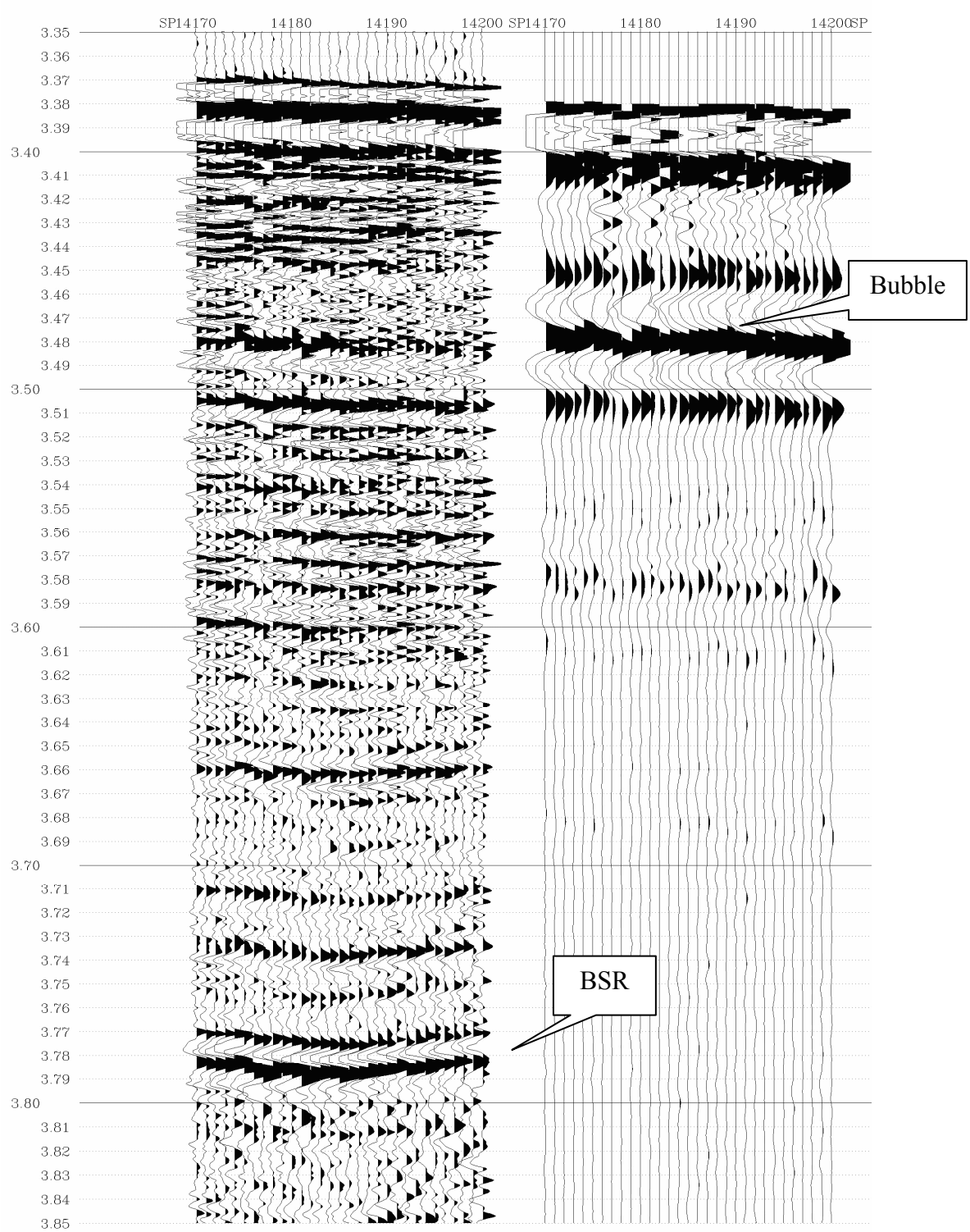

Figure B.3 (left) uppermost sediments reflections with bubble ghost and clear BSR (after the spherical divergence compensation with factor t). (right) Corresponding autocorrelation function with time shift to approximately match bubble events.

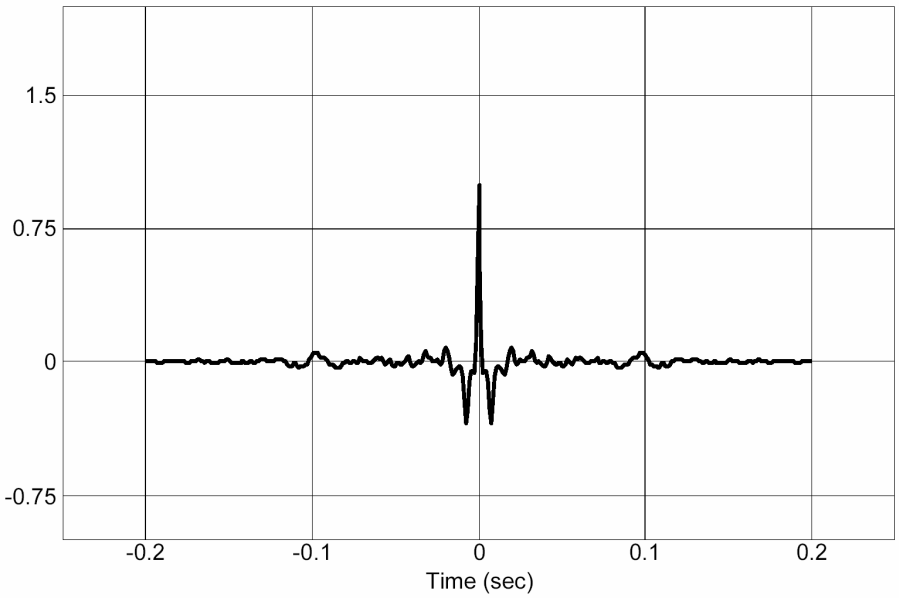

Figure B.4 Extracted wavelet from the recorded seismogram in Figure B.3 using the Frequency-Matching method from the Kingdom Suite. The wavelet is zero phase and 400 ms in length with sample interval of 1 ms.

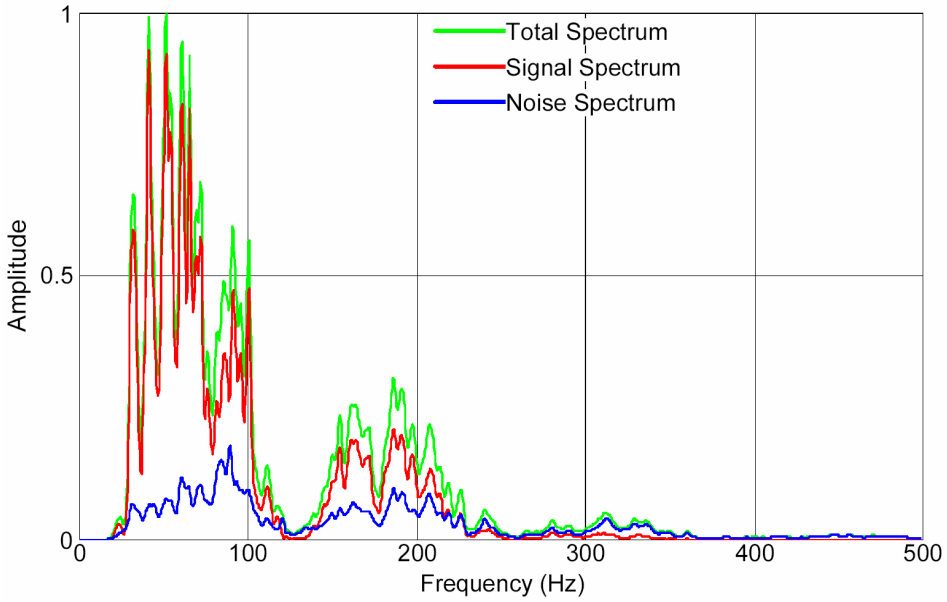

Figure B.5 The computed amplitude spectra of the 2004 Teledyne data for the Frequency-Matching method. The green line is the total amplitude of the input data, the red line is the amplitude of extracted wavelet "signal", and the blue line is the amplitude of "noise" (remnant of green subtracting red). The high signal-noise ratio indicated that the Frequency-Matching method can produce good source signature wavelet for the 2004 Teledyne data.

Appendix C

Equations for DTAGS Cable Geometry

C.1 Equation 4.3 and Equation 4.4

As illustrated in Figure C.1, the ray path ***L*** of seasurface reflection ***ABC*** is equal to the straight line ***AC'*** in geometry using the mirror reflection rule, where ***C'*** is the mirroring point of ***C*** relative to the horizontal seasurface.

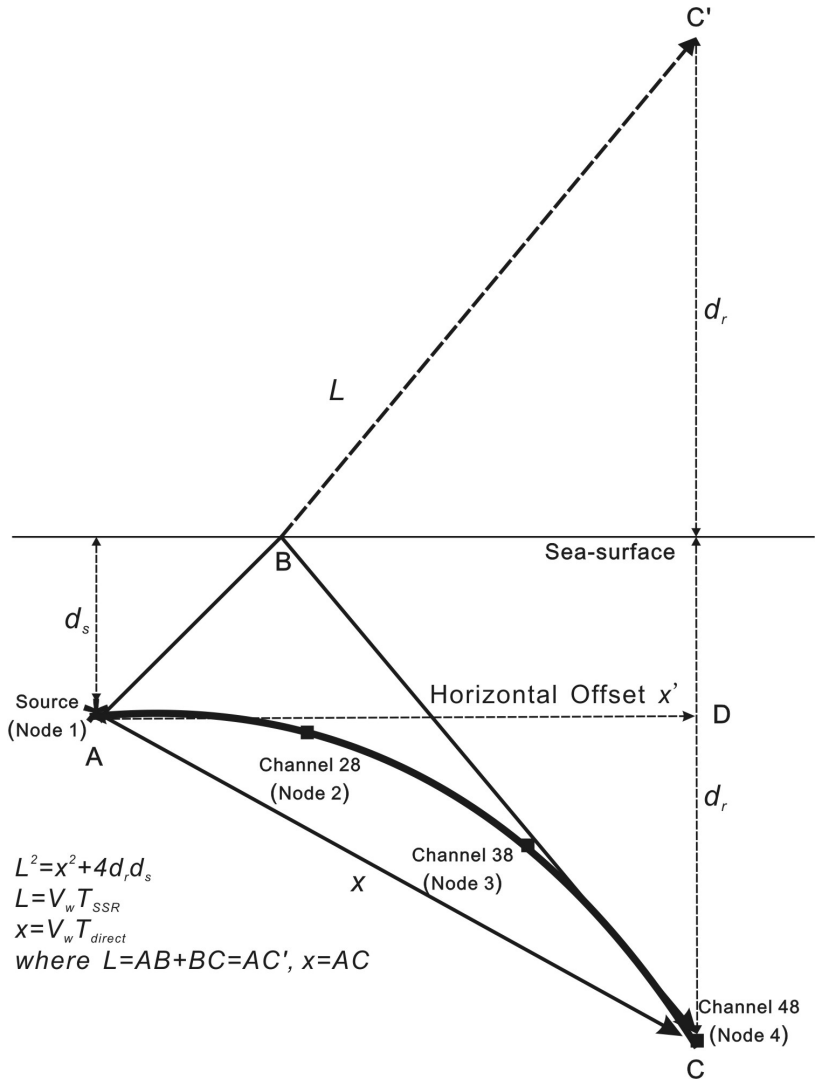

Figure C.1 Illustration of ray path related with Equation 4.3 and Equation 4.4.

Thus,

$$L^2 = (AC')^2 = (AD)^2 + (DC')^2 = x^2 - (CD)^2 + (DC')^2,$$

and then

$$(V_w T_{SSR})^2 = (V_w T_{direct})^2 - (d_r - d_s)^2 + (d_r + d_s)^2$$
$$\Rightarrow V_w = \sqrt{\frac{4 d_r d_s}{T_{SSR}^2 - T_{direct}^2}} \quad .$$

After V_w is determined with Equation 4.3, the horizontal offset ***x'*** (***AD***) can be directly calculated using relation $(AD)^2=(AC)^2-(CD)^2$, which results in Equation 4.4.

C.2 Equation 4.9 and Equation 4.10

According Figure 4.22 and Equation 3.1,

$$Ve = 1516 + 0.5556 \times D,$$

and the velocity increasing ratio from seawater ***Vw*** at seafloor to ***Ve*** at depth of ***D*** mbsf in sediments is

$$dV = (Ve - Vw)/D.$$

Thus the velocity potential ***Vs*** on DE is

$$Vs = Vw + dV \cdot s,$$

and the linear average velocity ***Va*** of DE is

$$Va = (Vw + Vs)/2.$$

Using condition of equal travel time and above substitutes, the following equation is obtained

$$\frac{s}{Va} = \frac{t - t_0}{2} \quad \Rightarrow \quad \frac{s}{\left(Vw + \left(Vw + \frac{Ve - Vw}{D} \cdot s\right)\right)/2} = \frac{t - t_0}{2},$$

and then

$$4s = \left(Vw + \left(Vw + \frac{Ve - Vw}{D} \cdot s \right) \right) \cdot (t - t_0)$$

$$\Rightarrow \quad \left[4 - \frac{(Ve - Vw)(t - t_0)}{D} \right] s = 2Vw(t - t_0) \qquad .$$

$$\Rightarrow \quad s = \frac{2Vw(t - t_0)}{4 - \frac{(Ve - Vw)(t - t_0)}{D}} = \frac{Vw}{\frac{2}{t - t_0} - \frac{Ve - Vw}{2D}}$$